Mechanistic models for the evaluation of biocatalytic reaction conditions and biosensor design optimization

Semenova, Daria

Publication date:
2018

Document Version
Publisher's PDF, also known as Version of record

Mechanistic models for the evaluation of biocatalytic reaction conditions and biosensor design optimization

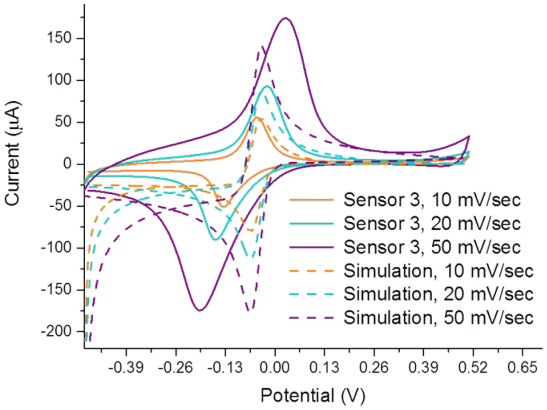

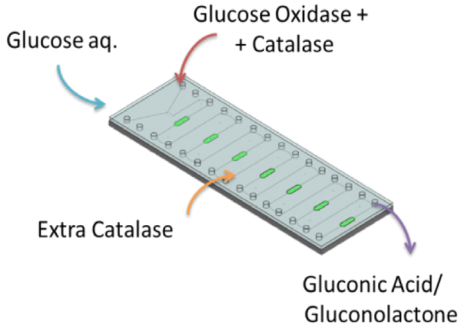

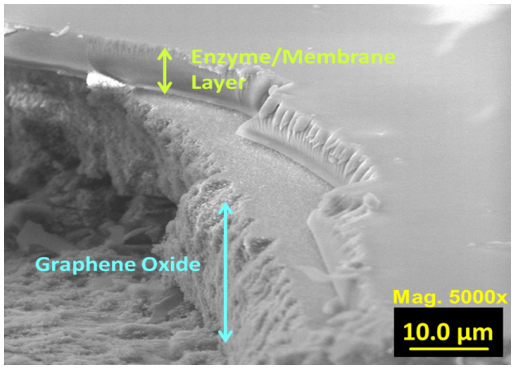

Daria Semenova

PhD Thesis

February 2018

DTU Chemical Engineering
Department of Chemical and Biochemical Engineering

Mechanistic models for the evaluation of biocatalytic reaction conditions and biosensor design optimization

Ph.D. Thesis

Daria Semenova

Process and Systems Engineering Centre

Department of Chemical and Biochemical Engineering

Technical University of Denmark

February 2018

Address: Process and Systems Engineering Center (PROSYS)

Department of Chemical and Biochemical Engineering

Technical University of Denmark

Building 229

Dk-2800 Kgs. Lyngby

Denmark

Phone: +45 4525 2800

Web: www.kt.dtu.dk/forskning/prosys

Print: STEP

DTU Chemical Engineering
Department of Chemical and Biochemical Engineering

"Facts not explained by the existing theories are probably the most valuable for science, for their study is most likely to lead to its early advancement."

Alexander Mikhaylovich Butlerov

Russian chemist, one of the principal creators of the theory of chemical structure for organic compounds
(1828 – 1886)

"What is impossible today will become possible tomorrow."

Konstantin Eduardovich Tsiolkovsky

Russian and Soviet rocket scientist and pioneer of the astronautic theory
(1857 – 1935)

"Only the controversy stimulates the progress in science. It must be emphasized, but not to be hidden."

Sergey Petrovich Kapitsa

Russian physicist
(1928 – 2012)

Preface

The proposed thesis manuscript was prepared in order to partly fulfil the general requirements for acquiring a PhD degree at the Technical University of Denmark (DTU). The presented research was accomplished in the period from August 2014 to February 2018 and supported by the EUROMBR project that received funding from the People Programme (Marie Curie Actions, Multi-ITN) of the European Union's Seventh Framework Programme for research, technological development and demonstration under grant agreement no. 608104. The work demonstrated in the thesis was mainly developed at the Process and Systems Engineering Center (PROSYS) at the Department of Chemical and Biochemical Engineering (DTU Kemitkenik) under supervision of Professor Krist V. Gernaey and co-supervision of Doctor Alexandr Zubov and Associate Professor Ulrich Krühne. The external research projects were held at the following universities and research institutes:

- Oulu University, at the Measurement Technology Unit (MITY), Kajaani, Finland under supervision of Dr. Adama M. Sesay from June to August 2015.
- Technical University of Graz (TU Graz), at the Institute of Analytical Chemistry and Food Chemistry (Chemo- and Biosensors Group) and the Institute of Biotechnology and Biochemical Engineering, Graz, Austria under supervision of Assoc. Prof. Torsten Mayr and Dr. Juan Manuel Bolivar, respectively, from November to December 2016.
- Leibniz Institute for New Materials (INM), at the Chemical Analytics and the Physical Analytics Divisions, Saarbrücken, Germany under supervision of Dr. Yuliya E. Silina and Dr. Marcus Koch, respectively, in September 2017.
- Università di Roma Tor Vergata, at the Department of Chemical Science and Technologies, Rome, Italy, under supervision of Prof. Laura Micheli in September 2017.

Acknowledgments

The time of my PhD work coincided with a very upsetting phenomenon in the world history – demonization of the Soviet Soldier and rewriting the results of World War II. Therefore, first I would like to thank all my relatives, who were involved in the Great Patriotic War. Most of them have lost their youth, dreams, happiness, families and the rest of their lives fighting for our future and all of us living in a free world. And thanks to them I could be today in Denmark and present the results of the work that has been done in collaboration with people who might have never seen this world. During my PhD, I had an opportunity to travel all over the globe and observe a great miracle: people of all nationalities, religions, sexual orientations, with or without disabilities are being friends that live, work and try all together to make this world a better place to be. And this was one of the most inspiring and motivating thoughts that helped me to go through my entire research together with help and support of many great people on my side.

Therefore, I would like to express my sincere gratitude to all of my supervisors Professor Krist V. Gernaey, Dr. Alexandr Zubov and Associate Professor Ulrich Krühne for the given trust and opportunity to begin my scientific journey as a part of PROSYS Research Centre. Moreover, Alexandr Zubov and Krist V. Gernaey are greatly acknowledged for all their patience and understanding, high level of support (even of the craziest ideas and plans) and very fruitful discussions in the past 3.5 years. Thank you for always finding the right words of motivation and encouragement that not only allowed me to grow as a researcher but also as a person. And what was the most priceless in this collaboration – that you have never doubted in me and always believed in what I do.

I would like to acknowledge all my colleagues and friends from inside and outside DTU, as well as from the EUROMBR project. I want to thank all my fantastic colleagues from PROSYS for all that great fun we shared together. A very special thank you deserve Katrin, Peam, Francesco & Çiğdem, Carolina & Tiago, Hilde, Carina & Søren together with Luca, Inês, Stefano & Elena together with Lorenzo & Agnese, Eduardo, Soheil & Tannaz, Marina & Manolis, Andrijana, Aleksandar, Gisela, Pau, Jifeng, Lisa & Rasmus, Ivonne, Mafalda, Teresa, Héctor, Łukasz, Frederico, Robert & Lisa for their friendship and making me a part of a big international family. I would like to thank Yuliya & Aleksey together with their kids Angelina & Anton for their friendship and being such amazing people. Moreover, I would like to thank Sasha & Jana together with their kids Jindřiška & Jeronym for their friendship and support. I would also like to acknowledge my friend Gitte W. Høyer, who (to some extent ☺) made me like and understand better the Danish culture, cuisine & the word *hygge*, and for sure made everything to help me to enjoy my stay in Denmark. Moreover, I would like to give a special thanks to two PROSYS 'fairies' – Gitte Læssøe & Eva Mikkelsen, without whom I would simply get drowned in all administration work. Great colleagues from DTU Energy and the Danish Polymer Centre, especially Aleksey Nikiforov, Larisa Seerup, Jon Trifol Guzman, Liyun Yu and Peter Mazurek, additionally deserved a big thank you for all the support and help in using of some of their equipment.

I would like especially to thank all the people I have been collaborating with in the past years and who made my external stays so fruitful, productive and happy. I would like to acknowledge colleagues from the Measurement Technology Unit (MITY), especially Adama Sesay, Peter Panjan, Pekka Kilpeläinen, Tuija Kallio (and her family), Tina Tolonen and Adriana Ferancová, who not only opened the world of biosensors to me but also made my Finnish experience so memorable. The nature and the beauty of Karelia will be always in my heart. I would like to thank BioNem Laboratory at the University ''Magna Graecia'' of Catanzaro, and especially Gerardo Perozziello, Patrizio Candeloro, Immanuel Valpapuram, Pushparani Micheal Raj and Maria Laura Coluccio, for being such great hosts and introducing me to the PCA analysis and Raman spectroscopy for non-invasive measurement of biological samples. I would like to thank Barbara Vadot for being interested in my research and who helped me to improve my teaching skills. I would like to acknowledge the amazing people I met during my stay at the Technical University of Graz, especially Juan M. Bolivar, Donya Valikhani, Rama Krishna Gudiminchi, Torsten & Melanie Mayr (and their lovely family), Birgit Ungerböck, Shiwen Sun, Sergey Borisov & Liliana Carolina, Daria Rybakova & Tim, Alexander Mannsberger and Leopold, who introduced me to the world of biocatalysis ("make biocatalysis great again") and optical sensors. Juan M. and Donya are greatly acknowledged for all their support, help and making me see the light in the darkest times. I would like to thank Laura Micheli from Università di Roma Tor Vergata for her friendship and very interesting research done together. The scientific consortium of INM, namely Yuliya E. Silina and Marcus Koch, are highly acknowledged for being such great hosts and for their incredible level of professionalism and knowledge, fruitful discussions and beautiful work done together. I would like to thank also the rest of the ESRs from the EUROMBR project - Gulsim Kulsharova, Pia Gruber and Susanne Llado - for all the fun and interesting research we shared in the past 3 years.

Я хочу от всего сердца поблагодарить всех моих учителей из России, которые на протяжении моей юности не только делились со мной своими знаниями и научным опытом, но и помогли направить меня в этой жизни на светлый путь: Салимова Наталья Борисовна и вся её семья, Лидия Петровна Богачкина, Петропавловская Ирина Александровна, Соловьев Сергей Николаевич, Мативосян Карине Рафаэловна, Коваленко Леонид Владимирович, Власенко Константин Капитонович, Сенаторова Светлана Валерьевна, Офицеров Евгений Николаевич, Моисеев Сергей Константинович, Сандуленко Ирина Владимировна и Колдобский Андрей Борисович.

Я хочу поблагодарить всю мою семью за любовь, силу духа и умение найти слова поддержки в трудную минуту. Спасибо вам за ваше неимоверное терпение, благодаря которому вы всегда ждали моего возвращения домой. В особенности я хотела бы поблагодарить моих родителей Владимира и Ирину, самого классного брата Семена, а также бабушку Любовь и дедушку Александра.

I would like to thank my family for all their love and who has been always able to find the right words to cheer me up, being my tower of strength and being every time patient and strong

enough to wait for me to come back home. And last but not least, the great man and moon of my life, Roberto, who despite all these years living in a Brownian motion cherishes our love and every day finds the forces to be so close to me being so many km away. Without you being in my life, I would never learn how to risk and to fight for what/who you believe in.

The musicians of present and past, who inspired and helped to find me the right inspiration while writing scientific papers and the dissertation, deserve to be mentioned as well: Antonio Lucio Vivaldi, Edvard Grieg, Giacomo Puccini, Wolfgang Mozart, Johann Bach, Antonin Dvořák, Bryan Ferry, Roxy Music, The Bryan Ferry Jazz Orchestra, Antônio Carlos Jobim & Elis Regina, João Gilberto, Miles Davis, Luis Nelson, Benny Goodman, Duke Ellington, Billie Holiday, Sting, Florence Welch, The Cure, The Verve, The Smiths, Morrissey, John Lennon, Led Zeppelin, The Clash, The Kooks, Moby, Arctic Monkeys, The xx, The Who, New Order, Joy Division, R.E.M., Cranberries, Mick Jagger, the Rolling Stones, U2, Enya, Enigma, Coldplay, Пётр Ильич Чайковский, Кино, Вячеслав Бутусов, Борис Гребенщиков, DDT, Алиса, Гарик Сукачев, Калинов мост, АукцЫон, Машина времени, Аквариум, Воскресение & Би 2.

Daria Semenova,

Kgs. Lyngby, February 2018

Summary

Nowadays, a great variety of industrial products, including pharmaceuticals, fuels, bulk and fine chemicals, etc., is produced *via* bio-based manufacturing. Handling of renewable plant, animal and/or microbial-based biological resources as raw materials is in general a more environmentally friendly approach compared to the use of fossil fuels, and does not require the frequent use of aggressive solvents, heavy metals and other toxic chemicals. However, the identification, development and further industrial integration of novel bio-based pathways are very resource and time consuming processes. Therefore, various scaling-down approaches within industrial biotechnology have gained significant popularity in the last decades. It has resulted in the development and implementation of small scale reactors such as microbioreactors (μBRs) that potentially could serve as tools for the identification of interesting and valuable reaction or production strain candidates for further scaling-up of bioprocesses. The design and development of μBR technologies with integrated sensors is an adequate solution for rapid, high-throughput, and cost-effective screening, with considerably reduced reagent usage and waste generation.

One of the significant challenges in the successful application of μBR technology remains the lack of the appropriate software and automated data interpretation of the μBR experiments. The μBR supporting software and data interpretation tools should allow maximizing the exploitation of the flexibility and the capabilities of the microfluidic platforms to deliver information-rich experiments on the one hand, and on extracting as much information as possible from the obtained experimental data on the other hand. Therefore, the main goal of this work is the development of mathematical models that can provide qualitative and quantitative information on the biological variables of interest. The capabilities of the presented mechanistic models are demonstrated by applying them for the evaluation of the biocatalytic reaction conditions inside μBRs and in amperometric biosensor design optimization.

In the first case study a mechanistic model was developed to describe the enzymatic reaction of glucose oxidase and glucose in the presence of catalase inside a commercial microfluidic platform with integrated oxygen sensor spots. The simplicity of the proposed model allowed an easy calibration of the reaction mechanism structure and estimation of the kinetic rate constants. Moreover, the obtained simulation results were independently confirmed for μL- and mL- scale experiments. Thereby, the developed model recommended itself as a helpful tool in achieving better understanding of the reaction mechanism inside the microfluidic device.

In the second case study the flexible microfluidic platform with integrated amperometric glucose biosensors was developed for continuous monitoring of glucose consumption rates. The integration of the mixing chamber inside the platform allowed performing sample dilutions which subsequently adjusted the concentration of analytes of interest to the sensor's detection range. The platform was developed using a simple design, standard connectors and low-cost materials, which

allows further exploiting of its multi-functional capabilities in a “plug-and-play” approach connection to other μBRs.

In the third case study the mechanistic model of the cyclic voltammetry response of the first generation glucose biosensors was developed and applied for the biosensor design optimization. Furthermore the obtained qualitative and quantitative dependencies between the model output and experimental results were independently confirmed by thorough electrochemical and morphological studies.

In the fourth case study the novel analytical procedure for simultaneous multiple-substrate monitoring in a droplet was developed. Moreover, the specific protocols were developed for detection of oxygen conversion, iron and Nafion elution rates inside the biosensor system. The presented analytical methods were evaluated for their optimal operating conditions and glucose biosensor designs in order to provide the most stable electrochemical response.

Thereby, the novel tools, approaches and workflow schemes associated with supporting experimental data are presented throughout the thesis. Throughout the thesis, the role of performing a substantial number of experiments supported by multi-analytical analysis and validation of the obtained results was emphasized, in order to guarantee the reliability and accuracy of the proposed mathematical models.

List of publications and conference contributions

Publications:

- D. Semenova, A. Zubov, Y. E. Silina, L. Micheli, M. Koch, A. C. Fernandes and K. V. Gernaey, Mechanistic modeling of cyclic voltammetry: a helpful tool for understanding biosensor principles and supporting design optimization, *Sensors and Actuators B Chem. 259 (2018) pp. 945-955.* doi:10.1016/j.snb.2017.12.088.
- D. Semenova, Y. E. Silina, M. Koch, A. Zubov and K. V. Gernaey, Morphological studies and tandem monitoring in robust biosensor design and operating conditions identification, *Sensors and Actuators B Chem., submitted.*
- A. C. Fernandes, D. Semenova, P. Panjan, A. M. Sesay, K. V. Gernaey and U. Krühne, Multi-function microfluidic platform for sensor integration, *N. Biotechnol. (2018) In press.*
- T. Tajsoleiman, D. Semenova, A. C. Fernandes, J. K. Huusom, K. V. Gernaey and U. Krühne, An Efficient Experimental Design Strategy for Modeling and Characterization of Processes, *in: 27th Eur. Symp. Comput. Aided Process Eng., Elsevier Masson SAS, 2017: pp. 2827–2832,* doi:10.1016/B978-0-444-63965-3.50473-6.

Conference contributions:

- D. Semenova, A. C. Fernandes, U. Krühne and K. V. Gernaey, Development of advanced mathematical data interpretation methods for bioprocesses in microbioreactors, 3rd International Conference on Implementation of Microreactor Technology in Biotechnology (IMTB) 2015, Opatija, Croatia, (10 – 13 May). Poster presentation.
- D. Semenova, A. C. Fernandes, U. Krühne and K. V. Gernaey, Development of mechanistic models for the description of bioprocesses in microbioreactors, 3rd European Congress of Applied Biotechnology (ECAB 3) 2015, Nice, France (September 27th – October 1st). Poster presentation.
- D. Semenova, A. C. Fernandes, P. Panjan, U. Krühne, K. V. Gernaey and A. M. Sesay, Electrochemical biosensor integration in a microfluidic platform for on-line biocatalytic reaction monitoring, 26th Annual World Congress on Biosensors (BIOSENSORS) 2016, Gothenburg, Sweden, (25 – 27 May). Poster presentation.
- D. Semenova, A. C. Fernandes, A. Zubov, U. Krühne and K. V. Gernaey, Mathematical modeling of amperometric biosensors for process intensification, 14th International Conference on Microreaction Technology (IMRET14) 2016, Beijing, China (12 – 14 September). Oral presentation.
- D. Semenova, A. C. Fernandes, B. Vadot, J. M. Bolivar, T. Mayr, U. Krühne, A. Zubov and K. V. Gernaey, Mechanistic models in the development of microfluidic screening technologies, 4th International Conference on Implementation of Microreactor Technology in Biotechnology (IMTB) 2017, Bled, Slovenia (23 - 26 April). Oral presentation.
- D. Semenova, A. Zubov, A. C. Fernandes, U. Krühne and K. V. Gernaey, Application of mechanistic models to cyclic voltammograms for the optimization of biosensor design,

5th International Conference on Bio-Sensing Technology (BITE2017) 2017, Riva del Garda, Italy (7 – 10 May). Poster presentation.

- D. Semenova, A. Zubov, Y. E. Silina, L. Micheli, A. C. Fernandes and K. V. Gernaey, Mechanistic modeling as an effective approach for the understanding and optimization of biosensor performance, 12th Workshop on Biosensor; Bioanalytical Microtechniques in Environmental, Food & Chemical Analysis (BBMEC) 2017, Rome, Italy (26 – 30 September). Oral presentation.
- D. Semenova, A. Zubov, A. C. Fernandes, U. Krühne and K. V. Gernaey, Mechanistic modeling of amperometric biosensors, 10th World Congress of Chemical Engineering (WCCE) 2017, Barcelona, Spain (1 – 5 October). Poster presentation.

Contents

List of general and chemical abbreviations

ACR	agitated cell reactor
AM	chronoamperometry
BG	Berlin green
Cat	catalase
Cat*	extra catalase
Cat^{*air}	air saturated extra catalase
CE	counter electrode
CFD	computational fluid dynamics
CID	collision-induced dissociation
CSTR	continuously stirred tank reactor
CV	cyclic voltammetry
DAT	double-sided pressure sensitive adhesive tape
DO	dissolved oxygen
E_{ox}/E_{red}	oxidized or reduced forms of enzyme
$E_{red}O_2$	reduced enzyme-oxygen complex
$E_{red}P_1$	reduced enzyme-gluconic acid complex
$E_{ox}P_2$	oxidized enzyme-hydrogen peroxide complex
$E_{ox}S$	oxidized enzyme-glucose complex
$E_{red}S$	reduced enzyme-glucose complex
EC	electrochemical sensors
EDX	energy dispersive X-ray spectroscopy
EFB	European Federation of Biotechnology
EIC	extracted ion chromatogram
ESBES	European Society of Biochemical Engineering Science
ESEM	environmental detection module of scanning electron microscope
ET	energy transfer
FAD	flavin adenine dinucleotide
FDM	finite difference method
G	glucose
GO	graphene oxide
GOx	glucose oxidase
$GOx(FAD)/GOx(FADH_2)$	oxidized/reduced forms of glucose oxidase
HPLC	high-performance liquid chromatography
HTS	high-throughput screening
IC/ISC	internal conversion or intersystem crossing
ICP-MS	inductively coupled plasma mass spectrometry
LC-ESI-MS/MS	liquid chromatography-electrospray ionization-tandem mass spectrometry

M3C	measurement, monitoring, modeling and control
µBR	microbioreactor
M_{ox}/M_{red}	oxidized or reduced forms of mediator
ODEs	ordinary differential equations
Ox/Red	oxidized or reduced forms
P_1/P_2	reaction products referring to gluconic acid or hydrogen peroxide
PB	Prussian Blue
PDEs	partial differential equations
PDMS	polydimethylsiloxane
PFTR	plug-flow tubular reactor
PMMA	polymethylmethacrylate
PoC	point-of-care
PP	polypropylene
PW	Prussian White or Everitt's salt
QbD	quality by design
RE	reference electrode
S/T	single or triplet states
RSD	relative standard deviation
SEM	scanning electron microscopy
SPE	screen printed electrode
STR	stirred tank reactor
TIC	total ion chromatogram
TFE	tetrafluoroethylene
TR	tubular reactor
WBM	whole-bioprocess model
WE	working electrode

List of symbols

A	surface area of the working electrode
C	concentration
C_{AL}^{*}	solubility of component A in the liquid
C_i/C_i^{inlet}	concentration of the i system component inside the reactor
C_{Ox}/C_{Red}	surface concentrations of the oxidized and reduced species
c_s	speed of sound
D	diffusion coefficient
$D_{M_{red,e}}/D_{M_{ox,e}}$	diffusion coefficients of the reduced or oxidized forms of the mediator inside the enzyme/membrane layer
$D_{O_{2,e}}/D_{O_{2,d}}$	oxygen diffusion coefficient inside the enzyme/membrane or diffusion layers
d_d	thickness of the diffusion layer
d_e	thickness of the enzyme/membrane layer
D_H	hydraulic microchannel diameter
E	applied potential vs. the reference electrode
E^0	standard electrode potential
E_{app}	square-wave potential applied to the working electrode
E_{pa}/E_{pc}	anodic or cathodic peak potentials
ΔE	difference of peak potential values
F	Faraday constant
$f_i(\vec{x_i}, \vec{\beta})$	predicted by the model oxygen conversion rate
H	Henry's constant
I_0/I	luminescence intensities in the absence or presence of the quencher
i_{pa}/i_{pc} or I_{pa}/I_{pc}	anodic or cathodic peak currents
ΔI	difference of peak current values
$J\ (x,t)$	flux density of the electroactive species at position x and time point t
$K_{M\ [O_2]}/K_{M\ [S]}$	Michaelis constant for the reaction substrates (oxygen or glucose)
Kn	Knudsen number
K_{SV}	Stern-Volmer quenching constant
L	length scale of the flow
n_e	number of electrons involved in the transfer
p	pressure
p_{AG}	partial pressure of component A in the gas
pO_2	oxygen partial pressure
p_T	total gas pressure
Q	volumetric flowrate

Q_0/Q_E	volumetric flow at the inlet or outlet
R	universal gas constant
r or ϑ	overall reaction rate
r_i	net reaction rate of i system component
Re	Reynolds number
res_i	i^{th} residual value
S_0/S_E	initial or final substrate concentration
T	temperature
$\vec{u}$	velocity field of the fluid
$V(x,t)$	hydrodynamic velocity at position x and time point t
V_L	reactor liquid volume
V_{max}	maximum velocity
y_i	experimental oxygen conversion rates
z	charge
$\vec{\beta}$	estimated model parameters vector
γ	dimensionless specific heat ratio for gases
γ_{AG}	mole fraction of component A in the gas
δ	diffusion layer thickness
λ_M	molecular mean free path length
μ	dynamic viscosity of the fluid
ν	scan rate
ρ	fluid density
τ/τ_0	luminescence lifetimes in the presence or absence of the quencher

Chapter 1
Research Motivation & Goals

1.1. Introduction

Looking back to the history of human inventions, one can easily see the trend of the technological revolutions that takes place almost every 50 - 80 years. The first industrial revolution (the middle of the 18th century) was mainly focused on the textile, iron and steam engine technologies, and followed by the subsequent rise of industrial capitalism. However, the time of the significant progress in science, as well as the breakthrough discoveries, was aligned together with the second industrial revolution (1867 – 1914) that was revolved around steel, oil-refinery and chemical production together with factory electrification. It was an era of great ideas and innovations, when both science and engineering kept up with the times. However, more than a hundred years of experience and knowledge allowed nowadays prioritizing the interest of both industrial and scientific committees all over the world on the development of not only cost-effective but also environmentally friendly technologies. Therefore, the biotechnological revolution that took place in the early 1970's has already brought the undeniably fundamental changes to the lifestyle of the 21st century.

Although the concept of malting, brewing as well as cheese and wine making were already known in 7000 BC, the word "biotechnology" appeared as term for the first time in the work of Károly Ereky (Biotechnology of Meat, Fat and Milk Production in an Agricultural Large-Scale Farm) in 1919 [1]. It was used to define the general processes that can be applied for the production of useful goods from raw materials. The biotechnology area today is a complex multi-disciplinary field that is mainly focused on use of bio-based processes (e.g. biocatalysis, fermentation) in the design of novel technologies for the production of compounds of interest, or in the optimisation of production of already existing products (e.g. replacing chemical production from fossil fuels by production routes from renewable raw materials). Various tools and products proposed within biotechnological strains are widely exploited not only for research purposes, but have become an essential part of daily life. The tremendous success of biotechnology in medicine, pharmacology, agriculture, the chemical and many other industries can be partly attributed to the extensive development and use of high-throughput screening (HTS) and point-of-care (PoC) technologies.

Different approaches for scaling-down within industrial biotechnology became significantly more popular in the last decades. One of the main driving forces behind this concept was the achievement of high yields and volumetric productivities, which are crucial to economic viability of the production process. It has resulted in the development and implementation of small scale reactors such as microbioreactors (μBRs) that potentially could facilitate the process flow in the identification of interesting and valuable reaction or production strain candidates for further

scaling-up of bioprocesses, as shown in Figure 1. The design and development of μBR technologies with integrated sensors is an adequate solution for rapid, high - throughput, and cost - effective screening, with considerably reduced reagent usage and waste generation [2]. Moreover, the low sample volumes and the small size of μBRs subsequently open up the possibilities for numbering-up *via* parallelization of bio-based processes [3] with minimized efforts in terms of continuous monitoring and control of various biological parameters. The current status in the development of μBRs for bioprocesses, as well as the advantages, challenges and future perspectives were explored in a series of recent publications [4–7].

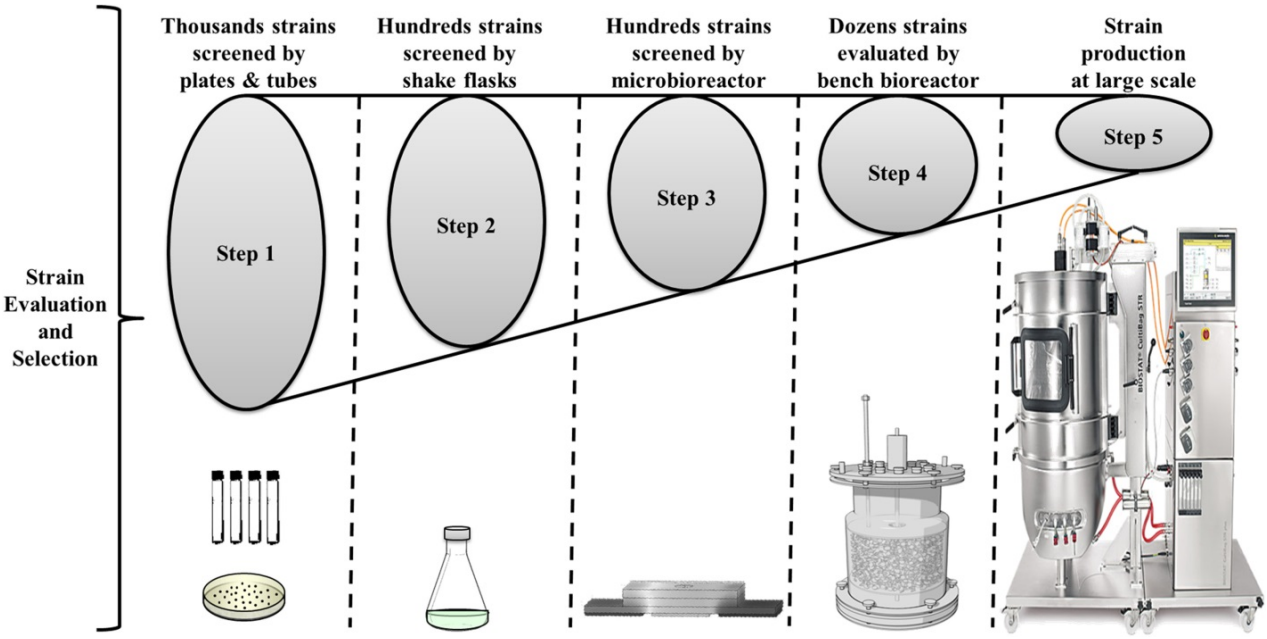

Figure 1 - Schematics of the process flow for the strain screening and evaluation with high throughput μBR positioned prior to the bioreactor scaling-up step [6].

One of the significant challenges in the successful application of μBR technology remains the lack of the appropriate software and automated data interpretation of the μBR experiments. The μBR supporting software and data interpretation tools should allow maximizing the exploitation of the flexibility and the capabilities of the microfluidic platforms to deliver information-rich experiments on the one hand, and on extracting as much information as possible from the obtained experimental data on the other hand. This can be achieved by designing model-based state and parameter estimators that can provide reliable on-line information on the biological variables and model parameters. Thus, applying mathematical models to μBR experimental data will allow a better understanding of both the bioprocess and the reactor performance. Therefore, within the EUROMBR project the expertise in sensing technologies, biocatalysis and microfluidics were brought together addressing the needs in further promoting of μBRs for more efficient screening and scale-up of biocatalytic processes.

1.2. Scientific scopes

In order to provide reliable model-based state and parameter estimators, the development of robust sensing technologies is required for further integration and on-line monitoring of bioprocesses inside the microfluidic platforms. Thus, mathematical models should be constructed not only being focused on streamlining the data interpretation of the bio-based processes inside the μBRs but also on identifying the optimal operating conditions for both reaction kinetics and sensing mechanisms. Therefore, the dissertation is devoted to application of the mechanistic modeling approach for the characterisation of cascade enzymatic reactions inside a microfluidic platform and for the development of a novel tool for electrochemical biosensor design optimization. In the presented case studies, the glucose sensitive biocatalyst glucose oxidase (GOx) was selected for its potential interest in both industrial applications (e.g. glucose monitoring for fermentation processes) and clinical diagnostics (e.g. glucose monitoring for diabetes patients).

1.3. Thesis outline

The dissertation consists of six chapters and includes the theoretical background, experimental investigations and simulation results for the presented case studies. It is important to note that for the initial mechanistic model development step presented in Chapter 2 the μBR experimental results were provided by PhD student Ana C. Fernandes from the PROSYS Research Centre, Technical University of Denmark (DTU). Moreover, the results of the model structure selection studies were a part of the internship research project called "Development of mechanistic models for the description of glucose oxidase reaction inside a microfluidic platform" conducted from May to September 2016 by M. Sc. Barbara Vadot from INP - Ecole Nationale des Ingénieurs en Arts Chimiques et Technologiques (INP ENSIACET). The further evaluation of the sensor response and enzymatic reaction conditions in the μBR was carried out by the author of this thesis at the Technical University of Graz in collaboration with Dr. Juan Manuel Bolivar and Assoc. Prof. Torsten Mayr. The multi-purpose microfluidic platform presented in Chapter 3 was developed in collaboration with Ana C. Fernandes from PROSYS (DTU), Peter Panjan and Adama M. Sesay from the Measurement Technology Unit (MITY) at Oulu University. The mechanistic model for the cyclic voltammetry response of the biosensors presented in Chapter 4 was constructed in collaboration with Dr. Alexandr Zubov from PROSYS (DTU). The Nafion membrane preparation method for glucose biosensors presented in Chapter 4 was optimized in collaboration with Prof. Laura Micheli from Università di Roma Tor Vergata. Moreover, the complete morphological studies of the glucose biosensors demonstrated in Chapter 4 and Chapter 5 were performed in collaboration with Dr. Yuliya E. Silina and Dr. Marcus Koch from Leibniz Institute for New Materials (INM).

In Chapter 2 the available strategies in the development of mathematic models for bio-based processes are discussed together with the main aspects regarding microreactor and kinetic modeling. Moreover, the chapter includes the introduction to the first case study, where the mechanistic modeling approach was applied to describe the enzymatic reaction of glucose oxidase

and glucose in the presence of catalase inside a microfluidic platform with integrated oxygen sensor spots. Therefore, the basic principles behind the mechanism of oxidation of the glucose in the presence of GOx and the operation of the optical chemical sensors are introduced. The results of the model structure selection are summarized and compared with the experimental data. Finally, to ensure the accuracy of the signal response provided by oxygen sensor spots at the initial reaction conditions, an additional set of experiments was proposed for the ideally mixed millilitre scale reactor. The optimized reaction conditions were further evaluated in the μBR with integrated oxygen sensors.

In Chapter 3 the multi-purpose microfluidic platform was developed for further integration of electrochemical glucose biosensors for the in-flow quantification and dilution of glucose solutions. Therefore, the chapter contains a theoretical background regarding electrochemical biosensors and the basic principles of operation, as well as a short summary of the available glucose sensing technologies. The presented work can be regarded as a continuation of Chapter 2, since the presented platform potentially can be connected to a μBR with integrated oxygen sensor spots in a "plug-and-play" approach for the direct on-line monitoring of glucose consumption rates. The main focus is the development and use of amperometric glucose biosensors for continuous monitoring.

In Chapter 4 the aim was, by the use of mechanistic models, to predict the electrochemical response for the first generation glucose biosensors used in Chapter 3. Therefore, a brief overview and the main aspects of mathematical modeling of amperometric biosensors are presented. As an initial step in the model development, the interpretation of experimental voltammograms obtained in aerobic conditions in the absence of glucose at low scan rates is proposed. In this part of the work, it is demonstrated that combining the results of multi-analytical studies, such as scanning electron microscopy, energy dispersive X-ray spectroscopy and liquid chromatography-electrospray ionization-tandem mass spectrometry, together with mechanistic modeling is an effective approach in identifying the key parameters of the biosensor system crucial for the optimal biosensors operation and design. Therefore, a more favorable composition of glucose biosensors was proposed and further proved to be stable at various operation conditions during cyclic voltammetry measurements. Moreover, the analytical merit of the optimized biosensors was evaluated *via* chronoamperometric studies in the presence of glucose.

In Chapter 5 the series of experimental procedures for further optimization of the glucose biosensors were coupled with complete morphological analysis (Chapter 4). Moreover, a novel approach for tandem glucose and oxygen monitoring in a droplet was demonstrated for amperometric glucose biosensors. The main objective of the presented study was the identification of a more favourable glucose biosensor composition for a robust electrochemical response in the presence of glucose that can be proposed for the next step in the amperometric model development.

Finally, in Chapter 6 the overall conclusions are summarized for the presented case studies. Moreover, the perspectives and suggestions for future research in model-based analysis as a helpful tool for process intensification and design optimization are discussed.

The workflow of this dissertation is schematically shown in Figure 2.

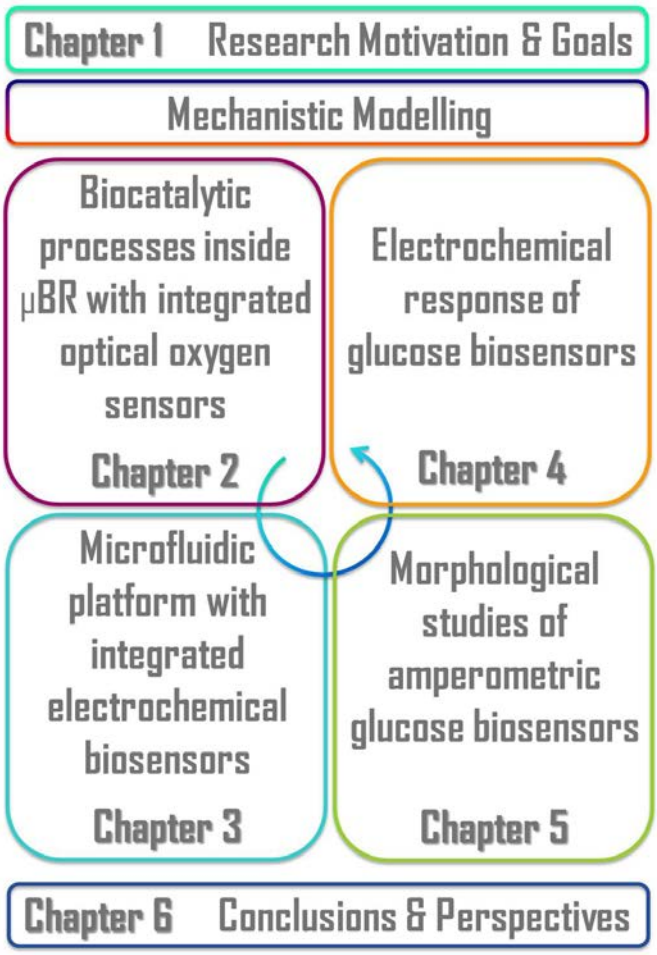

Figure 2 - Schematics of the thesis roadmap.

Chapter 2
Model-based analysis of biocatalytic processes inside µBRs with integrated optical sensors

Abstract

One major obstacle to the further growth of biotechnology and biotechnological production remains the development and systematic application of mathematical models in this field. The widespread integration of modeling and simulation techniques has already recommended itself, and has proven to be a successful approach towards gaining increased process understanding. Furthermore, starting from a mathematical model, often the development of improved process monitoring and control applications have been achieved in various fields of the chemical industry. For a long time, the complexity of the macromolecular systems coupled with the variability of physical phenomena and parallel chemical reactions, as well as the incomplete information available on system parameters, has been a hindrance towards the widespread use of mathematical modeling for bio-based processes. However, in recent years, this attitude has slowly changed, which has resulted in a significant increase of interest in the use of mathematical models for bio-based processes.

Therefore, as an example, in this chapter we demonstrate how fundamental models can be used in describing and unravelling the underlying mechanisms of cascade enzymatic reactions inside a microfluidic platform. Moreover, it is shown how the comparison of the simulation results with the experimental data allowed identifying the crucial parameters for the specific application of microbioreactor (µBR) reaction conditions. The optimized experimental conditions inside the mL-scale reactor *via* oxygen monitoring with a fiber- optic oxygen microsensor were further evaluated inside the microfluidic system with integrated oxygen sensor spots. As the case study, the enzymatic reaction of glucose and glucose oxidase was chosen to be investigated inside µL- and mL-scale reactors in the presence of catalase and hydrogen peroxide.

2.1. Theoretical background

2.1.1. Mathematical modeling of bio-based processes

Driven by novel tools for more efficient optimization of operating conditions, mathematical models nowadays are well integrated in the chemical industry and have become a key component for the development of chemical processes. The main objective of such models is to provide a sufficient amount of information on the system state variables by use of built-in numerical relationships between process inputs and outputs. The variables of interest for bio-based processes include not only the crucial components of the fermentation or biocatalytic reactions (e.g. reaction rates, substrate concentration, biomass growth, etc.) but also involve the characteristic features of the bioreactor. Thus, the bioreactor state and input parameters can be grouped as follows: (a) chemical (e.g. pH, oxygen concentration); (b) macro-biological (e.g. mutation, contamination); (c) physical (e.g. agitation speed, feed rate, pressure, temperature); (d) biochemical (e.g. enzymes, cells composition) [8]. The research scopes set by the European Federation of Biotechnology (EFB) and the European Society of Biochemical Engineering Science (ESBES) today are mainly focused on the development of efficient measurement, monitoring, modeling and control (M3C) strategies. The state-of-the-art as well as the main principles of automated measurement and monitoring techniques, process optimization and control, modeling and quality by design (QbD) approaches in biotechnology were carefully summarized and discussed in [9].

Modeling of bioprocesses involves data-driven (black-box or empirical models) and deterministic/mechanistic (white-box models) approaches, as well as the hybrid combinations of both (grey-box models), as shown in Figure 3. Empirical models are constructed based on correlations between the systems input and output parameters, and do not require any detailed process knowledge. Thus, the applicability and variability of such models are limited by the dataset involved in developing the correlation. On the other hand, mechanistic models are based on first principles and include the mathematical formulation of (part of) the fundamental mechanisms of a system. The choice of the right modeling approach mainly depends on the model purpose (e.g. analysis, optimization, control, etc.), which subsequently defines the model structure and complexity, as well as spatial and temporal resolution of the model.

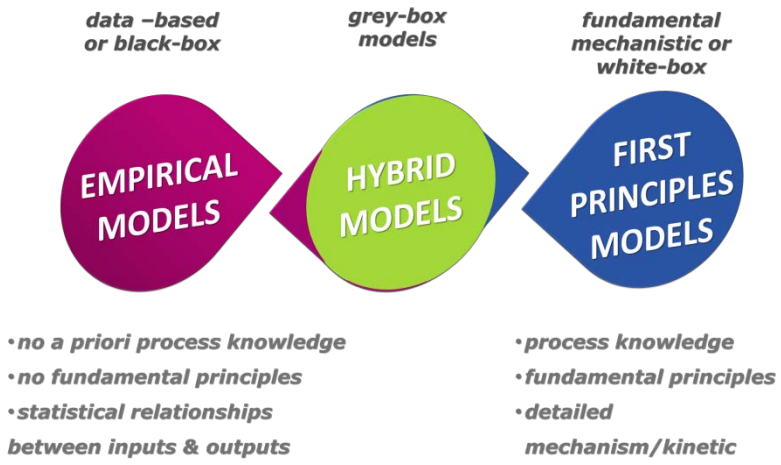

Figure 3 - Schematic representation of the different types of mathematical models and their main principles.

Moreover, mathematical models developed for the description of biocatalytic processes can also be classified according to their scope as catalyst, reaction, reactor and process models. The purpose of the catalyst models is to study the interactions on the molecular level between the enzyme active site and the substrate, the enzyme selectivity and its variation according to the different reaction conditions. On the contrary, the reaction, reactor and process models are focused on the analysis of the performance of the whole system, including reaction mechanism/kinetics, thermodynamics, mass heat and momentum transfer for various unit operations. The connection between all four types of biocatalytic models is schematically shown in Figure 4, where – as a rule of thumb – the complexity of the model increases with the subsequent increase of the physical boundaries size [10].

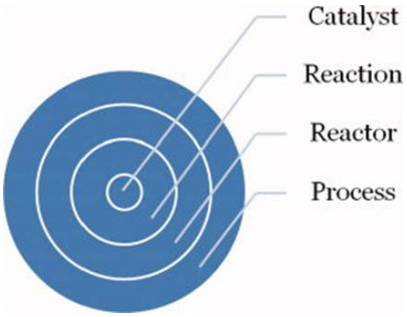

Figure 4 - A schematic illustration of different models applied in biocatalysis given in order of increasing scope: (i) intrinsic properties of the biocatalyst (enzyme), (ii) reaction kinetics, (iii) reactor performance, and (iv) process dynamics [10].

The standard model building procedure includes five steps, as shown in Figure 5. First, the scope and general objective of the model should be formulated (step I), which is then followed by the mathematical definition of the reaction or process unit mechanisms (step II). At this point in the model construction, the crucial system parameters are defined and the additional experimental data are collected which might be required for further determination of the model structure (step III), which includes reaction kinetics, mass transfer characteristics etc.

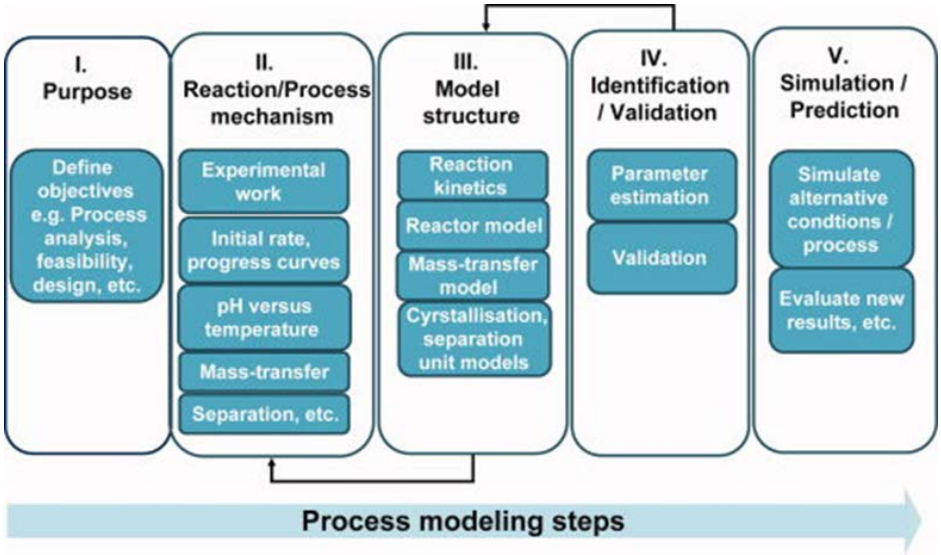

Figure 5 - Typical steps involved in building a process model: black arrows indicate feedback loops (iterations between different model development steps) [10].

Therefore, the model parameters (either found in literature or estimated experimentally) should be validated (step IV) utilizing different strains, products or experimental conditions in order to verify the suitability of the model structure and to ensure that all the key reaction mechanisms and processes were included in the model. When the formulated model guarantees the qualitative and quantitative response towards the experimental data, it can be further used as a proper simulation tool (step V), addressing the needs of the initial scope of the model development. In a series of recent publications the current status and trends on the use of first principles models in biotechnology [11,12] and in the pharmaceutical industry [13] have been carefully discussed, as well as the development of integrated whole-bioprocess models (WBMs) and the relevance of such models in process design, monitoring and control [14]. Moreover, the successful application of model-based tools for on-line monitoring [15] and control [16] of fermentation processes has already been demonstrated at pilot scale.

Throughout this thesis chapter the focus will be on the development of a mechanistic model that combines a reaction and a reactor model for the description of the enzymatic reaction inside a microfluidic platform under various experimental conditions. Therefore, the basic principles behind reaction and reactor modeling, including the microreactor configurations, the mechanism of the enzymatic process studies (glucose oxidase and glucose conversion) and the principles of dissolved oxygen sensing *via* optical chemical sensors will be introduced in the following paragraphs.

2.1.2. Enzymatic μBRs

Microfluidics as a science and technology of systems using transport channels with dimensions of tens to hundreds of micrometres and operating with small liquid volumes (10^{-9} to 10^{-18} litres) was only defined in the past decade [17]. The compact size of the microfluidic devices combined with reduced reagent usage, waste generation and flexibility towards sensor integration simplified the

on-line monitoring and control of the desired analyte and made microfluidic lab-on-a-chip applications mainly focused on *in vitro* diagnostics, drug discovery, biotechnology and ecology [18,19]. Moreover, the characteristic high surface-to-volume ratio and lower diffusion distances of microstructures allow for more efficient heat and mass transfer, which significantly improves the selectivity, reaction rates and yields in comparison to macro-scale systems. All these benefits explain the recent increase in the use of microreactors for enzymatic or whole cell biocatalysis, where the enzyme is either free in the solution or immobilized [20,21]. Challenges related to handling different analyte solutions (e.g. cells, antibodies, enzymes, etc.) and their surface properties (e.g. surface tension, contact angle, etc.), as well as the application purposes of the microfluidic device, resulted not only in the variation of materials (e.g. glass, ceramics, polymers, silicon, or steel) but also in a broad range of configurations of μBRs [22]. The most common configurations of enzymatic microreactors are summarized in Figure 6. The classification of enzymatic μBRs can be simplified based on system operation: homogeneous (free enzyme), heterogeneous (immobilized enzyme) or multiphase (enzyme-containing droplets, membrane, monoliths or beads) [5,21].

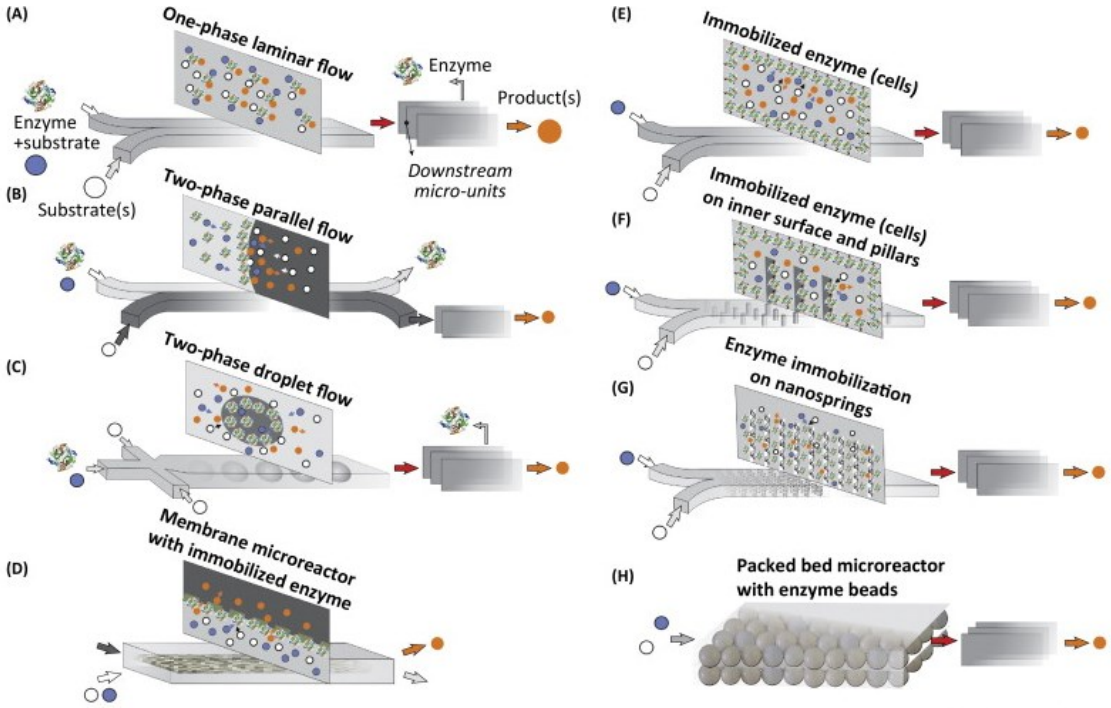

Figure 6 - Schematic representation of enzymatic microreactors: free enzyme in a one-phase laminar flow (A), in a two-phase parallel flow (B) and in a droplet (C) flow; enzyme immobilized on the membrane in a membrane microreactor (D), on the inner surface of a microchannel (E), on the inner surface and pillars (F), on nanosprings (G) and on beads inside a packed-bed microreactor (H). Adapted from [5].

The enzyme immobilization includes binding the enzyme to a support (carrier), entrapment (encapsulation) and crosslinking (formation of new covalent bonds between polypeptides). The applications, advantages and related drawbacks of various immobilization techniques and supports

were discussed in detail in several reviews [23–25]. Although microreactors with immobilized enzymes have already proven to be more effective in view of further reuse of the carrier [26,27] and simplified product separation inside the microfluidic systems [28], the product sorption to the surface or activity dilution, irreversible deactivation and leakage of immobilized enzyme still remain significant challenges [21]. Therefore, the use of free enzyme microreactors is an adequate solution for a more robust and straightforward operation. Moreover, an easy flow control (tuneable pumping systems) and small fluid volumes inside the μBRs guarantee mainly diffusion-controlled mass transport and laminar flow.

Similar to catalytic (chemical) reactors the enzyme-based reactors can be represented by two basic types, namely stirred tank reactor (STR) and tubular reactor (TR) that can operate under batch, continuous or fed-batch modes [29]. The ideal performance of different types of large scale bioreactors is schematically compared in Figure 7.

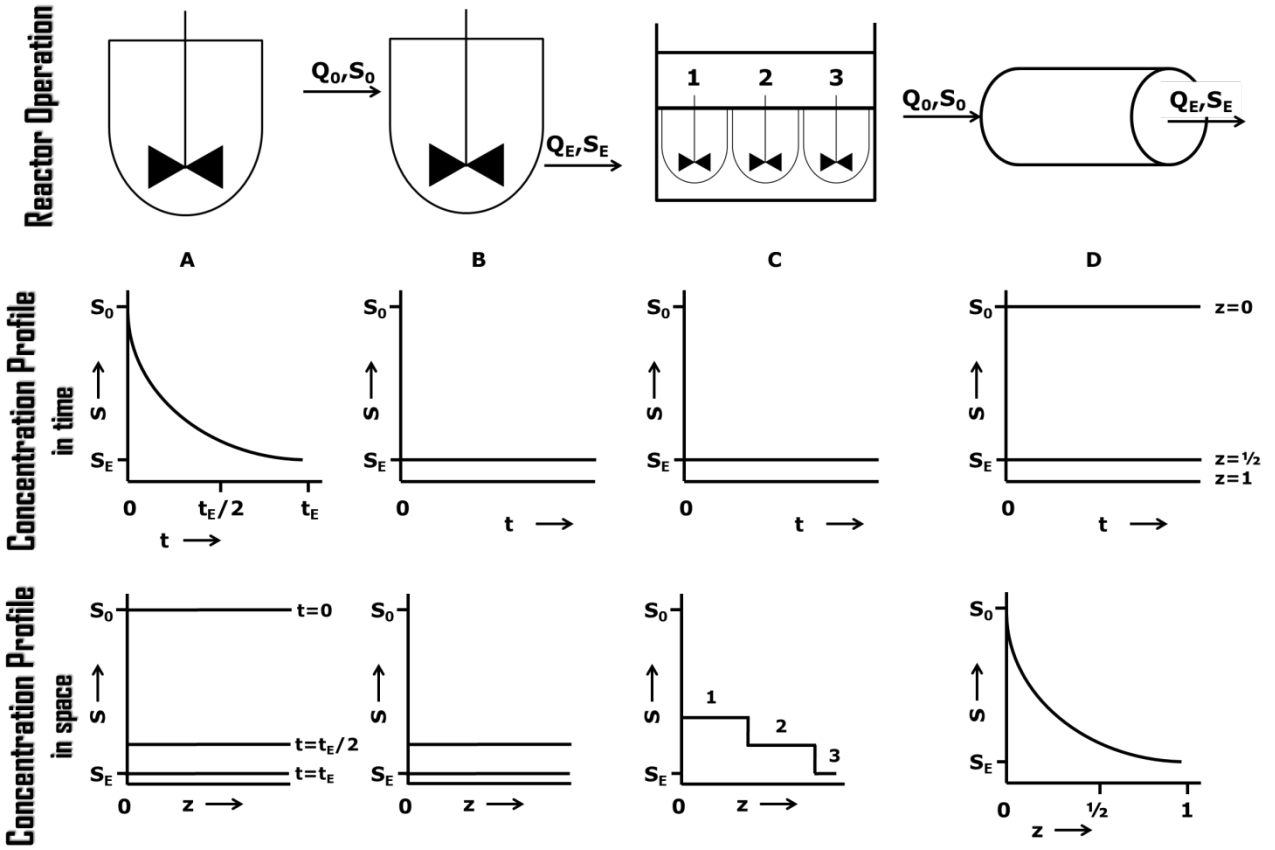

Figure 7 - Basic (ideal) types of bioreactors and their operating modes: A – batch STR; B - continuous STR; C – cascade STR; D - continuous TR. The evolution of the substrate from the initial (S_0) to the final (S_E) concentration is plotted as a function of (residence) time (t) and length (z). The volumetric flow at the inlet is Q_0 and at the outlet it is equal to Q_E. Adapted from [29].

Due to the laminar flow inside the microfluidic platforms, the handling of the (bio)chemical samples is performed under stable hydrodynamic conditions. The introduction of the solutions into the chip

inlets is either done in batch or continuous mode and requires external pressure sources (e.g. pumps) [18]. The liquid flow through the channel or pipe with no variation of the axial velocity (the radial diffusion is faster in comparison to the convection along the flow) would lead to changes of the substrate concentration profiles along the tube length in a plug-flow tubular reactor (PFTR) [30]. However, the micromixing inside the microfluidic channels is much more complex and significantly deviates from the ideal plug-flow conditions [31]. The microfluidic platforms with integrated sensors presented in this thesis were either chosen (Chapter 2) or designed (Chapter 3) in such a way that they could guarantee the ideally mixed flow profiles.

2.1.3. µBR flow and fluid physics

Since the operation of the majority of the enzymatic microfluidic devices is based on applied pressure differences and deals with uniform viscous aqueous solutions (*Newtonian fluids*), the flow inside the microchannels can be described as the rate of change of momentum equal to a sum of the convection, pressure and viscous forces (no body forces) acting on an incompressible liquid [32,33] and referred to in the following form of the Navier-Stokes equation (1):

$$\rho \frac{\partial \vec{u}}{\partial t} = -\rho(\vec{u} \cdot \nabla \vec{u}) - \nabla p + \mu \nabla^2 \vec{u} \quad (1)$$

where $\vec{u}$ is the velocity field of the fluid at space location $\vec{x}$ and time point t; ρ is the fluid density; p is the pressure; μ is the dynamic viscosity of the fluid.

The Reynolds (Re), Mach (Ma) and Knudsen numbers (Kn) are the most important dimensionless group of parameters describing the fluid state in motion [34]. The laminar fluid flow inside smooth round and/or square microchannels is characterized by low Reynolds numbers ($Re \leq 2300$) [35] that represents the ratio between inertial and viscous forces as shown in equation (2).

$$Re = \frac{\rho \, \| \vec{u} \| \, D_H}{\mu} \quad (2)$$

where D_H is the hydraulic microchannel diameter. Therefore, the fluid flow regime can be characterized by the Reynolds number. The fluid flow for microfluidic channels can be negligible with Reynolds numbers less (i.e. Stokes/creeping flow) or equal to 1 (presence of vortices) since the viscous effects dominate or are comparable to inertial effects, respectively [33,34]. The Mach number allows to compare the velocity of the flow towards the speed of sound (c_s) as shown in equation (3).

$$Ma = \frac{\| \vec{u} \|}{c_s} \quad (3)$$

The Mach number allows classifying the flow as supersonic ($Ma > 1$), sonic ($Ma = 1$) and subsonic ($Ma < 1$). Both the Reynolds and the Mach number are related by the Knudsen number (4) that

quantifies the flow regime inside the microchannels and estimates the degree of continuum behaviour of the fluid:

$$Kn = \frac{\lambda_M}{L} = \sqrt{\frac{\gamma\pi}{2}}\frac{Ma}{Re} \tag{4}$$

where λ_M - molecular mean free path length, L - length scale of the flow and γ – dimensionless specific heat ratio for gases. For the continuum flow ($Kn \leq 0.001$) the Navier-Stokes equation can be applied with no-slip boundary conditions (the fluid velocity is equal to zero at a solid boundary), whereas for $0.001 \leq Kn \leq 0.1$ the slip flow conditions (non-zero velocity near the wall) are applied. The transient behaviour of the fluid flow can be obtained for $0.1 \leq Kn \leq 10$ which transforms into the free-molecule flow with $10 \leq Kn \leq \infty$ [18,34,36]. The molecular diffusion can be obtained for $Kn \to 0$ ($Re \to \infty$).

Throughout the dissertation, the temperature of the μBR experiments was assumed constant and the use of gases and liquids with molecular weight over 5000 (*non-Newtonian fluids*) was not considered, and therefore the characteristic aspects of such fluidic flow is not discussed. The influence of the various factors on the liquid flow inside the microfluidic channels, including the channel entrance, wall slip, non-Newtonian fluid, surface roughness, viscous dissipation and turbulence effects, and further comparison of the experimental results with numerical analyses was discussed in detail elsewhere [37,38]. The main aspects of the microfluidic mixing together with recent advances in the application of microreactors with improved mixing has been carefully reviewed elsewhere [7,39].

2.1.4. μBR and reaction modeling

Combining the reactor model (diffusion, mixing, etc.) together with a kinetics expression (reaction rates, inhibition, etc.) that is capable of predicting the enzyme behaviour under various operating conditions (different enzyme and/or substrate concentrations, temperature, pH, etc.) is an optimal approach towards obtaining a process model (reaction kinetics, mass balances, etc.), allowing not only to reproduce the productivity of enzymatic μBRs, but also to design new experiments for microfluidic platforms. Due to the complexity of bio-based processes the formulation of a robust process model requires initially to run a sufficient number of experiments. Sufficient experimental data of high quality would guarantee the accuracy of the proposed model assumptions, simplifications, initial and boundary conditions, together with the reliability of the model itself. Therefore, the methodology for kinetic model parameter estimation proposed by Chen et al. [40] and further developed by Al-Haque et al. [41] can be used as a guidance for the (bio)reaction model development. The presented approach consists of the five step procedure (e.g. Step 1) supported by individual experimental validation stages (e.g. Data Set 1), as schematically illustrated in Figure 8.

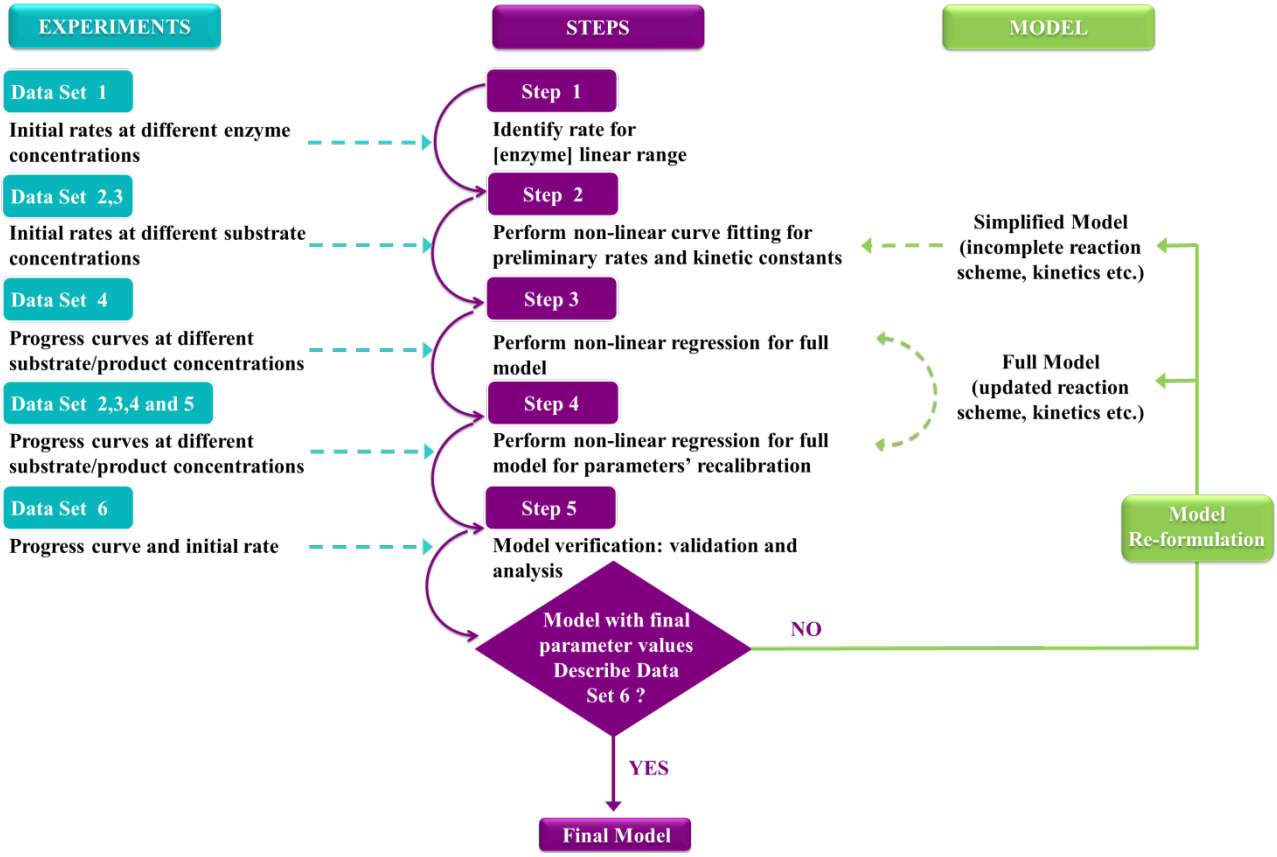

Figure 8 – Methodology for kinetic parameter identification. Adapted from [40,41].

The non-linear ordinary differential equations (ODEs) or non-linear second order partial differential equations (PDEs) presented in the dissertation describe the dynamic system behaviour together with the chemical, biochemical and electrochemical reactions. The mechanistic model approach was applied to systems containing the glucose oxidase enzyme either in a free enzyme solution inside the microfluidic platform (Chapter 2) or immobilized inside the membrane over the electrode surface (Chapter 4). Both models were derived using the steady-state experimental results and enabled to reproduce the transient response of the system. Therefore, a brief overview of the general aspects of glucose oxidase/glucose interaction is presented in the following section.

2.1.5. Glucose oxidation by glucose oxidase

The highly selective oxidation of glucose to gluconolactone can be easily performed in the presence of the large (the molecular weight is 160 kDa) dimeric protein glucose oxidase (GOx). At the active site of each 80 kDa subunit, this enzyme contains not covalently but tightly bound flavin adenine dinucleotide (FAD) which is a redox-active molecule (one FAD unit per monomer) [42]. The enzymatic transformation of the glucose requires the presence of molecular oxygen (mediator) which is involved in the transformation of the flavoprotein-oxidase system ($FAD^+/FADH_2$) followed by the two electrone transfer associated with deprotonation/protonation [43], as shown in Figure 9.

$$\text{Glucose} + \text{GOx(FAD)} \longrightarrow \text{Gluconolactone} + \text{GOx(FADH}_2\text{)}$$

$$\text{GOx(FADH}_2\text{)} + \text{O}_2 \longrightarrow \text{GOx(FAD)} + \text{H}_2\text{O}_2$$

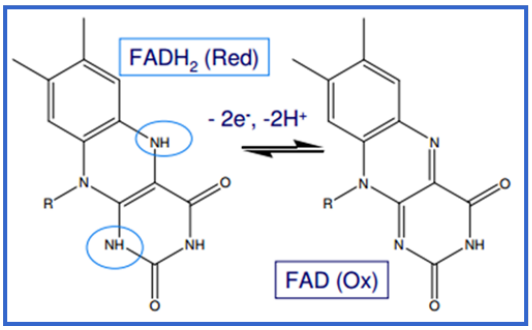

Figure 9 - The enzymatic oxidation of glucose and the stoichiometry of the FAD/$FADH_2$ redox couple: GOx(FAD)/GOx($FADH_2$) – oxidized/reduced forms of glucose oxidase, respectively [43].

Although the glucose oxidase is the most well-studied and commonly used commercial enzyme, the reaction mechanism and kinetic parameters vary a lot not only under different experimental conditions but also depending on the enzyme producing strains. The first investigation of the oxidation mechanism and kinetics was performed spectrophotometrically by the use of the rapid flow and stopped flow methods as reported in the work of Nakamura and Ogura [44]. The absorption spectrum of flavin groups was recorded at different oxygen, glucose and enzyme concentrations in the system. As the result of their studies, the following sequence of reactions (5)-(7) was proposed and the kinetic constant k_4 obtained at various oxygen concentrations (6-360 μM) varied from 1 to 1.7×10^6 M^{-1} sec^{-1}.

$$\text{Glucose} + \text{GOx(FAD)} \underset{k_2}{\overset{k_1}{\rightleftharpoons}} \text{Glucose-GOx(FAD)} \tag{5}$$

$$\text{Glucose-GOx(FAD)} \xrightarrow{k_3} \text{Gluconolactone} + \text{GOx(FADH}_2\text{)} \tag{6}$$

$$\text{GOx(FADH}_2\text{)} + \text{O}_2 \xrightarrow{k_4} \text{GOx(FAD)} + \text{H}_2\text{O}_2 \tag{7}$$

The first order reaction of the enzyme-glucose complex dissociation (6) to the reduced form of the enzyme was proposed as the rate-limiting step. Moreover, the mechanism was later used to study (*via* stopped flow and rapid flow methods) the enzyme behaviour at various temperatures, glucose and oxygen concentrations for the glucose oxidase obtained from different strains [45]. The D-glucono-δ-lactone inhibition of glucose oxidation was confirmed in a turnover experiment by Gibson et al. [46]. The oxidation mechanism was investigated with different sugars (glucose, mannose, xylose, and galactose) *via* manometric and stopped flow methods. Although no evidence of the enzyme-substrate complex was found and the chemical nature of the reduced enzyme remained unknown, the following reaction mechanism (8)-(11) was proposed.

$$\text{Glucose} + \text{GOx(FAD)} \xrightarrow{k_1} \text{GOx(FADH}_2\text{)-Gluconolactone} \quad (8)$$

$$\text{GOx(FADH}_2\text{)-Gluconolactone} \xrightarrow{k_2} \text{Gluconolactone} + \text{GOx(FADH}_2\text{)} \quad (9)$$

$$\text{GOx(FADH}_2\text{)} + \text{O}_2 \xrightarrow{k_3} \text{GOx(FAD)-H}_2\text{O}_2 \quad (10)$$

$$\text{GOx(FAD)-H}_2\text{O}_2 \xrightarrow{k_4} \text{GOx(FAD)} + \text{H}_2\text{O}_2 \quad (11)$$

The estimated kinetic parameters for the glucose (reacts much faster in comparison to other sugars) are summarized in Table 1.

Table 1 - Kinetic constants of the reaction of glucose oxidase in the presence of glucose [46].

T °C	V_{max} sec^{-1} M	$K_{M\ glucose}$ M	$K_{M\ oxygen}$ mM	k_1 $M^{-1}sec^{-1}$	k_2 sec^{-1}	$k_3, 10^{-6}$ $M^{-1}sec^{-1}$	k_4 sec^{-1}
0	235	0.12	0.21	2100	650	1.3	370
13	590	0.11	0.29	5500	3300	1.7	720
27	1150	0.11	0.48	10000	-	2.1	1150
38	2000	0.12	0.83	16000	-	2.4	2000

Betrame et al. [47] performed the selective oxidation of D-glucose to D-gluconic acid (controlled pH) in a semibatch reactor (50 mL) in the presence of the commercial glucose oxidase/catalase mixture (Hyderase). The reactions (8)-(11), where gluconolactone was substituted by gluconic acid, were used to obtain the kinetics of the glucose oxidase mechanism at the temperature range from 25 to 30ºC, constant oxygen concentration and atmospheric pressure. The obtained activation energy value for the initial (8) reaction (49.6 kJ mol^{-1}) was much higher in comparison to the combination of the remaining reaction steps (26.7 kJ mol^{-1}). The use of deuterated glucose in anaerobic conditions in conventional and stopped flow spectrophotometric methods allowed to confirm the formation of the intermediate complex compounds [48]. The established reaction scheme (12)-(16) together with experimental kinetic parameters was further validated by computer simulations of this mechanism. Moreover, Duke et al. [49] applied an oxygen electrode for achieving a more accurate data analysis and proposed an additional reaction (17) necessary to complete the glucose-glucose oxidase mechanism.

$$\text{Glucose} + \text{GOx(FAD)} \underset{k_2}{\overset{k_1}{\rightleftharpoons}} \text{GOx(FAD)-Glucose} \quad (12)$$

$$\text{GOx(FAD)-Glucose} \xrightarrow{k_2} \text{GOx(FADH}_2\text{)-Gluconolactone} \quad (13)$$

$$\text{GOx(FADH}_2\text{)-Gluconolactone} \xrightarrow{k_3} \text{GOx(FADH}_2\text{)} + \text{Gluconolactone} \quad (14)$$

$$\text{GOx(FADH}_2\text{)} + \text{O}_2 \xrightarrow{k_4} \text{GOx(FAD)-H}_2\text{O}_2 \quad (15)$$

$$\text{GOx(FAD)-H}_2\text{O}_2 \xrightarrow{k_5} \text{GOx(FAD)} + \text{H}_2\text{O}_2 \quad (16)$$

$$\text{GOx(FADH}_2\text{)-Gluconolactone} + \text{Glucose} \xrightarrow{k_6} \text{GOx(FADH}_2\text{)} + \text{Gluconolactone} + \text{Glucose} \quad (17)$$

The ping-pong bi-bi reaction mechanism [50] of the glucose oxidase enzyme catalyzed glucose conversion to gluconolactone is summarized in Figure 10 and clearly defines the molecular oxygen as a second substrate in the kinetic scheme. The oxygen adsorption accompanying the enzymatic cascade reaction was studied by Fukushima et al. [51]

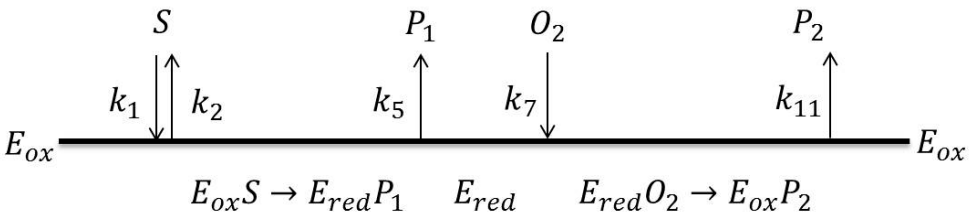

Figure 10 - Ping-pong bi-bi mechanism of enzymatic oxidation of glucose: S – reaction substrate (glucose); E_{ox}/E_{red} – oxidized and reduced forms of the enzyme (glucose oxidase); P_1/P_2 - reaction products referring to gluconic acid and hydrogen peroxide, respectively. Adapted from [49].

According to the scheme presented in Figure 10, $E_{ox}S$ complex formation is assumed to be the only reversible step. Therefore, the kinetic constants k_6, k_8 and k_{12} are equal to zero and are not shown in Figure 10. The formation of the other intermediate compounds ($E_{red}P_1, E_{red}O_2, E_{ox}P_2$) is instantaneous which significantly simplifies the model and calculation of the overall reaction rate (18). In case $k_5 \gg k_{11}$, the equation (18) can be simplified considering Michaelis–Menten kinetics, and can thus be rewritten as shown in equation (19) [52].

$$\vartheta = \frac{k_{11}\, E_{ox}}{\left[\left(\frac{k_5}{k_7\, O_2} + \frac{k_2}{k_1 S} + 1\right) \cdot \frac{\left(\frac{k_1}{(k_2 + k_5)} \cdot S \cdot \frac{k_{11}}{k_1\, S}\right)}{\left(1 - \frac{k_1}{(k_2 + k_5)} \cdot S \cdot \frac{k_2}{k_1\, S}\right)} + \frac{k_{11}}{k_1\, S} + 1\right]} \tag{18}$$

$$\vartheta = \frac{V_{max} \cdot [S] \cdot [O_2]}{[S] \cdot [O_2] + [S] \cdot K_{M\,[O_2]} + [O_2] \cdot K_{M\,[S]}} \tag{19}$$

where ϑ – overall reaction rate; V_{max} - maximum velocity achieved by the system, at maximum (saturating) substrate concentrations; $K_{M\,[O_2]}/K_{M\,[S]}$ – Michaelis constant that represents the reaction substrate (oxygen or glucose) concentration at which the reaction velocity reaches half of the maximum value (½ V_{max}).

In the case study presented later in this chapter, the mechanistic model was built based on the mechanism structure selection method (i.e. combination of the reactions). The simulation results were further compared with the experimental data obtained during the glucose oxidation reaction in the presence of glucose oxidase and catalase. The reaction was monitored by measuring the concentration of the produced gluconic acid in the outlet by means of high-performance liquid chromatography (HPLC). Moreover, the online monitoring (i.e. fully automated) of the reaction was achieved by the catalyzed decomposition of the hydrogen peroxide. Oxygen produced during the reaction was controlled at the oxygen sensor spots integrated along the microfluidic channel. The basic operation principles of the optical chemical sensors will be introduced in the section below.

2.1.6. Optical oxygen sensors

The on-line monitoring of the key variables in biotechnology such as dissolved oxygen, pH, fluorescent protein expression, optical density, etc., would provide a better understanding that can be translated into improved control and optimization of the bio-based processes themselves. The compactness and easy handling of the optical sensors together with their capability to provide the non-invasive and non-destructive (i.e. they do not consume analyte) quantitative response makes them an attractive technology for *in situ* (i.e. at the representative volume element of the reactor) monitoring. Despite the fact that the optical oxygen sensors are extensively used for oxygen sensing and imagining in various macroscale applications [53], the development and application of this robust technology for microfluidic applications still faces a lot of challenges [54]. In a recent review by Gruber et al. [55] the current applications, formats, trends, limitations and benefits related to the integration of optical sensors into microfluidics and biotechnology are thoroughly discussed.

The principles behind the direct analyte detection *via* optical sensors are mainly based on the absorption or photoluminescence. The photoluminescence is the combination of fluorescence,

phosphorescence and delayed fluorescence phenomena that are referred to as molecular luminescence methods. The luminescent molecule absorbs a photon and excites from its ground state (S_0) to the higher vibrational state (i.e. S_1 or S_2). The recorded emission spectrum contains data for the qualitative and quantitative analysis of the system [56]. The comparison between absorbance, fluorescence and phosphorescence is schematically shown in Figure 11.

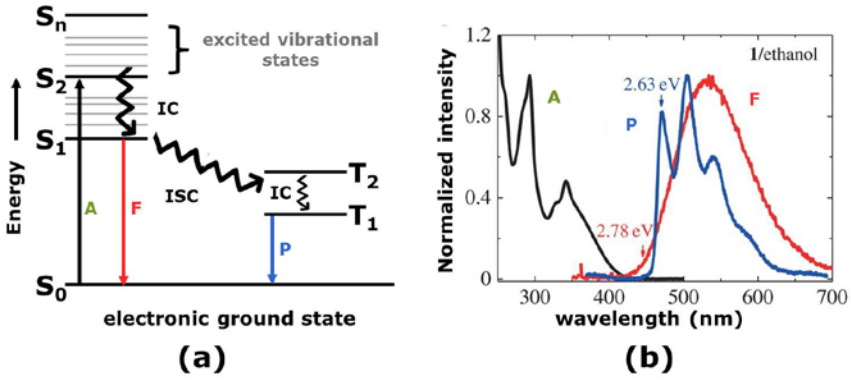

Figure 11 - The simplified Jablonski diagram (a) and the wavelength intensities (b) for the absorbance (**A**), fluorescence (**F**) and phosphorescence (**P**) phenomena: S/T - single or triplet states state; IC/ISC - internal conversion or intersystem crossing. The energy diagram and spectra in ethanol were adapted from [57] and [58], respectively.

The partial energy diagram (Figure 11A) represents the energy of the analyte molecule in different states: $S_0 \rightarrow S_n$ – excitation (light absorption) ~10^{-15} sec; $S_n \rightarrow S_1$ – internal conversion from 10^{-14} to 10^{-11} sec; $S_n \rightarrow T_1$ – intersystem crossing from 10^{-11} to 10^{-6} sec; $T_1 \rightarrow S_0$ – phosphorescence from 10^{-3} to 100 sec. The rates of the vibrational relaxations are in the range from 10^{-12} to 10^{-10} sec. The differences of each method can be visualized by recording the emission/excitation relative intensities at corresponding wavelengths (Figure 11B).

Throughout the thesis the luminescent oxygen sensors, namely optical sensor spots or microsensors, have been mentioned. The basic layout of the optical oxygen sensors comprises of an indicator embedded into a polymeric matrix that can be further deposited over a solid surface (i.e. microfluidic channel, optical fiber, etc.). Therefore, the sensitivity of the sensor can be tuned by varying individual elements or the combination of indicator luminescent (lifetime) and membrane material (permeability) properties [54]. The majority of the indicators are based on the use of luminescent dyes (luminophore) quenched by molecular oxygen (quencher). The theories explaining such quenching mechanism consider either that the luminophore undergoes the intersystem crossing to the triplet state while the paramagnetic oxygen goes to the excited state with the formation of singlet oxygen, as shown in Figure 12; or an alternative theory is that quenching occurs under the electron transfer control leading to the formation of superoxide [56].

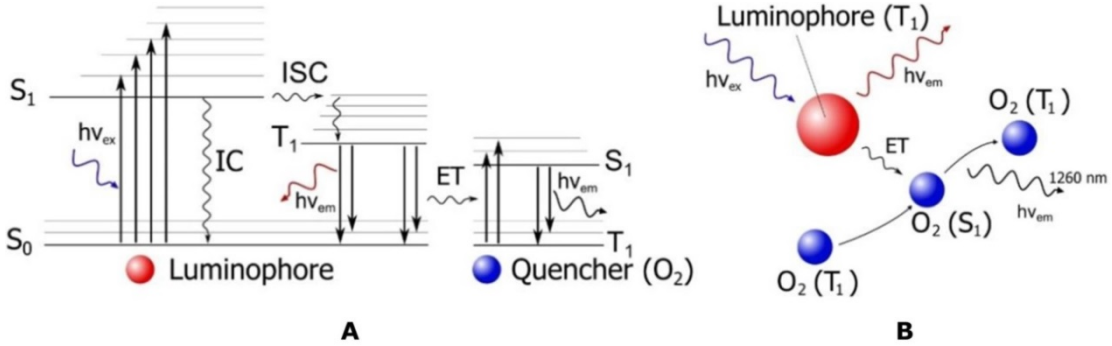

Figure 12 - Schematics of the luminescent oxygen sensing principles for the dynamic (A) and collisional (B) quenching [59].

The luminescence lifetime and intensity affected by the collisional quenching can be quantified by using the linear Stern-Volmer equation (20) independently from the mechanism nature (energy or electron transfer) [56].

$$\frac{I_0}{I} = \frac{\tau_0}{\tau} = 1 + k_q\,\tau_0\,pO_2 = 1 + K_{SV}\,pO_2 \tag{20}$$

where I_0 and I are the luminescence intensities obtained in the absence and presence of the quencher; τ_0 and τ are the luminescence lifetimes in the absence and presence of the quencher; k_q is the bimolecular quenching constant of the energy transfer (ET) shown in Figure 12A; pO_2 is the oxygen partial pressure; K_{SV} is the Stern-Volmer quenching constant which represents the quenching efficiency of the sensor and therefore characterizes its sensitivity. In a microheterogeneous environment (e.g. in polymers) the optical sensors do not exhibit a linear response. In such cases the so-called Demas's two-site model describes the sensor behaviour [60]. Thus, the optical oxygen detection can be performed with a rapid response only by measuring fluorescence lifetime. When the equilibrium between the system pressure and oxygen partial pressure for dilute liquid solutions is reached, the measured oxygen concentration range can be calculated from Henry's law (21) .

$$p_{AG} = \; p_T \gamma_{AG} = H\,C^*_{AL} \tag{21}$$

where p_{AG} and γ_{AG} are the partial pressure and the mole fraction of component A in the gas, respectively; p_T is a total gas pressure; H is Henry's constant which is a function of temperature and C^*_{AL} is the solubility of component A in the liquid [30]. For more detailed information covering the oxygen sensor principles, indicators and sensing methods several helpful publications [61,62] and books [57,63] can be recommended.

2.2. Case Study 1: Mechanistic modeling of the enzymatic biocatalysis inside the microfluidic platform with integrated optical oxygen sensors

2.2.1. Introduction

In this case study, the oxidation reaction of glucose in the presence of glucose oxidase (GOx) and catalase (Cat) was chosen as example system for monitoring inside the commercial microfluidic platform. The mechanistic model approach was applied for description of the biocatalytic reaction behaviour inside the microfluidics. As the initial step, the various reaction schemes were tested in order to identify the most suitable mechanism. Therefore, the model is based on solving non-linear ordinary differential equations (ODEs) which combine the biocatalytic kinetic term and the reactor performance. In order to validate the model, the simulation results were compared with the experimental data. The on-line reaction monitoring was possible by quantifying the oxygen production during catalyzed decomposition of hydrogen peroxide *via* integrated optical oxygen sensors spots along a meander channel. The off-line measurements of gluconic acid at the outlet provided by high-performance liquid chromatography (HPLC) were used as a set of reference data supporting the model selection. Moreover, the reliability of the integrated sensors' response in the proposed reaction conditions was further validated in the presence of hydrogen peroxide. Prior to the microfluidic experiments, the optimal experimental conditions were estimated in ideally mixed mL-scale reactors by use of the optical oxygen microsensor. A case study overview is summarized in Figure 13.

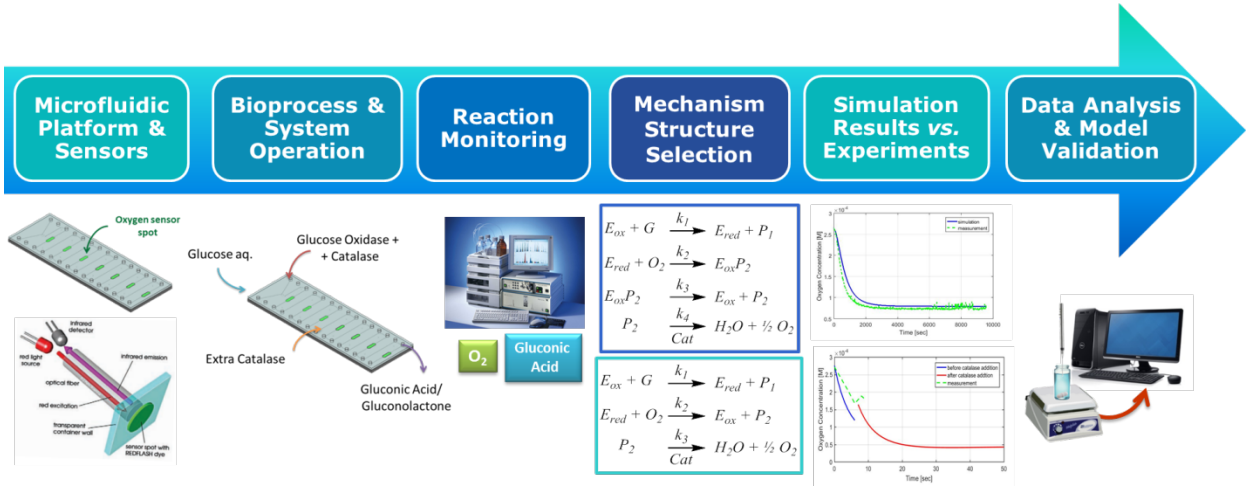

Figure 13 - Case study 1, graphical roadmap.

2.2.2. Mathematical modeling

2.2.2.1. Governing equations and mechanism structure selection

The main objective of the model was to predict the component's conversion rates underlying the mechanism for the cascade enzymatic reaction inside the microfluidic platform at different operating conditions. The non-linear ordinary differential equations (ODEs) combined the liquid flow inside the microfluidic meander channel (mass balance) coupled with biochemical reactions (first and second order reaction kinetics) in the presence of the substrate (glucose) and in the absence/presence of the additional catalyst (catalase) in air saturated phosphate buffer solutions. The diffusion of the system components was not considered. Therefore, the ODEs describe the system dynamics and correspond to the mass balance (22) for each variable of interest. The total number of equations depends on the number of reactant and product species included in the mechanism.

$$\frac{d(C_i)}{dt} = \frac{Q}{V_L} \cdot \left(C_i^{inlet} - C_i\right) \pm r_i \tag{22}$$

where V_L – th e re actor li quid vo lume; C_i and C_i^{inlet} – the conce nt rati on of the i^{th} system component inside the reactor (meander channel/sensor spot) and inflow (inlet), Q – the volumetric flowrate, r_i – the net reaction rate of i^{th} system component.

The microreactor liquid content volume was controlled after all measurements and it was confirmed that it remains constant for the experiments carried out at room temperature (i.e. no evaporation occurs). Therefore, it was assumed to be constant in the model together with the inlet (glucose and enzyme mixtures) and outlet (gluconic acid) mass densities. Since no turbulent flows were expected, the molecular mixing pattern was idealized for the microchannel/sensor spots cross-sectional area. The surface roughness and ideal geometric shape of both meander channel and sensor spots could not be guaranteed after all the chip-manufacturing processes. Therefore these parameters were not included in the reactor model. A continuous stirred tank reactor (CSTR) type of model was proposed for the microfluidic platform. Various scenarios for the biochemical reactions studied at the mechanism structure selection step are summarized in Figure 14.

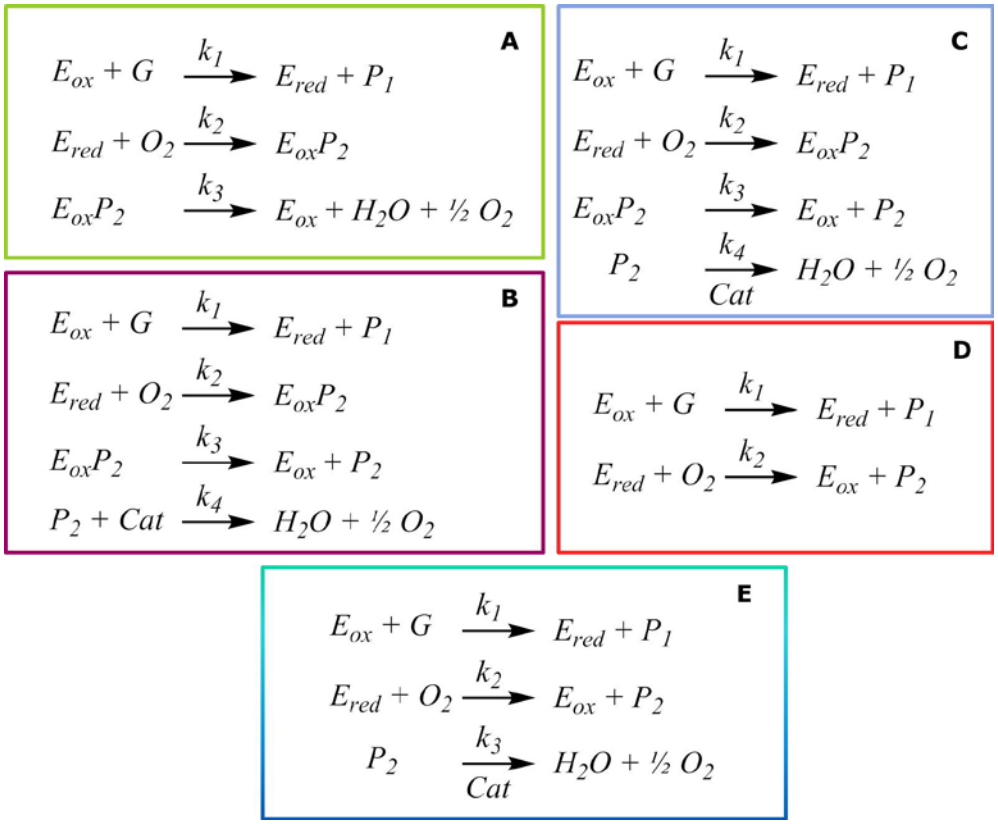

Figure 14 - Mechanism structure selection: G – glucose; E_{ox}/E_{red} – oxidized and reduced forms of glucose oxidase; P_1/P_2 - products referring to gluconic acid and hydrogen peroxide; *Cat* – catalase. In scheme B the catalase is assumed to be consumed during the reaction, whereas in mechanisms C and E the catalase acts as a standard catalyst (concentration remains constant).

The set of equations characterizing the relevant conversion/formation rates of the species inside the meander channel ($t > 0$) are summarized below for each of the proposed mechanisms. The *Mechanism A* (23)-(28) is based on the work of Linek et al. [64]:

Oxidized Enzyme

$$\frac{d(E_{ox})}{dt} = \frac{Q}{V_L} \cdot \left(E_{ox}^{inlet} - E_{ox}\right) - k_1 \cdot G \cdot E_{ox} + k_3 \cdot E_{ox}P_2 \tag{23}$$

Reduced Enzyme

$$\frac{d(E_{red})}{dt} = \frac{Q}{V_L} \cdot \left(E_{red}^{inlet} - E_{red}\right) + k_1 \cdot G \cdot E_{ox} - k_2 \cdot E_{red} \cdot O_2 \tag{24}$$

Glucose

$$\frac{d(G)}{dt} = \frac{Q}{V_L} \cdot \left(G^{inlet} - G\right) - k_1 \cdot G \cdot E_{ox} \tag{25}$$

Gluconic acid

$$\frac{d(P_1)}{dt} = \frac{Q}{V_L} \cdot \left({P_1}^{inlet} - P_1\right) + k_1 \cdot G \cdot E_{ox} \tag{26}$$

Oxygen

$$\frac{d(O_2)}{dt} = \frac{Q}{V_L} \cdot \left(O_2^{inlet} - O_2\right) - k_2 \cdot O_2 \cdot E_{red} + 0.5 \cdot k_3 \cdot E_{ox}P_2 \tag{27}$$

Complex
$$\frac{d(E_{ox}P_2)}{dt} = \frac{Q}{V_L} \cdot \left(E_{ox}P_2^{inlet} - E_{ox}P_2\right) + k_2 \cdot O_2 \cdot E_{red} - k_3 \cdot E_{ox}P_2 \quad (28)$$

The *Mechanism B* (23)-(26),(29)-(32) involves the reaction of hydrogen peroxide (P_2) formation followed by catalyzed decomposition.

Oxygen
$$\frac{d(O_2)}{dt} = \frac{Q}{V_L} \cdot \left(O_2^{inlet} - O_2\right) - k_2 \cdot O_2 \cdot E_{red} + 0.5 \cdot k_4 \cdot Cat \cdot P_2 \quad (29)$$

Complex
$$\frac{d(E_{ox}P_2)}{dt} = \frac{Q}{V_L} \cdot \left(E_{ox}P_2^{inlet} - E_{ox}P_2\right) + k_2 \cdot O_2 \cdot E_{red} - k_3 \cdot E_{ox}P_2 \quad (30)$$

Peroxide
$$\frac{d(P_2)}{dt} = \frac{Q}{V_L} \cdot \left(P_2^{inlet} - P_2\right) + k_3 \cdot E_{ox}P_2 - k_4 \cdot Cat \cdot P_2 \quad (31)$$

Catalase
$$\frac{d(Cat)}{dt} = \frac{Q}{V_L} \cdot \left(Cat^{inlet} - Cat\right) - k_4 \cdot Cat \cdot P_2 \quad (32)$$

In *Mechanism C* (23)-(26),(29)-(31),(33) the catalase concentration along the reaction channel is considered to be constant, with catalase acting as an ideal catalyst.

Catalase
$$\frac{d(Cat)}{dt} = \frac{Q}{V_L} \cdot \left(Cat^{inlet} - Cat\right) \quad (33)$$

The simplified *Mechanism D* (24)-(26),(34)-(36) was based on the experimental results previously obtained in our group in the frame of the master project of Ana Teresa de Melo Machado Simões Carvalho (PROSYS, DTU) when studying the kinetics of glucose oxidation by commercial glucose oxidase (Novozymes, Denmark) in the absence of catalase inside a novel continuous agitated cell reactor (ACR) [65,66]. In their work, the hydrodynamic behavior of the reactor (150 mL of working volume) was modeled as CSTRs in series.

Oxidized Enzyme
$$\frac{d(E_{ox})}{dt} = \frac{Q}{V_L} \cdot \left(E_{ox}^{inlet} - E_{ox}\right) - k_1 \cdot G \cdot E_{ox} + k_2 \cdot O_2 \cdot E_{red} \quad (34)$$

Oxygen
$$\frac{d(O_2)}{dt} = \frac{Q}{V_L} \cdot \left(O_2^{inlet} - O_2\right) - k_2 \cdot O_2 \cdot E_{red} \quad (35)$$

Peroxide
$$\frac{d(P_2)}{dt} = \frac{Q}{V_L} \cdot \left(P_2^{inlet} - P_2\right) + k_2 \cdot O_2 \cdot E_{red} \quad (36)$$

The final *Mechanism E* consisted of (24)-(26),(33),(34),(37),(38) system of ODEs.

Oxygen
$$\frac{d(O_2)}{dt} = \frac{Q}{V_L} \cdot \left(O_2^{inlet} - O_2\right) - k_2 \cdot O_2 \cdot E_{red} + 0.5 \cdot k_3 \cdot Cat \cdot P_2 \quad (37)$$

Peroxide

$$\frac{d(P_2)}{dt} = \frac{Q}{V_L} \cdot \left(P_2^{inlet} - P_2\right) + k_2 \cdot E_{ox}P_2 - k_4 \cdot Cat \cdot P_2 \quad (38)$$

As the initial conditions ($t = 0$) the values of the dissolved oxygen (O_2), the glucose (G), the oxidized form of the glucose oxidase (E_{ox}) and the catalase (Cat) at the entrance of the meander channel (Figure 15A) were set equal to the inlet concentrations, and the concentrations of the rest of the components involved in the reaction were set to zero, unless stated otherwise.

2.2.2.2. Model implementation

The proposed reaction mechanisms were implemented in the MATLAB® language. The governing equations were solved using *ode15s* solver. The major part of the bio- and physicochemical parameters required for the mathematical model were estimated based on experimental data. Initially, the kinetic constant values were found in the literature (see Table S1, Appendix A). However, no qualitative or quantitative response between the model predictions and experimental results were obtained. Therefore, the MATLAB® built-in function *fminsearch*, that allows finding the minimum of an unconstrained multivariable function using a derivative-free method, was introduced to the code. First, the kinetic parameters related to the reactions involving oxygen were estimated since the experimental data obtained on-line (oxygen sensor spots) are the most reliable. Therefore, the difference in oxygen conversion rates between predicted and experimental values was chosen as a cost function (39). In order to find the optimal kinetic values and to fit the model output to each data point, the sum of the squared residuals (40) (i.e. the difference between the experimental data and the model predictions) was minimized as objective function:

$$res_i = y_i - f_i(\vec{x_i}, \vec{\beta}) \quad (39)$$

$$S = \sum_{i=1}^{n} res_i{}^2 \quad (40)$$

where res_i – the i^{th} residual value; y_i – experimental oxygen conversion rates; $f_i(\vec{x_i}, \vec{\beta})$ – oxygen conversion rate predicted by the model; $\vec{x_i}$ – model state variables; $\vec{\beta}$ – estimated model parameters vector. The sum of squares of the obtained residuals for a number of data points *n* was denoted as S.

The obtained kinetic values (see Table S2 - Table S5, Appendix A) were further validated with an additional set of experimental data for oxygen and for another component of the system – gluconic acid.

2.2.3. Experimental section

The experimental data for µBR and mL- scale batch reactor presented and used in the initial model development step in the current thesis chapter were provided by A. C. Fernandes [67] and A. T. de M. M. S. Carvalho [65], respectively. Therefore, no work related to enzymatic reaction

handling and monitoring is shown. Further investigation and optimization of the reaction conditions required the performance of additional experiments in the well-mixed mL-scale reactor with subsequent validation in a µBR. The presented procedures were acquired during an external stay at the Technical University of Graz in collaboration with Dr. Juan Manuel Bolivar and Assoc. Prof. Torsten Mayr.

2.2.3.1. Reagents and materials

Glucose oxidase (EC 1.1.3.4, type II, from *Aspergillus niger*, ≥15,000 U/g solid) and Catalase (EC 232-577-1, from bovine liver, lyophilized powder, 2000-5000 units/mg protein) were obtained from Sigma - Aldrich (Deisenhofen, Germany). D- Glucose and hydrogen peroxide solution (30 %) were provided by Carl Roth (Karlsruhe, Germany). Mono– and di-potassium hydrogen phosphates (anhydrous) were obtained from Merck (Darmstadt, Germany). All the solutions were prepared with air saturated 50 mM phosphate buffer solution (pH = 7.4), unless stated otherwise.

2.2.3.2. Enzyme activity vs. optical sensor response

The catalase activity estimation was performed in a Genesys™ 10s Uv-Vis spectrophotometer (Thermo Fisher Scientific Inc., Waltham, Massachusetts, USA). The measurement was based on the recording of the decrease in the absorbance (proportional to the analyte concentration) of the hydrogen peroxide solution obtained at 240 nm in the presence of catalase [68]. The glucose oxidase activity was determined by the use of a fiber-optic oxygen microoptode (Pyroscience GmbH, Aachen, Germany) connected to a fiber optic oxygen meter (model Firesting, Pyroscience). The measurement was based on the on-line monitoring of the dissolved oxygen (DO) consumption in the reaction with glucose. The general setup assembly, as well as the experimental procedure, were adapted from the works of Bolivar et al. [69,70]. Regardless the enzyme, the activity measurements were performed at 30°C in air saturated phosphate buffer solutions. For the enzyme activity calculations, one unit (U) of enzyme corresponds to a substrate consumption of 1 µmol per minute. The objective of the following studies was to evaluate in a well-mixed mL-scale reactor the experimental conditions that were previously validated at the initial model development step (see section 2.2.4.1.). Therefore, the optimal reaction conditions for an accurate detection of the dissolved oxygen within the response limit of optical microsensors were identified for further characterization inside the microreactor with integrated oxygen sensors.

Catalase activity measurement:

The degradation of the hydrogen peroxide in the presence of catalase was studied in a crystal cuvette of 4mL liquid working volume. The catalase solution was added to the stirred solutions of hydrogen peroxide placed inside the spectrophotometer. The concentration range of the peroxide varied between 5, 10 and 20mM in order to record the dynamic response of the absorbance assuming that the complete catalase induced degradation would occur in 0.5, 1, 2, 4, 6, 8 and 10 min. The obtained experimental curves are summarized in Figure S8 (see Appendix B). The 20 mM hydrogen peroxide solution was proposed for further experiments.

Glucose oxidase activity measurement:

The oxygen consumption measurements were carried out in a glass vial of 4mL liquid working volume placed in a water bath. Magnetic stirring was carried out at 300 rpm with an 8-mm stirrer bar (IKA® RET Basic, Staufen im Breisgau, Germany). The fiber-optic oxygen microoptode was immersed in the buffer solution containing the following glucose concentrations: 2.5, 10 and 100 mM. The addition of enzyme to the stirred solution was performed after a stable signal response was obtained for the dissolved oxygen sensor (approximately 250 µmol/L). The optical sensor response was recorded for various glucose/glucose oxidase reaction conditions discussed below.

- *Glucose Oxidase and Glucose*

The glucose oxidase was added to the stirred 3.8 mL glucose solutions (2.5, 10 and 100 mM) with stabilized oxygen signal. The dynamic response of DO consumption was measured assuming that the total amount of glucose in a vial would be consumed in 0.5, 1, 2, 4, 6, 8, 10, 30, 60, 120 and 200 min. The obtained experimental curves were summarized in Figure S9 (see Appendix B). The glucose concentration equal to 2.5 mM was established as the most favourable condition for further experiments.

- *Glucose and Glucose Oxidase in presence of Catalase*

Fifty µL of glucose oxidase solution were added to well-stirred solutions of 3.5 mL glucose (2.5 mM) and 50 µL of catalase. The influence of catalase on the reaction kinetics was studied for different glucose/glucose oxidase reaction rates, namely 0.402 U/mL, 0.304 U/mL and 0.245 U/mL. Moreover, the impact of the catalase activity on the final reaction volume was tested for the solutions having the same activity as glucose oxidase, or 10 and 100 times higher activity in comparison with GOx. The obtained experimental curves were summarized in Figure S10 (see Appendix B). The glucose/glucose oxidase reaction rate equal to 0.402 U/mL and the activity of catalase equal to the activity of glucose oxidase were established as the most favourable conditions for further experiments.

- *Glucose/Glucose Oxidase/Catalase in presence of Extra Catalase*

Fifty µL of glucose oxidase solution were added to an ideally stirred solution of 3.5 mL glucose (2.5 mM) and 50 µL of catalase (GOx and Cat activities are equal). The extra amount of catalase was added when the DO concentration reached a value of 150 µmol/L. The impact of the extra catalase on the final reaction volume was tested for catalase solutions having the same activity as glucose oxidase, or 10 and 100 times higher activity in comparison with GOx. Moreover, the influence of the addition of aerated extra catalase solution (the activities of catalase, glucose oxidase and extra catalase were equal) to the reaction volume on the sensor response was studied. The obtained experimental results were discussed in section 2.2.4.2. (see 2.2.4. Results and discussion).

- *Glucose/Glucose Oxidase/Catalase in presence of Hydrogen Peroxide*

Various volumes of 20 mM hydrogen peroxide solution were added to the glucose/glucose oxidase/catalase reaction mixture when the DO concentration reached the value of 150 µmol/L. The effect of the catalase activity (10 and 100 times higher than glucose) on the peroxide degradation was studied in the presence of 0.274 mM H_2O_2 (total reaction volume). The obtained experimental results were discussed in section 2.2.4.2. (see 2.2.4. Results and discussion).

2.2.3.3. Microfluidic platform with integrated optical oxygen sensors

When designing the microfluidic experiments, the main focus was to guarantee the fast and reliable response of the oxygen sensor spots at various operation and reaction conditions. The microreactor glass-silicon chip (Figure 15A) was produced by iX – factory GmbH (now part of Micronit, Enschede, the Netherlands) with integrated oxygen sensors spots developed and fabricated at the Technical University of Graz in the Working Group Sensor Materials of Prof. Ingo Klimant (Graz, Austria). The operation of the oxygen sensors located along the meander channel was based on the detection of the probe (oxygen) by a molecular oxygen sensitive dye entrapped in a polymeric layer of the sensor spot, as schematically shown in Figure 15B.

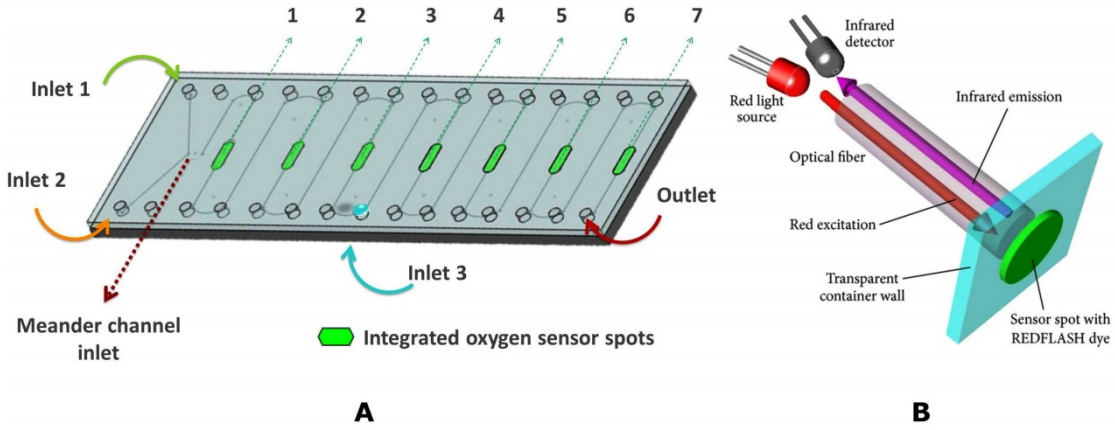

Figure 15 - Schematics of the microreactor glass - silicon chip (A). All the inlets and oxygen sensors spots involved in the reaction handling and monitoring are highlighted. The principles of operation of oxygen sensors spots inside the meander channel with connected optical fiber are shown in B.

The microreactor geometric characteristics and setup assembly for the online analysis of oxygen have been previously provided by Ehgartner et al. [71]. The microreactor chip presented in the current thesis was referred in their work as *microreactor 2*. The microfluidic chip was placed into the in-house developed chip holder and the inlets were connected to the syringe pumps (Cavro® Centris pumps from Tecan) which were controlled via an external Lab VIEW program. Seven oxygen sensor spots were connected to optical fibers (Plastic fibre cable, simplex fibre 1 mm, PE-jacket 2.2 mm) to two 4-channel FireStingO2 fiber-optic meters (PyroScience GmbH, Aachen, Germany) and controlled by Pyro Oxygen Logger software (PyroScience GmbH, Aachen, Germany). A two-point

calibration was performed before each experiment for each oxygen sensor spot located along the channel in an air saturated and deoxygenated meander chip. In contrary to [67] where the experimental results were obtained inside the microfluidic chip with only four active oxygen sensor spots having equal sensitivity properties, the microreactor presented in the current thesis chapter was chosen to have two types of oxygen sensor spots with various sensitivity properties. The sensors located in the positions from 1 to 3 (Figure 15A) were more sensitive towards low oxygen concentrations, whereas the sensor spots from 4 to 7 exhibited a high sensitivity to high oxygen concentrations. The substrate solutions and the enzymatic mixtures were introduced separately into the chip through the main meander channels *inlet 1* and *inlet 2*, respectively. In the experiments where the extra amount of catalase or hydrogen peroxide was introduced into the channel, the lateral *inlet 3* (between sensor 3 and sensor 4 spots) connected to a programmable syringe pump NE-1000 (SyringePump) was activated. The experimental setup is illustrated in Figure 16.

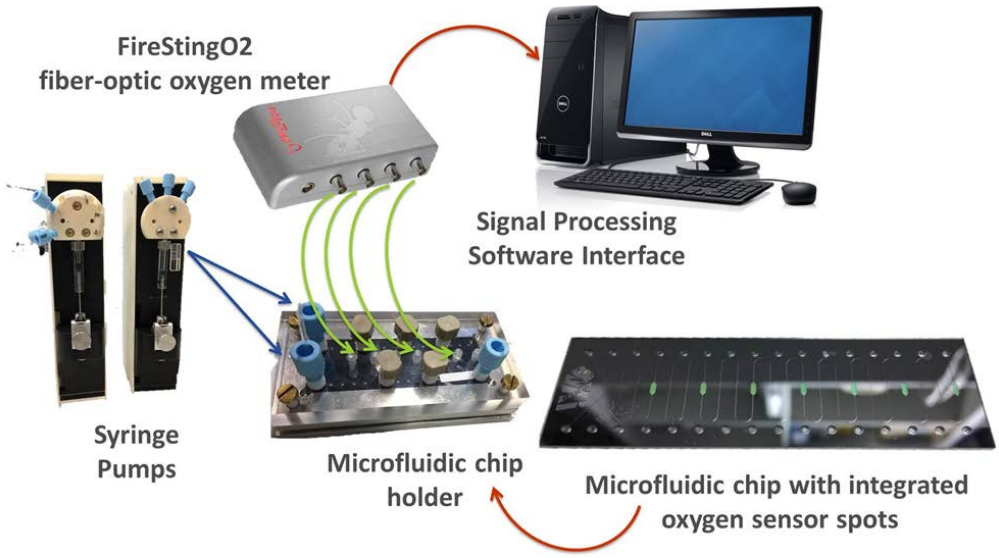

Figure 16 - Elements of the experimental setup assembly for enzymatic cascade reaction monitoring inside the microfluidic reactor.

The reaction on-line monitoring was based on the DO detection at all seven sensors spots integrated inside the meander channel at room temperature. The enzyme and substrate solutions were introduced at different flow rates for various experiments as discussed below. All the experimental results were recorded after the steady-state behaviour (i.e. stable sensor signal) was obtained on seven oxygen sensor spots and summarized in Figure S11 (see Appendix B).

- *Glucose and Glucose Oxidase/Catalase*

For the glucose/glucose oxidase enzymatic reaction the 0.402 U/mL rate was chosen and the activity of catalase was equal to the activity of glucose oxidase. The glucose solution (5 mM) was pumped through *inlet 1* with a flow rate equal to 0.083 µL/sec and the mixture of glucose oxidase and catalase was introduced through *inlet 2* with the same flow rate.

- *Glucose and Glucose Oxidase/Catalase + Extra Component*

The glucose solution (5 mM) was pumped through *inlet 1* at a 0.097 µL/sec flow rate and the mixture of glucose oxidase and catalase (same activities) was introduced through *inlet 2* with equal flow rate. The initial glucose/glucose oxidase reaction rate was calculated as 0.402 U/mL. The extra amount of catalase or hydrogen peroxide (20 mM) solutions was introduced to the system at a 1.164 µL/min flow rate (*inlet 3*) in order to minimize the influence on the main flow pattern inside the meander channel.

2.2.4. Results and discussion

2.2.4.1. Model structure selection

The initial model was based on the *Mechanism A* (with no extra catalase added) structure and the kinetic parameters found in the literature for a batch process. Comparing the simulation results with experimental data, no quantitative response was obtained (see Figure S1, Appendix A). It was proposed with the help of the model to study the impact of the extra catalase solution on the microsystem behaviour. Therefore, *Mechanism B* where the catalase was assumed as a normal system component (i.e. the concentration would decrease along the reactor channel) was modelled. A fair agreement between *Mechanism B* model predictions and experimental results was obtained in the absence of extra catalase (see Figure S2, Appendix A). It allowed extracting the relevant kinetic parameters (see Table S2, Appendix A) that were further validated in the presence of extra catalase (see Figure S3, Appendix A). Since the good qualitative response of the model was maintained, it was concluded that a sufficient number of system components was assumed in the model. Thus, in the next model development step *Mechanism B* was transformed to *Mechanism C* (see Table S3, Appendix A) where the catalase acted as a classical catalyst (i.e. its concentration would remain constant). The numerical values of the kinetic parameters estimated using the *fminsearch* function were validated with the experimental results obtained in the presence of the extra catalase solution (see Figure S4, Appendix A). Although the model was able to reproduce a reasonable qualitative response (see Figure S5, Appendix A), no quantitative agreement with experimental data sets has been obtained. Therefore, it was decided to validate the *Mechanism D* model with experiments performed in a batch mL-scale reactor. It is important to note that when comparing the simulation results with experimental curves the main focus was to guarantee the accuracy of the model response towards the changes in the oxygen concentration profile. Since the data points for oxygen were obtained on-line, this concentration profile is the most valuable data source for the model to describe the overall system behaviour. The good quantitative results for the oxygen and good qualitative response towards glucose/gluconic acid conversion are shown in Figure 17 for the evaluation of the *Mechanism D* model structure with the experimental data obtained in batch mode experiments.

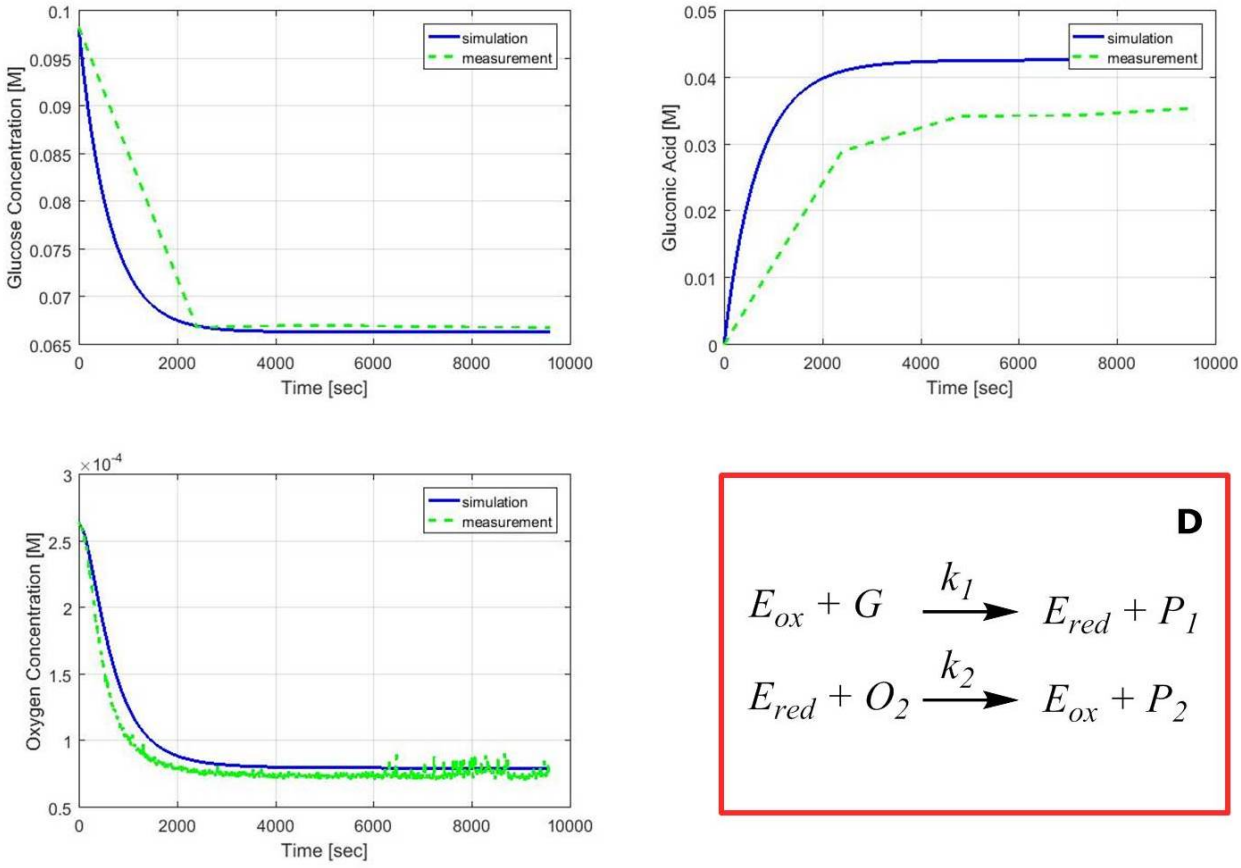

Figure 17 - *Mechanism D*. Comparison of concentration profiles for glucose, gluconic acid and oxygen inside the mL- scale reactor: simulation results (solid line) vs. experimental data (dashed line).

Therefore, the kinetic parameters were further adjusted using the *fminsearch* function (see Table S4, Appendix A). The predicted oxygen, glucose and gluconic acid concentration profiles were compared to the experimental curves (see Figure S6, Appendix A).

In order to also represent the catalyzed decomposition of the hydrogen peroxide inside the microfluidic platform, *Mechanism D* was supplemented with the relevant reaction in *Mechanism E* with tuned kinetic parameter values (see Table S5, Appendix A). The obtained simulation results (see Figure S7, Appendix A) were in a reasonable agreement with the μBR experimental curves obtained for oxygen, gluconic acid and glucose, as shown in Figure 18.

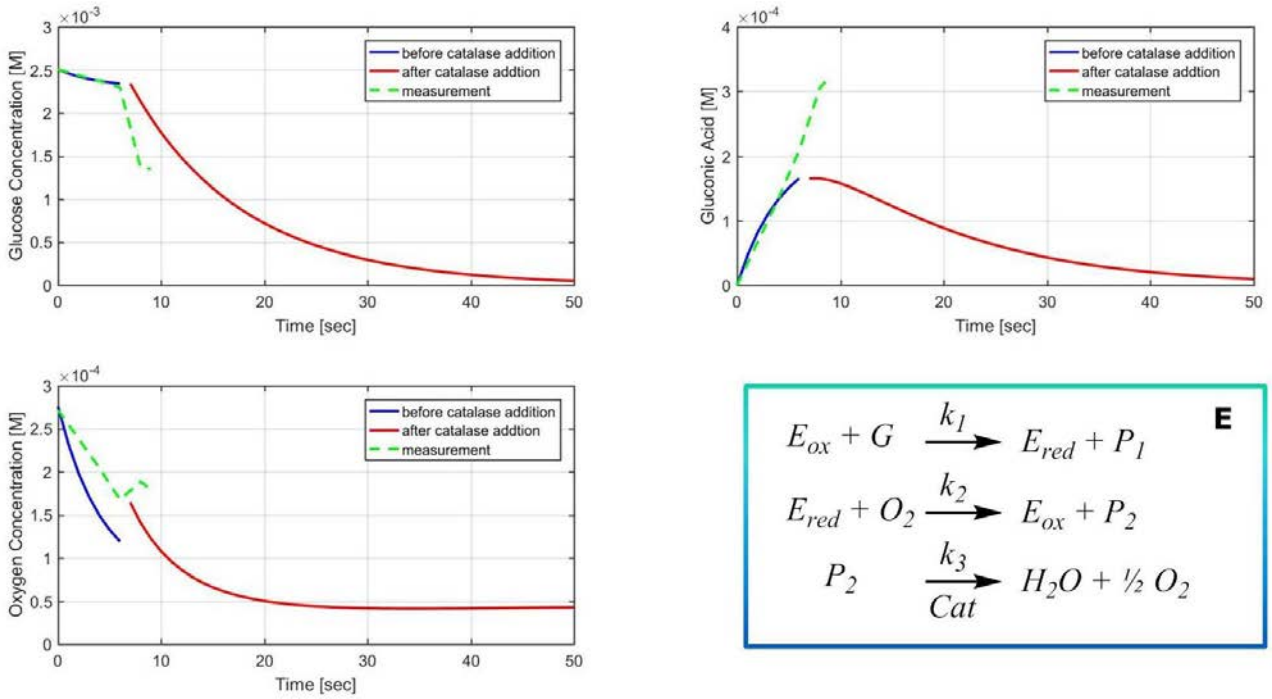

Figure 18 - *Mechanism E*. Comparison of the concentration profiles for glucose, gluconic acid and oxygen inside the microreactor before and after addition of catalase: simulation results *(blue solid line* – before catalase; *red dashed line* - after) *vs.* experimental data (*green dashed line*).

The addition of extra catalase solution in the reactor between sensor spots 2 and 3 was meant to significantly increase the oxygen concentration inside the microchannel due to the catalyzed decomposition of the peroxide. However, none of the provided experimental curves recorded by the integrated oxygen sensor spots has demonstrated a significant influence on the reaction kinetics by adding various extra amounts of catalase [67]. Moreover, the same system behaviour was confirmed by the model. The variation of experimental settings in the model, in particular the initial concentration of the dissolved oxygen inside the meander channel after catalase addition, and further comparison of the simulation results with the experimental curves allowed proposing a different explanation of the obtained phenomena. Thus, it was hypothesized that the minor increase in the oxygen concentration shown in Figure 18 (at $t \approx 7$ sec) was related to the introduction of the dissolved oxygen to the system through the lateral inlet. The increase of the dissolved oxygen concentration into the channel occurs as a consequence of adding an air saturated solution containing extra catalase. Moreover, the proposed hypothesis was also confirmed by the low peroxide concentration inside the channel prior to catalase addition predicted by the model (see Figure S7, Appendix A). The further investigation of the catalase and hydrogen peroxide impact on the reaction kinetics based on the oxygen sensor response was carried out in a well-mixed mL-scale reactor. The optimized experimental conditions were further validated inside the microfluidic platform with on-line reaction monitoring at all integrated sensor spots. The obtained results are summarized in the following section 2.2.4.2.

2.2.4.2. The effect of experimental conditions on the optical sensor response

Since the simulation results presented above considered equal activity values for glucose oxidase and catalase inside the mixture introduced to *inlet 2* of the microreactor, the influence of the higher catalase activity was studied. Moreover, the impact on the sensor response and reaction kinetics of the extra catalase (Cat*) was compared with the effect of adding an air saturated solution (Cat*^{air}). The obtained oxygen consumption rates are summarized in Figure 19.

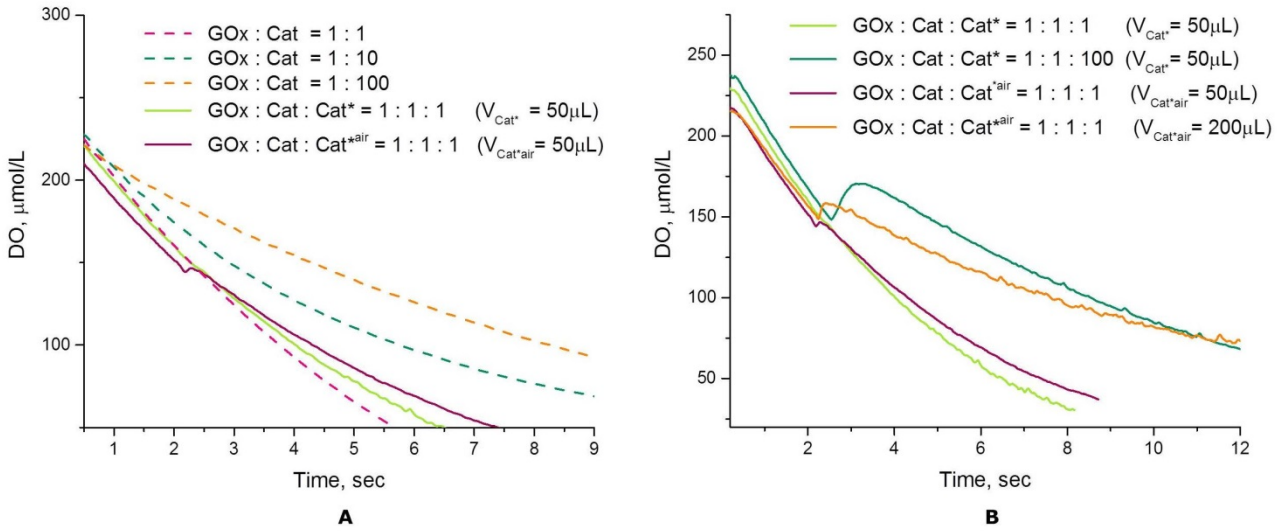

Figure 19 – Dynamic response of the oxygen consumption rates expressed as the number of moles of oxygen dissolved in the reaction mixture. The experimental curves obtained for activities of catalase equal to glucose oxidase, 10 times and 100 times higher (dashed lines) were compared with experimental curves in the presence of extra catalase (Cat*) and air saturated extra catalase solution (Cat*^{air}) (full lines) in A. The impact of the higher concentration of an air saturated catalase on the dissolved oxygen (DO) concentration recorded by optical sensor is summarized in B. The extra amount of catalase was added when the DO concentration reached a value equal to 150 µmol/L.

From Figure 19A it is clear that the addition of extra catalase having equal activity as the glucose oxidase does not influence the reaction kinetics, and has a negligible impact on the oxygen sensor response which can only be registered after introducing the air-saturated solution. On the contrary, the addition of extra catalase with significantly higher activity values compared to the glucose oxidase, or adding higher volumes of the air-saturated solution allows to detect the significant shift in DO consumption rates, as shown in Figure 19B. In order to obtain a more pronounced influence on the kinetics, different volumes of a 20 mM hydrogen peroxide solution were introduced to the glucose/glucose oxidase/catalase reaction mixture resulting in a different activity of the catalase, as shown in Figure 20. From the consumption rate curves in Figure 20B, it is clear that a more significant shift in oxygen concentration can be obtained even with the low peroxide concentration in the presence of catalase when having higher activity. Although the higher peroxide concentration affects more the overall reaction kinetics, the introduction of the various hydrogen

peroxide volumes at 150 µmol/L value of the dissolved oxygen resulted in a minor shift in the sensor response between the experiments (Figure 20A).

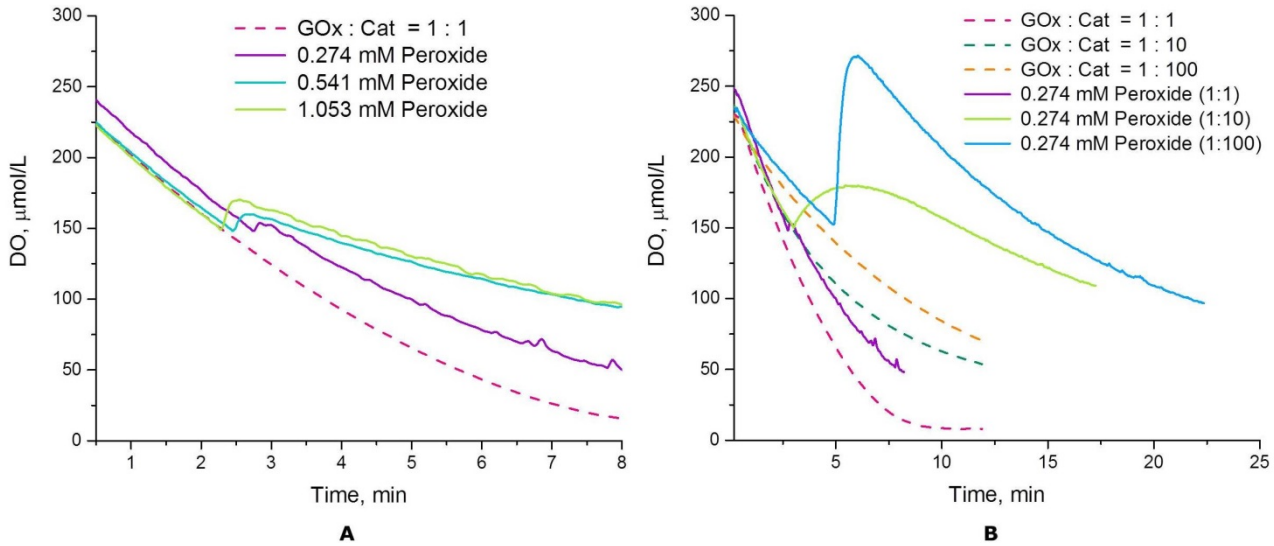

Figure 20 - Dynamic response of the oxygen consumption rates expressed as the number of moles of oxygen dissolved in the reaction mixture. The impact on the sensor response of various concentrations of hydrogen peroxide is summarized in A. A scenario with activity of the catalase equal to glucose oxidase, and then 10 times and 100 times higher is compared with experimental curves in the presence of different amounts of 20 mM hydrogen peroxide in B. The peroxide concentrations were calculated based on the total reaction volume. The peroxide solution was added when the DO concentration reached a value equal to 150 µmol/L.

In order to validate the experimental conditions optimized in mL-scale, the microfluidic chip with activated seven sensor spots was used to perform the glucose/glucose/catalase reaction in the presence of extra catalase and hydrogen peroxide solution. The objective of this study was to reproduce the DO conversion rates registered for 10 min in the 4 mL reactor inside the microfluidic platform (total volume approx. 11.8 µL). In Figure 21 the steady-state response by integrated sensor spots was compared with the dynamic response of the microoptode in the mL-reactor. The responses obtained at the 7th sensor spot were not included, since no reliable signal values were registered neither during the calibration, nor while performing the experiments (see Figure S11, Appendix B).

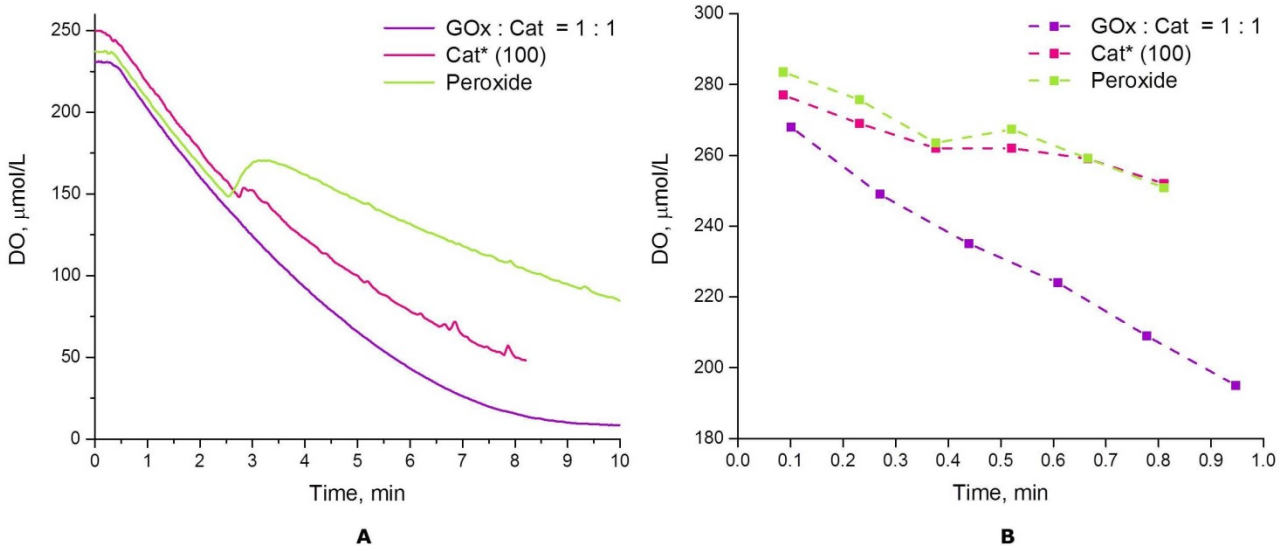

Figure 21 - Comparison of the reaction performance and sensor response for optimized experimental conditions in mL- (A) and µL- (B) scale reactors.

Only the oxygen signal shift tendency obtained in the presence of extra catalase and peroxide in mL-scale experiments (Figure 21A) was maintained in the microfluidic platform (Figure 21B). However, due to the low flow rate of the additional components inside the chip, no significant difference was registered when adding the extra catalase and peroxide solutions. Moreover, the long stabilization time for each oxygen sensor spot together with the lack of correlation for the DO conversion rates when comparing the mL- and µL-scale reactors indicated the presence of a much more complex mixing pattern inside the meander channel of the microscale reactor.

2.2.5. Conclusions and future perspectives

A mechanistic model describing the glucose oxidase/catalase cascade reaction in the presence of glucose inside a commercial microfluidic platform was developed. The simplicity of the model expressions allowed an easy modification and time effective calibration of the mechanism structure. The kinetic rate constants required for simulations were estimated numerically using various experimental data sets. The identified model mechanism structure was independently confirmed in micro- and batch scale experiments. The estimated kinetic constants were further validated with different glucose/glucose oxidase/catalase reaction scenarios and in the presence of extra catalase solution. Moreover, the model demonstrated itself as an effective tool in getting better insights into the reaction mechanism and understanding the correlations between the system parameters. The model-based theory explaining the minor signal shift detected by the oxygen sensor spots in the presence of extra catalase was further evaluated in an ideally mixed mL-scale reactor and confirmed by testing the optimized experimental conditions inside the µBR. The addition of hydrogen peroxide instead of catalase was suggested as a more effective approach for increasing the oxygen concentration inside the meander channel.

However, the applicability of the proposed model is limited by the lack of explanation of the transport phenomena occurring inside the microchannel and oxygen sensors spots. In order to improve the quality and the accuracy of the model the following steps should be considered. First, the phenomena of diffusion and convection (assuming a parabolic velocity profile in the channel) should be introduced to the model structure. This has already been shown as an effective approach by Ungerböck et al. [72] for on-line monitoring of oxygen profiles inside a microreactor. Moreover, the dependency of reaction kinetics on the reaction conditions, geometry and scale of the microfluidic chip presented in this thesis chapter has been previously studied in our group [73]. By use of computational fluid dynamics (CFD), the simulations of the system were performed for transamination reactions catalysed by ω−transaminase and for the oxidation of glucose catalysed by glucose oxidase (GOx). Although the integration of luminescent lifetime sensor spots inside the microreactors [55,71,74] has recommended itself as an accurate and inexpensive approach for on-line monitoring, the CFD simulations of the enzyme adsorption to the wall inside the chip allowed to explain the variation in the experimental data, as shown in Figure 22.

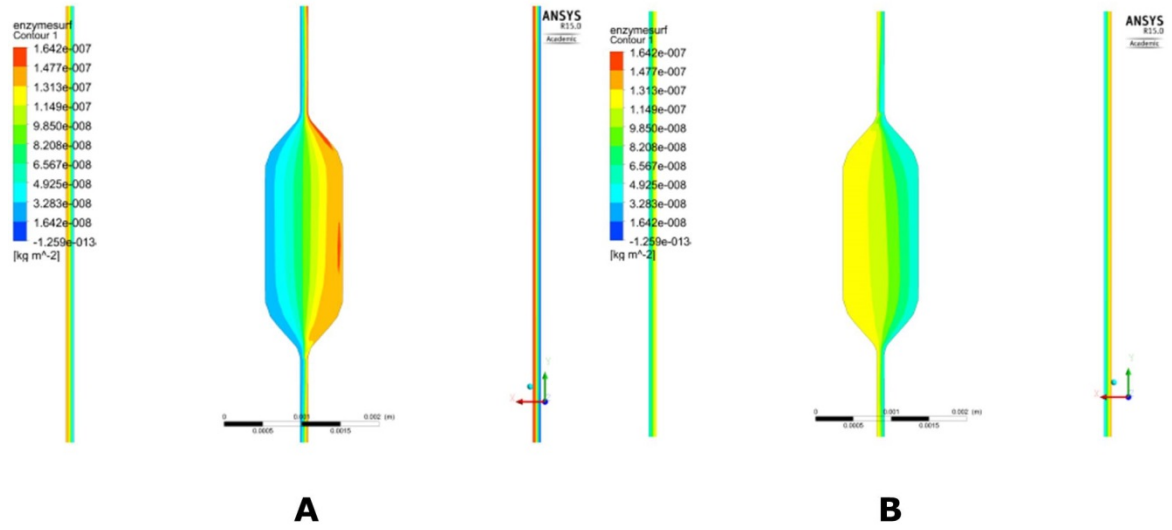

Figure 22 – The results of the CFD simulations of the adsorbed glucose oxidase concentration profiles. The contour plots represent the concentration on the walls of the first (A) and second (B) sensor spots obtained at the same time interval (31 seconds). Adapted from [73].

Therefore, the enzyme adsorption together with the gas bubble formation induced by catalysed degradation of peroxide inside the oxygen sensor spots would significantly affect the signal response. The application of the iterative robust model-based optimal experimental design approach could be an alternative solution for the parameter calibration of the proposed model [75]. Regardless of the model formulation method, the further validation of the simulation results requires reliable experimental data sets. Thus, the design and development of more robust sensing technologies that could support the on-line monitoring of additional variables of interest, apart from dissolved oxygen, is one of the crucial aspects of the successful application of mathematical models to bio-based processes.

Chapter 3
Multi-purpose platform for electrochemical sensors integration

The content of this chapter was partly redrafted from the following publications:

- A. C. Fernandes, D. Semenova, P. Panjan, A. M. Sesay, K. V. Gernaey and U. Krühne, *Multi-function microfluidic platform for sensor integration* [76].
- D. Semenova, A. Zubov, Y. E. Silina, L. Micheli, M. Koch, A. C. Fernandes and K. V. Gernaey, *Mechanistic modeling of cyclic voltammetry: a helpful tool for understanding biosensor principles and supporting design optimization* [77].

Abstract

Being compact, relatively stable and cheap, biosensors nowadays found their application in medicine [78,79], pharmacology [80], microbiology [81], the food industry [82], defence technologies [83] and others. Design, optimization and integration of biosensors and biochips hold a great potential for the development of cost-effective screening and point-of-care (PoC) technologies and instrumentation [84,85]. Therefore, the application of biosensors to bio-based processes would not only allow the on-line detection and monitoring of the desired biochemical species, but also lead to a better understanding of the complex fermentation and biocatalytic processes [86]. Therefore, this chapter demonstrates a practical approach for integration of an amperometric glucose biosensors inside a microfluidic platform for continuous monitoring purposes.

Despite the high integration of glucose biosensors for the monitoring in clinical diagnostics, further promotion of these sensors in industrial biotechnology still remains one of the crucial bottlenecks. One of the main reasons behind the lack of practical applications of such glucose biosensors in industrial biotechnology is a low glucose sensitivity of the commercially available biosensors. However, a considerable amount of research has been devoted to extend the upper limit of glucose detection in fermentations processes [87–89]. The developed microfluidic platform presented in the current thesis chapter allows detection of glucose concentrations outside of the biosensor detection range by simple in-line dilution (up to 10 times) of the initial sample due to the integration of a mixing/dilution chamber in between the two-sensors system. The presented glucose biosensors demonstrated the capability of continuous monitoring (up to 12 hours) of pure glucose samples and a potential for further application with fermentation media. Moreover, the platform was designed to promote the use and simple replacement of various sensors. The presence of standardized fittings could in principle allow an easy connection of the platform with other analytical devices, in particular with other microfluidic systems in a simplified “plug-and-play” approach.

3.1. Theoretical background

3.1.1. Electrochemical biosensors

In general, an electrochemical biosensor can be defined as an analytical device which by use of a biological recognition element allows converting biological, chemical and/or biochemical signals into a quantifiable electric response [90]. Such bioreceptor (e.g. an enzyme, an antibody, etc.) combined with appropriate electrical interface, represents the principal elements of the biosensor architecture (Figure 23) [91].

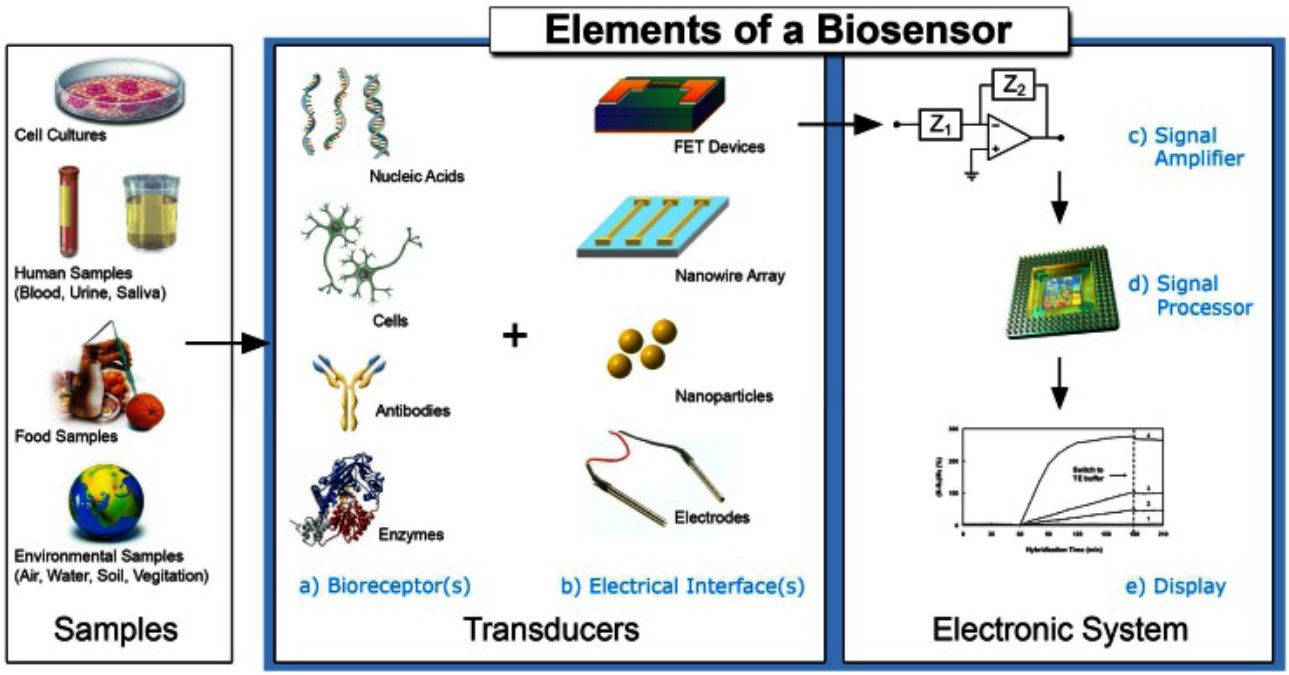

Figure 23 - Examples of biological probes (Samples), biosensor architectures (Transducers) and electric signal processing elements (Electronic System) [91].

A classical electrochemical cell of the sensor consists of the working electrode (WE), reference electrode (RE) and counter electrode (CE). The WE (or sensing electrode) is involved in the interaction with the target analyte; the CE provides the current required for the WE, whereas the RE maintains a stable potential for the entire experiment. Nowadays, the majority of the commercial electrochemical (EC) sensors are fabricated by screen printing technology on various substrates (e.g. silicon, glass, ceramics, etc.), as schematically shown in Figure 24. All three electrodes should be made of conductive and chemically stable materials. The choice of the right electrode material (e.g. carbon, platinum, gold), as well as the electrodes surface arrangement and design for EC sensors strongly depends on the biosensor application, the type of biochemical reaction and the target analyte [92].

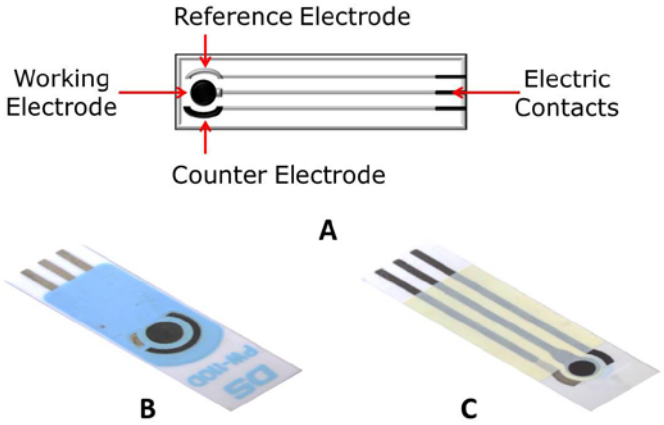

Figure 24 - Schematic representation (A) of the screen printed electrode (SPE). Examples of the disposable SPEs printed on polyester substrate used within the thesis are shown: DRP-PW-110DGPHOX SPE (B) customized by DropSens (carbon CE, silver RE, carbon WE modified with graphene oxide); IS-C SPE (C) purchased from ItalSens (silver RE, carbon CE and WE).

Mass transfer inside the EC systems consists of three distinct phenomena: diffusion, migration and convection. In the diffusion processes the transport of the species proceeds against the concentration gradient and tends to minimize the concentration differences close to the surface of the electrode (Figure 25A). The migration happens as a result of the potential gradients and the movement of the charged particles (ions) along an electrical field (Figure 25B). In convection the transport of the species to the electrode surface is induced either by external mechanical forces (e.g. stirring, vibration, and solution flow) or as a result of the density gradients (Figure 25C).

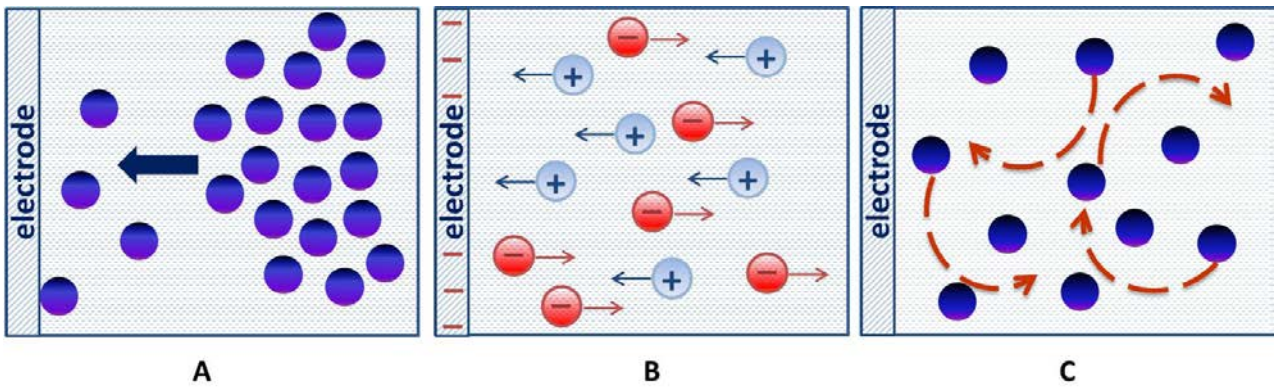

Figure 25 - The mass transfer phenomena in EC systems: diffusion (A), migration (B) and convection (C).

The operation principles of EC systems are based on the monitoring of the electron transfer for the redox reactions (41) and obtaining the current response correlated with the analyte concentration.

$$Ox + ne^- \rightleftharpoons Red \tag{41}$$

where *Ox* and *Red* refer to the oxidized and reduced forms, respectively. As any other chemical reaction, such redox process follows the thermodynamic and the kinetic control. In case no current

flows through the cell, the potential of the WE will eventually reach a steady state (Nernstian equilibrium) in which the concentration of the electroactive species can be established by the Nernst equation (42):

$$\frac{C_{Ox}}{C_{Red}} = \exp\left\{\frac{n_e \cdot F}{R \cdot T} \cdot (E - E^0)\right\} \tag{42}$$

where C_{Ox} and C_{Red} are the surface concentrations of the oxidized and reduced species, respectively; n_e is a number of electrons involved in the transfer; F is the Faraday constant; R represents the universal gas constant; T is temperature; E is the applied potential vs. the reference electrode and E^0 is the standard electrode potential.

However, the electrochemical processes occurring inside the biosensor system in the presence of the analyte solution are a complex combination of the electron transfer, chemical and/or biochemical reactions and surface processes (e.g. adsorption, electrocrystallization). Therefore, the transient behaviour of the EC systems plays an important role not only in tracing/monitoring the desired species but also in getting a better understanding of the sensing mechanisms, the electrode reactions and kinetics. In this case, the Nernstian equilibrium is disturbed so that the electrode reaction rates controlled by mass transport (mixed control region) and the obtained signal (current or potential) are measured as a function of the mass transfer rate at a fixed point - the flux. Assuming that all the three modes of mass transport (Figure 25) occur simultaneously, the flux of the molecules/particles to the electrode surface considering one-dimensional diffusion can be described by the Nernst–Planck equation (43).

$$J(x,t) = -D\frac{\partial \mathrm{C}(x,t)}{\partial x} - \frac{zFDC(x,t)}{RT} \cdot \frac{\partial \varphi(x,t)}{\partial x} + C(x,t) \cdot V(x,t) \tag{43}$$

where $J(x,t)$ is the flux density of the electroactive species at position x and time point t; D, z and C are the diffusion coefficient, charge and concentration, respectively; $V(x,t)$, ${}^{\partial C(x,t)}/_{\partial x}$ and ${}^{\partial \varphi(x,t)}/_{\partial x}$ correspond to the hydrodynamic velocity, concentration and potential gradients, respectively. The current is measured as a function of time, $i(t)$, and its magnitude follows the equation (44).

$$i(t) = n_e \cdot A \cdot F \cdot J(x,t) \tag{44}$$

where A is the surface area of the working electrode.

To avoid the influence of electromigration, the excess amount of the supporting electrolyte (e.g. an inert salt) can be employed to enhance the solution conductivity. Moreover, the convection effects are relevant for non-quiescent conditions (e.g. mixing of analyte). Thus, for the majority of electroanalytical processes the transport of the electroactive species will be limited only by the diffusional flux. Therefore, the equation (43) can be simplified so that the rate of diffusion is

proportional to the concentration gradient (Fick's first law). Hence, the local current response follows a more specific equation (45).

$$i(t) = -n_e \cdot A \cdot F \cdot D \frac{\partial C(x,t)}{\partial x} \tag{45}$$

Assuming linear diffusion, the time dependent local balance of the transported species can be described by Fick's second law as follows [93,94]:

$$\frac{\partial C(x,t)}{\partial t} = D \frac{\partial^2 C(x,t)}{\partial x^2} \tag{46}$$

The boundary region where the diffusion plays the main role in the mass transport is called the diffusion layer, and its thickness is denoted as δ. The convection forces outside the boundary region maintain the concentration profile of the species uniform and equal to the bulk values.

The most common detection techniques used for the characterisation of biosensor systems include potential-sweep and potential-step experiments, such as cyclic voltammetry (CV) and chronoamperometry (AM), respectively. In cyclic voltammetry, by varying the applied potential in a fixed range and with a constant speed (scan rate), the current between the counter and working electrodes is measured and plotted versus the potential normalized to the potential of the reference electrode. Following the IUPAC recommendation, the arising positive current in the voltammogram corresponds to the oxidation process (anodic current) occurring on the surface of the WE, whereas the negative current represents the reduction process (cathodic current), as shown in Figure 26, where the voltage is swept between -0.5 and +0.5 V at 50 mV/sec scanning speed (ν). When the voltage reaches the value +0.5 V, the scan is reversed and the voltage is swept to -0.5 V.

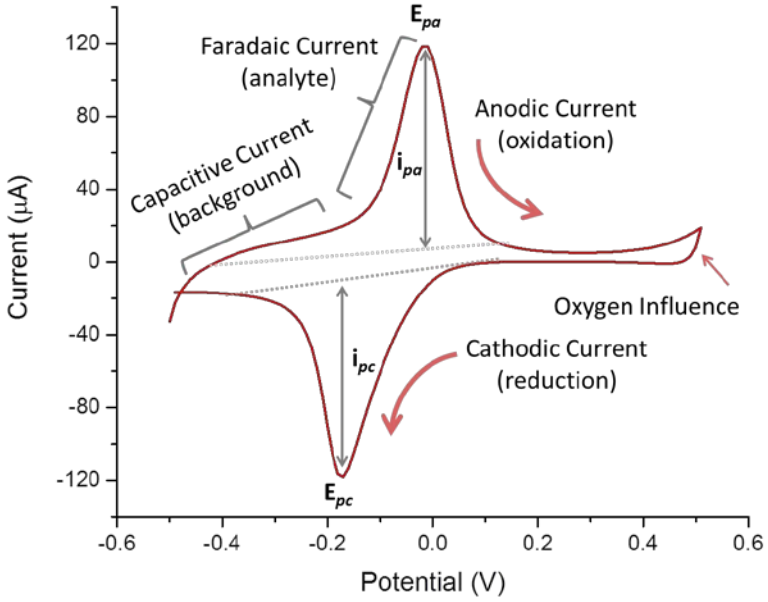

Figure 26 - Cyclic voltammogram obtained in air saturated buffer solution (pH = 6) for Prussian Blue modified SPEs (ν = 50 mV/sec). The analytical values, such as peak currents (i_{pa}, i_{pc}) and peak potentials (E_{pa}, E_{pc}), are highlighted in the graph, as well as the influence of the oxygen, capacitive and faradaic currents on the voltammogram.

In chronoamperometry a fixed value of the potential (E_{app}) is applied to the WE and the Faradaic current arising from the electrochemical oxidation or reduction of an electroactive species is measured as a function of time (45). In Figure 27A, the changes in the current *vs.* dynamic response depending on the value of the applied voltage are shown for the glucose biosensors in phosphate buffer. The evolution of the concentration profiles *vs.* time (Figure 27B) is recorded at the fixed value of the applied potential but for the different glucose concentrations.

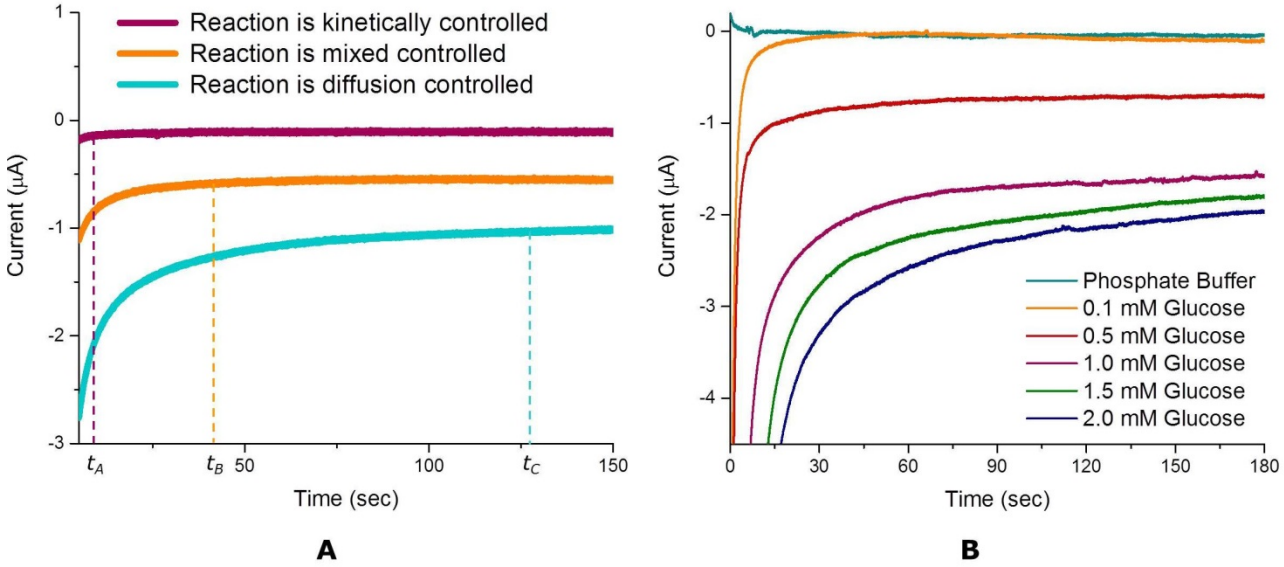

Figure 27 - Chronoamperometric response of glucose biosensors: at various values of applied voltage in phosphate buffer (A) and constant potential (B) for different glucose solutions.

In case of very small rate constants in the reaction (41), the diffusion does not play an important role and the reaction is under kinetic control. Due to the applied pulse, the surface concentration of the oxidized form (*Ox*) does not vary significantly. As soon as the diffusion rate is comparable with the rate of the electron transfer, the system behaviour shifts to the mixed control region. The redox system obeys the full diffusion control when the current rises steeply and requires more time to reach a steady state ($t_A < t_B < t_C$). Consequently, the concentration gradient decreases with the increase of the diffusion layer thickness ($\delta_A < \delta_B < \delta_C$).

3.1.2. Glucose biosensors

The development of a crucial tool for an accurate and reliable diagnostics and continuous monitoring of various physiological parameters, such as glucose concentration levels for diabetes patients resulted in more than 50 years of biosensor research and the establishment of the electrochemical glucose biosensors in clinical diagnostics [95]. Comprehensive reviews on the principles of operation and evolution [96–98], as well as the recent advances in electrochemical glucose biosensing [99] and its application in diabetes management [100,101] have already been published. The advantages and disadvantages of the enzymatic glucose sensing towards non-enzymatic sensing were previously compared in the work of Toghill and Compton [102]. Therefore, the current thesis section will be mainly focused on the historical overview and basic principles of glucose biosensing.

The concept of the enzyme electrode was proposed for the first time by Clark and Lyons [103] in 1962 for monitoring purposes during cardiovascular surgery. A thin layer of glucose oxidase (GOx) entrapped in a semipermeable dialysis membrane was placed over an oxygen sensitive electrode. The glucose monitoring in the enzymatic reaction (47), (48) was allowed by the detection of oxygen depletion on the Pt cathode (49) as a result of the potential change.

$$\mathrm{GOx(FAD)} + \mathrm{Glucose} \longrightarrow \mathrm{GOx(FADH_2)} + \mathrm{Gluconic\ Acid} \quad (47)$$

$$\mathrm{GOx(FADH_2)} + \mathrm{O_2} \longrightarrow \mathrm{GOx(FAD)} + \mathrm{H_2O_2} \quad (48)$$

$$\mathrm{O_2} + 4\mathrm{H^+} + 4e^- \longrightarrow 2\ \mathrm{H_2O} \quad (49)$$

However, the amperometric glucose sensitive electrode based on quantitative monitoring of hydrogen peroxide was constructed only in 1973 by Guilbault and Lubrano [104]. Similar to Clark's oxygen sensor, the physiological mediator - oxygen was involved in the reoxidation of the flavin groups of glucose oxidase (47), (49) and the peroxide detection (50) was performed on a platinum or a special thin film electrode at a moderate anodic potential of approximately +0.6 V (vs Ag/AgCl).

$$\mathrm{H_2O_2} \longrightarrow \mathrm{O_2} + 2\mathrm{H^+} + 2e^- \quad (50)$$

The stable response and simplified sensing mechanism (either O_2 consumption or H_2O_2 production rates) allowed to use the first generation glucose biosensors (Figure 28A) in miniaturized devices.

However, the presence of the other electro-active species in blood samples could initiate parallel redox reactions that would significantly interfere with the main signal. Moreover, highly pronounced oxygen dependency of the proposed biosensors combined with the characteristic "oxygen deficit" of the system in the presence of the physiological glucose concentrations (the dissolved oxygen concentration in blood is approximately one order of magnitude lower than for glucose) resulted in a series of efforts focused on the improvement of both selectivity and sensitivity of glucose biosensors. Therefore, two main approaches were suggested: (i) use of permselective membranes that would reduce or inhibit the interference of other electroactive species; (ii) use of catalysts that would decrease the applied potential value for peroxide detection [99]. One of the most common and highly selective catalysts to hydrogen peroxide, Prussian Blue (PB) has been widely used for analytical purposes and mainly for the glucose monitoring at low potentials [105]. Other aspects regarding the behaviour of Prussian Blue films in aqueous solutions and the reaction mechanisms in the presence of hydrogen peroxide are carefully summarized in Chapter 4. The further improvement of the sensing mechanisms resulted in the second and third generations of glucose biosensors, as shown in Figure 28B,C.

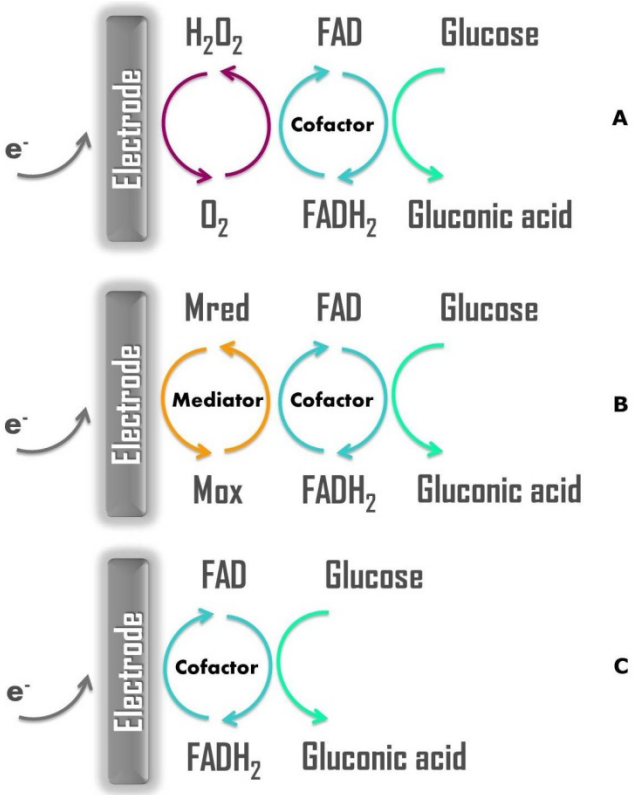

Figure 28 - Assembly and operation principles comparison of glucose biosensors: first (A), second (B) and third (C) generations. The GOx cofactor groups (FAD)/($FADH_2$) – oxidized/reduced forms, as well as the mediator oxidized (Mox) and reduced (Mred) forms (e.g. Prussian Blue/Prussian White redox couple) are highlighted. The schematic representation was adapted from [106].

In the second generation glucose biosensors (Figure 28B), oxygen was substituted by the artificial electron acceptor – mediator. The presence of mediator (e.g. conducting organic salts, quinone derivatives, etc.) either inside the biosensor system or in the analyte solution, allows faster electron shuttling from the enzyme redox active site to the electrode surface. However, the ultimate goal remains the development of the "reagentless" third generation glucose biosensors (Figure 28C). Using novel electrode materials and varying electrode configurations, an electron transfer from the enzyme redox active site directly to the surface of the electrode could be achieved. Thus, the glucose detection should be possible at very low potentials similar to the glucose oxidase redox potential (approximately -0.50 V vs. Ag/AgCl), which would subsequently guarantee high selectivity of such biosensor. The current trends in the development of bioelectrocatalytic devices for personalized and non-invasive glucose monitoring were briefly summarized in Figure 29.

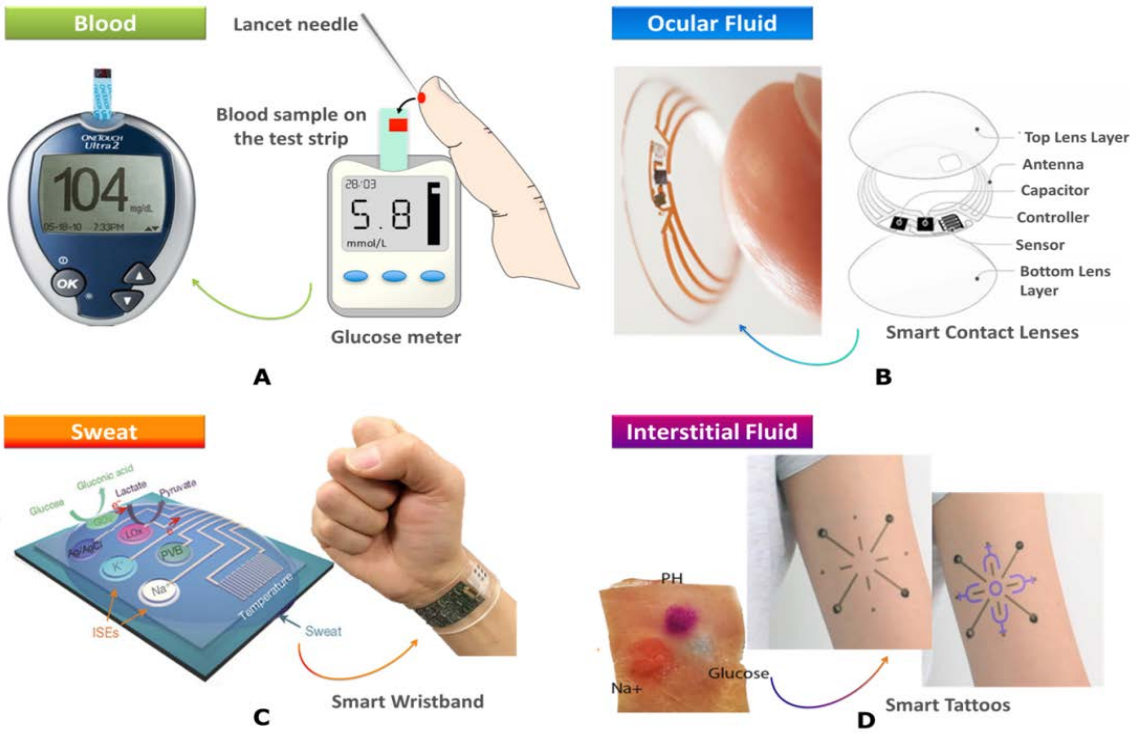

Figure 29 - Schematic illustrations and photographs of the available devices and prototypes for glucose monitoring.

The most common technique is based on the *in vitro* glucose monitoring in blood samples (Figure 29A) which involves disposable strips and a glucometer (e.g. OneTouch® Ultra®2) [107]. As an alternative for the non-invasive glucose monitoring the more accessible biological samples such as ocular and interstitial fluids, sweat, breath, urine and saliva were proposed [100]. In Figure 29B the prototype of the smart contact lens developed by Google and Novartis [108] is shown. The flexible sensor arrays (glucose, lactate, temperature etc.) can also be integrated into a wearable wristband (Figure 29C) [109]. An *ex vivo* skin model was developed for the printing of fluorescent and colorimetric biosensor arrays (sodium, pH, glucose) as tattoos [110] for the direct monitoring *via* colour changes in interstitial fluids (Figure 29D).

3.2. Case Study 2: Multi-function microfluidic platform for sensor integration

3.2.1. Introduction

In this case study, the adaptable screening platform with integrated glucose biosensors was developed addressing the need for an accurate reaction monitoring inside the microreactor presented in Case Study 1. The proposed multi-function platform, with disposable and changeable sensors, allows flexible integration with other microfluidic platforms through a "plug-and-play" approach by using standardized finger tight fittings. Moreover, the platform can be easily connected to external equipment (e.g. syringe pumps, HPLC), while offering the advantage of in-line use, thus not interfering with the reaction vessel. The choice of material (polymethylmethacrylate) and fabrication technology (laser ablation) considered both design flexibility and costs. Polymethylmethacrylate (PMMA) in combination with laser ablation is an adequate solution towards fast optimization cycles: from design, to fabrication and testing with fluids. Furthermore, since PMMA is a widely available biocompatible and low cost material, it enables a low cost device fabrication with good reproducibility. The developed platform includes a two-sensor system interspersed with a mixing channel, which allows the detection of samples that might be outside the first sensor's range of detection, through dilution of the sample solution up to 10 times. Furthermore, the influence of the fluid flow velocity on the substrate diffusion was observed, indicating the need for in-flow calibration to achieve a good quantitative output. The case study overview is summarized in Figure 30.

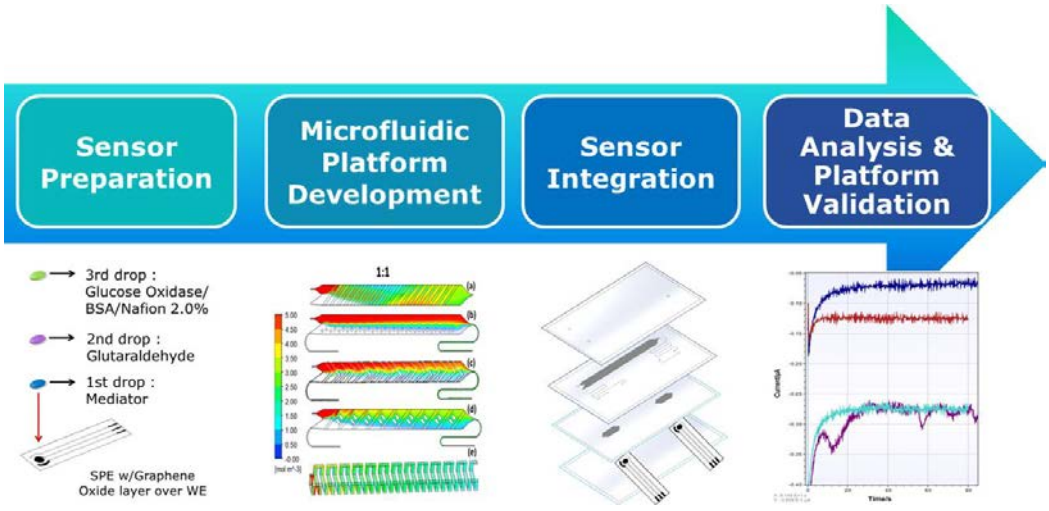

Figure 30 - Case study 2, graphical roadmap.

3.2.2. Experimental section

The microfluidic platform presented in this section was designed and fabricated at the PROSYS Research Center in collaboration with A. C. Fernandes. No work related to mixing/dilution chamber geometry optimization and CFD validation is presented here, since all the designs and simulations were performed by A. C. Fernandes and Assoc. Prof. Ulrich Krühne, respectively. Moreover, the

extensive procedure for the evaluation of the electrochemical sensors response towards glucose in the fermentation samples was developed at the Measurement Technology Unit (MITY) at Oulo University by P. Panjan and will not be discussed in the following sections.

3.2.2.1. Reagents and materials

Glucose oxidase (EC 1.1.3.4, type VII, from *Aspergillus niger*, ≥100,000 U/g solid) and bovine serum albumin (BSA) were obtained from Sigma (St. Louis, MO, USA). Nafion®117 solution (~5% (v/v) in a mixture of lower aliphatic alcohols and water) and iron (III) chloride (anhydrous, 99.99%) were obtained from Aldrich (Steinheim, Germany). Potassium hexacyanoferrate (III) (ACS reagent, ≥99.0%), glutaraldehyde solution (25% (v/v)), phosphate buffer saline (PBS) and ethanol (UV HPLC gradient, 99.9%) were obtained from Sigma – Aldrich (St. Louis, MO, USA). Yeast extract and peptone were bought from BD (France) and dextrose from Difco (MI, USA). The hydrochloric acid to set the pH of the fermentation medium was diluted to 10 mM from concentrate (Merck, Germany). D-Glucose (anhydrous) was provided by Fluka (Loughborough, UK). Mono– and di-potassium hydrogen phosphate (anhydrous) were obtained from Merck (Darmstadt, Germany). All the solutions for sensor preparation were prepared with 0.1 M phosphate buffer + 0.1 M KCl, pH = 6. All other solutions were prepared in 0.1 M phosphate buffer.

Screen printed electrodes (SPEs) DRP-PW-110DGPHOX were customized by DropSens (Llanera, Spain), and ItalSens IS-C electrodes were acquired from PalmSens (Utrecht, The Netherlands). Both types of electrodes were printed on polyester substrate and each sensor consists of a carbon working electrode (modified with graphene oxide layer for DRP-PW-110DGPHOX), a carbon counter electrode and a silver reference electrode. The diameter of the working electrodes was 0.4 cm (DRP-PW-110DGPHOX) and 0.3 cm (ItalSens IS-C), resulting in apparent geometric areas of 0.126 cm^2 and 0.07 cm^2, respectively.

The PMMA sheets for extrusion with thickness of 2 mm were acquired from Nordisk Plast (Assentoft, Denmark). The PMMA plates were patterned using laser ablation with a CMA-4030 Laser Engraving machine from GD Han's Yueming Laser Technology co., Ltd (Guangdong, China). The chemical bonding procedure for PMMA plates was performed using an anhydrous chloroform solution (288306, ≥99%) from Sigma-Aldrich (St. Louis, MO, USA). Adhesive assembly and integration of the sensors on the platform were performed with a 140 µm thick mcs-foil 008 from microfluidic ChipShop (Jena, Germany). The polydimethylsiloxane (PDMS) thin sheets used as gaskets were fabricated using the elastomer and curing agent kit of Sylgard® 184 from Dow Corning (Auburn, Michigan). The two 10 mm thick acryl plates that form the custom-made holder were from Rias A/S (Roskilde, Denmark). The holder was completed with two outer 5 mm thick SS304 stainless steel plates from Sanistål (Aalborg, Denmark). Flangeless polypropylene (PP) fingertight 1.5875 mm (ID) fittings (XP-201) and flangeless ferrules (P200X) from Upchurch Scientific® (Washington, USA) were used to connect polytetrafluoroethylene (PTFE) 1.5875 mm (OD) x 1 mm (ID) tubing (S 1810-12) from Bohlender (Grünsfeld, Germany).

3.2.2.2. Sensor preparation and characterization

The chemical deposition procedure of PB was adopted from works of Ricci et al. [111]. A 10 µL drop (total volume) of freshly made precursor solution, containing 0.1 M potassium ferricyanide ($K_3Fe(CN)_6$) in 10 mM HCl mixed with 0.1 M ferric chloride ($FeCl_3$) solution in 10 mM HCl (1:1 proportion (v/v)), was directly placed over the working electrode (WE) surface of the 110DGPHOX SPEs. In the IS-C SPEs a 2:1 proportion was used for the detection sensor and a 1:2 proportion for the reference sensor. The sensors were left to dry for 10 min at room temperature and then washed with a 10 mM HCl solution and deionized water. In order to stabilize the PB layer, the sensors were placed in the oven at 100°C for 1 h. Prior to glucose oxidase (GOx) immobilization, a 2.5 µL droplet of freshly prepared glutaraldehyde solution (1% (v/v) diluted in water) was placed over the WE of the PB modified SPEs and was left to dry at room temperature for 30 min. After the glutaraldehyde solution layer was dried, the enzyme/membrane layer was deposited. The fresh enzyme/membrane solution was made by mixing GOx solution (0.074 U in phosphate buffer), BSA (5 vol. % diluted in water) and Nafion®117 (5 vol. % diluted in water) in a 1:1:1 proportion (v/v/v). A drop of 3 µL of the final solution was placed over the working electrode of the PB/glutaraldehyde modified SPEs and sensors were placed to dry overnight in a climate chamber at 40% of humidity and 8°C. The complete glucose biosensors were stored in the dark, at room temperature and at 4°C.

Cyclic voltammetry (CV) and amperometric measurements (AM) were carried out using a MultiEmStat with a DRP-CAST1X8 interface (DropSens, Llanera, Spain) for 8 independent electrodes under MultiTrace Software 3.4 control (PalmSens, Utrecht, The Netherlands). Fluid flow was maintained by Cavro® XL 3000 syringe pumps from Tecan (Männedorf, Switzerland). The cyclic voltammograms obtained in droplets using phosphate buffer solution (0.1 M phosphate + 0.1 M KCl, pH = 6) were registered by cycling in a potential range between - 0.5 and + 1.2 V with a scan rate of 50 mV/s, as shown in Figure 31. The chronoamperometric measurements were performed in a droplet (50 µl of the glucose solution) at an applied potential of -0.16 V (DRP-PW-110DGPHOX) or -0.04 V (ItalSens IS-C) versus a screen printed internal silver reference electrode.

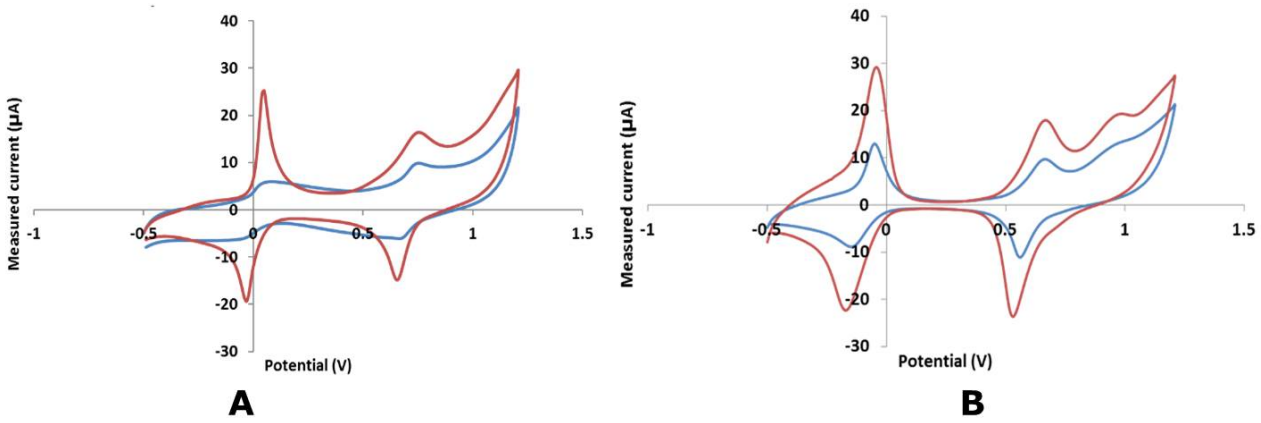

Figure 31 – Cyclic voltammograms obtained in droplet for ItalSens IS-C (A) and DRP-PW-110DGPHOX (B) based glucose biosensors. The sensors used in the reference and detection sensor chambers correspond to blue and red curves, respectively. Adapted from [76].

In flow measurements were carried out at the flowrates used for the mixing/dilution chamber characterization. The flowrates during characterization varied between 0.25 and 10 µL/s. When a stable baseline current was reached (after 30 s and 60 s, for DRP-PW-110DGPHOX and ItalSens IS-C based sensors, respectively) with phosphate buffer solution (0.1 M phosphate + 0.1 M KCl, pH = 6), different analyte concentrations were tested and the measurements were recorded. In the droplet characterization of the glucose biosensors, the drop of 50 µl of known glucose concentration (0.1 mM – 8 mM) was placed on top of all the electrodes and the current was recorded until it reached a stable value. When the sensors were characterized in flow, a volume corresponding to 3 times the internal volume of the microfluidic platform was first pumped to guarantee that only the target analyte concentration was inside the system. Data was retrieved after stabilization of the signal.

3.2.2.3. Microfluidic platform fabrication and sensor integration

A microfluidic system containing two inlets, two sensing/measurement chambers for sensor integration, and one mixing unit was developed and is schematically shown in Figure 32. One of the microfluidic inlets is connected to the first sensor chamber, where the reference sensor is located. The second inlet is connected to the mixing chamber, which serves here as a dilution unit but can also be used as a reactor or target labelling unit.

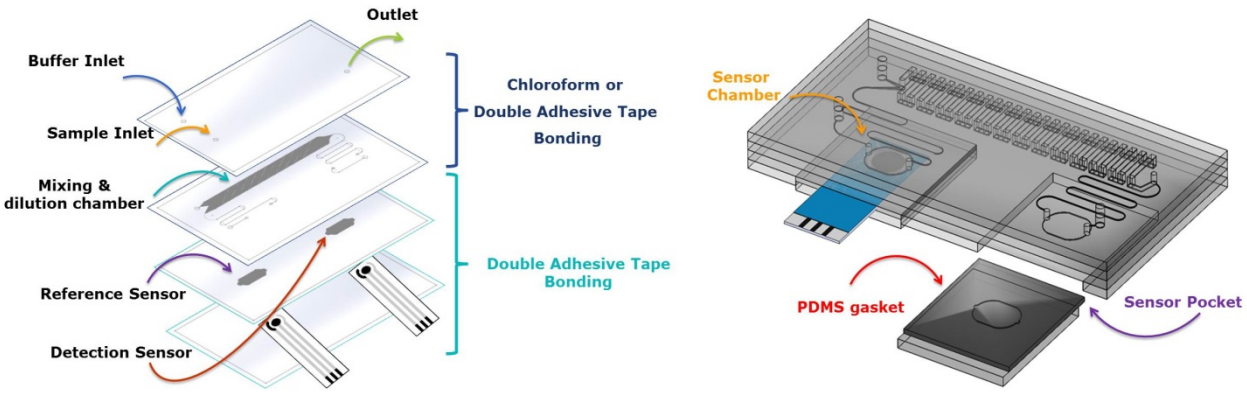

Figure 32 - Schematics of the different PMMA plate's assembly (A) and SolidWorks 3D representation of the developed platform (B). All the important microfluidic chip elements together with the sensor positions are highlighted.

One of the microfluidic inlets is connected to the first sensor chamber, where the reference sensor is located. The second inlet is connected to the mixing chamber, which serves here as a dilution unit but can also be used as a reactor or target labelling unit. The second chamber is positioned after the mixing unit. The sensor integrated in this chamber is the one used for sample quantification (detection sensor). Moreover, the generic rectangular sensor pockets at the bottom plate of the device allow a straightforward access to the sensing chambers. The sensor can thus be

directly placed in the chamber and covered with a thin polymeric gasket. The system is then closed by placing PMMA inserts in the pockets and sealing the whole platform with help of an outside mechanical holder system.

The design of the device was performed in SolidWorks 2015 (Dassault Systèmes SolidWorks Corporation, Waltham, Massachusetts, USA). This microfluidic platform consists of four PMMA plates ablated by laser ablation, as shown in Figure 32A. After ablation, the plates were thoroughly washed with deionized water, dried and then placed in an oven at 80ºC for 1 hour to release thermal stress before proceeding with the assembling. Two different approaches were tested when assembling the PMMA plates: (i) lamination with double sided pressure sensitive adhesive tape (DAT) and (ii) chloroform bonding. In the first approach cooled PMMA plates were glued together and pressurized with clamps placed in an oven at 80ºC for at least 1 hour to avoid air bubble formation disturbing the adhesion. The chloroform bonding procedure was adapted from the work of Ogilvie et al. [112]. Prior to the solvent exposure, PMMA plates rinsed in DI water were thoroughly washed with isopropanol solution (99.5%) followed by ethanol, and dried with air. The prepared substrates were suspended with the surfaces to be bound on four glass stand-offs at a height of approximately 2 mm from the top of the standoffs above a chloroform solution inside a closed glass Petri dish. After 2 min of exposure the PMMA plates were carefully removed and pressed together manually in order to guarantee a complete bonding. In both approaches, the sensors were integrated into the platform using thin PDMS gasket films that sealed the sensor around the sensing chamber. PDMS gaskets were fabricated by mixing in a SpeedMixer^{TM} DAC 150.1 FVZ-K from Synergy Devices Limited (High Wycombe, UK). A 1:10 proportion mixture of the curing agent and the Sylgard® elastomer, was poured into a 1 mm PMMA mold having the shape of the sensor pockets followed by curing at 70ºC inside the oven for 1h.

Once the chip was assembled, the sensors were placed in the sensor pockets with the PDMS gaskets on top followed by a bottom PMMA plate. The microfluidic platform with integrated sensors was connected to an in-house fabricated casing, which provided the necessary uniform pressure to achieve leakage-free flow. The platform holder was built from two acrylic plates of 100x100 mm^2 that were micromilled to obtain a cavity the size of a chip, and two outer SS304 stainless steel plates with a thickness of 5 mm, to avoid bending of the acryl plates when assembling (screwing) holder elements together. The experimental setup is summarized in Figure 33.

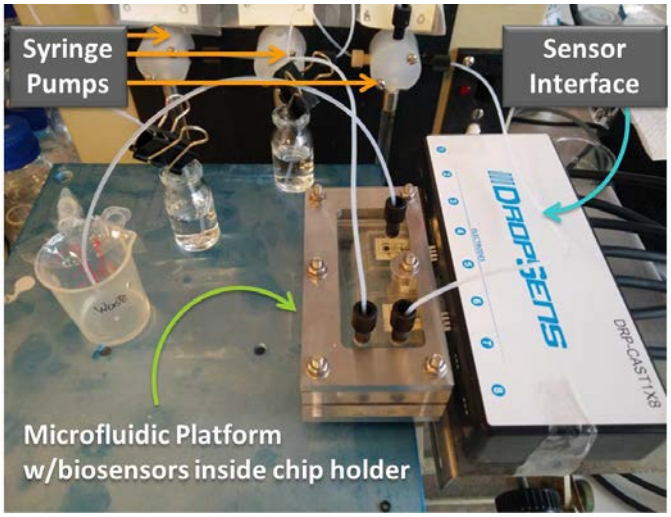

Figure 33 - The elements of the experimental setup assembly for glucose continuous monitoring inside the microfluidic platform with integrated ItalSens IS-C based glucose biosensors.

3.2.2.4. Mixing/dilution chamber

Several passive mixing geometries were designed in SolidWorks 2015 (Dassault Systèmes SolidWorks Corporation, Waltham, Massachusetts, USA) and studied with the help of computational fluid dynamics (CFD), as shown in Figure 34.

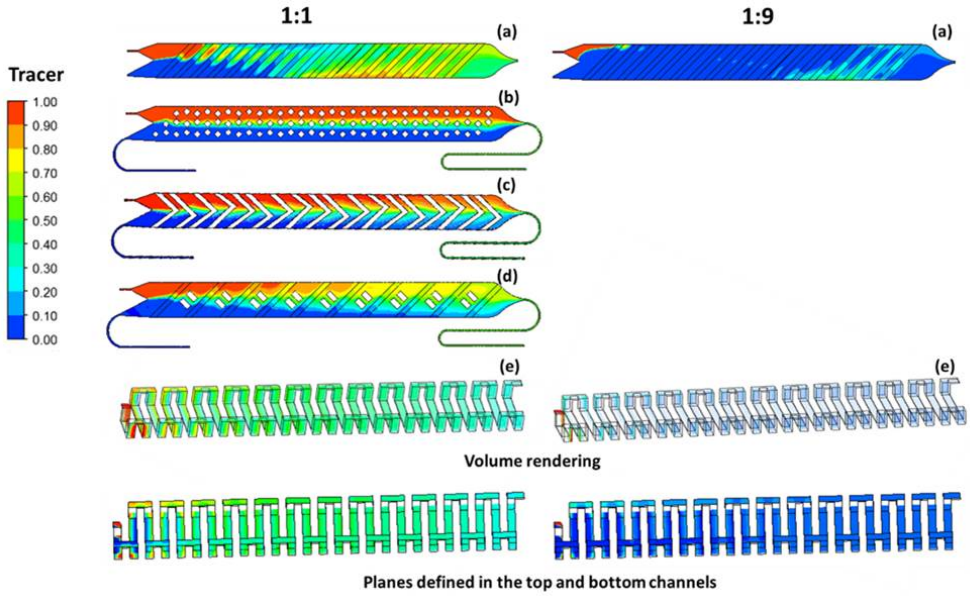

Figure 34 - Comparison of the mixing capability of different mixing chamber geometries using CFD simulation for 1:1 dilution at 10^{-3} m/s, and of a 10 times difference between inlet velocities for two geometries (straight diagonal barriers channel and the 3D serpentine channel). The following mixing geometries were tested: (a) slanted groves, (b) squared baffles, (c) staggered herringbone, (d) combination of herringbone and obstacles and (e) three-dimensional serpentine channel. For the three-dimensional serpentine channel (e), a view of the entire fluid with volume rendering is presented on the top, with the initial section for 1:1 dilution enlarged, while the bottom images present two planes defined at the top and bottom of the three-dimensional channel. Adapted from [67].

The three-dimensional serpentine channel (e) allowed a proper target sample mixing and was implemented in the final design of the platform (Figure 32B). Therefore, the dilutions were performed inside the microfluidic platform using a 3 mM glucose solution introduced through the inlet connected to the first sensing chamber (reference sensor) and a buffer solution introduced in the second inlet (connected to the mixing/dilution chamber). The flow rate for the substrate was maintained the same (1 µL/s) whereas for the buffer solution it was increased in order to achieve the correct dilution as presented in Table 2. The diluted samples quantified by the detection sensor were further collected at the outlet of the microfluidic platform and measured in an HPLC for validation of the mixing unit, and results were compared with the data retrieved from the integrated sensors. The linear sensor response in the presence of glucose was obtained from 0 to 5 mM and from 0 to 2 mM for the DRP-PW-110DGPHOX and the ItalSens IS-C based biosensor, respectively.

Table 2 - Flowrates used to test the mixing/ dilution chamber inside the developed microfluidic platform. Adapted from [76].

Dilution	Flowrate in buffer inlet (µL/s)	Flowrate in second sensing chamber (µL/s)	Flowrate used for data interpretation (µL/s)
1:1	1	2	2
1:2	2	3	4
1:5	5	6	6
1:9	9	10	10

3.2.2.5. High-performance liquid chromatography (HPLC)

All the reaction probes were analyzed with HPLC for quantification of consumed glucose and produced gluconic acid. The measurements were performed with reversed-phase chromatography on an Ultimate 3000 HPLC (Dionex, Sunnyvale, CA, USA) equipped with a Phenomenex column with 5-µm sized amine particles (Luna 5u NH2 100A), operated at 40°C and 140 bar. The mobile phase consisted of a 20 mM phosphoric acid (H_3PO_4) solution, flowing at 1 mL/min. The eluted gluconic acid was quantified in the ultraviolet (UV) multiple wavelength detector at 205 nm, while the glucose concentration was determined in the Refract Max 520 refractive index (RI) detector. The amount of each component was obtained by integration of the areas under the corresponding peaks using the HPLC commercial analytical software (Chromeleon 6.8), based on a calibration curve performed for each component. Samples were measured mixed with 0.5 M sodium hydroxide solution in a proportion 1:2 of solution relative to the sample.

3.2.3. Results and discussions

3.2.3.1. Design of a platform for sensor integration

The presented platform was developed to address the current need for in/on-line monitoring of several components (e.g. product formation, cell viability and media composition) in bioprocesses.

It was designed to be a part of a multi-component microfluidic platform, where each system is connected to others via a "plug-and-play" approach. Even though custom-made connections can be developed [113], the approach chosen in this work aimed at developing a platform compatible with connection with external analytical devices and integration in the "plug-and-play" platform. Therefore, commercial finger tight fittings (such as, HPLC-type connectors) and standard tubing were used. The platform was built in order to be suitable for a high range of applications. To this end, the final design, a closed channel connected to a chamber where the sensor can be placed, enabled the required flexibility in terms of the sensors used and their easy replacement. The sensor is introduced in the platform through rectangular pockets which allow a wide variety of sensor shapes and widths to be integrated without requiring the modification of the whole platform. Furthermore, it is important to note that the sensor and platform fabrication are independent from each other. In this way, any sensor technology compatible with the platform material can be used, which considerably broadens the future opportunities for the platform applications.

The assembly of the microfluidic platform, using lamination with double-sided pressure sensitive adhesive tape (DAT), allowed a fast assembly of the different plates that form the platform (less than 15 min required), while also achieving a leakage-free flow and enabling the re-usability of the platform. As proof-of-concept, screen-printed electrochemical sensors were chosen due to their cheap fabrication and wide use in microfluidic and health related applications. The possibility of applying these sensors as single-use detection elements is also an appealing concept due to the impending challenges of biofouling that bio-applications can generate during long-term measurements. Furthermore, two different types of electrodes were selected with the same detection principle and target, but with different materials and thicknesses. The choice of electrochemical sensors influenced the final design of the platform. The distance between the measurement chambers (37.2 mm center to center) was defined based on the gap between the inlets of the interface connecting the sensors to the potentiostat used for measurement. In principle, due to the fast fabrication and assembly cycle of the platform (< 2 h), adaptation of the platform to most types of sensors (by adjusting the sensing chamber) can easily be performed. The two integrated sensors are subjected to different flow rates during measurements, since one is positioned before the mixing/dilution chamber (first sensing chamber), while the other is positioned after the mixing/dilution unit (second sensing chamber). So, the first sensing chamber is only affected by the flow of one of the inlets (sample inlet). The second sensing chamber, on the other hand, experiences a higher flow rate which is the sum of the flow rate from the two inlets (sample plus buffer for dilution). The overall internal volume of the developed platform is approximately 500 µl.

3.2.3.2. Sensor characterization

The sensors integrated in the developed microfluidic platform were characterized both in a static (droplet characterization) and in a dynamic environment (in-flow characterization). Both types of measurements were performed for the same substrate concentrations; and, in the case of the

dynamic measurements, the used flowrates were identical to the flow rates that the sensors would be subjected to during the mixing/dilution experiment (0.25 to 10 µL/s). All the obtained results were summarized in Figure 35.

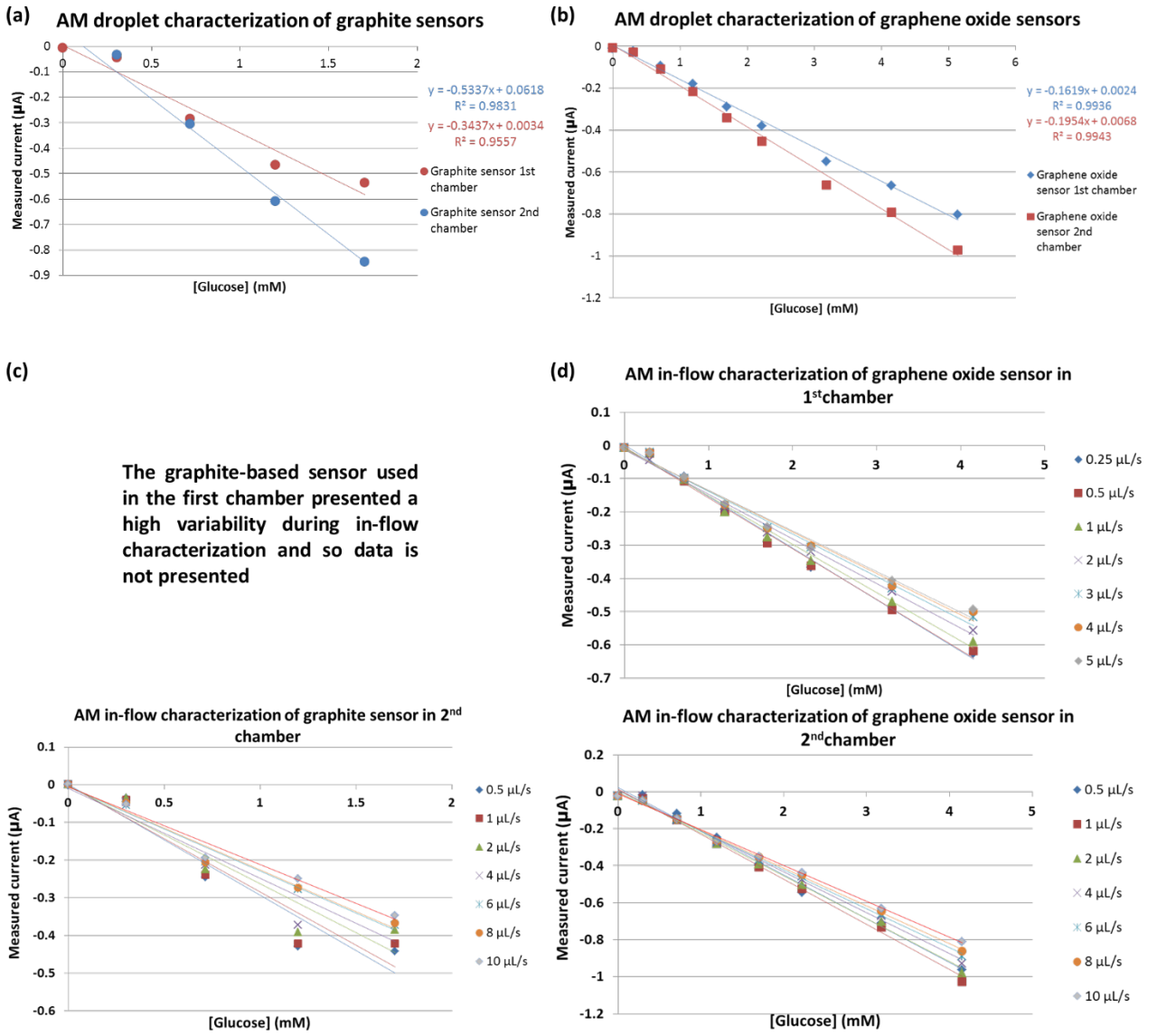

Figure 35 - Amperometric characterization in droplet of the biosensors before integration in the microfluidic platform, (a) graphite-based biosensors and (b) graphene oxide-based biosensors, and in-flow amperometric characterization of the sensors used to test the microfluidic platform, (c) graphite-based biosensors and (d) graphene-based biosensors. Adapted from [76].

In Figure 35 (a) and (b) the measured calibration curves from the droplet chronoamperometry measurements are presented. It can be observed that the graphite-based biosensors show a decreased linear range (until 1.7 mM of glucose) with a slightly higher apparent sensitivity than the graphene oxide-based biosensors. The latter sensors display a wider range of detection (up to 5 mM of glucose) with sensitivity lower than 0.2 µA/mM. This difference in the biosensor response can be partly explained by the presence of the graphene oxide layer which not only changes the electrochemical but also surface properties of SPEs. Both sensor types were tested inside the

platform and their dynamic response compared with the static approach. In Figure 35 (c) and (d) the measured calibration curves for the dynamic method using the microfluidic platform are presented at different flow rates. This characterization was performed by introducing the same flow rate at the two inlets, and as a result the first sensing chamber was subjected to half the flow rate as the second sensing chamber. The graphite-based biosensors (Figure 35 (c)) present a reduced linear behaviour than previously obtained in the droplet chronoamperometry, while the graphene oxide-based biosensors (Figure 35 (d)) show a decrease in the linear range (up to ~4 mM). Both biosensor types however display a variation of the calibration curve with flow. A decrease of the sensitivity (slope), as well as of the detection range, is observed when the applied flowrate increases. The higher difference in static vs. flow behaviour observed for the graphite-based biosensors can be related to the difference in electrode substrate (graphite instead of graphene oxide) as well as SPE substrate (thickness of polymeric layer) that can lead to a lower stability of the layers deposited over graphite-based sensors. Furthermore, the higher surface area of the graphene oxide sensors enables the immobilization of higher amounts of both mediator and glucose oxidase, possibly contributing to the different output observed.

3.2.3.3. Influence of the flow

The distribution of the current measured relative to the flow rates applied for the integrated graphite and graphene oxide-based biosensors was also assessed. A similar trend can be observed for both, being however more pronounced in the graphene oxide-based biosensors (Figure 36). At low substrate concentrations, a slight decrease of the measured current is observed with increasing flow rates. For concentrations higher than 1 mM, the opposite trend is observed, where the measured current increases with increasing flowrates. Both trends are however less prominent for flow rates higher than 5 µL/s. It might indicate that the flow rate affects the thickness of the diffusion layer on top of the sensor's enzyme/membrane film which results in the variation of the measured current values for the same glucose concentrations. The observed phenomena should be further investigated for the evaluation of the optimal or critical operation conditions of the presented platform and biosensors.

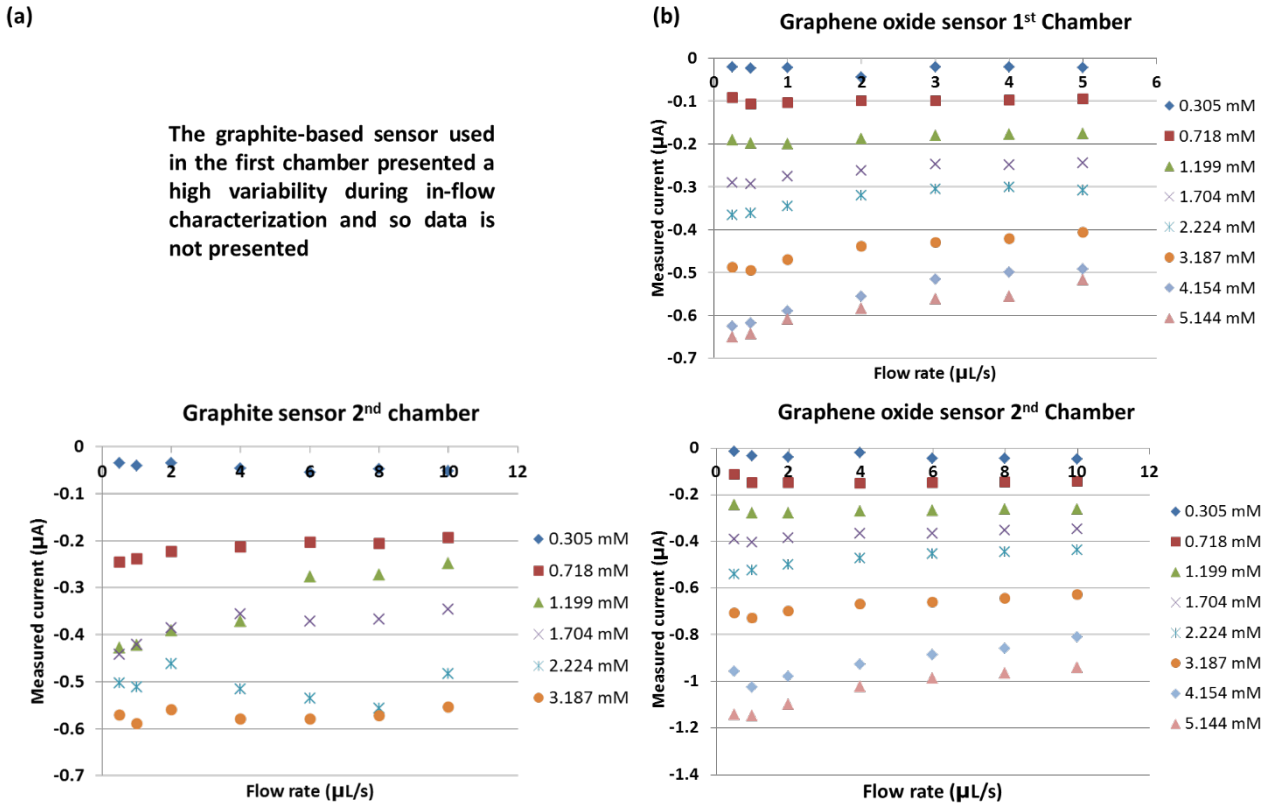

Figure 36 - Influence of flow rate on the amperometric response measured for the range of glucose concentrations tested for two types of biosensors: (a) graphite-based sensors and (b) graphene oxide-based sensors.

3.2.3.4. Continuous monitoring of diluted glucose solutions

A successful integration of these sensors and the continuous monitoring of glucose samples in a microfluidic platform were achieved. Figure 37 presents the results of the mixing/dilution chamber test where the integrated sensors were used for continuous monitoring of diluted glucose solutions. The current values measured by the sensors were converted into glucose concentrations through the in-flow calibration curve (Figure 35) corresponding to the applied flow rates (Table 2) and were compared with the HPLC substrate quantification results. Both graphite and graphene oxide-based sensors demonstrated a different sensitivity to the substrate (glucose) under flow conditions and a deviation from the HPLC data. From Figure 37 it follows that the graphite-based sensor under-estimates the glucose concentration and the graphene oxide-based sensor over-estimates it. This can be explained either by the influence of the flow rates on the biosensor response or by a HPLC measurement error.

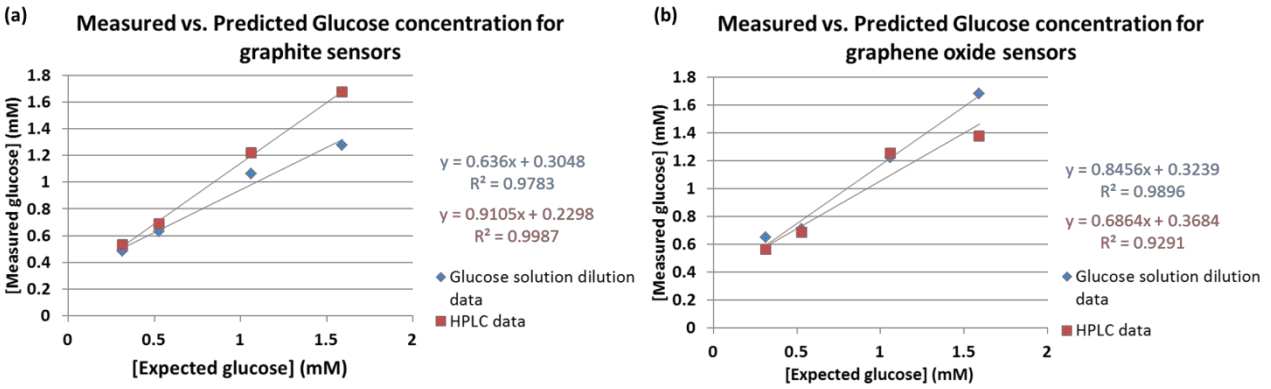

Figure 37 - Comparison of diluted glucose concentration values measured on-line with the sensors and at the outlet using HPLC, for both types of SPEs: (a) graphite-based sensors and (b) graphene oxide-based sensors [76].

The platform was capable of operating continuously for approximately 12 h in a wide range of flowrates, and with different sensor substrates and geometries. For each sensor type, the in-flow sensor calibration and dilution experiments in the assembled platform were performed sequentially and on the same day. Regarding the mixing/dilution unit, the measured glucose concentrations at the outlet were higher than the expected concentration for the dilution used, with a variation of around 0.2 mM. This error margin is acceptable in biotechnological applications

3.2.4. Conclusions and future perspectives

A flexible microfluidic platform with two types of integrated biosensors was developed and applied for continuous monitoring of pure substrate samples. The platform demonstrated the capability of performing up to 10 times sample dilutions, even at high flow rates, through the use of an integrated mixing unit. The presence of a mixing/dilution chamber allowed tuning the sample concentration according to the sensor's detection limit, and can still be improved by increasing the number of bends in the meandering channel or by introducing some obstacles within the channel. Moreover, the platform may be further applied to different sensing technologies (e.g. optical, magnetic), due to the presented flexibility in terms of sensor format, as well as ease of assembly and possibility for re-use of both platform and integrated sensors. Furthermore, a combination of electrochemical and other sensor technologies (especially optical sensing) could be achieved with this platform, by using the predefined pockets for sensor integration. Likewise, the integrated mixing chamber can display a high variety of functions besides the demonstrated dilution ability. It may be further used as a reaction chamber for the screening of biocatalysts, as an inactivation chamber or as a labeling unit, by mixing the sample stream with a fluorescent or magnetic marker, depending on the sensing approach chosen. The developed platform presented in this work exhibits a multi-function capability using a simple design, standard connectors and low-cost materials. Such platform can contribute to increasing the number of bioprocess parameters measured online during monitoring, by enabling the integration of different sensor approaches, as well as their replacement, without the need of changing the platform itself. The overall cost of such

platform makes it accessible both to research laboratories and industries. Additionally, the simple design and assembly method allows mass production, by changing the fabrication method to e.g. injection moulding, and is consequently feasible for parallelization at a bigger scale.

The obtained deviation in the sensor response during static (droplet) and dynamic (flow) measurements can be partly attributed to the fluid dynamic influence on the diffusion of the target analyte to the electrode surface. In other words, by varying the flow rates one can manipulate the current response behaviour and shift the enzymatic reaction from diffusion to kinetic control (see Figure 27A). Gunasingham et al. [114] have previously shown that normal amperometric detection, where the potential is applied continuously, is more susceptible to flow rate in comparison with pulsed amperometric mode, where a series of pulses is periodically repeated. Moreover, the switch from the reduction to the oxidation potential for approximately a few hundred milliseconds during each pulse cycle may reactivate the electrode and prevent it from fouling and passivation. Furthermore, the difference in current output at low and high flow rates might indicate that fluid flow at this scale of geometries might affect the biosensor topology. Therefore, development of mathematical models could not only reproduce the fluid dynamics inside the microfluidic platform but also incorporation of the biosensor response is required. Such models would allow a better understanding of the biosensor operation principles and can be further used for the optimization of the biosensor design and response.

Chapter 4
Mechanistic modeling of cyclic voltammetry: a helpful tool in biosensor design optimization

The content of the current thesis chapter was partly redrafted from the following manuscript:

- D. Semenova, A. Zubov, Y. E. Silina, L. Micheli, M. Koch, A. C. Fernandes and K. V. Gernaey, *Mechanistic modeling of cyclic voltammetry: a helpful tool for understanding biosensor principles and supporting design optimization* [77].

Abstract

Design, optimization and integration of biosensors hold a great potential for the development of cost-effective screening and point-of-care technologies. However, significant progress in this field can still be obtained on condition that sufficiently accurate mathematical models will be developed. Herein, a novel approach is presented for the improvement of mechanistic models which do not only combine the fundamental principles but readily incorporate the results of electrochemical and morphological studies. The first generation glucose biosensors were chosen as a case study for model development and to perform cyclic voltammetry (CV) measurements. As initial step in the model development, the interpretation of experimental voltammograms obtained in the absence of substrate (glucose) is proposed. The model equations describe dynamic diffusion and reaction of the involved species (oxygen, oxidized/reduced forms of the mediator – Prussian Blue/Prussian White). Furthermore, the developed model was applied under various operating conditions as a crucial tool for biosensor design optimization. The obtained qualitative and quantitative dependencies towards amperometric biosensors design optimization were independently supported by results of cyclic voltammetry and multi-analytical studies, such as scanning electron microscopy (SEM), energy dispersive X-ray spectroscopy (EDX) and liquid chromatography-electrospray ionization-tandem mass spectrometry (LC-ESI-MS/MS). Remarkably, a linear response of the optimized biosensors tested at the applied voltage (-0.14 V) in the presence of the glucose was obtained from 10^{-3} to 10^{-5} M (relative standard deviation (RSD) < 7% per electrode). It is believed that the presented model can be used to determine the exact mechanism driving the electrochemical reactions and to identify critical system parameters affecting the biosensor response that would significantly contribute to the knowledge on biosensing, the device design and bioengineering strategies in the future.

4.1. Theoretical background

4.1.1. Mathematical modeling of amperometric biosensors

Driven by desire of getting a better understanding of the nature of the electrode reactions and improving the biosensor performance, mathematical models were applied to amperometric biosensors [115]. The first model for the amperometric response of an enzyme electrode for the glucose - glucose oxidase system was presented by Mell and Maloy [116] in the seventies, after Guilbault and Lubrano [104] constructed an amperometric glucose sensitive electrode. The presented simulation results included the steady-state current response (droplet characterization) for the immobilized glucose oxidase on the surface of a platinum electrode. The developed model allowed evaluating different reaction parameters, namely the diffusion coefficient of the substrate, enzyme inhibition, electrode coverage and maximum and relative rates of the enzymatic reaction. Moreover, two types of calibration curves were proposed depending on whether the current response is kinetic or diffusion controlled. The model was further used to predict the amperometric response of the immobilized glucose oxidase electrode following periods of electrode inactivity. The numerical results proved the ability of the enzyme electrode to amplify the amperometric response over the steady-state current and provided theoretical maxima for the time allowed for product build-up inside the membrane layer and electrolysis time as the potential enhancement factors of the amperometric response [117]. The main weaknesses of the presented model were related to the difficulties in choosing boundary conditions at the membrane-solution interface, and validation with biosensors operating under kinetic control [118].

First simulations of the transient responses of enzyme amperometric electrodes were presented by Bergel and Comtat [119]. Their model referred to the system, where the soluble enzyme in the reaction chamber was bounded to the electrode surface by a semi-permeable membrane. The numerical simulations (implicit finite difference method) were applied to reproduce the enzymatic reaction following first order kinetics with respect to the substrate and zero order kinetics for the oxidized form of the cofactor. Therefore, the model was extended to electrodes with more complex enzymatic kinetics, calculating the transient response through the substrate oxidation by the oxidized form of the enzyme and the regeneration of this form by constant amperometric potential. The simulations were applied to predict the response time curve of the amperometric lactate-specific electrodes [120]. In the subsequent work [121] the model was presented for analyzing the transient response of amperometric biosensors by a finite-volume method, in which the immobilized enzyme was linked to one of the sides of a polymeric membrane placed against the electrode surface. The developed model was further employed to study free and immobilized NADHP-diaphorase biosensor systems [122]. The mathematical model describing transient behaviour of the one-layer enzyme electrode with two co-immobilized enzymes (homogeneously distributed in one layer) was formulated by Schulmeister [123]. The partial differential equations allowed to predict dynamic evolution of concentration profiles and the current response of the amperometric biosensors and were solved using the explicit Euler method. The model was

evaluated for an L-lactate sensing electrode [124]. In later work, Schulmeister [125] presented a detailed review of the available mathematical approaches for modeling both steady-state and dynamic behaviour of one- or multi-layer amperometric systems containing either one or two-enzyme electrodes. The author also discussed the advantages and drawbacks of each mathematical approach. One of the significant challenges in modeling amperometric biosensors is related to the enzyme/membrane layer behaviour and properties that cannot be reproduced with the same accuracy, which subsequently makes it difficult to define the exact dynamics and boundary conditions for such system.

However, the above-mentioned problems resulted in a series of publications where the authors tried to get more insight into the principles of amperometric biosensor operation and aimed at the design of modified electrodes with improved characteristics. Albery and Hillman [126] presented several analytical solutions for describing the dynamics of modified mono-layer electrodes, considering that the electrochemical reaction can occur on the surface of the electrode or interfaces, throughout or in the middle of the layer. In the subsequent publication, Albery and Bartlett [127] derived a theory of the steady-state response of amperometric biosensors, and presented a reaction–diffusion model with direct enzyme regeneration on the surface of the electrode. Moreover, the developed theoretical treatment was further applied to investigate the electrocatalytic activity of conducting salts on the oxidation of different enzyme systems [128,129] and resulted in the design of an amperometric ethanol biosensor [130]. Therefore, modeling the behaviour of enzyme electrodes and comparing the simulation results with experimental data, proved to be a very powerful tool in determination of the exact mechanism of the electrochemical response, together with the kinetics of the bioprocess, which can allow the design of the ultimate biosensor performance. Bartlett and Pratt, in their review [131], presented both the available mathematical models and experimental designs for the following enzyme electrode systems: membrane enzyme electrodes (the enzyme is a thin film of solution behind the membrane), enzyme membrane electrodes (the enzyme is immobilized within the membrane), and homogeneously mediated enzyme electrodes (both mediator and the enzyme are free in the solution). The major problem in modeling such systems (even in case of the simplest enzyme electrode design) referred to non-linear second order partial differential equations, which combine a Michaelis-Menten kinetic term and a diffusion flux, and which do not have a complete analytical solution. The advantages and disadvantages of the available approaches were demonstrated for explicit, implicit, Crank Nicolson and hopscotch schemes for the finite difference method, and for the orthogonal collocation method. A better understanding of both kinetic and electrochemical aspects of the biosensor response lead to a series of studies where the sensor characteristics could be improved by increasing the rate of electron transfer between the biologically active molecule (enzyme) and the electrode surface by the use of mediators. A very detailed review on electrochemistry of chemically modified redox enzyme electrodes can be found in the work of Bartlett et al. [132]. The first complete mathematical description of mediation of the amperometric

biosensor operation in homogeneous solution, where the source of the mediator could be either the bulk solution , or the electrode itself, was presented by Albery et al. [133].

The first theoretical treatment of the cyclic voltammograms was presented by Nicholson and Shain [134]. In their work, the reversible and irreversible charge transfer mechanisms were coupled with homogenous first order chemical or electrochemical reactions. Moreover, the analytical solution was also presented for the electrochemical reaction followed by the mediated enzyme reaction. A commercially available simulation program for cyclic voltammetry, DigiSim (Bioanalytical Systems, West Lafayette, IN), developed by Feldberg and Rudolph [135] describes the electrochemical reactions coupled with first- and/or second-order chemical reactions. However, the mechanism of the enzymatic reactions is very complex and the assumption that the kinetics obey a first-order reaction can only be applied in very rare cases. Yokoyama and Kayanuma [136] developed a cyclic voltammetry simulator for electrochemically mediated enzyme reactions for various mediator and substrate concentrations, therefore not being limited by first- or pseudo-first-order reaction kinetics. The presented model allowed determining the kinetic constants for the homogeneous reaction between glucose oxidase (GOx) and glucose in the presence of ferrocene derivatives. Later on, the model principles were applied for modeling the reversible electrochemical reaction with one electron followed by the mediated reaction of immobilized enzyme with two electrons [137]. The simulation of cyclic voltammetry was also applied for studying the influence of ohmic drop [138,139], electrode area, electrochemical reaction constants and transferring coefficients [140], as well as the effect of flow rates [141–143] on the current response and wave shape. Analyzing the curve shape, peak shifts and amplitudes between the first cycle and successive scans in the obtained cyclic voltammograms is an important key in providing useful information on the mechanism of the electrochemical reaction as well as the adsorption mechanism and the diffusivities of the electrochemical species [94]. All these experimental data make CV a powerful analytical tool to identify the correlations between the sensor morphology and system parameters, underlying the desired biosensor response. However, only the works of Cannes et al. [144,145] demonstrated how the analytical techniques, such as CV measurements and scanning electrochemical microscopy (SECM), can be combined with simple numerical simulations for quantitative estimation of biosensor system parameters. The recent advances, different approaches and challenges in respect to mathematical modelling of various biosensor systems were carefully discussed in several books [115,146].

4.1.2. Prussian blue films

The classical response of the Prussian Blue (PB) modified SPEs during the cyclic voltammetry measurement with an applied potential range from -0.5 to 1.2 V, as well as the mechanism of the redox processes are summarized in Figure 38.

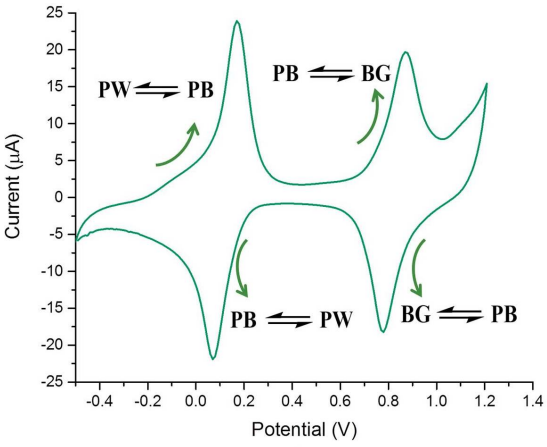

***Mechanism* I :**

$KFe^{III}Fe^{II}(CN)_6 + K^+ + e^- \rightleftharpoons K_2Fe^{II}Fe^{II}(CN)_6$

Prussian Blue (PB) — **Prussian White (PW)**

$KFe^{III}Fe^{II}(CN)_6 \rightleftharpoons 2/3\ K^+ + 2/3\ e^- + K_{1/3}(Fe^{III}(CN)_6)_{2/3}(Fe^{II}(CN)_6)_{1/3}$

Prussian Blue (PB) — **Berlin Green (BG)**

***Mechanism* II :**

$Fe_4^{III}[Fe^{II}(CN)_6]_3 + 4K^+ + 4e^- \rightleftharpoons K_4Fe_4^{II}[Fe^{II}(CN)_6]_3$

Prussian Blue (PB) — **Prussian White (PW)**

$Fe_4^{III}[Fe^{II}(CN)_6]_3 + 3\ A^- \rightleftharpoons 3\ e^- + Fe_4^{III}[Fe^{III}(CN)_6A]_3$

Prussian Blue (PB) — **Berlin Green (BG)**

B

Figure 38 - Cyclic voltammogram obtained at a scan rate of 50 mV/sec in air saturated buffer solution (pH = 6) for PB modified glucose biosensors (A). The reaction mechanism for soluble (Mechanism I) and insoluble (Mechanism II) stoichiometric forms of PB films is shown in B [147].

In Figure 38A the thin film reduction of Prussian Blue to Prussian White (PW) (also known as Everitt's salt) on a graphene oxide WE at 0.195 V is followed by the subsequent oxidation to Berlin Green (BG) at 0.870 V [148]. The structure of PB and associated compounds (Figure 39) was confirmed for the first time in the X-rays studies described by Keggin and Miles [149].

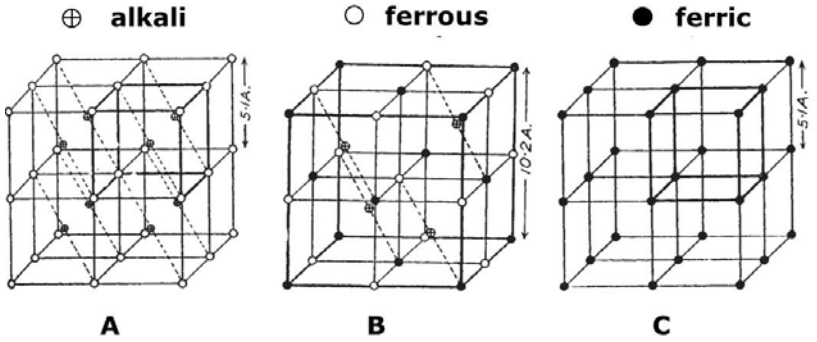

Figure 39 – Schematics of the unit cell of Prussian White (A), Prussian Blue (B) and Berlin Green (C). Adapted from [149].

The Prussian Blue crystal was studied by powder neutron diffraction in four different states of hydration that allowed to estimate the original structure as $Fe_4[Fe(CN)_6]_3 \cdot x\ H_2O$ [150]. It was confirmed that PB is a typical mixed-valence compound, containing iron atoms in both 2^+ and 3^+ oxidation states that are interconnected by carbon-nitrogen pairs. The face-centered cubic lattice is composed of Fe^{3+} ions surrounded by an octahedral nitrogen environment, whereas Fe^{2+} ions are located next to the carbon. The charge neutrality requirement and Fe^{2+}/Fe^{3+} stoichiometry (3:4) results in a 25 % $[Fe^{2+}(CN)_6]^{4-}$ vacant cluster regions filled with water molecules. Six molecules of water are coordinated to Fe^{3+} at empty nitrogen sites ("coordinated water"), as shown in Figure 40. The additional water molecules (maximum $x = 14 - 16$) are either isolated in the centre of the unit cell or connected by hydrogen bonds to the coordinated ones [150,151]. Such an open- framework

structure coupled with mixed-valence nature guarantees the robustness of the overall crystal structure and allows various chemical modifications without breaking the cell.

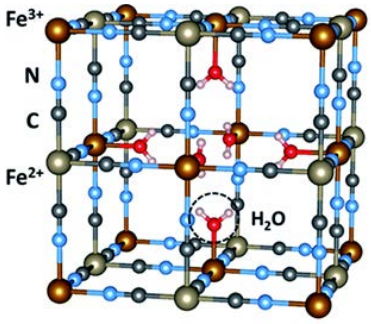

Figure 40 – Unit cell of the original Prussian blue (PB) $Fe_4[Fe(CN)_6]_3 \cdot x\,H_2O$ compound. Only "coordinated" water molecules are shown. Adapted from [151].

The application of PB as a catalyst for the oxygen and hydrogen peroxide reduction/oxidation was proposed for the first time by Itaya et al. [152] who have previously developed the spectroelectrochemical and electrochemical methods for the preparation of the PB modified electrodes [153]. They demonstrated that in oxygen-saturated solutions the autoxidation of Prussian white (PW) to Prussian blue occurs within 20-30 min, whereas in nitrogen bubbled (i.e. oxygen-free) solutions PB films showed a very good stability. From the obtained voltammograms (Figure 41) it was assumed that the oxygen reduction takes place approximately at 0.2 V and it was related to the reduction of half of the high-spin iron ions (Fe^{3+}) to the low-spin ones (Fe^{2+}).

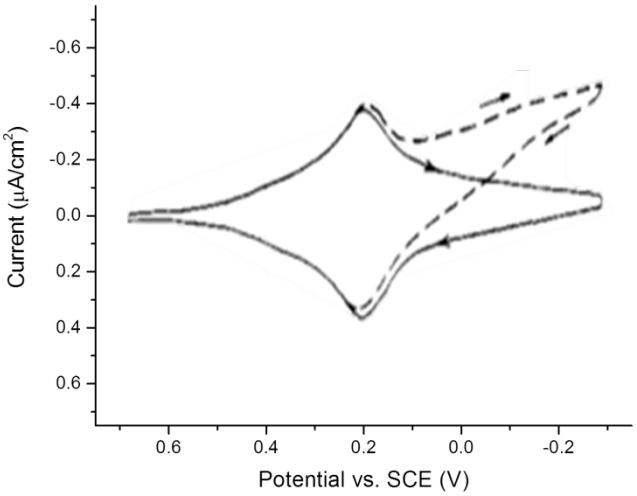

Figure 41 - Cyclic voltammograms of a rotating PB-modified glassy carbon electrode in the absence (solid line) and in the presence of oxygen (dashed line). The electrode was rotated at 1000 rpm. The potential was scanned at 20 mV/s. The supporting electrolyte was 1 M KCl (pH 3.0). Adapted from [152].

This led to further investigation of PB and the capabilities of its related compounds on delivering two or four electrons, more or less simultaneously, to the oxygen molecule inside the crystals [154,155]. Moreover, it was also proposed that two kinds of electron-transfer channels in the PB crystal are involved in the process of catalytic reduction and oxidation of hydrogen peroxide

due to the redox reactions of the high-spin iron ions, $Fe^{3+}/Fe^{2+}$and of the low-spin iron ions, Fe^{2+}/Fe^{3+}, respectively [152,156,157]. The fundamental aspects, deposition methods, electroactivity together with the biosensing application of Prussian blue and related advantages and drawbacks were carefully discussed in several comprehensive reviews [105,158].

4.2. Case Study 3: Mechanistic modeling of cyclic voltammetry: a helpful tool for understanding biosensor principles and supporting design optimization

4.2.1. Introduction

The general idea underlying this case study is the development of a novel mathematical tool for amperometric biosensor operation and design optimization. To achieve this goal, we have used, as a first step, the combination of a mechanistic model for cyclic voltammograms with experimental multi-analytical studies has been used. As a case study, the biosensor design with enhanced stability was adopted from the works of Ricci et al. [111,159]. The surface of the working electrode (WE) of commercially available screen-printed electrodes was chemically modified with a hydrogen peroxide sensitive catalyst, Prussian Blue [160], and covered with an enzyme/membrane layer, as shown in Figure 42.

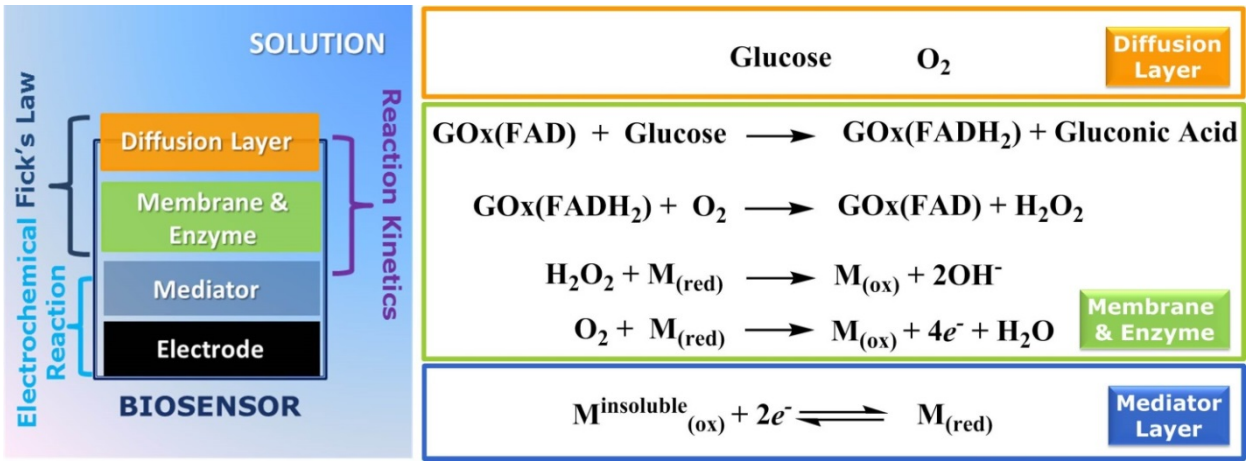

Figure 42 - Schematics of the biosensor design and operation: GOx(FAD)/GOx($FADH_2$) – oxidized/reduced forms of glucose oxidase, M_{ox}/M_{red} - oxidized/reduced forms of mediator (i.e. Prussian Blue).

The experimental voltammograms were compared with simulation results, which allowed to use the formulated model not only for studying the processes occurring inside the biosensor system, but also to identify the critical system parameters. The results of the model predictions were fully supported by subsequent electrochemical (CV), bioanalytical (LC-ESI-MS/MS, EDX) and morphological (SEM) studies. The case study overview is summarized in Figure 43.

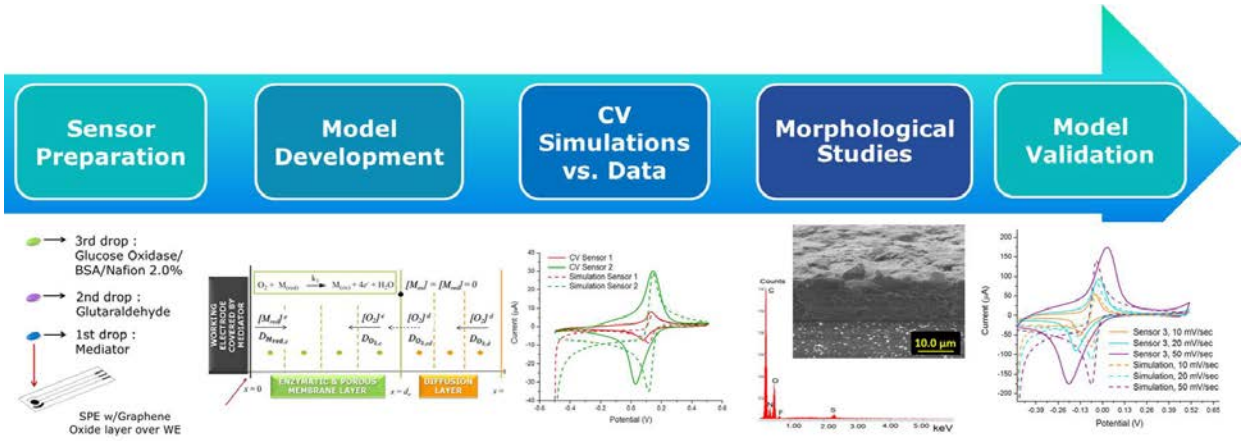

Figure 43 - Case study 3, graphical roadmap.

4.2.2. Mathematical modeling

4.2.2.1. Computational domain and governing equations

The main objective of the model was to predict cyclic voltammetry curves for the reversible electrochemical reaction coupled with oxidation/reduction of the catalyst in the absence of substrate (glucose) for an air saturated phosphate buffer solution, at different operating conditions. The biosensor was modeled spatially as a one-dimensional system. Non-linear second order partial differential equations combine the dynamic diffusion and reaction of the involved chemical species in the enzymatic/membrane layer, as well as electrochemical reaction on the surface of the electrode. Different regions of the multi-layer glucose biosensor system (electrode surface, enzyme/membrane layer and stagnant diffusion layer) were associated with diffusion fluxes, chemical and electrochemical reactions summarized in Figure 44.

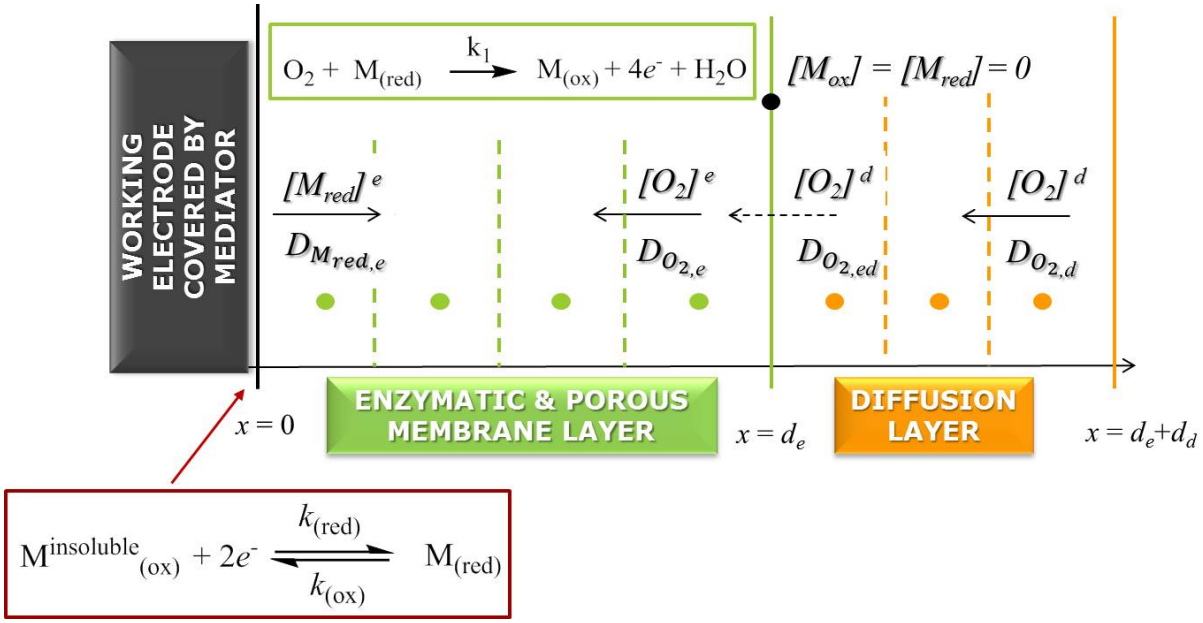

Figure 44 - Schematic representation of the sensor geometry coupled with redox reaction of the mediator (M_{ox}/M_{red}) and a homogeneous oxygen reduction, occurring on the electrode surface area and inside the enzymatic layer, respectively.

It was assumed that the oxidized form (M_{ox}) of artificial peroxidase - Prussian Blue (PB), was deposited on the surface of the working electrode, whereas the reduced form (M_{red}) - Prussian White (PW), was produced during the reversible two - electron transfer (51) reaction [147] (note that the PB/PW abbreviation is simplified to M_{ox}/M_{red} since historically Prussian Blue was called a "mediator" in the literature):

$$\mathrm{M^{insoluble}_{(ox)}} + 2e^- \underset{k_{(ox)}}{\overset{k_{(red)}}{\rightleftharpoons}} \mathrm{M_{(red)}} \tag{51}$$

The complete reduction of molecular oxygen (52) in the presence of Prussian White was described as a four - electron transfer reaction taking place inside of the enzyme/membrane layer [152]:

$$\mathrm{O_2} + \mathrm{M_{(red)}} \xrightarrow{k_1} \mathrm{M_{(ox)}} + 4e^- + \mathrm{H_2O} \tag{52}$$

The kinetics of the electrochemical reactions was assumed to be fully reversible, whereas the oxygen reduction followed a second order kinetics. Considering one-dimensional diffusion, the governing equations for oxygen (53),(56), oxidized (54) and reduced (55) forms of the mediator were formulated as follows:

Enzyme/membrane layer, $t > 0$, and $0 < x < d_e$:

$$\frac{\partial [O_2]}{\partial t} = D_{O_{2,e}} \frac{\partial^2 [O_2]}{\partial x^2} - r([O_2], [M_{red}]) \tag{53}$$

$$\frac{\partial [M_{ox}]}{\partial t} = D_{M_{ox,e}} \frac{\partial^2 [M_{ox}]}{\partial x^2} + r([O_2], [M_{red}]) \tag{54}$$

$$\frac{\partial [M_{red}]}{\partial t} = D_{M_{red,e}} \frac{\partial^2 [M_{red}]}{\partial x^2} - r([O_2], [M_{red}]) \tag{55}$$

Diffusion layer, $t > 0$, and $d_e < x < d_e + d_d$:

$$\frac{\partial [O_2]}{\partial t} = D_{O_{2,d}} \frac{\partial^2 [O_2]}{\partial x^2} \tag{56}$$

where $D_{O_{2,e}}$ and $D_{O_{2,d}}$ are diffusion coefficients for the oxygen inside the enzyme/membrane and diffusion layers, respectively. Inside the enzyme/membrane layer, $D_{M_{red,e}}$ and $D_{M_{ox,e}}$ refer to the diffusion coefficients of the reduced and oxidized form of the mediator, respectively. The thickness of the enzyme/membrane layer was denoted as d_e, whereas for the diffusion layer it was marked as d_d. The mediator layer thickness was neglected in the model, assuming that PB crystals are adsorbed inside the cavities of the graphene oxide layer surface (Figure 45).

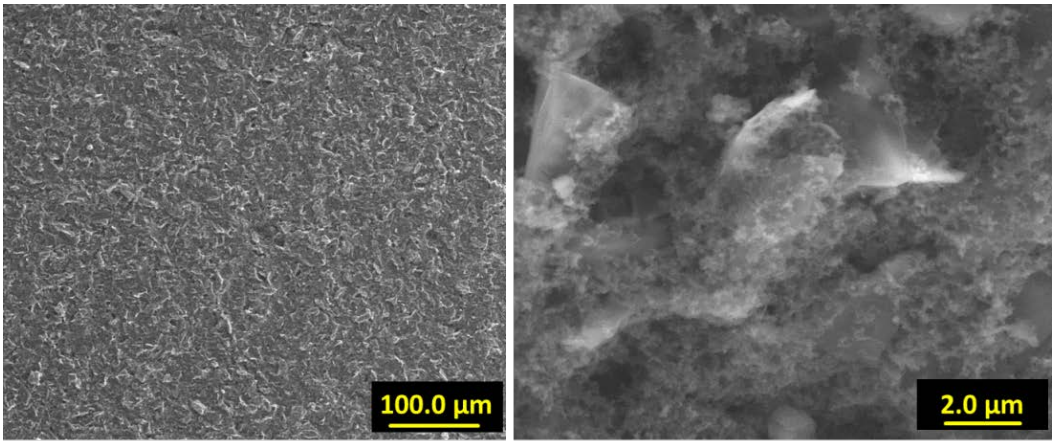

Figure 45 - SEM images of the graphene oxide (GO) layer covering the surface of the working electrode (A). The top view of the GO layer is enlarged in B.

The rate (r) of the pseudo-homogeneous reaction (57) inside the enzyme/membrane layer between the reduced form of the mediator and oxygen is provided in the equation below:

$$r([O_2],\ [M_{red}]) = \ k_1 \cdot [O_2] \cdot [M_{red}] \tag{57}$$

where k_1 is a kinetic constant for the complete PW oxidation in the presence of oxygen for air saturated solutions [152].

4.2.2.2. Initial and boundary conditions

The zero mediator concentration inside the enzyme/membrane layer (58), as well as the oxygen absence (59) inside the diffusion and enzyme/membrane layers, were set as the initial conditions of the model following the equations below:

$t = 0$, and $0 < x < d_e$ $\qquad [M_{ox}] = [M_{red}] = 0$ (58)

$t = 0$, and $0 < x < d_e + d_d$ $\qquad [O_2] = 0$ (59)

The boundary conditions for oxygen dissolved in the bulk solution (60), the continuity of oxygen diffusion fluxes at the interface between the enzyme/membrane and diffusion layer (61) and the zero oxygen flux at the electrode surface (62) were set in the model as follows:

$t > 0$, and $x = d_e + d_d$ $\qquad [O_2] = [O_{2,\,bulk}]$ (60)

$t > 0$, and $x = d_e$ $\qquad D_{O_{2,e}} \dfrac{\partial [O_2]}{\partial x} = D_{O_{2,d}} \dfrac{\partial [O_2]}{\partial x}$ (61)

$t > 0$, and $x = 0$ $\qquad D_{O_{2,e}} \dfrac{\partial [O_2]}{\partial x} = 0$ (62)

The zero mediator concentration at the boundary of the enzyme/membrane layer (63) and the concentration ratio between oxidized and reduced forms of the mediator controlled by the Nernst equation at the electrode surface (64) were given by:

$$t > 0, \text{and } x = d_e \qquad [M_{ox}] = [M_{red}] = 0 \tag{63}$$

$$t > 0, \text{and } x = 0 \qquad \frac{[M_{ox}]}{[M_{red}]} = \exp\left\{\frac{n_e \cdot F}{R \cdot T} \cdot (E - E^0)\right\} \tag{64}$$

where n_e is a number of electrons involved in a charge transfer, F is the Faraday constant, R represents the universal gas constant, T is temperature, E is the applied potential vs. the reference electrode and E^0 is the standard potential. The biosensor response (65), measured as the current as a function of time, $i\ (t)$, was governed by:

$$i(t) = n_e \cdot A \cdot F \cdot D_{M_{red,e}} \cdot \frac{\partial\,[M_{red}]}{\partial x} \tag{65}$$

where A is the surface area of the working electrode.

4.2.2.3. Model implementation

The governing model equations were discretized by the finite difference method (FDM) and numerically solved using an explicit Euler scheme. The proposed model for cyclic voltammetry responses was implemented in both MATLAB® and FORTRAN languages. Following the IUPAC recommendation, the arising positive current in the voltammogram corresponds to the oxidation process (anodic current), whereas the negative current represents the reduction process (cathodic current). The major part of the physicochemical parameters required for the mathematical model was found in the literature (Table 3). The mediator concentration and standard redox potential values had to be adjusted based on the difference between the fabrication procedures of biosensor systems (values are also presented in Table 3). The thickness of the enzyme/membrane layer was estimated from SEM analysis presented in section 4.2.4.3. The thickness of the diffusion layer was set as 1 μm in all simulations.

Table 3 - Values of the biosensor system parameters used in simulations.

Parameter	Description	Model value	Reference
$D_{O_{2,e}}$ [m^2/s]	Diffusivity of oxygen in polymeric membrane	5.0×10^{-12}	[161]
$D_{M_{ox,e}}$ [m^2/s]	Diffusivity of oxidized form of mediator in polymeric membrane	10.0×10^{-14}	[162,163]
$D_{M_{red,e}}$ [m^2/s]	Diffusivity of reduced form of mediator in polymeric membrane	7.0×10^{-13}	
$D_{O_{2,d}}$ [m^2/s]	Diffusivity of oxygen in diffusion layer	2.0×10^{-09}	[161]
k_1 [M^{-1} s^{-1}]	Kinetic constant for the oxygen reduction by PB	0.107	[152]
n_e	Electrons involved in the PB redox reaction	2	[154,155]
O_2 [mol/m^3]	Oxygen concentration dissolved in water	0.271563	[164]
M_{ox} [mol/m^3]	Prussian Blue concentration deposited over WE	5/20/100	*experiment*
E^0 [V]	Standard Potential PW/PB redox couple	0.13/-0.05	*CV experiment*
d_e [m]	Thickness of the enzyme/membrane layer	7.0×10^{-06}	*SEM experiment*
d_d [m]	Thickness of the diffusion layer	1.0×10^{-06}	*estimation*
A [m^2]	Surface area of the working electrode	1.257×10^{-05}	*experiment*
T [K]	Temperature	298.15	*experiment*

4.2.3. Experimental section

4.2.3.1. Materials and reagents

Screen printed electrodes (SPEs) DRP-PW-110DGPHOX were customized by DropSens (Llanera, Spain). The electrodes were printed on polyester substrate and each sensor consists of a carbon working electrode modified with graphene oxide, a carbon counter electrode and a silver reference electrode. The diameter of the working electrode was 0.4 cm, resulting in an apparent geometric area of 0.126 cm^2.

Glucose oxidase (GOx) (EC 1.1.3.4, type VII, 248 U/g solid) and bovine serum albumin (BSA) were obtained from Sigma (St. Louis, MO, USA). Glutaraldehyde solution (25% (v/v)), ethanol (UV HPLC gradient, 99.9%) and potassium hexacyanoferrate (III) (ACS reagent, ≥99.0%) were purchased from Sigma – Aldrich (St. Louis, MO, USA). Iron (III) chloride (anhydrous, 99.99%) and Nafion®117 solution (~5% (v/v) in a mixture of lower aliphatic alcohols and water) were provided by Aldrich (Steinheim, Germany). D-Glucose (anhydrous) was provided by Fluka (Loughborough, UK). Mono – and di-potassium hydrogen phosphates (anhydrous) were obtained from Merck (Darmstadt, Germany). Sodium hydroxide (50% (w/w)) and hydrochloric acid (37% (w/w)) solutions were

purchased from VWR International A/S (Søborg, Denmark). All the solutions were prepared with 0.1 M phosphate buffer supplemented with 0.1 M KCl (pH = 6), unless stated otherwise.

4.2.3.2. Glucose biosensor preparation

Preparation method 1:

The chemical deposition procedure of PB was adopted from Ricci et al. [111]. A 10 µL drop (total volume) of freshly made precursor solution, containing 0.1 M potassium ferricyanide ($K_3Fe(CN)_6$) in 10 mM HCl mixed with 0.1 M ferric chloride ($FeCl_3$) solution in 10 mM HCl (1:1 proportion (v/v)), was directly placed over the working electrode (WE) surface of the SPEs. The sensors were left to dry for 15 (*sensor 1*) or 40 (*sensor 2*) minutes at room temperature and then washed with a 10 mM HCl solution and deionized water. In order to stabilize the PB layer, the sensors were placed in the oven at 100°C for 2 h. Prior to glucose oxidase (GOx) immobilization, a 2.5 µL droplet of freshly prepared glutaraldehyde solution (1% (v/v) diluted in water) was placed over the WE of the PB modified SPEs and was left to dry at room temperature for 30 min. After the glutaraldehyde solution layer was dried, the enzyme/membrane layer was deposited. The fresh enzyme/membrane solution was made by mixing GOx solution (53.7 U in phosphate buffer), BSA (5 vol. % diluted in water) and Nafion®117 (0.2 vol. % diluted in water) in a 1:1:1 proportion (v/v/v). A drop of 3 µL of the final solution was placed over the working electrode of the PB/glutaraldehyde modified SPEs.

Preparation method 2:

In order to remove the impurities, the surfaces of all electrodes were pre-treated in a phosphate buffer solution under chronoamperometric conditions with applied potential of +1.7 V. The chronoamperometric measurement was performed using a MultiEmStat (PalmSens, Utrecht, The Netherlands) with a DRP-CAST1X8 interface (DropSens, Llanera, Spain) controlled by MultiTrace 3.4 software (PalmSens, Utrecht, The Netherlands). After the stable current curve was obtained, the surface of the working electrode was modified with a Prussian Blue (PB) layer. The PB chemical deposition procedure presented in preparation method 1 was modified. Thus, a 5 µL drop of a 0.1 M solution of potassium ferricyanide $K_3Fe(CN)_6$ in 10 mM HCl was placed over the working electrode and mixed with a 5 µL drop of 0.1 M solution of ferric chloride, $FeCl_3$ in 10 mM HCl directly on the surface of the electrode. The sensors were left to dry for 40 min at room temperature and then washed with a 10 mM HCl solution, deionized water and dried with air. In order to stabilize the PB layer, the sensors were placed in the oven at 100°C for 1 h. Similar to preparation method 1, the surface of WE for PB modified SPEs was pretreated with glutaraldehyde solution prior to enzyme/membrane layer deposition. In contrast to preparation method 1, Nafion®117 (2 vol. %) neutralized in ethanol [165] was mixed with GOx solution (53.7 U in phosphate buffer) and BSA (5 vol. % diluted in water) in a 1:1:1 proportion (v/v/v). A drop of 3 µL of final solution was placed over the working electrode of the PB/glutaraldehyde modified SPEs, yielding the *sensor 3* batch of electrodes.

Regardless of the preparation method, sensors with deposited enzyme/membrane layer were placed to dry overnight in a climate chamber at 40% of humidity and 8°C. Moreover, both PB

modified SPEs and complete glucose biosensors were stored in the dark, at room temperature and 4°C, respectively.

4.2.3.3. Glucose oxidase activity measurement

The GOx activity measurement prior to the immobilization step of the stock solutions, as well as the enzyme/membrane mixtures, was performed by using an OXSOLV solvent-resistant, fiber - optic oxygen sensor (PyroScience GmbH, Aachen, Germany) connected to a FireStingO2 fiber - optic meter (PyroScience GmbH, Aachen, Germany) and controlled by Pyro Oxygen Logger software (PyroScience GmbH, Aachen, Germany). The measurement was based on on-line monitoring of the dissolved oxygen (DO) consumption in the reaction of GOx with 100 mM glucose solution at room temperature (Figure 46).

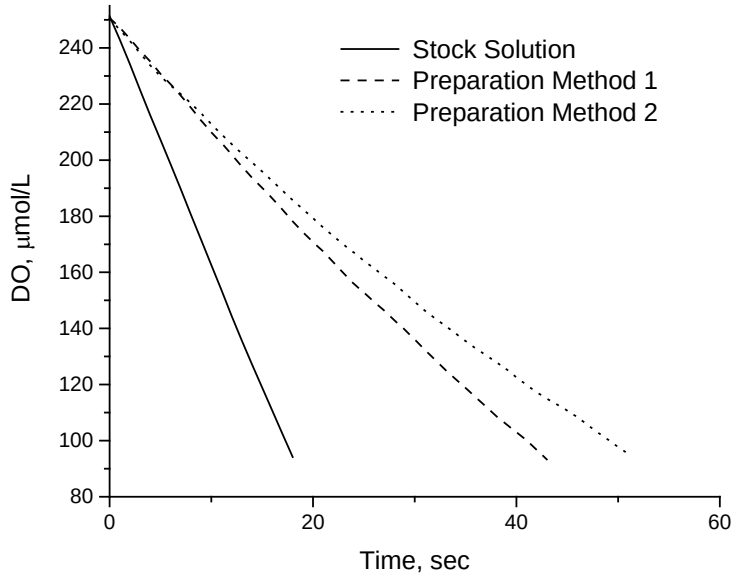

Figure 46 - Dynamic response of the oxygen consumption rates, expressed as the number of moles of oxygen dissolved in a stock glucose oxidase solution (full line) and enzyme/membrane mixtures: 0.2% (dashed line) and 2.0% (dotted line) Nafion®117 membranes are compared.

The setup assembly, as well as the experimental procedure, were adopted from the works of Bolivar et al. [69,70]. A glass beaker with a liquid working volume of 10 mL and a magnetic stirrer (10 ×5 mm) were used for the experiments. The magnetic stirring was performed at 600 rpm (IKA® RET Basic, Staufen im Breisgau, Germany). The 100 µL of glucose solution were dissolved in 7 mL of buffer solution. The oxidation reaction was initialized by addition of different volumes of the GOx stock solution or the enzyme/membrane mixtures after the value of DO was stabilized. For the enzyme activity calculations, one unit (U) of enzyme corresponds to a substrate consumption of 1 µmol per min. The GOx activity in the enzyme/membrane mixture prior to immobilization was estimated as 0.179 U/µL.

4.2.3.4. Cyclic voltammetry behaviour of glucose biosensors in phosphate buffer

Cyclic voltammetry (CV) measurements were performed using MultiEmStat (PalmSens, Utrecht, The Netherlands) with a DRP-CAST1X8 interface (DropSens, Llanera, Spain) controlled by MultiTrace 3.4 software (PalmSens, Utrecht, The Netherlands). A 100 µL droplet of phosphate buffer was placed over all three electrodes of the SPE. The voltammograms were recorded at different scan rates in a potential range from -0.5 V to +0.5 V. After each run sample droplets were collected for subsequent LC-ESI–MS/MS analysis.

4.2.3.5. Biosensor sensitivity determination

In order to estimate the sensitivity of the developed biosensors, chronoamperometric studies were carried out in the presence of glucose solutions (concentration range: 10^{-7}-10^{-3} M) at the applied voltage equal to the peak potential of the reduction curve (-0.14 V). Moreover, the biosensors were characterized in the presence of the analytical range of glucose concentrations (0.1 to 2 mM). All measurements from the same biosensor were repeated at least in triplicates.

4.2.3.6. Scanning electron microscopy (SEM) and energy dispersive X-ray spectroscopy (EDX)

Micrographs of the bare and PB/(GOx + Nafion) modified SPEs were obtained by scanning electron microscopy (SEM) using a FEI (Hilsboro, OR, USA) Quanta 400 FEG, operating at 10 kV accelerating voltage. Secondary (SE) and backscattered (BSE) electron images were collected in low vacuum mode (pH_2O = 100 Pa). The microscope was equipped with an EDAX (Mahwah, NJ, USA) Genesis V6.04 energy dispersive X-ray (EDX) system in order to obtain information on elemental composition of the biosensor surfaces. The measuring time per sample was equal to 100 sec. In addition, the correlative SEM/EDX analysis allowed determining the composition of the multi-layer biosensor.

4.2.3.7. Liquid chromatography-electrospray ionization-tandem mass spectrometry (LC-ESI-MS/MS)

In order to verify the chemical stability of the biosensor layers deposited over the surface of the working electrode, liquid chromatography electrospray ionization tandem mass spectrometry (LC-ESI-MS/MS) was utilized. The HPLC analysis was performed on an Agilent Infinity 1260 series instrument (Agilent Technologies, CA, USA) coupled with a quadrupole time-of-flight mass spectrometer Q-TOF LC/MS 6545 (Agilent Technologies, CA, USA) equipped with Jet Stream Thermal Focusing Technology ESI source. The data acquisition was controlled by MassHunter Software Tools. For LC-ESI-MS/MS experiments, a 30 µL water droplet spotted for 30 min on the glucose biosensors, previously not used in electrochemical studies, was taken. The obtained results were compared with data obtained in the LC-ESI-MS/MS study of buffer samples collected after

each scan in CV. Chromatographic separation was achieved on the ZORBAX Eclipse Plus C 18 column (2.1 × 50 mm, particles size 1.8 µm) (Agilent, CA, USA). The mobile phase consisting of 0.3% formic acid in water (Solvent A) and acetonitrile (Solvent B) was used in the following gradient elution step: 90% Solvent A, was held for 2 min, then decreased to 10% in 9 min and held for 2 min, and returned back to the starting conditions in 0.5 min for 8 min equilibration. The column operation temperature was fixed at 30ºC, the mobile phase flow rate was 0.3 mL/min and the injection volume was 10 µL.

MS scans were performed in a negative ion mode, operating under capillary voltage at 4500 V; the fragmentor voltage was set at 70 eV; dry gas temperature at 350°C; gas flow at 9 L/min; nebulizing gas pressure at 45 psi. The mass spectra for all samples were recorded at *m/z* 100-1500. The MS/MS experiments were conducted in product ion scan mode at collision energies ranging from 10 to 50 eV. The elemental compositions were identified based on the accurate mass measurements and data processing of total ion chromatograms (TICs) of the parent ions and fragments obtained in the MS/MS experiments.

4.2.4. Results and Discussion

4.2.4.1. Mathematical model validation

The initial design of the glucose biosensor system was based on the preparation method 1. In Figure 47 a good qualitative response of the numerical solutions is presented together with the experimental voltammograms obtained at 50 mV/sec for the two types of glucose biosensors with different PB modification time.

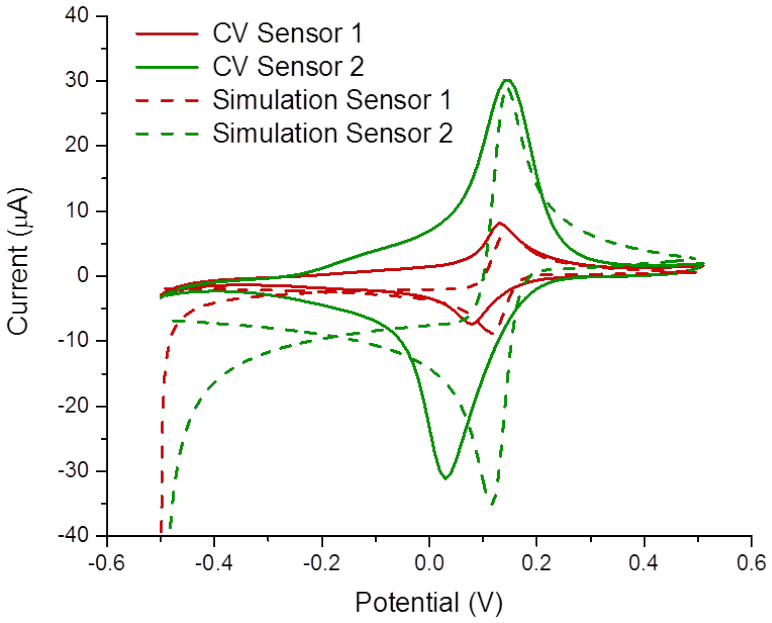

Figure 47 - Comparison of the model output (dashed line) vs. experimental data (solid line) for two types of glucose biosensor fabricated according to preparation method 1: *sensor 1* represents the results of 15 min PB deposition time, whereas *sensor 2* refers to the 40 min procedure. The presented voltammograms were recorded/simulated for a scanning speed of 50 mV/sec.

In both simulations, the initial value for the deposited PB had to be adjusted for the two different types of biosensor: for *sensor 1* the concentration of the deposited oxidized form of mediator (M_{ox}) was estimated as 5 mM, whereas for *sensor 2* this parameter value was equal to 20 mM. From Figure 47 it is clear that no significant quantitative response can be obtained for the reduction curve, especially in case of higher mediator loadings. In order to validate the developed model, an additional set of experiments for the glucose biosensors was proposed. The *sensor 2* type was tested at a potential range from -0.5 V to +0.5 V with higher scan rates: from 100 to 500 mV/sec. The obtained voltammograms were compared with the model output shown in Figure 48.

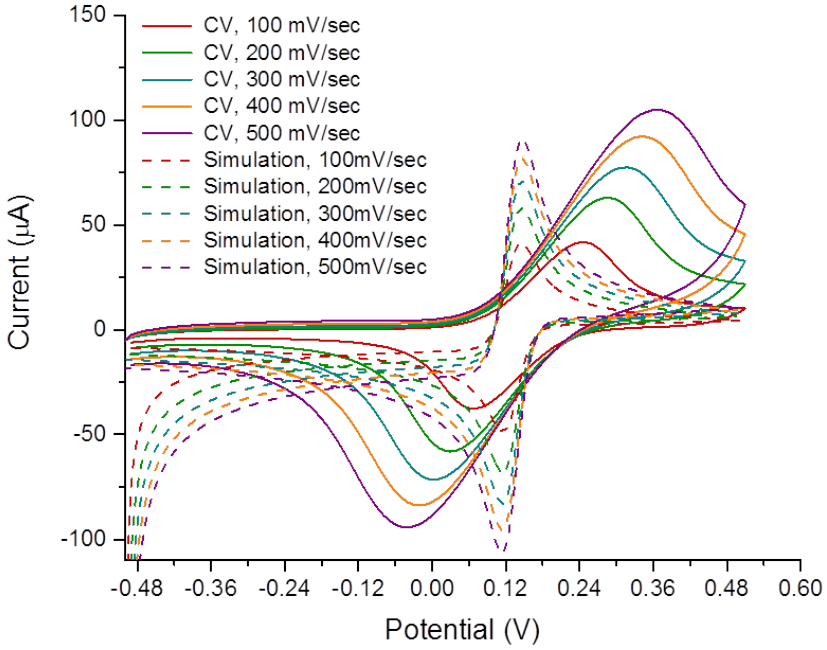

Figure 48 - The experimental voltammograms (solid line) vs. the model output (dashed line). Glucose biosensors were cycled at different scan rates (100 to 500 mV/sec).

The results presented in Figure 48 clearly demonstrated a strong disagreement between the model predictions and experimental data at high cycling speeds: no relevant peak potential shifts and peak current increase were obtained with the model. Therefore, it was concluded that the assumed mechanisms of chemical and physical processes taking place inside the biosensor system proposed in the model were not sufficient. However, the variation of model parameters, namely d_e and M_{ox}, and further comparison of the simulation results with the experimental voltammograms allowed assuming that irreversible changes occur inside the biosensor system. Thus, the disagreement between the model predictions and the experimental data was mainly attributed to the constant decrease in the thickness of the enzyme/membrane layer, as well as in the concentration of deposited mediator after each scan. Moreover, a reversible electron transfer behaviour estimated at the lower scan rates was not present in the experimental voltammograms obtained at cycling speeds higher than 50 mV/sec. Varying the values of only two parameters (d_e and M_{ox}) within the model allowed to understand better the additional processes taking place inside the biosensor, and to focus on the optimization of the PB deposition and membrane composition methods. In a

subsequent part of the study the model was used to identify the crucial biosensor system parameters that were further optimized in a new preparation method for the glucose biosensors.

4.2.4.2. Biosensor design optimization

In order to achieve a reproducible response and improved stability of the biosensor system layers the preparation method 2 was proposed. In this procedure, two crucial requirements had to be fulfilled: first, to achieve a higher and stable loading of PB; and second, to guarantee the stability of the enzyme/membrane layer under different operating conditions. Therefore, the deposition procedure of the PB layer had to be modified together with the composition of the Nafion membrane. In order to avoid changes in the biosensor topology, such as mechanical decomposition of the PB and the membrane layer and its subsequent leakage, that affected the switch from reversible to irreversible electron transfer behaviour of the biosensor system, the optimized biosensors from preparation method 2 (*sensor 3* type) were cycled at scan rates lower than 50 mV/sec. The potential range of the PB/PW redox couple from -0.5 V to +0.5 V was applied, as shown in Figure 49. Similar model parameters were used as for the simulations carried out for the preparation method 1. The value for the concentration of the deposited PB and the standard redox potential were now fixed to 100 mM and -0.05 V, respectively.

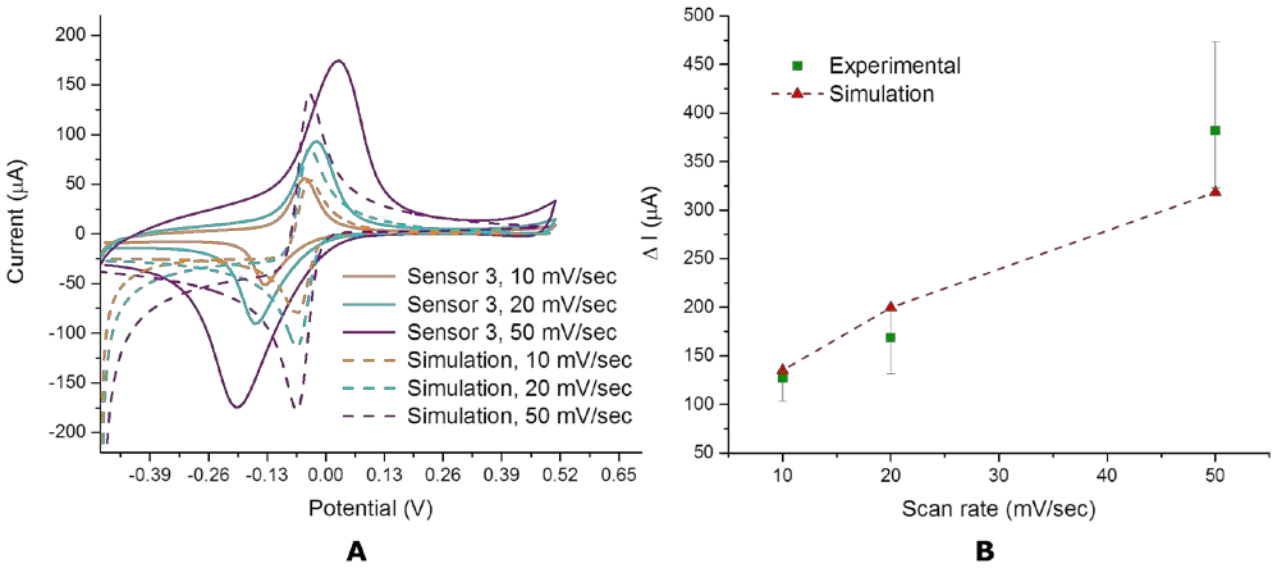

Figure 49 - Comparison of the experimental voltammograms obtained at various scan rates for the optimized glucose biosensor design (preparation method 2) and the model output (A). The recorded difference of peak current values (ΔI, µA) *vs.* scan rates is summarized in graph B, comparing experimental and simulation results.

The optimized method was analyzed for the *sensor 3* type and the expected increase in the current response following the increase in the scan rates was obtained in all experiments for both oxidation and reduction processes (Figure 49B). Moreover, the simulated voltammograms presented in Figure 49A showed a fair agreement with the experimental curves, especially with respect to the peak current values. To study the influence of the scan rate and the amount of Nafion®117 present

in the enzyme/membrane mixture on the stability of the biosensor layers and the response, PB modified SPEs from preparation method 2 were used to design *sensor 4* type, where the preparation method 1 for the enzyme/membrane mixture was adapted. Thus, the principal difference between the *sensor 3* and *sensor 4* series was the composition and concentration of the Nafion membrane: 2.0% and 0.2% Nafion, respectively. The constructed glucose biosensors were tested for different scan rates and the results of electrochemical studies were further compared with the data obtained by liquid chromatography-electrospray ionization-tandem mass spectrometry (LC-ESI-MS/MS) and scanning electron microscopy (SEM) coupled with energy dispersive X-ray (EDX) analysis. The obtained results are presented in the following section 4.2.4.3.

4.2.4.3. The effect of the scan rate and membrane composition on the biosensor layers stability and response

Concerning the changes in the topology of the biosensor system from one scan to another in CV, it was interesting to investigate the content of the buffer probes collected after each measurement by means of liquid chromatography tandem mass spectrometry (LC-MS/MS). Therefore, the glucose biosensors from the *sensor 3* and *sensor 4* series were scanned at the potential range from -0.5 V to +0.5 V at 10, 20 and 50 mV/sec potential sweep speeds (Figure 50).

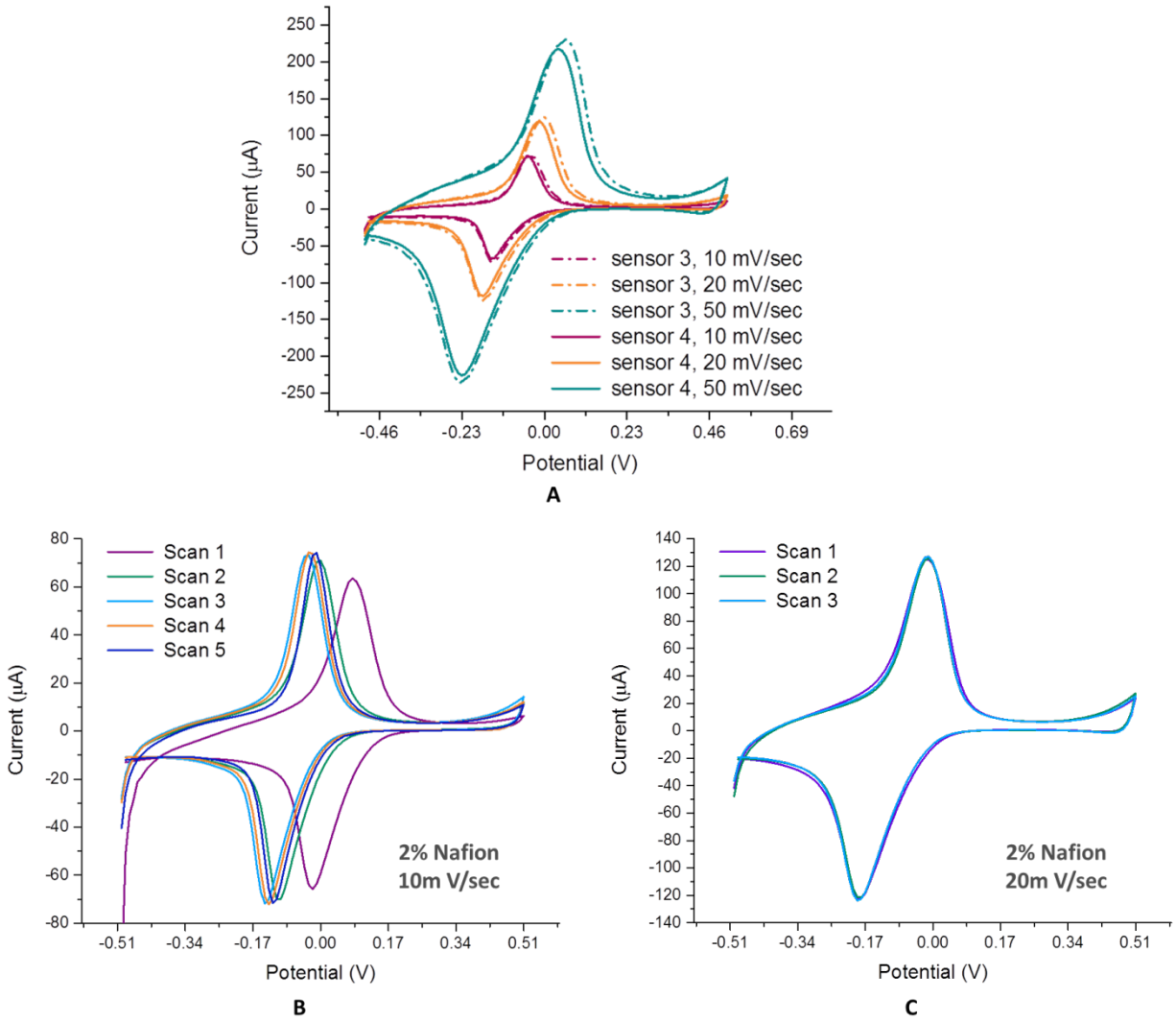

Figure 50 - The results of the experimental CV studies for different membrane composition (A), number of scans and sweep rates (B,C). The first scans recorded at various scanning speeds for *sensor 3* and *sensor 4* series are compared in A. Cyclic voltammograms obtained for two glucose biosensors from *sensor 3* series at 10 mV/sec and 20 mV/sec are presented in B and C, respectively.

Since no significant difference was obtained between the voltammograms for *sensor 3* and *sensor 4* designs (Figure 50A), the probes were collected for 10 and 20 mV/sec scan rate experiments. To verify the correlation between the scan rate value or number of scans and the enzyme/membrane film stability, a fresh sensor was used for each scan rate. Moreover, to prove the influence of the electrochemical measurements on the biosensor layer stability one of the non-used glucose biosensors (*sensor 3* and *sensor 4* series) was tested in a steady-state experiment with a water droplet (see section 4.2.3.7.). All the collected probes were investigated by subsequent LC-ESI–MS/MS analysis (Figure 51).

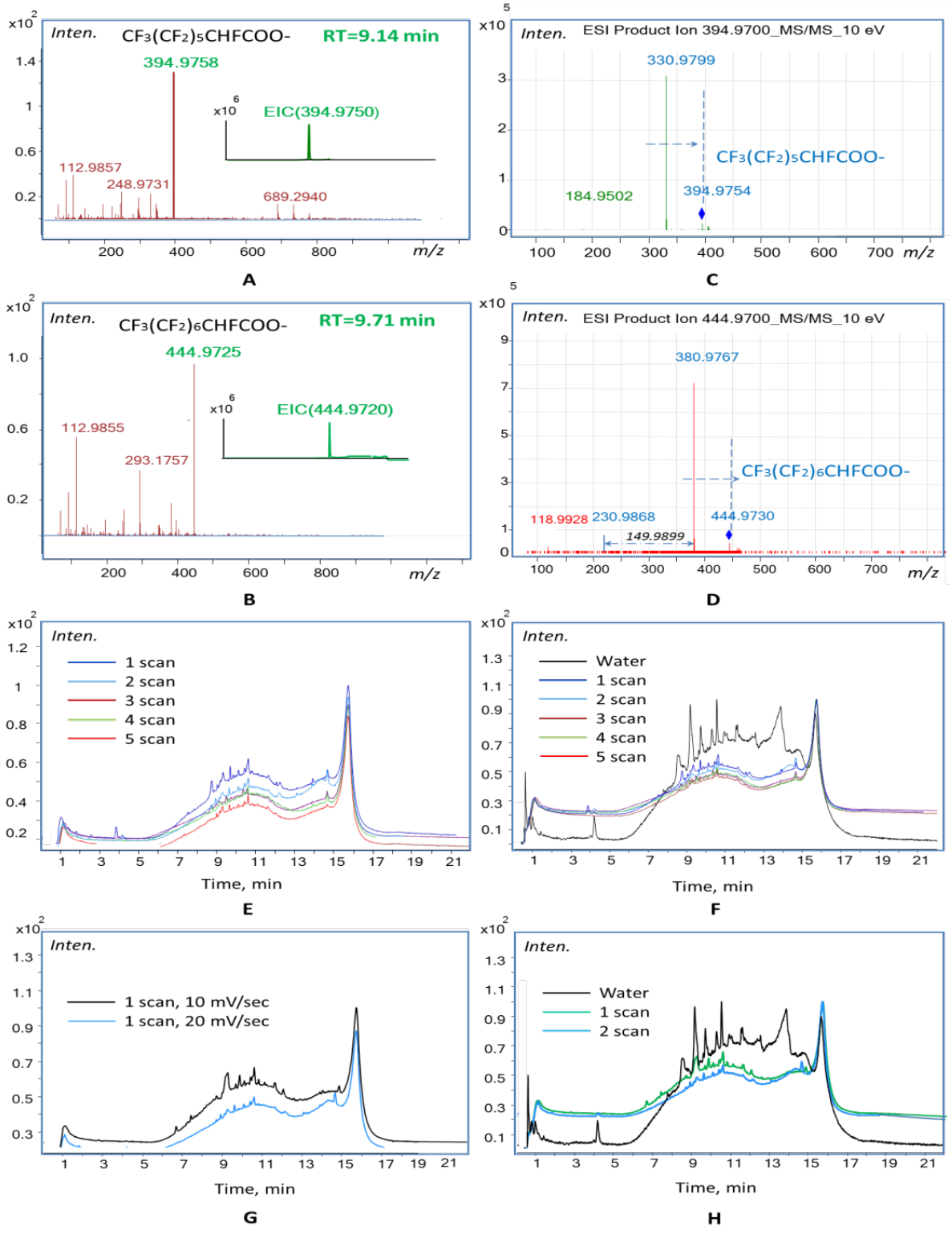

Figure 51 - Mass spectra (A-D), TIC and extracted ion chromatograms (EICs) (A,B) of buffer probes (coloured) and water droplets (black) of *sensor 3* (E-G) and *sensor 4* (H) series obtained for a different number of scans (E) and sweep rates (G). The results of the comparison of steady state experiment vs. CV probes collected for *sensor 3* and *sensor 4* series are presented in graphs F and H, respectively. Nafion - corresponding fragments in MS/MS spectra are shown at collision-induced dissociation (CID) experiments at 10 eV.

In all samples tested by mass spectrometry the fragments corresponding to the Nafion membrane were clearly observed (Figure 51, A-D). The mass spectra were shown for perfluorinated carboxylic acids as the most environmentally persistent compounds of the Nafion fluoropolymer [166]. Thus, peaks at *m/z* equal to 394.9758 and 444.9725 were tentatively identified as $CF_3(CF_2)_5CHFCOO^-$ and $CF_3(CF_2)_6CHFCOO^-$ fragments, respectively (Figure 51A,B). These structures were further confirmed by the major MS/MS fragments presented in Figure 51C and Figure 51D [167].

From the total ion chromatograms (TICs) presented in Figure 51E, it is clear that at low scan rates (10 mV/sec) the membrane layer (*sensor 3* series, 2.0% Nafion) stabilizes approximately at the fifth scan, whereas at 20 mV/sec (Figure 51F) the Nafion elution profile for the same type of membrane reaches a constant trend already at the third scan. The tendency of Nafion membrane stabilization at a higher sweeping speed was demonstrated for both probes collected after the first scans in Figure 51G and could also be traced in the voltammograms recorded at scan rates equal to 10 and 20 mV/sec (Figure 50B,C). Comparing the elution profiles of Nafion-corresponded products, for probes collected after a steady state experiment and different scans in Figure 51G and Figure 51H, it is clear that the CV measurements allow faster stabilization of the membrane layer regardless of its composition. Moreover, the concentration profiles of Nafion-corresponded products for the *sensor 4* (0.2% Nafion) series tested at 20 mV/sec (Figure 52) showed a higher signal in comparison to the *sensor 3* series (2.0% Nafion) at the first scans which corresponds to a lower stability of the 0.2% Nafion membrane.

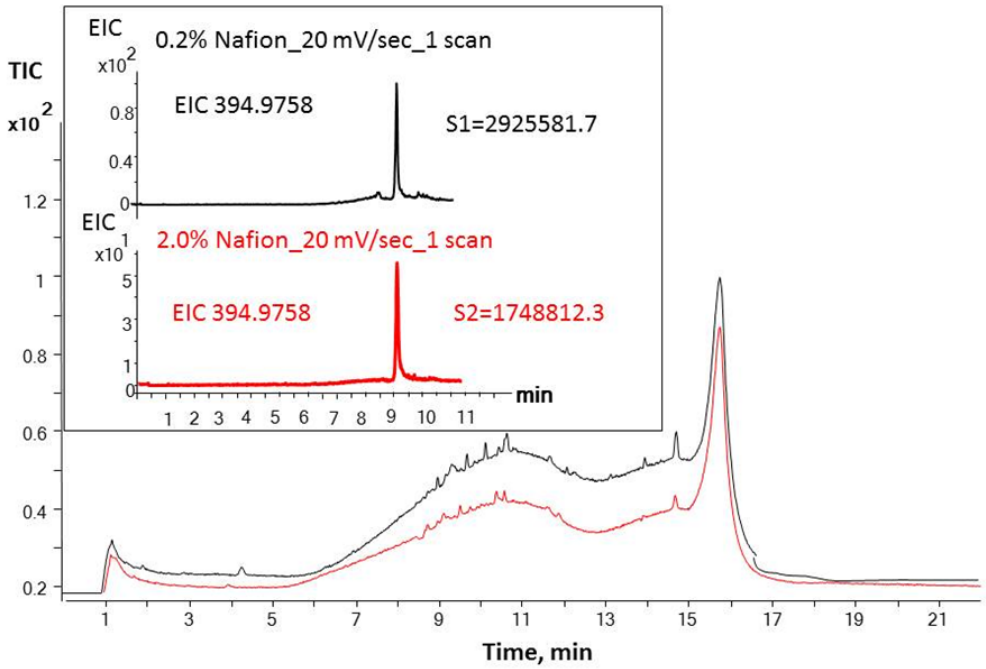

Figure 52 - TIC and EIC (shown for $CF_3(CF_2)_5CHFCOO^-$ at *m/z* 394.9758, RT = 9.14 min) chromatograms of Nafion corresponding products obtained for the probes collected after performing CV measurements (scan rate equal to 20 mV/sec) for glucose biosensors made with different polymer concentration in the enzyme/membrane layer (*sensor 3* series (red line) and *sensor 4* series (black line).

The stability of the 2.0% Nafion membrane was also confirmed in the subsequent SEM/EDX studies of the *sensor 3* and *sensor 4* samples (Figure 53), obtained after CV characterization.

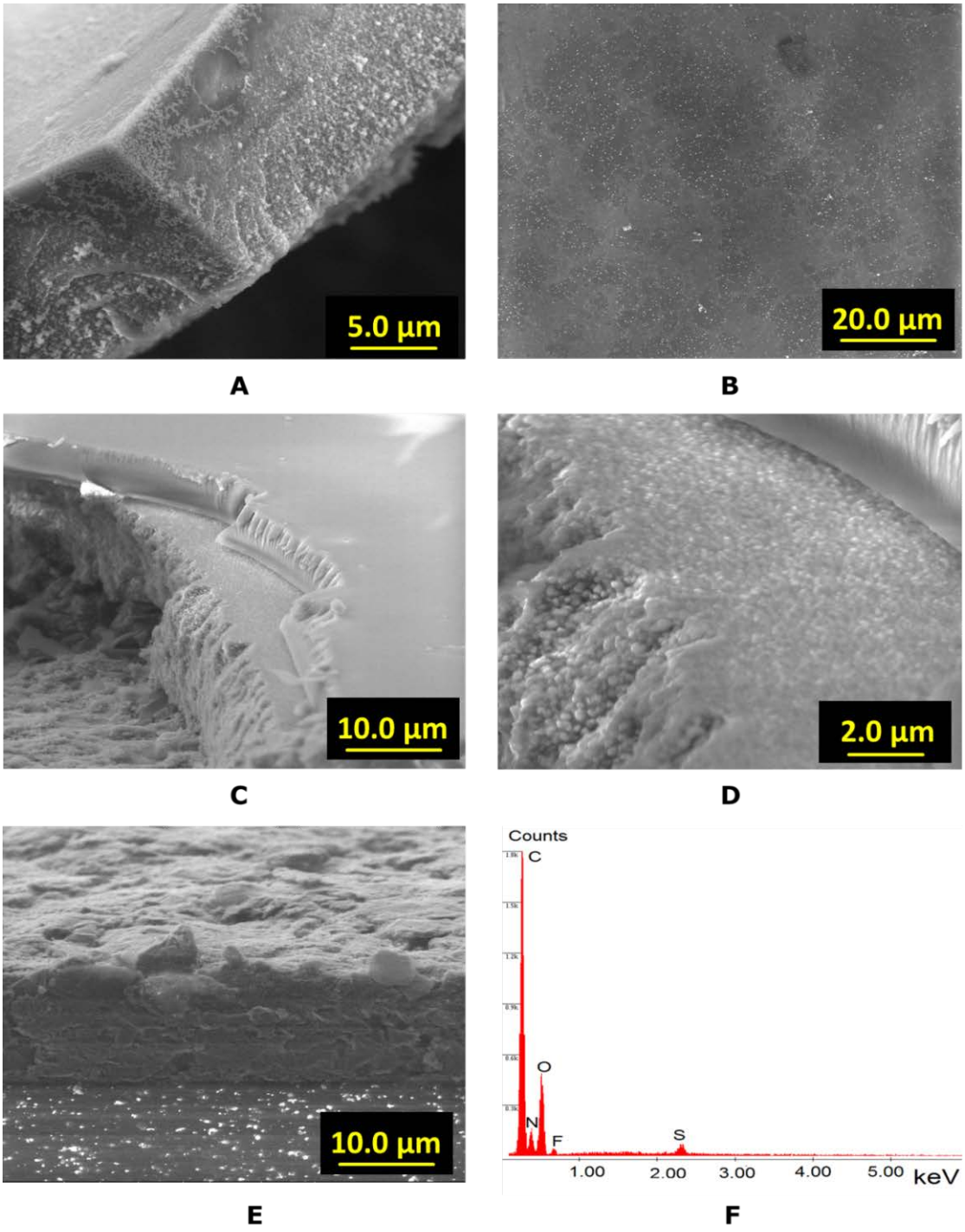

Figure 53 - SEM images (A-E) and EDX spectra (F) of glucose biosensor layers. The enzyme/membrane layer of the *sensor 4* series, without graphene oxide is presented in A. Top view of the enzyme/membrane layer is enlarged in B. For the *sensor 3* series graphene oxide, PB and enzyme/membrane layers are shown in C. The PB layer of the *sensor 3* series is enlarged in D, as well as a part of the enzyme/membrane layer (top right). The working electrode prior to modification steps is shown in E.

A non-uniform enzyme/membrane layered structure was observed in Figure 53A with a dense Nafion coating on top of the surface (Figure 53B). A more detailed view on the biosensor structure for the 2.0% Nafion membrane is presented in Figure 53C, where the graphene oxide layer with deposited Prussian Blue (Figure 53D) is covered by the enzyme/membrane film. Figure 53C clearly indicates that 2.0% Nafion coating allows the formation of a uniform layer with a final thickness equal to 5-7 µm (estimated by SEM). The graphene oxide layer (top) over the plastic substrate (bottom) for commercial SPEs was demonstrated in Figure 53E. Moreover, EDX spectra taken from the enzyme/membrane film, clearly indicated the presence of Nafion, based on the fluorine and sulphur spectral lines (Figure 53F). Therefore, EDX analysis demonstrated that the Nafion layer remains fixed on the biosensor surface after performing cyclic voltammetry measurements.

4.2.4.4. Chronoamperometric characterization of optimized biosensors

The analytical merit of the optimized biosensors (*sensor 3* series) was evaluated *via* chronoamperometric studies in the presence of glucose. The linear response (Figure 54A) of the constructed biosensors was obtained in the range of glucose concentrations from 10^{-3} to 10^{-5} M (RSD < 7% per electrode). The biosensors were also calibrated in the analytical range of glucose concentrations between 0.1 and 2 mM (Figure 54B). The mean value of the slope estimated for the linear response (0 to 2 mM) was - 1.25 µA/mM with a standard deviation equal to 0.035 µA/mM. The obtained results are in a good agreement with literature data reported for fermentation monitoring [76,87].

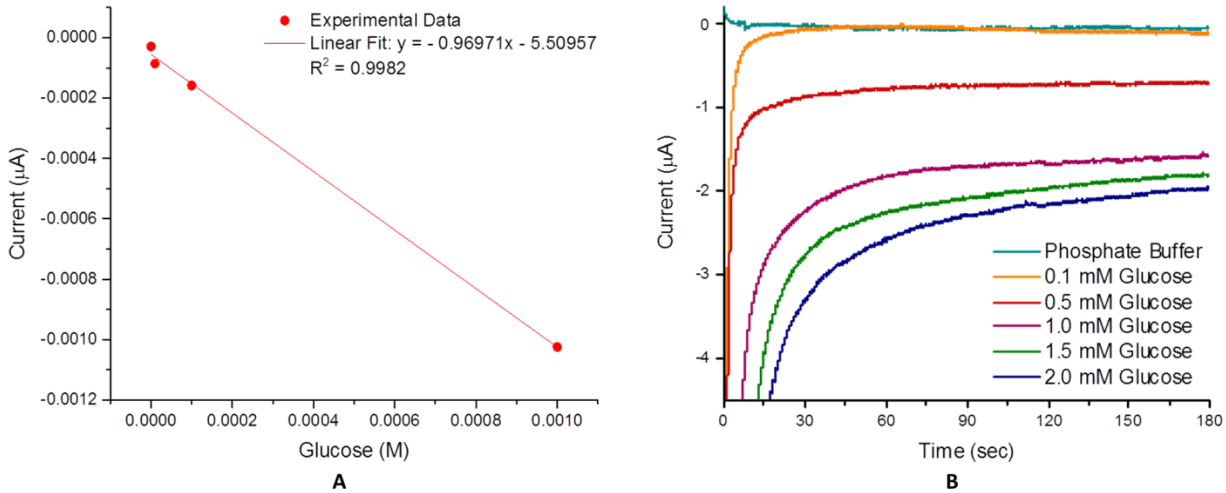

Figure 54 - Calibration curve (A) obtained for the optimized *sensor 3* biosensors in the presence of glucose. The current response is plotted towards the glucose concentration range equal to 10^{-5}-10^{-3} M. The zero glucose concentration corresponds to the phosphate buffer solution. The relative standard deviation per electrode is not shown, due to the low value (RSD = 7%). The chronoamperometric response (current *vs* time) of the analytical range of glucose concentrations is presented in B.

4.2.5. Conclusions and future perspectives

The mathematical model of the cyclic voltammetry response was developed for glucose biosensors operating in aerobic conditions in the absence of glucose at low scan rates. The model was validated with the biosensors with various amounts of immobilized mediator and different enzyme/membrane film compositions. The biosensor system parameters required for numerical simulations were either found in the literature or estimated from experimental data, therefore not limiting the applicability of the proposed model to a single biosensor design. In this work, we have demonstrated that combining the results of multi-analytical studies together with mechanistic modeling is an effective approach in identifying the key parameters of the biosensor system crucial for the optimal biosensors operation and design. Therefore, a more favorable composition of the enzyme/membrane layer (2.0% Nafion) was proposed and further proved to be stable at various operation conditions during cyclic voltammetry measurements.

In summary, the practical merit of the presented work is in the development of a time and cost effective tool crucial for amperometric biosensor design optimization. The demonstrated approach could potentially allow reducing the reagent usage and waste generation. As a future work, the optimized design of the glucose biosensor system will undergo further bioanalytical, morphological and amperometric studies, and the constructed model could be extended to describe the mediated enzymatic reaction of glucose oxidase in the presence of glucose. Thus, the proposed model will summarize all available process knowledge together with the results of bioanalytical and morphological analysis. Combining such model with global sensitivity and uncertainty analysis tools, will allow mapping the influence of the complete set of system input parameters on the biosensor response, which subsequently opens up the possibilities for optimization of the biosensor performance and ultimately the design of novel improved biosensors.

Chapter 5: Morphological studies and tandem monitoring in robust biosensor design and operating conditions identification

The content of the current thesis chapter was partly redrafted from the following manuscript:

- D. Semenova, Y. E. Silina, M. Koch, A. Zubov and K. V. Gernaey, *Morphological studies and tandem monitoring in robust biosensor design and operating conditions identification.*

Abstract

Understanding the biorecognition and transduction mechanisms is a key aspect in the development of the robust sensing technologies. Therefore, the design of tools and analytical approaches that could allow gaining a deeper insight into the bio- and electrochemical processes would significantly accelerate the progress in the field of biosensors. Herein, we present a novel effective strategy for biosensor tandem monitoring in a droplet combined with thorough electrochemical and morphological analysis. Two types of multilayer glucose biosensors (first generation) were chosen as a case study. The tandem approach was based on chronoamperometric characterization of the biosensors in the presence of analyte (glucose) coupled with oxygen monitoring using an optical microsensor. The various operating conditions were evaluated in cyclic voltammetry. The obtained results were independently confirmed using multi-analytical techniques, including scanning electron microscopy (SEM), energy dispersive X-ray spectroscopy (EDX), liquid chromatography-electrospray ionization-tandem mass spectrometry (LC-ESI-MS/MS) and inductively coupled plasma mass spectrometry (ICP-MS). Moreover, this work reports specific protocols developed for detection of oxygen conversion rates, iron and membrane elution inside the biosensor system. The presented approach allows to identify and build-up the correlations between the critical operation conditions and system parameters affecting the overall biosensor response and sensitivity. Remarkably, the optimal combination of Nafion membrane coatings and enzyme loadings for glucose biosensors was proposed. The optimized biosensor design resulted in the improved stability (up to 3 months) and linear detection range of glucose concentrations (up to 5 mM). The presented tandem monitoring methodology based on simultaneous multiple-substrate detection could be extended to the other oxygen dependent types of biosensors.

5.1. Theoretical background

5.1.1. Nafion® for biosensors

The purpose of the biosensors is to provide a highly selective detection of the specific substrates by using enzymes, whole cells, biomimetic receptors, etc., as bioreceptors. Hence, the operation of the biosensor involves the direct contact with low and high molecular weight substances present in the biological samples which would interfere with analyte sensing. The accumulation of the active compounds on the bioreceptor surface would lead to diminishing of the biosensor response and lifetime. The application of anti-interference membranes can eliminate the above mentioned interactions, decrease the impact of the thickness fluctuations and improve the overall biosensor stability. Moreover, the presence of the membrane layer can also affect the sensitivity of the biosensor. In the work of Ivanauskas et al. [168] two types of biosensors based on a single heterogeneous enzyme layer and containing an additional protecting membrane (polymer-based) layer were compared with the help of mathematical models. During the exploitation of biosensors with biological samples, an outer membrane extends the concentration gradients inside the system which minimizes the inactivation of immobilized enzyme. However, one has to keep in mind that the use of membranes that are too thick can lead to an increased response time. Varying the activity of the enzyme layer, membrane thickness and properties can significantly improve the stability and sensitivity of the biosensors.

In the past years a great variety of biocompatible membrane and coating materials has been developed to improve the biosensor performance [169]. One of the most widely used polymers for the enzyme encapsulation is the perfluorinated membrane Nafion®. Initially supplied as proton exchange membrane for fuel cells by DuPont [170,171], this sulfonated tetrafluorethylene copolymer played an important role in the development of glucose biosensors [111,172–175]. The copolymerization of a perfluorinated vinyl ether co-monomer with tetrafluoroethylene (TFE) results in the formation of the Nafion® membrane structure based on a polyfluoroethylene backbone and regularly spaced perfluorvinyl ether pendant side chains terminated by a sulphonate ionic group, as shown in Figure 55 [176]. Since Nafion structure units are not covalently cross-linked, it allows transforming them into a variety of shapes. The Nafion structure organisation models suggest that either hydrophilic sulphonate groups are rearranged in well-defined clusters and channels to maximize the interaction between similar fragments of the fluorocarbon backbone (cluster–network model) [177] or some region intermediates (i.e. counter-ions, side-chain ethers, etc.) are involved in the hydrophobic backbone and the aqueous phase connection [176].

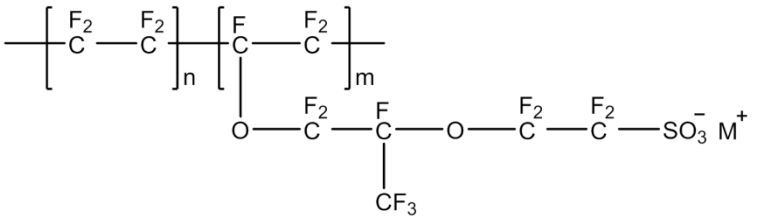

Cluster-network model for Nafion membranes

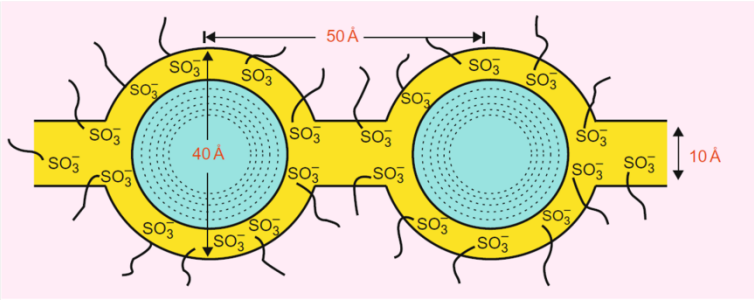

Figure 55 –The chemical structure and cluster-network model of Nafion® membranes. The polymeric ions and absorbed electrolyte phase-separate from the fluorocarbon backbone into approximately spherical clusters connected by short narrow channels. The polymeric charges are most likely embedded in the solution near the interface between the electrolyte and fluorocarbon backbone. This configuration minimizes both the hydrophobic interaction of water with the backbone and the electrostatic repulsion of proximate sulfonate groups. The dimensions shown were deduced from experiments. The areas around the interface (yellow) and inside a channel (blue) are the double layer regions from which the hydroxyl ions are excluded electrostatically. Adapted from [176,177].

However, the morphology of the Nafion ionomer thin films used in biosensors and their behaviour under various operating conditions is fundamentally different from membranes and is still not very well understood [178]. Therefore, different analytical and simulation approaches are applied to investigate structure and transport phenomena of wetted Nafion films [179,180]. The swelling and diffusion behaviour of Nafion® membranes were characterized in mixed simple alcohol/water solutions [181,182]. In the work of Freijanes et al. [183] chronopotentiometric characterization combined with swelling experiments in the presence/absence of glucose confirmed that the ion transport in Nafion membranes is significantly affected by different electrolyte and glucose concentrations. Moreover, it was established that the presence of glucose at low electrolyte concentrations leads to the complete loss of the membrane's permselectivity (ratio between the specific component flux and total flux through the membrane). However, combining Nafion membranes with novel transducer materials with enhanced electron transport (e.g. exfoliated graphite nanoplatelets) can significantly improve the stability, sensitivity and linear detection range of glucose biosensors [172]. Furthermore, thermal modification of Nafion membranes presented by Latif et al. [175] affected the diffusion properties of such coating that resulted in the increase of the upper limit of linearity up to a factor of five for glucose biosensors.

5.2. Case Study 4: Morphological studies and tandem monitoring in robust biosensor design and operating conditions identification

5.2.1. Introduction

The dependency of the catalytic current on the mediator loadings and membrane composition has been previously verified in Chapter 4 for the first generation glucose biosensors in the absence of substrate [77]. Therefore, the main objective of the presented work was to identify and analyse the factors underlying variation in the sensitivity, linear calibration range and detection limits of the biosensors in the presence of glucose. The glucose biosensor with confirmed enhanced stability [77] based on premixed enzyme and 2 vol. % Nafion®117 membrane layer (*sensor 3* in Chapter 4) was compared with a new biosensor design containing individual enzyme and outer membrane (2 vol. % Nafion®117) coatings. The electrochemical behaviour of both types of biosensors was fully characterized using cyclic voltammetry (CV) and chronoamperometry (AM). The activity of immobilized enzyme and oxygen conversion rates were quantified by an optical microsensor in the present analytical range of glucose concentrations. The probes collected after CV and AM measurements were further investigated for mediator layer stability (estimated as free iron content migrated through the membrane) by inductively coupled plasma mass spectrometry (ICP-MS). The stability of the polymer membrane (Nafion®117) was investigated by liquid chromatography-electrospray ionization-tandem mass spectrometry (LC-ESI-MS/MS). The morphological investigation of the layer-by-layer deposition for both types of glucose biosensors was performed by scanning electron microscopy (SEM) supported with energy dispersive X-ray spectroscopy (EDX). Moreover, the swelling behaviour of the membrane films was analyzed in dynamics using the environmental detection module of a scanning electron microscope (ESEM). The case study workflow is summarized in Figure 56.

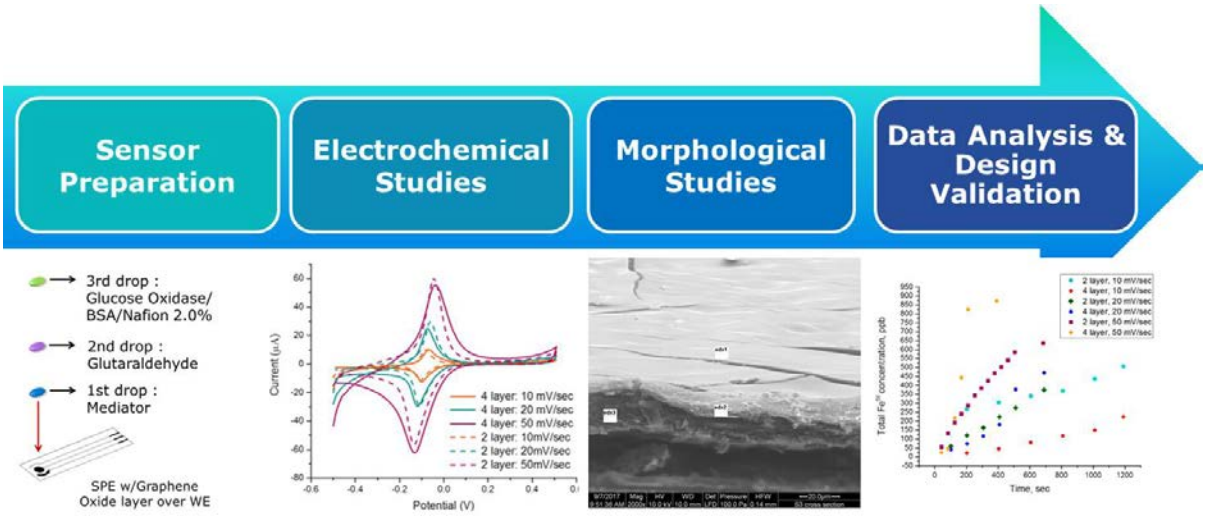

Figure 56 - Case study 4, graphical roadmap.

5.2.2. Experimental section

5.2.2.1. Reagents and materials

Screen printed electrodes (SPEs) DRP-PW-110DGPHOX were customized by DropSens (Llanera, Spain) and ItalSens IS-C electrodes were acquired from PalmSens (Utrecht, The Netherlands). Both types of electrodes were printed on polyester substrate and each sensor consists of a carbon working electrode (modified with graphene oxide layer for DRP-PW-110DGPHOX), a carbon counter electrode and a silver reference electrode. The diameter of the working electrodes was 0.4 cm (DRP-PW-110DGPHOX) and 0.3 cm (ItalSens IS-C), resulting in apparent geometric areas of 0.126 cm^2 and 0.07 cm^2, respectively.

Glucose oxidase (GOx) (EC 1.1.3.4, type VII, 248 U/g solid) and bovine serum albumin (BSA) were obtained from Sigma (St. Louis, MO, USA). Glutaraldehyde solution (25% (v/v)), ethanol (UV HPLC gradient, 99.9%) and potassium hexacyanoferrate (III) (ACS reagent, ≥99.0%) were purchased from Sigma – Aldrich (St. Louis, MO, USA). Iron (III) chloride (anhydrous, 99.99%) and Nafion®117 solution (~5% (v/v) in a mixture of lower aliphatic alcohols and water) were provided by Aldrich (Steinheim, Germany). D-Glucose (anhydrous) was provided by Fluka (Loughborough, UK). Mono – and di-potassium hydrogen phosphates (anhydrous) were obtained from Merck (Darmstadt, Germany). Sodium hydroxide (50% (w/w)) and hydrochloric acid (37% (w/w)) solutions were purchased from VWR International A/S (Søborg, Denmark). All the solutions were prepared with 0.1 M phosphate buffer supplemented with 0.1 M KCl (pH = 6), unless stated otherwise.

5.2.2.2. Glucose biosensor preparation

To avoid the biosensor surface modification prior to the modification steps no pre-treatment in phosphate buffer solution was applied (see Figure 58A). The optimized preparation methods of Prussian Blue deposition and membrane composition were acquired from preparation method 2 described in section 4.2.3.2. A 5 µL drop of a 0.1 M solution of potassium ferricyanide $K_3Fe(CN)_6$ in 10 mM HCl was placed over the working electrode and mixed with a 5 µL drop of 0.1 M solution of ferric chloride, $FeCl_3$ in 10 mM HCl directly on the surface of the electrode. The sensors were left to dry for 40 min at room temperature and then washed with a 10 mM HCl solution, deionized water and dried with air. In order to stabilize the PB layer, the sensors were placed in the oven at 100°C for 1 h. After cooling, the surface of WE for PB modified SPEs was pretreated with glutaraldehyde solution prior to the enzyme modification step. A 2.5 µL droplet of freshly prepared glutaraldehyde solution (1% (v/v) diluted in water) was placed over the WE of the PB modified SPEs and was left to dry at room temperature for 30 min. After the glutaraldehyde solution layer was dried, the premixed enzyme/membrane or individual enzyme and membrane layers were deposited. The immobilization steps for different sensor designs were schematically summarized in Figure 57. To simplify the reference to the specific glucose biosensor preparation method, the "two", "three" and "four" layer sensor terminology will be introduced below.

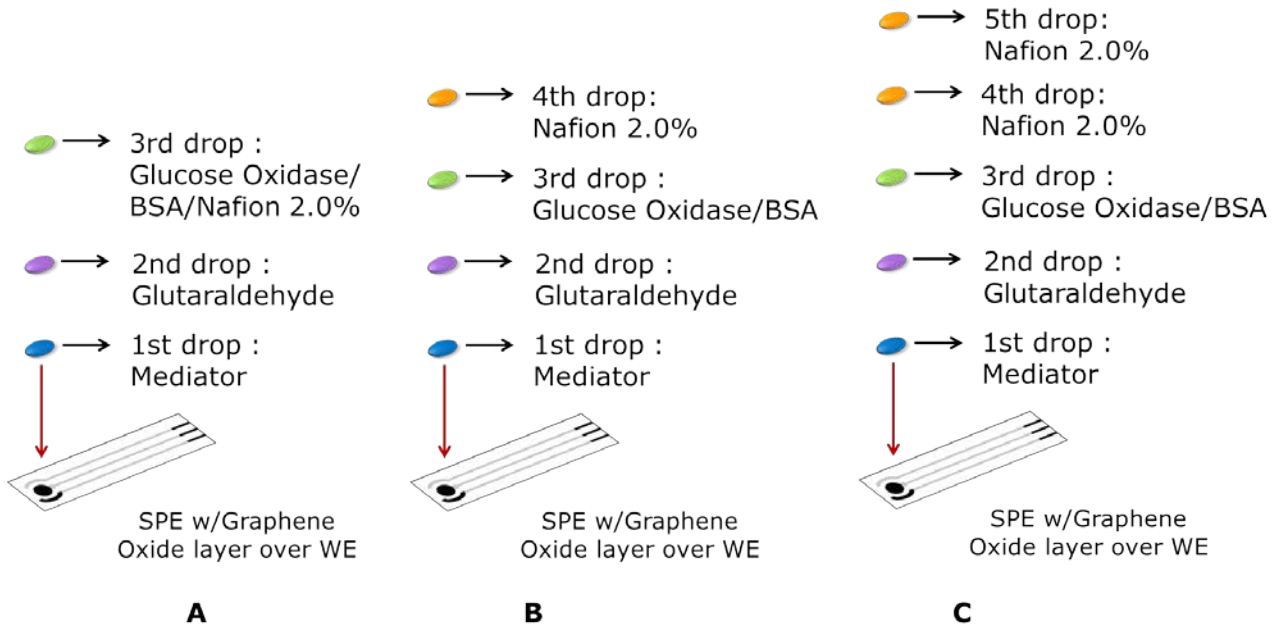

Figure 57 - Schematic representation of the layer deposition procedure for "two" (A), "three" (B) and "four" (C) layer biosensors.

The "two" layer glucose biosensors (Figure 57A) represent the *sensor 3* batch. A drop of 3 µL drop of Nafion®117 (2 vol. %) neutralized in ethanol [165] mixed with GOx dissolved in phosphate buffer and BSA (5 vol. % diluted in water) in a 1:1:1 proportion (v/v/v) was placed over PB/glutaraldehyde modified SPEs. For the "three" layer glucose biosensors (Figure 57B), the glutaraldehyde solution layer was dried and then a 3 µL drop of GOx dissolved in phosphate buffer mixed with BSA (5 vol. % diluted in water) in a 1:1 proportion (v/v) was placed over the surface of WE. The final Nafion®117 (2 vol. % neutralized in ethanol) membrane layer (3 µL) was deposited over the SPE/PB/Glut/(GOx + BSA) modified electrodes no less than 20 hours from the previous layer immobilization step. In case of "four" layer electrodes (Figure 57C) an additional layer (3 µL) of fresh Nafion®117 (2 vol. % neutralized in ethanol) solution was deposited after 24-32 hours. The "two" and "four" layer glucose biosensors were chosen for further multi-analytical studies.

Regardless of the biosensor design, the SPEs with deposited enzyme and/or membrane layers were placed to dry overnight in a climate chamber at 40% of humidity and 8°C. Moreover, both PB modified SPEs and complete glucose biosensors were stored in the dark, at room temperature and 4°C, respectively. Moreover, the number of units for GOx stock solutions was controlled prior to the immobilization step for all biosensor designs.

5.2.2.3. Glucose oxidase activity measurements

The GOx activity measurement prior to the immobilization step of the stock solutions, as well as the enzyme/membrane mixtures, was performed by using an OXSOLV solvent-resistant, fiber - optic oxygen sensor (PyroScience GmbH, Aachen, Germany) connected to a FireStingO2 fiber - optic meter (PyroScience GmbH, Aachen, Germany) and controlled by Pyro Oxygen Logger software

(PyroScience GmbH, Aachen, Germany). The measurement was based on on-line monitoring of the dissolved oxygen (DO) consumption rate in the reaction of 100 mM glucose solution with two types of GOx stock solutions A and B at room temperature. The setup assembly, as well as the experimental procedure, were described in section 4.2.3.3. For the enzyme activity calculations, one unit (U) of enzyme corresponds to a substrate consumption of 1 µmol per min. The GOx activity prior to immobilization was estimated for Stock A as 0.548 U/µL and for Stock B equal to 0.871 U/µL. The glucose biosensors prepared for electrochemical and morphological analysis are summarized Table 4.

Table 4 – Types of glucose biosensors prepared

Type of biosensor	Glucose oxidase Stock X- free enzyme activity	Characteristics
2 layer	Stock B - 0.871 U/µL	Nafion membrane mixed with GOx/BSA solution
4 layer	Stock A - 0.548 U/µL Stock B - 0.871 U/µL	2 individual layers of Nafion membrane

5.2.2.4. Cyclic voltammetry characterization of glucose biosensors

Cyclic voltammetry (CV) measurements were performed using MultiEmStat (PalmSens, Utrecht, The Netherlands) with a DRP-CAST1X8 interface (DropSens, Llanera, Spain) controlled by MultiTrace 3.4 software (PalmSens, Utrecht, The Netherlands). A 100 µL droplet of phosphate buffer was placed over all three electrodes of SPE. The voltammograms were recorded at different scan rates (10, 20 and 50 mV/sec) in a potential range from -0.5 V to +0.5 V (see Table S6, Appendix C). For each scan rate value a new glucose biosensor was used. After each run sample droplets were collected for subsequent LC-ESI–MS/MS and ICP-MS analysis. The voltammograms obtained for "two" and "four" layer glucose biosensors at 50 mV/sec were compared in Figure 58.

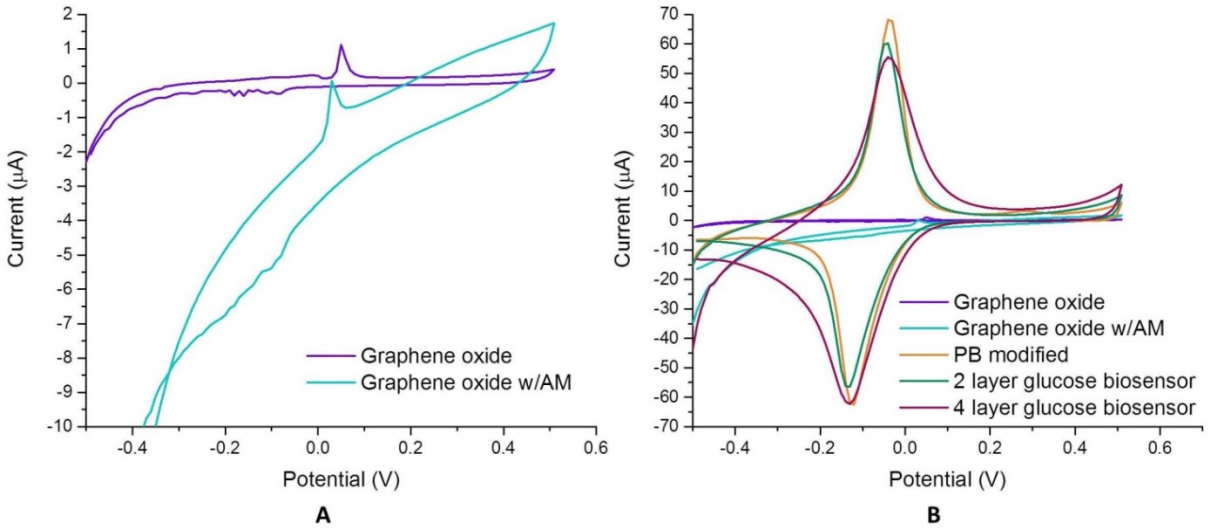

Figure 58 – Comparison of the cyclic voltammograms obtained in air saturated buffer solution (ν = 50 mV/sec) for unmodified graphene oxide -based SPEs without (*Graphene oxide*) and with (*Graphene oxide w/AM*) chronoamperometric pre-treatment (A), PB modified and complete "two" and "four" layer glucose biosensors (B).

Moreover, the dynamic response of the flavin adenine dinucleotide groups of immobilized glucose oxidase was studied in the presence of potassium ferricyanide. A 100 μL droplet of 0.01 M potassium ferricyanide prepared with phosphate buffer (pH = 7.4) was placed over all three electrodes of the "two" and "four" layer glucose biosensors. The CVs were registered at scan rates equal to 10, 20, 50 70 and 100 mV/sec. The obtained peak current values *vs.* scan rate were summarized in Table S7 (see Appendix C). Similar to oxygen in Figure 9A, ferricyanide being an electron acceptor participates in the reduction of the GOx flavin groups [184] following the two-step reactions (66) and (67):

$$GOx(FADH_2) + [Fe(CN_6)]^{3-} \longrightarrow GOx(FADH) + [Fe(CN_6)]^{4-} + H^+ \quad (66)$$

$$GOx(FADH) + [Fe(CN_6)]^{3-} \longrightarrow GOx(FAD) + [Fe(CN_6)]^{4-} + H^+ \quad (67)$$

5.2.2.5. Chronoamperometric characterization of glucose biosensors

Chronoamperometric (AM) studies were performed using MultiEmStat (PalmSens, Utrecht, The Netherlands) with a DRP-CAST1X8 interface (DropSens, Llanera, Spain) controlled by MultiTrace 3.4 software (PalmSens, Utrecht, The Netherlands). The biosensors were characterized in the presence of the analytical range of glucose concentrations (0 to 5 mM) at the applied voltage equal to the peak potential of the reduction curve (-0.14 V). All measurements from the same biosensor type were repeated at least in triplicates. After the AM signal was registered, the buffer probes with and without glucose were collected for subsequent LC-ESI–MS/MS and ICP-MS analysis.

5.2.2.6. Tandem oxygen and glucose monitoring

In order to obtain the simultaneous measurement of the glucose and dissolved oxygen concentration profiles in a droplet for glucose biosensors the chronoamperometric measurement (5.2.2.5.) and the fiber-optic oxygen minisensor (5.2.2.3.) tandem was applied. The experimental setup assembly is illustrated in Figure 59.

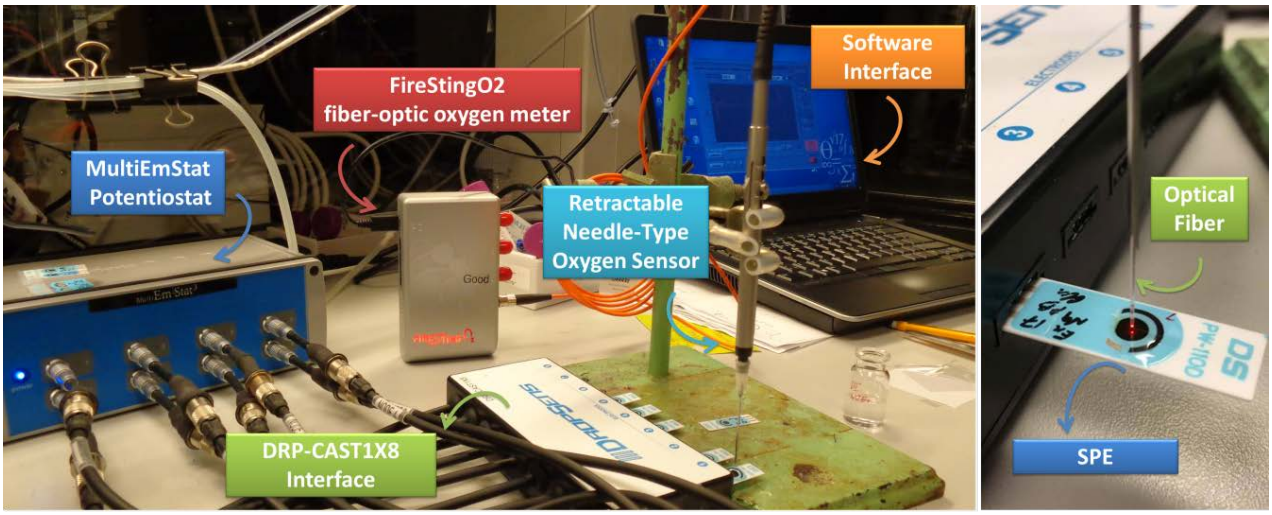

Figure 59 – The experimental setup (A) for the tandem monitoring of oxygen and glucose concentrations in a droplet for free enzyme solutions and enzyme immobilized on the surface of screen-printed electrodes (SPEs). The PB modified SPEs or complete glucose biosensors were connected through an interface (DRP-CAST1X8) to the potentiostat (MultiEmStat). The tip of the fiber-optic minisensor (Retractable Needle-Type Oxygen Sensor) was centred close to the surface of the working electrode (B). The microsensor was connected to the fiber-optic oxygen meter (FireStingO2). Both the potentiostat and the fiber-optic oxygen meter were PC-controlled.

To estimate the detection range of the developed biosensors, chronoamperometric studies were carried out in the presence of glucose solutions (concentration range: 0 – 2 mM) at the applied voltage equal to the peak potential of the reduction curve (-0.14 V). The dissolved oxygen (DO) measurement was performed by using an OXR430 retractable fiber - optic oxygen minisensor (PyroScience GmbH, Aachen, Germany) connected to a FireStingO2 fiber - optic meter (PyroScience GmbH, Aachen, Germany) and controlled by Pyro Oxygen Logger software (PyroScience GmbH, Aachen, Germany). In order to compare the activity of the enzyme (GOx) immobilized on the biosensor surface towards the free enzyme solution two types of experiments were proposed. First, the activity of the freshly made free enzyme solution mixture of Stock B (GOx:BSA = 1:1 (v/v)) was estimated *via* tandem monitoring over the PB modified ItalSens SPEs. A 300 µL droplet of glucose solution of known concentration was placed over all three electrodes and the tip of the fiber optic minisensor was immersed inside the droplet close to the surface of the SPE and centred towards the working electrode (Figure 60). After the DO signal stabilized, simultaneously a 3 µL droplet of enzyme mixture was added inside the glucose droplet and the -0.14 V potential was applied to the

surface of the WE. The obtained results were summarized in Table S8 and Figure S12 (see Appendix C).

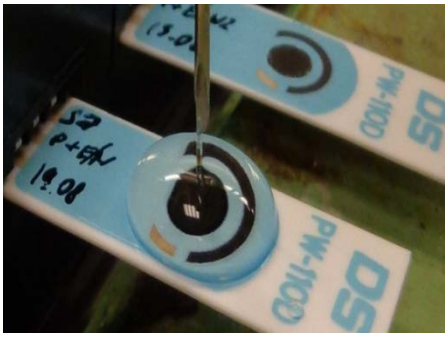

Figure 60 – Photograph showing the positioning of the optical fiber minisensor towards the electrochemical biosensor/SPE during the chronoamperometric studies. The analyte solution droplet was placed covering the surface of all three printed electrodes (reference, counter and working electrodes). The tip of the fiber optic minisensor was immersed inside the droplet and centred towards the working electrode.

The complete glucose biosensors (DropSens SPEs) with different layer composition and immobilized enzyme stock solutions were analysed *via* tandem monitoring in the presence of glucose. The tip of the fiber optic minisensor was centred towards the WE surface, as shown in Figure 59B. After the stable sensor response was obtained, simultaneously a 200 μL droplet of glucose solution of known concentration was placed over all three electrodes and the potential (-0.14V) was applied. The obtained results were summarized in Table S9 and Figure S13 (see Appendix C).

Regardless the type of the tandem monitoring applied (free or immobilized enzyme), the measurements were performed at room temperature for 180 sec after addition of enzyme mixtures or glucose solutions.

5.2.2.7. Scanning electron microscopy (SEM), energy dispersive X-ray spectroscopy (EDX) and environmental scanning electron microscopy (ESEM)

Micrographs for unmodified SPEs and for each layer modification step, namely PB, PB/Glutaraldehyde, PB/Glutaraldehyde/(GOx/BSA/Nafion) -2 layer or PB/Glutaraldehyde/(GOx/BSA) -4 layer, PB/Glutaraldehyde/(GOx/BSA)/Nafion and PB/Glutaraldehyde/(GOx/BSA)/Nafion/Nafion, were obtained by scanning electron microscopy (SEM) using a FEI (Hilsboro, OR, USA) Quanta 400 FEG, operating at 10 kV accelerating voltage. Secondary (SE) and backscattered (BSE) electron images were collected in low vacuum mode (pH_2O = 100 Pa). The microscope was equipped with an EDAX (Mahwah, NJ, USA) Genesis V 6.04 energy dispersive X-ray (EDX) system in order to obtain information on elemental composition of the biosensor surfaces. The measuring time per sample was equal to 100 sec. In addition, the correlative SEM/EDX analysis allowed determining the

composition of the multi-layer biosensor for individual deposition steps (see Figure S14, Appendix C).

In order to perform membrane swelling experiments, the water saturated "two" and "four" layer glucose biosensors were analyzed using environmental scanning electron microscopy (ESEM) by varying the applied pressure and temperature.

5.2.2.8. Liquid chromatography-electrospray ionization-tandem mass spectrometry (LC-ESI-MS/MS)

In order to compare the chemical stability of the Nafion membrane film for "two" and "four" layer glucose biosensors, liquid chromatography electrospray ionization tandem mass spectrometry (LC-ESI-MS/MS) was utilized. The HPLC analysis was performed on an Agilent Infinity 1260 series instrument (Agilent Technologies, CA, USA) coupled with a quadrupole time-of-flight mass spectrometer Q-TOF LC/MS 6545 (Agilent Technologies, CA, USA) equipped with Jet Stream Thermal Focusing Technology ESI source. The data acquisition was controlled by MassHunter Software Tools. For LC-ESI-MS/MS experiments for buffer samples collected after each scan in CV and AM measurements. Chromatographic separation was achieved on the ZORBAX Eclipse Plus C 18 column (2.1 × 50 mm, particles size 1.8 µm) (Agilent, CA, USA). The mobile phase consisting of 0.3% formic acid in water (Solvent A) and acetonitrile (Solvent B) was used in the following gradient elution step: 90% Solvent A, was held for 2 min, then decreased to 10% in 9 min and held for 2 min, and returned back to the starting conditions in 0.5 min for 8 min equilibration. The column operation temperature was fixed at 30ºC, the mobile phase flow rate was 0.3 mL/min and the injection volume was 10 µL.

MS scans were recorded in a negative detection mode in the range of m/z 100-1500, operating under capillary voltage at 4500 V; the fragmentor voltage was set at 70 eV; dry gas temperature at 350°C; gas flow at 9 L/min; nebulizing gas pressure at 45 psi. The MS/MS experiments were conducted in product ion scan mode at collision energies ranging from 10 to 50 eV. The elemental compositions were identified based on the accurate mass measurements and data processing of total ion chromatograms (TICs) and extracted ion chromatograms (EICs) of the parent ions and fragments obtained in the MS/MS experiments.

5.2.2.9. Inductively coupled plasma mass spectrometry (ICP-MS)

The buffer solution samples collected after each scan during CV and AM measurements with regards to mediator layer stability (estimated as an amount of Fe^{56} isotope migrated thought the membrane into solution) were analyzed on an ICP-MS, ELEMENT XR (Thermo Fisher Scientific, Bremen, Germany), equipped with an auto sampler SC-E2 DX (Elemental Scientific, Omaha, USA).

A 10 µl buffer probe was diluted in 50 mL of 2% HNO_3 (pH = 2) and measured on general Fe^{56} content at medium resolution (MR), with the following source parameters: cool gas, 16.00 L/min; sample gas, 1.161 L/min; Faraday deflection, -217 V; plasma power, 1250 W; peristaltic pump speed, 10 rpm; torch X-Pos., 1.9 mm; torch Y-Pos., 0.8 mm; torch Z-Pos., -5.0 mm. High-purity argon (99.999%), glass spray chamber, quartz-injector and Pt-sample cone were used throughout the study. All calibration solutions, blank and samples were supplemented with 2% HNO_3 to set pH = 2 prior to ICP-MS analysis.

To monitor changes occurring within the mediator layer from scan to scan and for various sensor designs, Fe^{56} amounts were collected for all CV and AM buffer probes (see Table S10 and Table S11, Appendix C). The accuracy of ICP-MS quantification was verified by calculating the recoveries between the determined and expected concentration values.

5.2.3. Results and discussion

5.2.3.1. Voltammetric behaviour of glucose biosensors

According to the procedure previously reported in [77], the influence of the scan rate on the sensors' topology was initially verified by scanning biosensors in the buffer solution at the potential range from -0.5 V to +0.5 V at 10, 20 and 50 mV/sec sweep rates. The fresh biosensor (containing GOx from Stock B) was used each time the new scan rate was applied and the probes collected after the measurements were further analysed by liquid chromatography tandem mass spectrometry (LC-MS/MS) and inductively coupled plasma mass spectrometry (ICP-MS). The equal linear increase in the current response following the increase in the scan rate was obtained for both "two" and "four" layer types of glucose biosensors (Figure 61A), although the distinct changes were made in layer-by-layer assembly and membrane compositions. Moreover, no significant differences for the peak potential (Figure 61C) and peak current (Figure 61D) shifts between oxidation and reduction curves were detected. The similar membrane diffusion properties were estimated by scanning the same "two" and "four" layer glucose biosensors in the phosphate buffer containing 0.01 M potassium ferricyanide at 10, 20, 50, 70 and 100 mV/sec (Figure 61B).

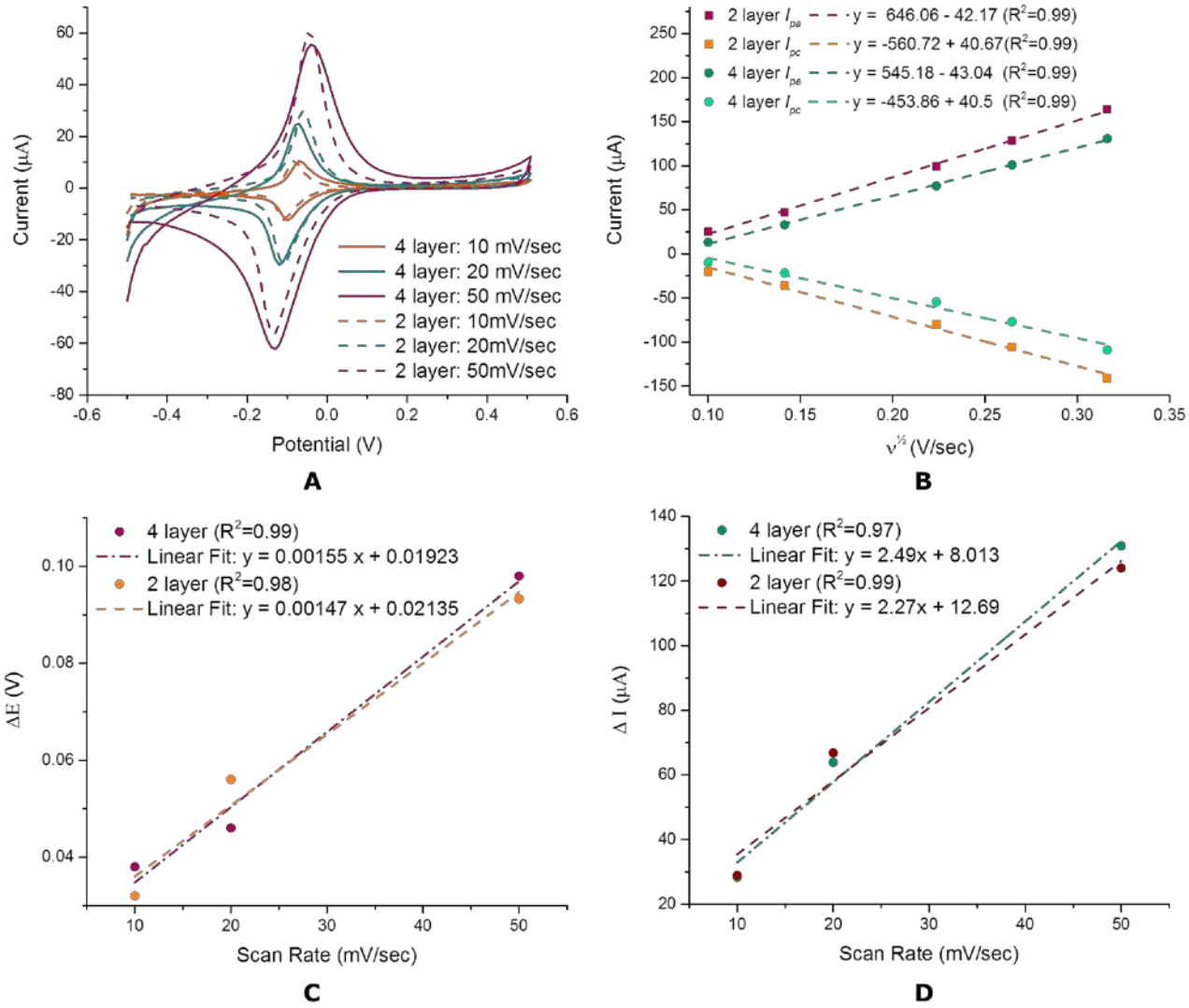

Figure 61 – Results of cyclic voltammetry studies for "two" and "four" layer glucose biosensors (Stock B). The cyclic voltammograms were obtained in phosphate buffer at low scan rates (using a new biosensor per new scan value) in A. The recorded difference of peak potential (*ΔE*, V) and peak current (*ΔI*, μA) values *vs*. scan rates are summarized in graph C and D, respectively. The anodic (I_{pa}) and cathodic (I_{pc}) peak current values *vs*. the square root of the scan rates (B) are presented for the glucose biosensors scanned from 10 to 100 mV/s in the presence of 0.01 M potassium ferricyanide.

5.2.3.2. Glucose and oxygen tandem monitoring

In order to identify the difference in the biorecognition mechanism between two types of glucose biosensors, the tandem monitoring approach was proposed. The chronoamperometric studies were performed for "two" and "four" layer glucose biosensors in the analytical range of glucose concentrations from 0.1 to 2 mM. Moreover, the detection limits and sensitivity were compared for "four" layer glucose biosensors containing immobilized glucose oxidase from different stock solutions (Stock A, Stock B). The linear response of the biosensors is demonstrated in Figure 62.

Note that *4*layer Stock A* glucose biosensor has been previously characterized and the results presented in the graph correspond to the second calibration made three months later.

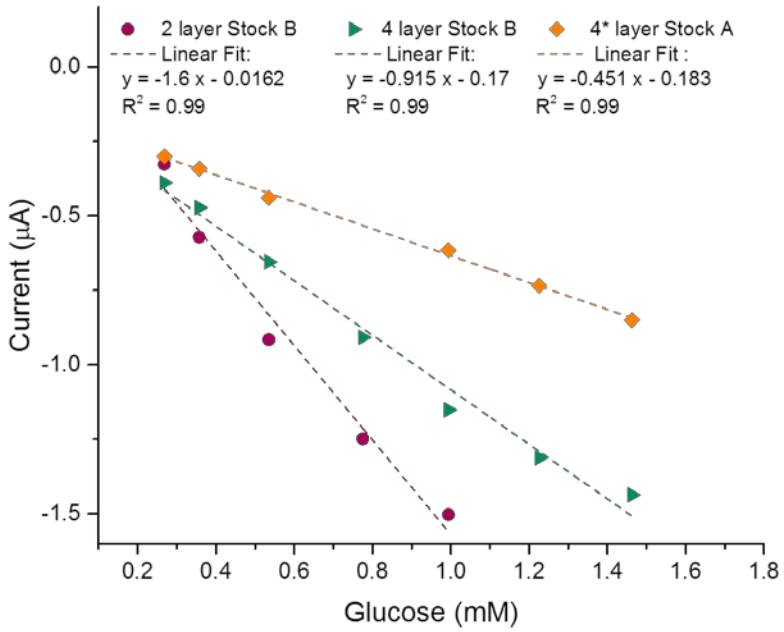

Figure 62 – Calibration curves obtained for "two" and "four" layer biosensors in the presence of glucose. The current response is plotted towards the glucose concentration and correspond to the first calibration for *2 layer Stock B* and *4 layer Stock B* and second calibration (after 3 months) for *4*layer Stock A* glucose biosensors. The relative standard deviation (RSD) is not shown due to the low values (RSD = 9%).

From Figure 62 it is clear that the sensitivity (slope value) and detection limits (glucose concentration range) significantly varied between the sensors. Although, "two" layer glucose biosensors showed a higher sensitivity (-1.6 µA/mM ± 0.13) with respect to both "four" layer sensors based on the GOx stock A (-0.451 µA/mM ± 0.01) and stock B (-0.915 µA/mM ± 0.05) solutions, the glucose detection limit is below a 1 mM concentration. Moreover, "four" layer glucose biosensors have a lower standard deviation (between 0.01 - 0.05 µA/mM) and the sensors with immobilized GOx from stock A were able to work with a broader range of glucose concentrations (Figure 64B).

The analysis of the oxygen consumption rates obtained within tandem monitoring allowed explaining the variation in the biosensors' response. The microsensor first applied for real time measurement of oxygen conversion rates in the liquid phase of different glucose concentrations during the reaction with GOx from Stock A and Stock B immobilized on the surface of the above mentioned biosensors. From Figure 63A we can easily see that for Stock B based biosensors the increase of the oxygen consumption follows the increase in glucose concentration, however the oxygen deficit observed at 1 mM (see Table S9, Appendix C) explains the limited detection range for "two" layer glucose biosensors. Moreover, the presence of the additional membrane films in the "four" layer biosensors prevent GOx from direct contact with higher glucose content and, although

the level of the dissolved oxygen for Stock B based enzymes is already low inside the droplet at 0.8 mM (see Table S9, Appendix C), these biosensors are capable to work in a broader range of concentrations. Therefore, it was interesting to compare the behaviour of "four" layer biosensors with immobilized GOx that showed different activity in the free enzyme stock solutions. The biosensors based on Stock A solution, where the free enzyme showed almost 63 % less activity in respect to Stock B, maintained both the dissolved oxygen and the conversion rate in the droplet constant (see Table S9, Appendix C). Moreover, comparing the activity of the free enzyme in the solution over PB modified SPEs and inside the "four" layer biosensors (Stock B) as shown in Figure 63B, a significant decrease is obtained after immobilization. However, the oxygen deficit in the reaction of the free enzyme solution was registered already at 0.5 mM glucose concentration (see Table S8, Appendix C) which again resulted in a higher slope value and limited detection range (see Figure S12B, Appendix C) of PB modified SPEs. This finding obtained with tandem monitoring is crucial because it allows understanding the principles of the biorecognition mechanism of glucose biosensors from inside together with the simple visualization and quantification of the correlations between system parameters.

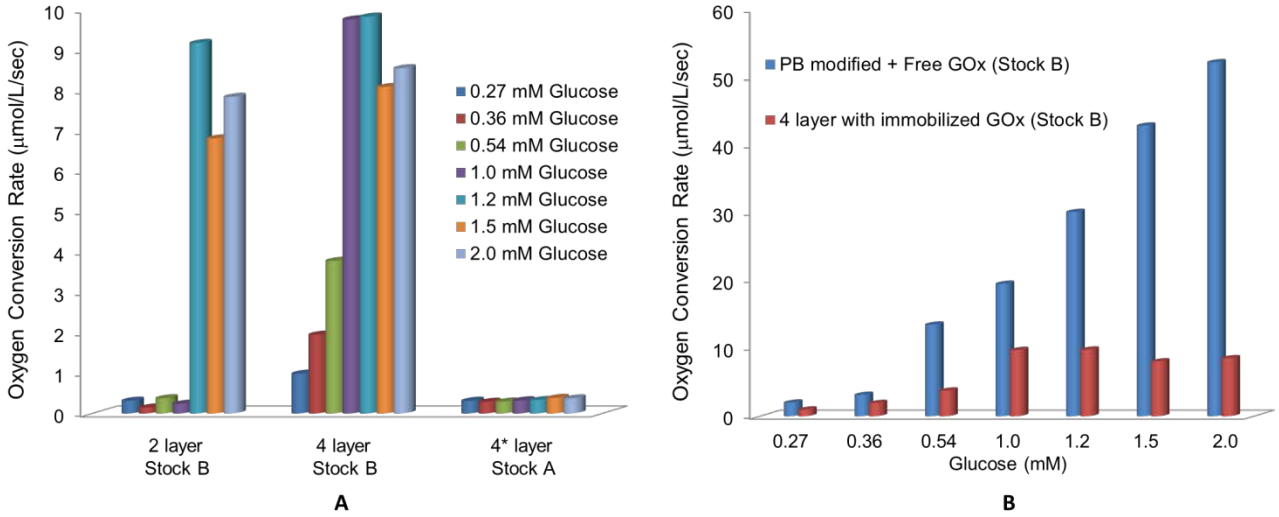

Figure 63 – Comparison of the oxygen conversion rates obtained at different glucose concentrations (0.27-2 mM) for various glucose biosensors (A) and PB modified SPEs (B) after addition of glucose oxidase solution (Stock B).

Furthermore, the first and second calibration curves made right after preparation of "four layer" glucose biosensors (based on GOx Stock A solution) and after three months are presented in Figure 64B. No major differences in the biosensor sensitivity was obtained between the first (-0.163 µA/mM ± 0.004) and second calibrations (-0.175 µA/mM ± 0.009). The significant increase of the intercept value after the first biosensor characterization can be attributed to the loss of the Prussian Blue registered during cyclic voltammetry studies (Figure 64A). Since PB is involved in the reaction of the hydrogen peroxide degradation, the content of the probes collected after CV and AM measurements was analyzed with respect to iron elution in the following section 5.2.3.3.

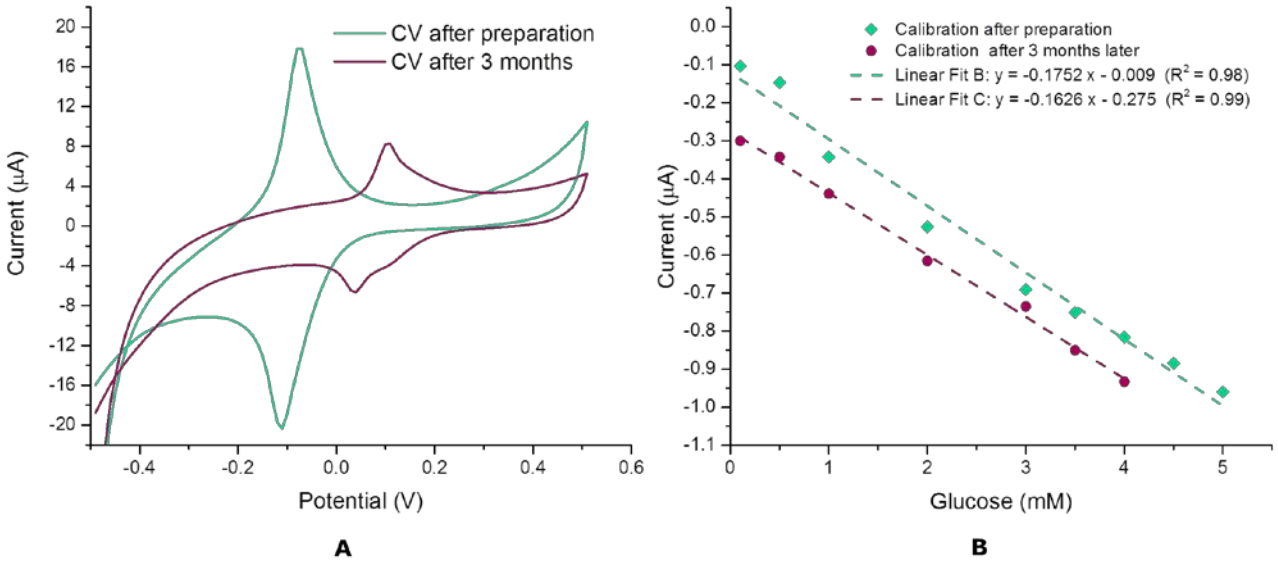

Figure 64 – Cyclic voltammograms (A) and calibration curves (B) obtained for a "four" layer glucose biosensor (Stock A) immediately after preparation and three months later. The CVs were registered in phosphate buffer at 20mV/sec scan rate prior to AM characterization. The chronoamperometric response was plotted against the analytical range of glucose concentrations from 0.1 to 5 mM.

5.2.3.3. The effect of operating conditions on the iron elution and biosensor response

As an initial step, the content of the buffer probes collected after cyclic voltammetry was evaluated for the presence of Fe^{56} ions by means of inductively coupled plasma mass spectrometry (ICP-MS). The obtained results are summarized in Figure 65. Comparing the behavior of glucose biosensors at the first CV scans registered at different scanning speeds (Figure 65B), the Fe^{56} elution remains approximately constant for the "four" layer sensors regardless the scan speed. On the other hand, summarizing the overall iron content obtained for the same period of time (approx. 202 sec) the potential was varied between -0.5 to +0.5 V at different scan rates (Figure 65A), the PB layer showed a better stability for "two" layer glucose biosensors. The impact of the number of scans on the mediator (PB) layer stability is presented for "two" and "four" layer biosensors in Figure 65C and Figure 65D, respectively. Regardless the biosensor design, with increased number of scans a higher overall iron content was obtained in buffer probes. The optimal scan rate that minimizes the mediator loss for both the "two" and the "four" layer biosensor is 20 mV/sec.

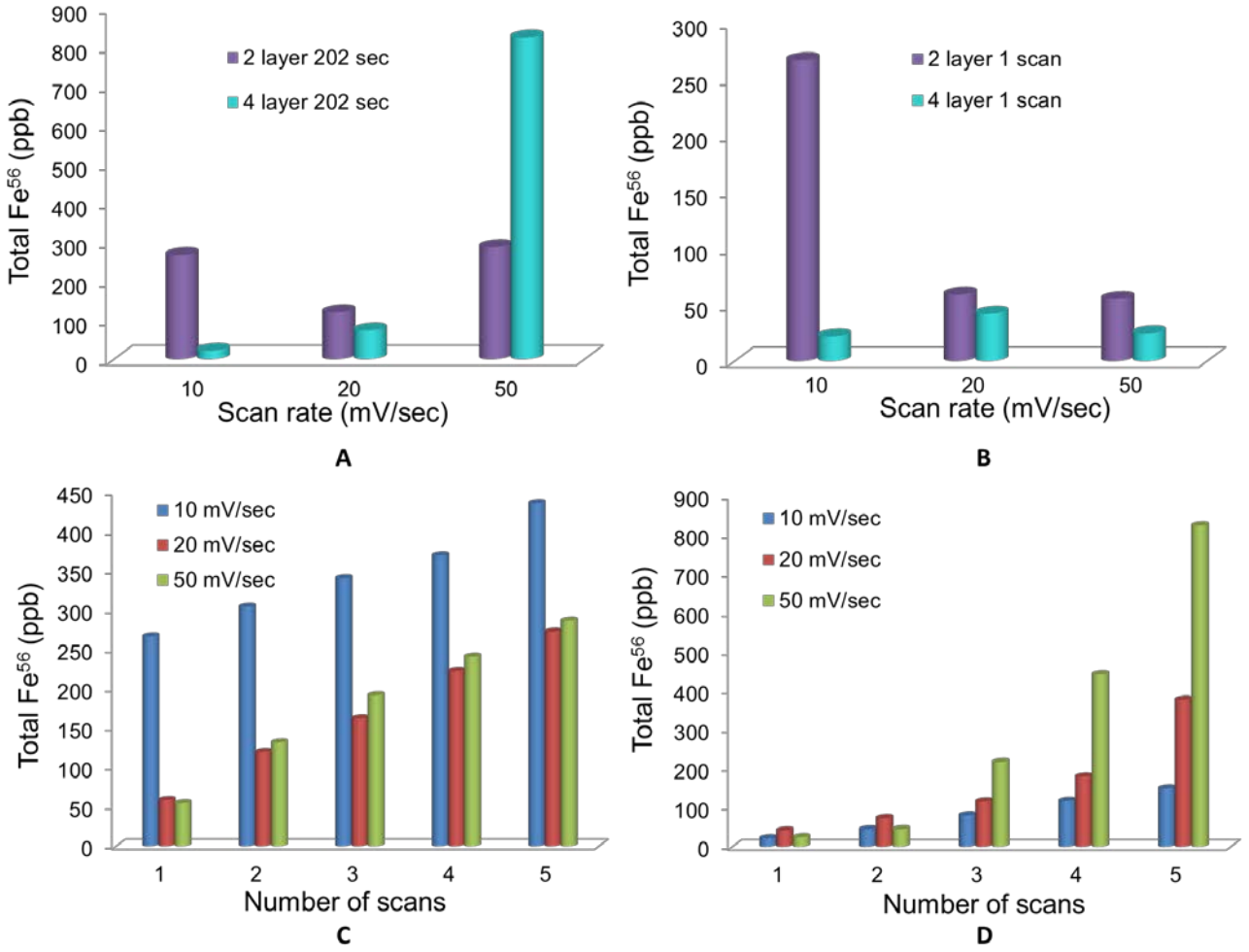

Figure 65 – Comparison of the Fe^{56} elution during cyclic voltammetry for "two" and "four" layer glucose biosensors. The impact of different scan rates on the Fe^{56} leakage is summarized for the first scans (A) and for an equal amount of time (B) the potential was varied. The effect of the number of scans for various speeds is shown for two" and "four" layer glucose biosensors in graphs C and D, respectively. The relative standard deviation (RSD) is not shown due to the low values (RSD = 2%).

The iron content of the AM probes collected after characterization with glucose of the "two" layer glucose biosensors (Stock B) previously studied at different scan rates (10 and 20 mV/sec) in cyclic voltammetry was identified using ICP-MS. In Figure 66A it is shown that, similar to the results presented in Figure 62, with higher glucose concentration the absolute current value is increased and the sensors detection range is below 1 mM glucose concentration (Figure 66C). Moreover, for both biosensors the equal voltammetric behaviour of Prussian Blue films (Figure 66D) measured prior to AM characterization resulted in quantitatively similar calibration curves. The increase of the iron content inside the probes at 1 mM concentration (Figure 66B) could be related to a higher amount of the peroxide produced during the oxidation of higher concentrations of glucose. However, the limited detection range and subsequent decrease in the iron elution rate for glucose solutions above 1 mM concentration indicates that the enzyme reaches the oxygen deficit phase.

The overall iron loss for both biosensors during chronoamperometric characterization was between 273-298 ppb (see Table S11, Appendix C).

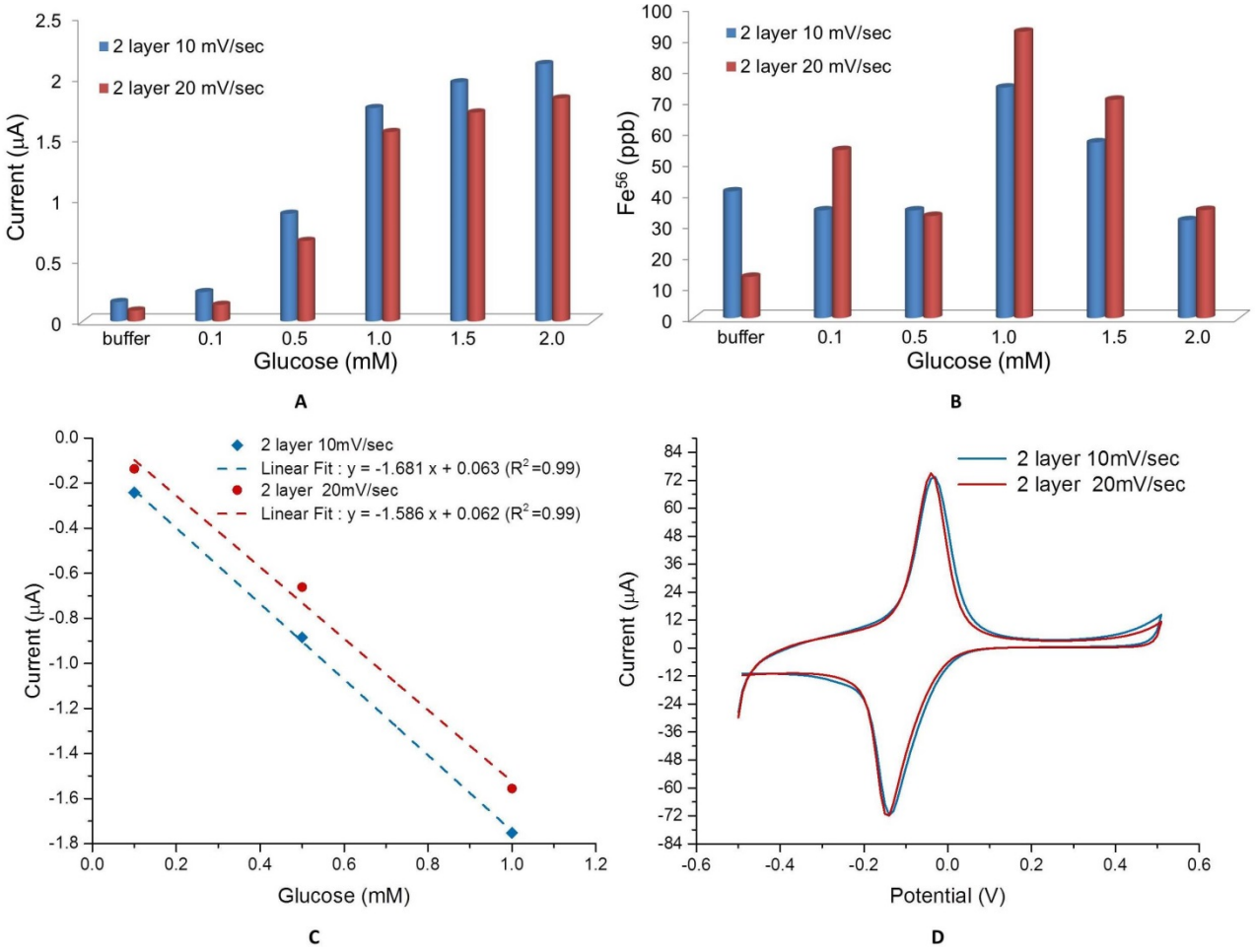

Figure 66 – The results of the chronoamperometric studies (A) and ICP-MS analysis (B) for "two" layer glucose biosensors previously characterized at 10 and 20 mV/sec scanning speed. The linear and chronoamperometric response was plotted in C against the analytical range of glucose concentrations from 0.1 to 2 mM. The CVs presented in D were registered at 10 mV/sec prior to AM characterization.

5.2.3.4. The effect of operating and preparation conditions on membrane stability

Similar to the procedure previously reported in [77], the buffer probes collected after CV studies of "two" and "four" layer glucose biosensors as described in section 5.2.3.1. were analyzed for their Nafion content using liquid chromatography electrospray ionization tandem mass spectrometry (LC-ESI-MS/MS). The results obtained in mass spectra, total ion chromatograms (TICs) and extracted ion chromatograms (EICs) are summarized in Figure 67 for characteristic perfluorinated carboxylic acid fragments [166], namely $CF_3(CF_2)_5CHFCOO^-$ and $CF_3(CF_2)_6CHFCOO^-$ peak areas detected at *m/z* equal to 394.9758 and 444.9725, respectively. In comparison with the non-used biosensor tested in a steady state experiment with a water droplet, the glucose biosensors used in

cyclic voltammetry studies possess a higher membrane stability especially in case of the "four" layer sensors, as shown in Figure 67A.

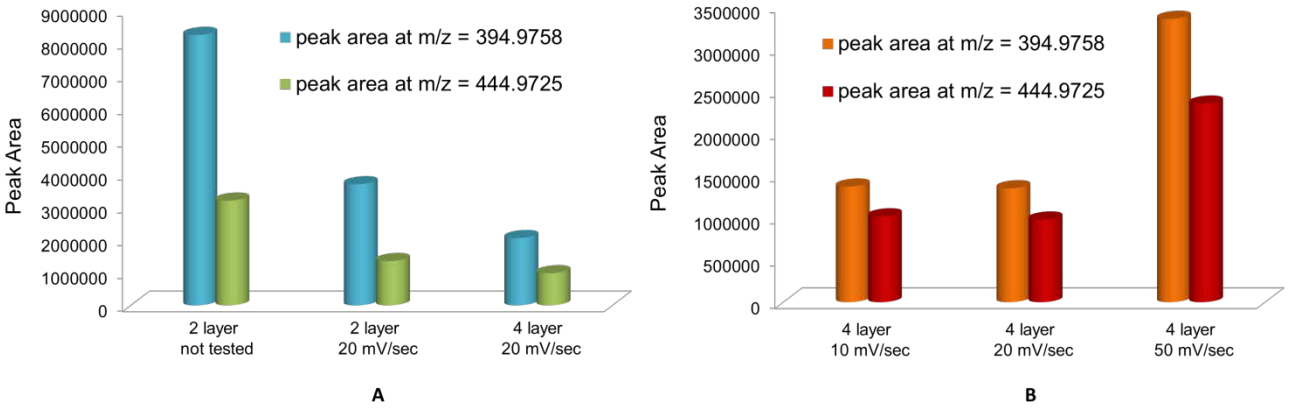

Figure 67 – The impact of the scan rate on the stability of the membrane layer. The mass spectra results were summarized for probes collected after first scans and correspond to peak areas of perfluorinated $CF_3(CF_2)_5CHFCOO^-$ and $CF_3(CF_2)_6CHFCOO^-$ carboxylic acid fragments registered at m/z equal to 394.9758 and 444.9725, respectively. The influence of the equal scan rate (20 mV/sec) on "two" and "four" layer biosensors is shown in A. The effect of different scan rates on the "four" layer biosensors is presented in B.

In contrast to previously characterized "two" layer sensors [77], no significant influence of the number of scans on the membrane stabilization was obtained for "four" layer glucose biosensors (data not shown). The role of the scanning speed on the Nafion elution rate for "four" layer biosensors was summarized in Figure 67B. Regardless the biosensor composition, the lower scanning speed, namely 20 mV/sec, allows faster stabilization of the membrane layer during cyclic voltammetry studies.

The architecture of "four" layer glucose biosensors was confirmed in the subsequent SEM/EDX studies presented in Figure 68. From the obtained results, it is clear that the double deposition of 2% Nafion coatings over the enzymatic layer yielded the formation of one uniform membrane film (Figure 68A,B). Moreover, the Nafion layer remains fixed on top of the glucose oxidase surface after performing cyclic voltammetry and chronoamperometric measurements (Figure 68C,D).

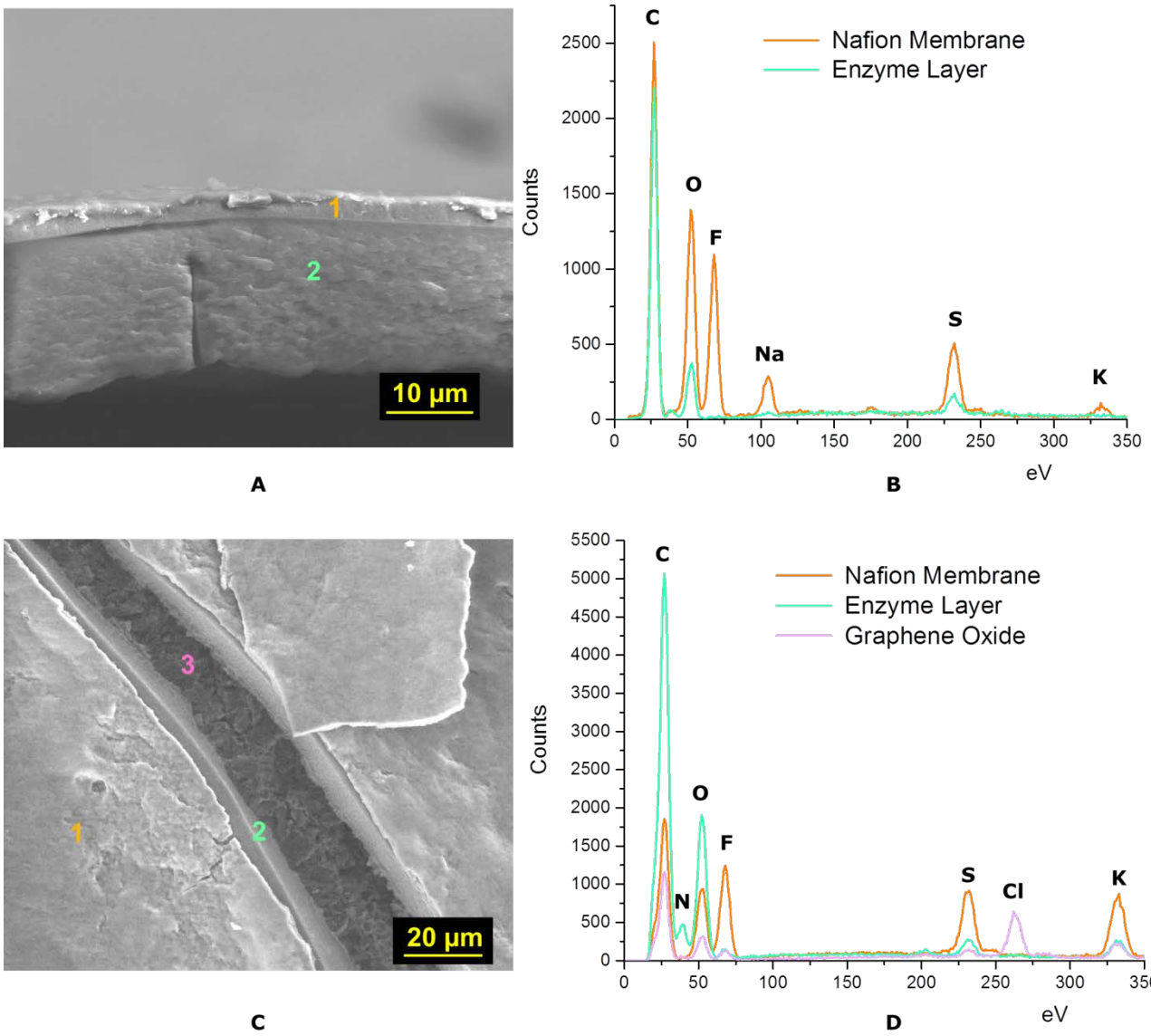

Figure 68 - SEM images (A,C) and EDX spectra (B,D) of the "four" layer glucose biosensor layers. The enzyme (1) and membrane (2) layers are shown in cross-section in A for a non-tested "four" layer glucose biosensor. The corresponding EDX spectra are presented in B. The top view of the membrane (1), enzyme (2) and graphene oxide (3) layers are enlarged in C for the glucose biosensor characterized in CV and AM. The corresponding EDX spectra are presented in D.

Numerous membrane cracks registered under vacuum in SEM on the surface of both tested and not tested "two" (Figure 53C) and "four" (Figure 68C) layer glucose biosensors were further investigated using environmental scanning electron microscopy (ESEM). The membrane swelling of the wetted glucose biosensors was confirmed in dynamic conditions at different temperatures by varying the water vapor pressure inside the ESEM chamber. The obtained results are summarized in Figure 69.

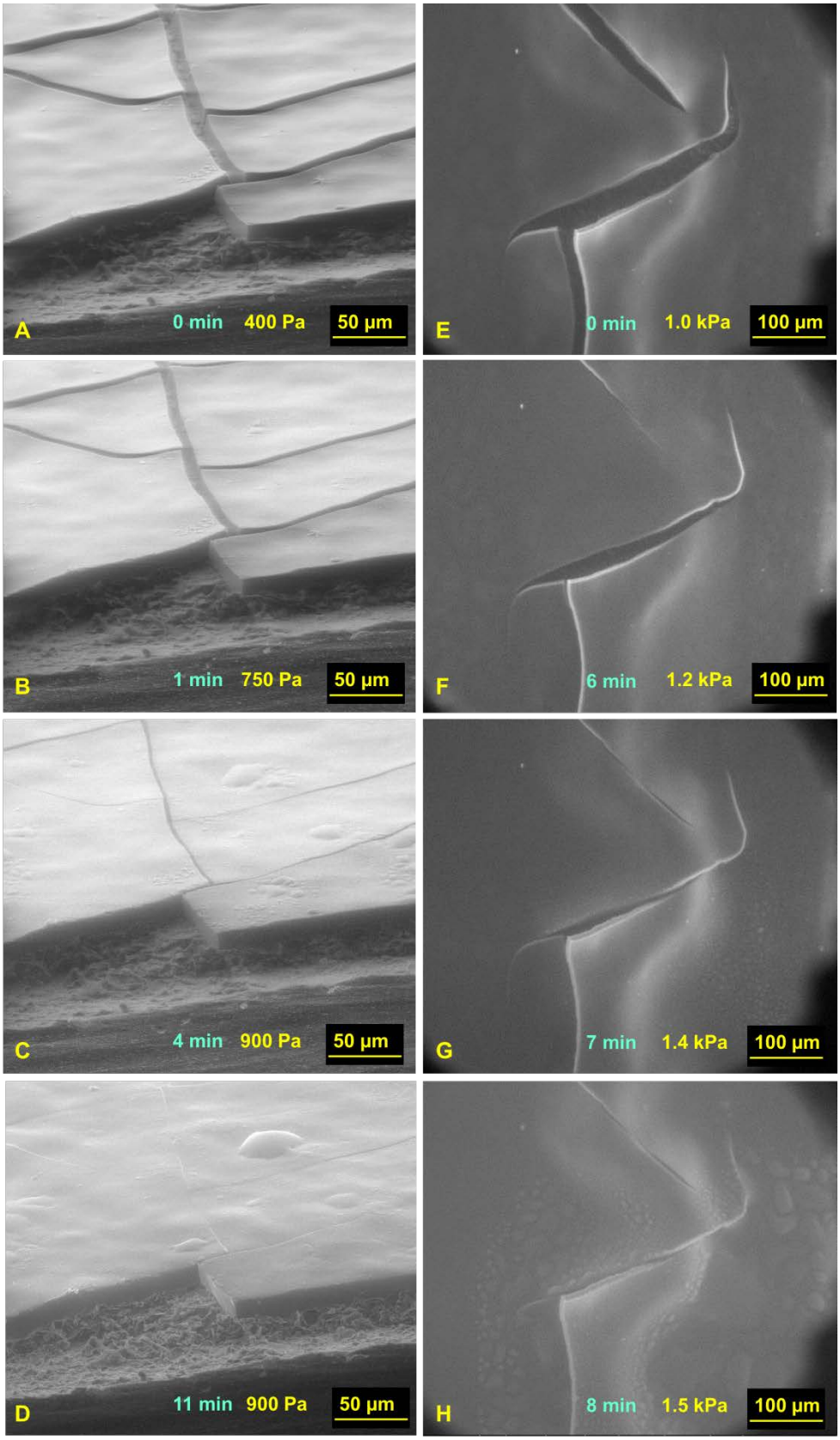

Figure 69 - ESEM images of the top surfaces of "two" (A-D) and "four" (E-H) layer glucose biosensors. The images illustrate the dynamics of the membrane cracks swelling at various experimental conditions.

The formation of water droplets on top of the biosensor layers is visible in Figure 69C,D and Figure 69G,H. Thus, the ESEM analysis demonstrated that the cracks observed in the enzyme and/or membrane films would transform to the monolayer being in contact with water-based analyte solutions. Moreover, the merit of the experimental conditions chosen for the membrane layer formation was evaluated for "two" layer glucose biosensors. Therefore, we have analyzed the sensors where the enzyme membrane layer was dried at 20°C (approx. 70% humidity) and 8°C (40% humidity maintained in the climate chamber) for 15 min and 12 hours, respectively. The results obtained *via* multi-analytical studies are summarized in Figure 70.

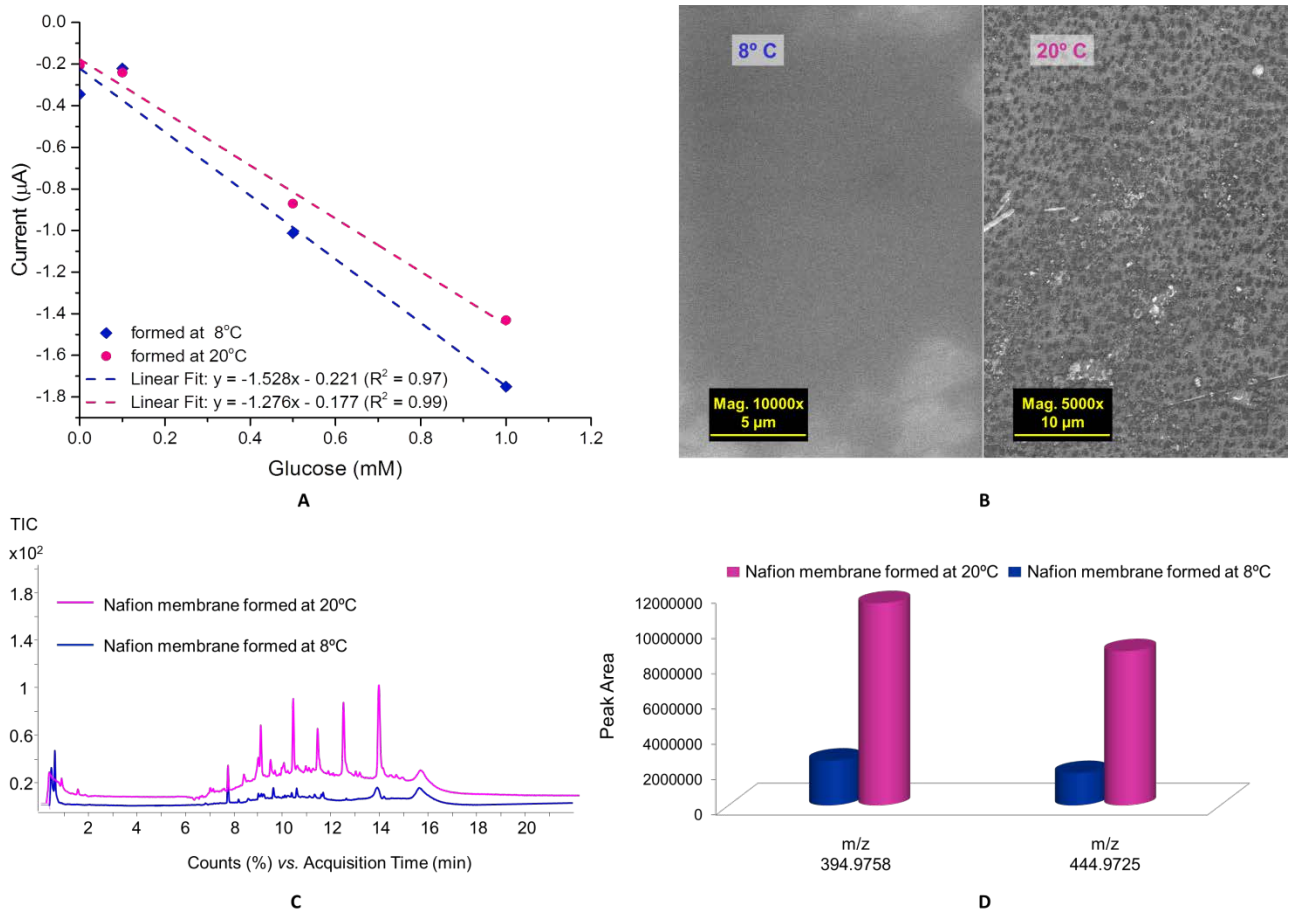

Figure 70 – The results of the multi-analytical analysis of "two" layer glucose biosensors (enzyme/membrane layer formed at 8°C or 20°C). The linear current response towards glucose is presented in A. SEM images of the enzyme/membrane (top view) were enlarged in B. The total ion chromatograms (TICs) registered for the Nafion content in buffer probes collected after CV measurements performed at 10 mV/sec are plotted in C. The EIC mass spectra results shown in D correspond with peak areas of perfluorinated $CF_3(CF_2)_5CHFCOO^-$ and $CF_3(CF_2)_6CHFCOO^-$ carboxylic acid fragments registered at m/z equal to 394.9758 and 444.9725, respectively.

Although no significant difference in the sensitivity and detection range between two biosensors was observed after first calibration (Figure 70A), the subsequent chronoamperometric studies with glucose resulted in a strong deviation of the biosensor response when the membrane was formed at 20°C (data not shown). It was confirmed in further analysis of the membrane layers by SEM

(Figure 70B) and buffer probes in LC-ESI-MS/MS tandem (Figure 70C,D) that mild drying conditions, namely 8ºC and 40% humidity maintained in a climate chamber, allow a uniform layer formation that is better fixed on the surface of the biosensor.

5.2.4. Conclusions and perspectives

The analytical approach for simultaneous multiple-substrate monitoring for biosensors in a droplet was developed. The presented methodology was validated for the first generation glucose biosensors with different layer-by-layer assembly in the presence of glucose. The results obtained *via* combined chronoamperometric characterization and oxygen monitoring were independently confirmed by the subsequent morphological studies. The specific protocols developed for detection of oxygen conversion, iron and Nafion elution rates inside the biosensor system allowed identifying a more favorable structure and operating conditions of the biosensors for continuous monitoring. Moreover, it was shown that the variation of the immobilized enzyme activity, additional membrane films and experimental conditions for the layer formation can significantly improve the lifetime and the detection range of the biosensors. Although the sensitivity of the "four" layer glucose biosensors was decreased, the presence of the individual enzymatic and Nafion coatings allowed to enhance the overall biosensor stability (up to 3 months) and to extend the linear detection range by up to a factor of five in comparison with the "two" layer glucose biosensors. Thus, the developed methodology can be applied for time effective design optimization of amperometric biosensors based on the oxygen dependent processes.

Chapter 6: Conclusions and future perspectives

The research presented in this thesis aimed at the development of mechanistic models for the evaluation of the biocatalytic reaction conditions inside microbioreactors (μBRs) and for amperometric biosensor design optimization. Therefore, novel tools, approaches and workflow schemes presented throughout the thesis were developed in order to meet the research objectives. Despite of all intensive progress in the field of miniaturized bioreactors and electrochemical biosensors, one of the significant challenges during this PhD project was the lack of the relevant and sufficient experimental data available in the literature. Therefore, the role of performing a substantial number of experiments supported by multi-analytical analysis and validation of the obtained results was emphasized throughout the thesis, in order to guarantee the accuracy of the proposed models at miniaturized scale.

In Chapter 2 a mechanistic model for biocatalyst screening purposes (glucose oxidase/catalase cascade reaction) was developed for a commercially available microreactor with integrated oxygen sensors. The model demonstrated itself as a time-effective tool in getting better insights into the reaction mechanism (mechanism structure determination), and for developing an improved understanding of the correlations between the system parameters (oxygen sensor signal shift), and finally also for kinetic rate constants estimation. The identified mechanism structure and kinetic constants were independently confirmed in μL- and mL- scale experiments. Moreover, the further evaluation of the reaction conditions in an ideally mixed mL-scale reactor with subsequent validation inside the μBR proposed the use of hydrogen peroxide for more effective *in situ* oxygen generation inside the microchannels.

In Chapter 3, for direct continuous monitoring of glucose consumption rates, a flexible microfluidic platform with integrated amperometric glucose biosensors was developed. The presented platform exhibits a multi-functional capability using a simple design, standard connectors and low-cost materials, and potentially can be connected in a "plug-and-play" mode to other μBRs. Moreover, the platform may be further applied to different sensing technologies (e.g. optical, magnetic), due to the presented flexibility in terms of sensor formats that can be incorporated, as well as the ease of assembly and the possibility for re-use of both the platform and the sensors. The integrated mixing/dilution chamber inside the platform allowed performing dilutions up to 10 times, even at high flow rates, adjusting the sample concentrations to the sensor's detection range. The obtained deviation in the sensor response during static (droplet) and dynamic (flow) measurements resulted in the development of a mechanistic model for the first generation glucose biosensors in Chapter 4.

A novel approach for the improvement of mechanistic models has been presented, and relies on combining the fundamental principles and the results of electrochemical and morphological studies. The mathematical model was developed to reproduce the cyclic voltammetry response of glucose biosensors operating in aerobic conditions in the absence of glucose at low scan rates. The system parameters required for numerical simulations were either found in the literature or estimated based on experimental data, and therefore the model was validated for various biosensor designs, namely different deposited mediator loadings and enzyme/membrane film compositions. Moreover, it was demonstrated that combining the results of multi-analytical studies together with mechanistic modeling is an effective approach in identifying the key parameters of the biosensor system crucial for optimal biosensor operation and design.

The proposed biosensor composition (*sensor 3* batch), proven to be stable at various operating conditions in Chapter 4, underwent further optimization coupled with thorough electrochemical and morphological studies in Chapter 5. Moreover, a novel analytical procedure for simultaneous multiple-substrate monitoring for biosensors in a droplet was developed. The presented tandem approach was based on chronoamperometric characterization of the biosensors in the presence of analyte (glucose) coupled with oxygen monitoring using an optical microsensor. Furthermore, the specific protocols were developed for detection of oxygen conversion, iron and Nafion elution rates inside the biosensor system. The study presented in Chapter 5 allowed identifying a more favorable composition and operating conditions of the biosensors that would significantly improve the lifetime and the detection range for the purpose of continuous monitoring.

As a future work, for the optimized design of the glucose biosensor, the developed cyclic voltammetry model should be further extended to describe the mediated enzymatic reaction of glucose oxidase in the presence of glucose. Combining such model with global sensitivity and uncertainty analysis tools will allow mapping the influence of the complete set of system input parameters on the biosensor response [185]. Although all presented case studies were related to a well-characterized biocatalyst – glucose oxidase, it is clear that with the help of mechanistic models a lot of interesting findings and observations were made regarding the combination of experimental conditions and system parameters, and especially their effect on the overall reaction kinetics and biosensor performance. The practical merit of the presented work is in the development of time and cost effective tools and procedures crucial for experimental and biosensor design optimization that potentially could allow reducing reagent usage and waste generation. In order to support a time-effective model development and validation, the web-based data tools for the research in biosensors, microfluidics and related scientific fields should be created. Such tools, similar to online databases SciFinder® [186] and Reaxys® [187] built to improve research in chemistry, could provide an easy access to experimentally measured data (i.e. reactions, physical and/or chemical properties) in one universal platform. Moreover, the data-based tools could significantly speed up the progress in biosensors and microfluidics due to the constant upgrade of the current state-of-the art research.

The greatest undersea explorer and conservationist of the 20th century Jacques Yves Cousteau defined the scientist as "a curious man looking through a keyhole, the keyhole of nature, trying to know what's going on". Working with microfluidics and biosensors, we are significantly narrowing the size of this "keyhole" which helps to focus on individual system interactions and mechanisms and understand better the underlying fundamental principles. But at the same time, such a "limited overview" makes it difficult to immediately appreciate the overall benefits of the proposed technologies and allow their further integration for bigger scale processes. In the past decades various miniaturized reactors with integrated mixers, optical and electrochemical sensors, pH and dissolved oxygen control were proposed and/or validated for bio-based processes [20,188–193]. Moreover, the mathematical approaches were developed and applied for bioprocess intensification inside microbioreactors [194] including topology [195,196] and enzyme distribution [197] optimization. However, the further promoting of μBRs for more efficient screening and scale-up in biotechnology is limited due to the lack of process knowledge. In order to improve the understanding of the bio-based processes inside the miniaturized systems, it is required to focus on the development and integration of:

1) reliable on-line (bio)sensors;

2) data analysis tools using computational intelligence;

3) mechanistic process models.

The workflow presented in the current thesis eventually leads to the design of "software sensors" [198–202]. Such model-based state and parameter estimators associate the sensor (hardware) with a mathematical algorithm (software) in order to provide reliable on-line information about unmeasurable variables of interest. Moreover, the model-based design and automation of experiments inside μBRs would allow the most optimal way of reaction performance [203]. Development of the "software sensors" for miniaturized systems is an adequate solution fulfilling the requirements of the measurement, monitoring, modeling and control (M3C) strategies in biotechnology and biotechnology-based production.

References

[1] S.T. Sharfstein, Biotechnology, Ref. Modul. Life Sci. (2017) 809633. doi:10.1016/B978-0-12-809633-8.12382-9.

[2] Z. Zhang, G. Perozziello, P. Boccazzi, A. Sinskey, O. Geschke, K. Jensen, Microbioreactors for Bioprocess Development, J. Assoc. Lab. Autom. 12 (2007) 143–151. doi:10.1016/j.jala.2006.10.017.

[3] Y. Asano, S. Togashi, H. Tsudome, S. Murakami, Microreactor technology: Innovations in production processes, Pharm. Eng. 30 (2010) 1–9. doi:10.1016/j.ces.2007.09.021.

[4] F. Von Stetten, D. Mark, S. Haeberle, Microfluidic lab-on-a-chip platforms: requirements, characteristics and applications, Chem.Soc.Rev. 39 (2010) 1153–1182. doi:10.1039/b820557b.

[5] R. Wohlgemuth, I. Plazl, P. Znidarsic-Plazl, K. V. Gernaey, J.M. Woodley, Microscale technology and biocatalytic processes: Opportunities and challenges for synthesis, Trends Biotechnol. 33 (2015) 302–314. doi:10.1016/j.tibtech.2015.02.010.

[6] H.M. Hegab, A. ElMekawy, T. Stakenborg, Review of microfluidic microbioreactor technology for high-throughput submerged microbiological cultivation, Biomicrofluidics. 7 (2013) 1–14. doi:10.1063/1.4799966.

[7] X. Yao, Y. Zhang, L. Du, J. Liu, J. Yao, Review of the applications of microreactors, Renew. Sustain. Energy Rev. 47 (2015) 519–539. doi:10.1016/j.rser.2015.03.078.

[8] M.C. Nicoletti, L.C. Jain, eds., Computational Intelligence Techniques for Bioprocess Modelling, Supervision and Control, Springer, Berlin, Heidelberg, 2009. doi:10.1007/978-3-642-01888-6.

[9] C. Mandenius, N.J. Titchener-Hooker, eds., Measurement, Monitoring, Modelling and Control of Bioprocesses, Springer Berlin Heidelberg, Berlin, Heidelberg, 2013. doi:10.1007/978-3-642-36838-7.

[10] G. Sin, J.M. Woodley, K. V Gernaey, Application of modeling and simulation tools for the evaluation of biocatalytic processes: a future perspective., Biotechnol. Prog. 25 (2009) 1529–38. doi:10.1002/btpr.276.

[11] K. V. Gernaey, A.E. Lantz, P. Tufvesson, J.M. Woodley, G. Sin, Application of mechanistic models to fermentation and biocatalysis for next-generation processes., Trends Biotechnol. 28 (2010) 346–54. doi:10.1016/j.tibtech.2010.03.006.

[12] R.L. Fernandes, V.K. Bodla, M. Carlquist, A.-L. Heins, A.E. Lantz, G. Sin, K. V. Gernaey, Applying Mechanistic Models in Bioprocess Development, in: Adv Biochem Eng Biotechnol, ? Springer, 2013: pp. 137–166. doi:10.1007/10.

[13] P. Pandey, R. Bharadwaj, X. Chen, Modeling of drug product manufacturing processes in the

pharmaceutical industry, Elsevier Ltd, 2016. doi:10.1016/B978-0-08-100154-7.00001-6.

[14] A. Velayudhan, Overview of integrated models for bioprocess engineering, Curr. Opin. Chem. Eng. 6 (2014) 83–89. doi:10.1016/j.coche.2014.09.007.

[15] L. Mears, S.M. Stocks, M.O. Albaek, G. Sin, K. V. Gernaey, Application of a mechanistic model as a tool for on-line monitoring of pilot scale filamentous fungal fermentation processes—The importance of evaporation effects, Biotechnol. Bioeng. 114 (2017) 589–599. doi:10.1002/bit.26187.

[16] L. Mears, S.M. Stocks, M.O. Albaek, B. Cassells, G. Sin, K. V. Gernaey, A novel model-based control strategy for aerobic filamentous fungal fed-batch fermentation processes, Biotechnol. Bioeng. 114 (2017) 1459–1468. doi:10.1002/bit.26274.

[17] G.M. Whitesides, The origins and the future of microfluidics, Nature. 442 (2006) 368–373. doi:10.1038/nature05058.

[18] S. Kakaç, B. Kosoy, D. Li, A. Pramuanjaroenkij, Microfluidics based microsystems: fundamentals and applications, 2009. doi:10.1007/978-90-481-9029-4.

[19] D.T. Chiu, A.J. deMello, D. Di Carlo, P.S. Doyle, C. Hansen, R.M. Maceiczyk, R.C.R. Wootton, Small but perfectly formed? Successes, challenges, and opportunities for microfluidics in the chemical and biological sciences, Chem. 2 (2017) 201–223. doi:10.1016/j.chempr.2017.01.009.

[20] R. Krull, S. Lladó-Maldonado, T. Lorenz, S. Demming, S. Büttgenbach, Microbioreactors, in: Microsystems Pharmatechnology Manip. Fluids, Part. Droplets, Cells, 2016: pp. 99–152. doi:10.1007/978-3-319-26920-7.

[21] E. Laurenti, A. dos Santos Vianna Jr., Enzymatic microreactors in biocatalysis: history, features, and future perspectives, Biocatalysis. 1 (2016) 148–165. doi:10.1515/boca-2015-0008.

[22] P.N. Nge, C.I. Rogers, A.T. Woolley, Advances in microfluidic materials, functions, integration and applications, Chem. Rev. 113 (2013) 2550–2583. doi:dx.doi.org/10.1021/cr300337x.

[23] S. Datta, L.R. Christena, Y.R.S. Rajaram, Enzyme immobilization: an overview on techniques and support materials, 3 Biotech. 3 (2013) 1–9. doi:10.1007/s13205-012-0071-7.

[24] R.A. Sheldon, S. van Pelt, Enzyme immobilisation in biocatalysis: why, what and how, Chem. Soc. Rev. 42 (2013) 6223–6235. doi:10.1039/C3CS60075K.

[25] T. Heck, G. Faccio, M. Richter, L. Thöny-Meyer, Enzyme-catalyzed protein crosslinking, Appl. Microbiol. Biotechnol. 97 (2013) 461–475. doi:10.1007/s00253-012-4569-z.

[26] S. Matosevic, G.J. Lye, F. Baganz, Design and characterization of a prototype enzyme microreactor: quantification of immobilized transketolase kinetics., Biotechnol. Prog. 26 (2009) 118–26. doi:10.1002/btpr.319.

[27] R. Fraas, M. Franzreb, Reversible covalent enzyme immobilization methods for reuse of

carriers, Biocatal. Biotransformation. 35 (2017) 337–348. doi:10.1080/10242422.2017.1344229.

[28] M. Cheng, Z. Chen, Screening of tyrosinase inhibitors by capillary electrophoresis with immobilized enzyme microreactor and molecular docking, Electrophoresis. 38 (2017) 486–493. doi:10.1002/elps.201600367.

[29] K. Buchholz, V. Kasche, Wiley-Blackwell, U.T. Bornscheuer, Biocatalysts and enzyme technology, Wiley-Blackwell, 2012.

[30] P.M. Doran, Bioprocess Engineering Principles, Second Edi, Elsevier Ltd., 2013. doi:10.1016/B978-0-12-220851-5.00006-X.

[31] K.D. Nagy, B. Shen, T.F. Jamison, K.F. Jensen, Mixing and dispersion in small-scale flow systems, Org. Process Res. Dev. 16 (2012) 976–981. doi:10.1021/op200349f.

[32] R.B. Bird, W.E. Stewart, E.N. Lightfoot, Transport Phenomena, Second, John Wiley & Sons, Inc., New York, NY, 2002. doi:10.1002/aic.690070245.

[33] K.W. Oh, K. Lee, B. Ahn, E.P. Furlani, Design of pressure-driven microfluidic networks using electric circuit analogy, Lab a Chip Chip. 12 (2012) 515–545. doi:10.1039/C2LC20799K.

[34] N.-T. Nguyyen, S.T. Wereley, Fundamentals and applications of microfluidics, Second, 2006.

[35] J. Judy, D. Maynes, B.W. Webb, Characterization of frictional pressure drop for liquid flows through microchannels, Int. J. Heat Mass Transf. 45 (2002) 3477–3489. doi:10.1016/S0017-9310(02)00076-5.

[36] E.B. Arkilic, M. a. Schmidt, K.S. Breuer, Slip flow in microchannels, Proc. Rarefied Gas Dyn. Symp. (1994) 1–7.

[37] J. Koo, C. Kleinstreuer, Liquid flow in microchannels: experimental observations and computational analyses of microfluidics effects, J. Micromechanics Microengineering. 13 (2003) 568–579. doi:10.1088/0960-1317/13/5/307.

[38] D. Liu, S. V. Garimella, Investigation of liquid flow in microchannels, J. Thermophys. Heat Transf. 18 (2004) 65–72. doi:10.2514/1.9124.

[39] C.Y. Lee, C.L. Chang, Y.N. Wang, L.M. Fu, Microfluidic mixing: A review, Int. J. Mol. Sci. 12 (2011) 3263–3287. doi:10.3390/ijms12053263.

[40] B.H. Chen, E.G. Hibbert, P.A. Dalby, J.M. Woodley, A new approach to bioconversion reaction kinetic parameter identification, AIChE J. 54 (2008) 2155–2163. doi:10.1002/aic.

[41] N. Al-Haque, P.A. Santacoloma, W. Neto, P. Tufvesson, R. Gani, J.M. Woodley, A robust methodology for kinetic model parameter estimation for biocatalytic reactions, Biotechnol. Prog. 28 (2012) 1186–1196. doi:10.1002/btpr.1588.

[42] S. Ferri, K. Kojima, K. Sode, Review of glucose oxidases and glucose dehydrogenases: A bird's eye view of glucose sensing enzymes, J. Diabetes Sci. Technol. 5 (2011) 1068–1076. doi:10.1177/193229681100500507.

[43] M.E.G. Lyons, G.P. Keeley, Carbon nanotube based modified electrode biosensors. Part 1. Electrochemical studies of the flavin group redox kinetics at SWCNT/glucose oxidase composite modified electrodes, Int. J. Electrochem. Sci. 3 (2008) 819–853.

[44] T. Nakamura, Y. Ogura, Studies on the action of glucose oxidase, J. Biochem. 52 (1962) 214–220.

[45] S. Nakamura, Y. Ogura, Action mechanism of glucose oxidase of Aspergillus niger, J. Biochem. 63 (1968) 308–316.

[46] Q.H. Gibson, B.E.P. Swoboda, V. Massey, Kinetics and mechanism of action of glucose oxidase*, J Biol Chem. 239 (1964) 3927–3934.

[47] P. Beltrame, M. Comotti, C. Pina, M. Rossi, Aerobic oxidation of glucose I. Enzymatic catalysis, J. Catal. 228 (2004) 282–287. doi:10.1016/j.jcat.2004.09.010.

[48] H.J. Bright, Q.H. Gibson, The oxidation of 1-deuterated glucose by glucose oxidase*, J. Biol. Chem. 242 (1967) 994–1003.

[49] F.R. Duke, M. Weibel, D.S. Page, V.G. Bulgrin, J. Luthy, The glucose oxidase mechanism. Enzyme activation by substrate, J. Am. Chem. Soc. 91 (1969) 3904–3909. doi:10.1021/ja01042a038.

[50] W.W. Cleland, S. 1mary, The kinetics of enzyme-catalyzed reactions with two or more substrates or products, Biochim. Biophys. Acta. 67 (1963) 104–137. doi:10.1016/0926-6569(63)90211-6.

[51] S. Fukushima, A. Uyama, S. Katayama, Oxygen absorption accompanying enzymatic reaction-oxidation of D-glucose in the presence of glucose oxidase and catalase, J. Chem. Eng. Japan. 11 (1978) 227–233. http://doi.wiley.com/10.1002/bit.260221203.

[52] A. Illanes, Enzyme biocatalysis: principles and applications, Springer Science + Business Media B.V, 2008.

[53] X. Wang, O.S. Wolfbeis, Optical methods for sensing and imaging oxygen: materials, spectroscopies and applications, Chem. Soc. Rev. 43 (2014) 3666–3761. doi:10.1039/C4CS00039K.

[54] S. Sun, B. Ungerböck, T. Mayr, Imaging of oxygen in microreactors and microfluidic systems, Methods Appl. Fluoresc. 3 (2015). doi:10.1088/2050-6120/3/3/034002.

[55] P. Gruber, M.P.C. Marques, N. Szita, T. Mayr, Integration and application of optical chemical sensors in microbioreactors, Lab Chip. 17 (2017) 2693–2712. doi:10.1039/C7LC00538E.

[56] M. Quaranta, S.M. Borisov, I. Klimant, Indicators for optical oxygen sensors, Bioanal. Rev. 4 (2012) 115–157. doi:10.1007/s12566-012-0032-y.

[57] J.R. Lakowicz, Principles of fluorescence spectroscopy, Third Ed., Springer Science+Business Media, LLC, 2006. doi:10.1007/978-0-387-46312-4.

[58] F.B. Dias, Kinetics of thermal-assisted delayed fluorescence in blue organic emitters with large singlet-triplet energy gap, Philos. Trans. R. Soc. A Math. Phys. Eng. Sci. 373 (2015) 20140447–20140447. doi:10.1098/rsta.2014.0447.

[59] B. Ungerböck, Integration of luminescent chemical sensors into miniaturized devices, Technical University of Graz, 2014.

[60] E.R. Carraway, J.N. Demas, B.A. DeGraff, Luminescence quenching mechanism for microheterogeneous systems, Anal. Chem. 63 (1991) 332–336. doi:10.1021/ac00004a006.

[61] R. Ramamoorthy, P.K. Dutta, S. a Akbar, Oxygen sensors : Materials , methods , designs, J. Mater. Sci. 38 (2003) 4271–4282. doi:10.1023/A:1026370729205.

[62] J.N. Demas, B.A. DeGraff, P.B. Coleman, Peer reviewed: Oxygen sensors based on luminescence quenching, Anal. Chem. 71 (1999) 793A–800A. doi:10.1021/ac9908546.

[63] B. Valeur, M.N. Berberan-Santos, Molecular fluorescence: principles and applications., Second Ed., Wiley-VCH Verlag GmbH & Co. KGaA, 2012. doi:10.1002/9783527650002.

[64] V. Linek, P. Beneš, J. Sinkule, O. Holeček, V. Malý, Oxidation of D -glucose in the presence of glucose oxidase and catalase, Biotechnol. Bioeng. 22 (1980) 2515–2527. doi:10.1002/bit.260221203.

[65] A.T. de M.M.S. Carvalho, Evaluation of Coflore technology for enzymatic carbohydrate oxidation, 2015.

[66] A. Toftgaard Pedersen, T.M. de Carvalho, E. Sutherland, G. Rehn, R. Ashe, J.M. Woodley, Characterization of a continuous agitated cell reactor for oxygen dependent biocatalysis, Biotechnol. Bioeng. 114 (2017) 1222–1230. doi:10.1002/bit.26267.

[67] A.C.O. Fernandes, K. V. Gernaey, U. Krühne, Micro scale reactor system development with integrated advanced sensor technology, Technical University of Denamrk, 2017.

[68] R.F. Beers, I.W. Sizer, A spectrophotometric method for measuring the breakdown of hydrogen peroxide by catalase, J Biol Chem. 1 (1951) 133–140.

[69] J.M. Bolivar, T. Consolati, T. Mayr, B. Nidetzky, Quantitating intraparticle O2 gradients in solid supported enzyme immobilizates: Experimental determination of their role in limiting the catalytic effectiveness of immobilized glucose oxidase, Biotechnol. Bioeng. 110 (2013) 2086–2095. doi:10.1002/bit.24873.

[70] J.M. Bolivar, S. Schelch, M. Pfeiffer, B. Nidetzky, Intensifying the O2-dependent

heterogeneous biocatalysis: superoxygenation of solid support from H2O2 by a catalase tailor-made for effective immobilization, J. Mol. Catal. B Enzym. 134 (2016) 302–309. doi:http://dx.doi.org/10.1016/j.molcatb.2016.10.017.

[71] J. Ehgartner, P. Sulzer, T. Burger, A. Kasjanow, D. Bouwes, U. Krühne, I. Klimant, T. Mayr, Online analysis of oxygen inside silicon-glass microreactors with integrated optical sensors, Sensors Actuators, B Chem. 228 (2016) 748–757. doi:10.1016/j.snb.2016.01.050.

[72] B. Ungerböck, A. Pohar, T. Mayr, I. Plazl, Online oxygen measurements inside a microreactor with modeling of transport phenomena, Microfluid. Nanofluidics. 14 (2013) 565–574. doi:10.1007/s10404-012-1074-8.

[73] S. Galvanin, U. Krühne, I.P. Rosinha, Study of the influence of reactor geometry on enzymatic reaction kinetics, Technical University of Denmark, 2014.

[74] T. V. Kirk, N. Szita, Oxygen transfer characteristics of miniaturized bioreactor systems, Biotechnol. Bioeng. 110 (2013) 1005–1019. doi:10.1002/bit.24824.

[75] T. Van Daele, K. V. Gernaey, R.H. Ringborg, T. Börner, S. Heintz, D. Van Hauwermeiren, C. Grey, U. Krühne, P. Adlercreutz, I. Nopens, Application of iterative robust model-based optimal experimental design for the calibration of biocatalytic models, Biotechnol. Prog. 33 (2017) 1278–1293. doi:10.1002/btpr.2515.

[76] A.C. Fernandes, D. Semenova, P. Panjan, A.M. Sesay, K. V Gernaey, U. Krühne, Multi-function microfluidic platform for sensors integration, N. Biotechnol. In press (2018).

[77] D. Semenova, A. Zubov, Y.E. Silina, L. Micheli, M. Koch, A.C. Fernandes, K. V. Gernaey, Mechanistic modeling of cyclic voltammetry: A helpful tool for understanding biosensor principles and supporting design optimization, Sensors Actuators B Chem. 259 (2018) 945–955. doi:10.1016/j.snb.2017.12.088.

[78] J. Sołoducho, J. Cabaj, Electrochemical and Optical Biosensors in Medical Applications, in: T. Rinken (Ed.), Biosens. - Micro Nanoscale Appl., InTech, 2015: p. 466. doi:10.5772/711.

[79] M.S. Belluzo, M.É. Ribone, C.M. Lagier, Assembling Amperometric Biosensors for Clinical Diagnostics, Sensors. 8 (2007) 1366–1399. doi:10.3390/s8031366.

[80] A.M. Gonçalves, A.Q. Pedro, F.M. Santos, L.M. Martins, C.J. Maia, J.A. Queiroz, L.A. Passarinha, Trends in protein-based biosensor assemblies for drug screening and pharmaceutical kinetic studies, Molecules. 19 (2014) 12461–12485. doi:10.3390/molecules190812461.

[81] M.A. Alonso-Lomillo, O. Domínguez-Renedo, M.J. Arcos-Martínez, Screen-printed biosensors in microbiology; A review, Talanta. 82 (2010) 1629–1636. doi:10.1016/j.talanta.2010.08.033.

[82] L.D. Mello, L.T. Kubota, Review of the use of biosensors as analytical tools in the food and drink industries, Food Chem. 77 (2002) 237–256. doi:10.1016/S0308-8146(02)00104-8.

[83] B.M. Paddle, Biosensors for chemical and biological agents of defence interest, Biosens.

Bioelectron. 11 (1996) 1079–1113. doi:10.1016/0956-5663(96)82333-5.

[84] S. Vigneshvar, C.C. Sudhakumari, B. Senthilkumaran, H. Prakash, Recent Advances in Biosensor Technology for Potential Applications – An Overview, Front. Bioeng. Biotechnol. 4 (2016) 1–9. doi:10.3389/fbioe.2016.00011.

[85] R. Iles, H. Kallichurn, What will be the Future Development of Electrochemical Biosensors for the Detection and Quantification of Biomarkers ?, Bioeng. Biomed. Sci. 2 (2012) 1–5. doi:10.4172/2155-9538.1000e110.

[86] J. Shi, D. Feng, Y. Li, Biosensors in Fermentation Applications, in: A.F. Jozala (Ed.), Ferment. Process., InTech, 2017: p. 310. doi:10.5772/711.

[87] S.F. White, I.E. Tothill, J.D. Newman, A.P.F. Turner, Development of a mass-producible glucose biosensor and flow-injection analysis system suitable for on-line monitoring during fermentations, Anal. Chim. Acta. 321 (1996) 165–172. doi:10.1016/0003-2670(95)00514-5.

[88] I. Queinnec, C. Destruhaut, J.B. Pourciel, G. Goma, An effective automated glucose sensor for fermentation monitoring and control, World J. Microbiol. Biotechnol. 8 (1992) 7–13. doi:10.1007/BF01200676.

[89] X.-L. Mao, J. Wu, Y.-B. Ying, Application of Electrochemical Biosensors in Fermentation, Chinese J. Anal. Chem. 36 (2008) 1749–1755. doi:http://dx.doi.org/10.1016/S1872-2040(09)60012-8.

[90] D.R. Thévenot, K. Toth, R.A. Durst, G.S. Wilson, Electrochemical Biosensors: Recommended Definitions and Classification, Anal. Lett. 34 (2001) 635–659. doi:10.1081/AL-100103209.

[91] D. Grieshaber, R. Mackenzie, J. Vörös, E. Reimhult, Electrochemical Biosensors -Sensor Principles and Architectures, Sensors. 8 (2008) 1400–1458. doi:10.3390/s8031400.

[92] M. Mehrvar, M. Abdi, Recent developments, characteristics, and potential applications of electrochemical biosensors, Anal. Sci. 8 (2004) 14. doi:10.2116/analsci.20.1113.

[93] J. Wang, Analytical Electrochemistry, Third Edition, 2006. doi:10.1002/0471790303.

[94] D. Pletcher, R. Greef, R. Peat, L.M. Peter, J. Robinson, Instrumental methods in Electrochemisty, First, Ellis Horwood Limited, Chichester, 1985. doi:http://dx.doi.org/10.1016/B978-0-12-525440-3.50002-X.

[95] E.H. Yoo, S.Y. Lee, Glucose biosensors: An overview of use in clinical practice, Sensors. 10 (2010) 4558–4576. doi:10.3390/s100504558.

[96] J. Wang, Glucose Biosensors : 40 years of advances and challenges, Sens. Updat. 10 (2002) 107–119.

[97] A. Heller, B. Feldman, Electrochemical glucose sensors and their applications in diabetes management, Chem. Rev. 108 (2008) 2482–2505. doi:10.1021/cr068069y.

[98] J. Wang, Electrochemical glucose biosensors, Electrochem. Sensors, Biosens. Their Biomed. Appl. (2008) 57–69. doi:10.1016/B978-012373738-0.50005-2.

[99] C. Chen, Q. Xie, D. Yang, H. Xiao, Y. Fu, Y. Tan, S. Yao, Recent advances in electrochemical glucose biosensors, RSC Adv. 3 (2013) 4473–4491. doi:10.1039/c2ra22351a.

[100] D. Bruen, C. Delaney, L. Florea, D. Diamond, Glucose sensing for diabetes monitoring: Recent developments, Sensors. 17 (2017) 1–21. doi:10.3390/s17081866.

[101] A. Salek-Maghsoudi, F. Vakhshiteh, R. Torabi, S. Hassani, M.R. Ganjali, P. Norouzi, M. Hosseini, M. Abdollahi, Recent advances in biosensor technology in assessment of early diabetes biomarkers, Biosens. Bioelectron. 99 (2018) 122–135. doi:10.1016/j.bios.2017.07.047.

[102] K.E. Toghill, R.G. Compton, Electrochemical Non-enzymatic Glucose Sensors : A Perspective and an Evaluation, Int. J. Electrochem. Sci. 5 (2010) 1246–1301.

[103] L.C. Clark, C. Lyons, Electrode systems for continuous monitoring in cardiovascular surgery, Ann. N. Y. Acad. Sci. 102 (1962) 29–45. doi:10.1111/j.1749-6632.1962.tb13623.x.

[104] G.G. Guilbault, G.J. Lubrano, An enzyme electrode for the amperometric determination of glucose, Anal. Chim. Acta. 64 (1973) 439–455. doi:10.1016/S0003-2670(01)82476-4.

[105] F. Ricci, G. Palleschi, Sensor and biosensor preparation, optimisation and applications of Prussian Blue modified electrodes, Biosens. Bioelectron. 21 (2005) 389–407. doi:10.1016/j.bios.2004.12.001.

[106] W. Putzbach, N.J. Ronkainen, Immobilization techniques in the fabrication of nanomaterial-based electrochemical biosensors: A review, Sensors. 13 (2013) 4811–4840. doi:10.3390/s130404811.

[107] J.D. Newman, A.P.F. Turner, Home blood glucose biosensors : a commercial perspective, Biosens. Bioelectron. 20 (2005) 2435–2453. doi:10.1016/j.bios.2004.11.012.

[108] M. Senior, Novartis signs up for Google smart lens, Nat. Biotechnol. 32 (2014) 856. doi:10.1038/nbt0914-856.

[109] W. Gao, S. Emaminejad, H. Yin, Y. Nyein, S. Challa, K. Chen, A. Peck, H.M. Fahad, H. Ota, H. Shiraki, D. Kiriya, D. Lien, G.A. Brooks, Fully integrated wearable sensor arrays for multiplexed in situ perspiration analysis, Nature. 529 (2016) 509–514. doi:10.1038/nature16521.

[110] N. Jiang, N. Barry, P. Maes, A. Yetisen, The Dermal Abyss: Interfacing with the Skin by Tattooing Biosensors, in: ISWC '17, 2017: pp. 138–145.

[111] F. Ricci, A. Amine, G. Palleschi, D. Moscone, Prussian Blue based screen printed biosensors with improved characteristics of long-term lifetime and pH stability, Biosens. Bioelectron. 18 (2003) 165–174.

[112] I.R.G. Ogilvie, V.J. Sieben, C.F. a Floquet, R. Zmijan, M.C. Mowlem, H. Morgan, Reduction of

surface roughness for optical quality microfluidic devices in PMMA and COC, J. Micromech.Microeng. 20 (2010) 65016. doi:10.1088/0960-1317/20/6/065016.

[113] N. Hlawatsch, R. Klemm, C. Carstens, T. Brandstëtter, H. Becker, R. Elbracht, C. Gärtner, A lab-on-a-chip system for the development of complex assays using modular microfluidic components, in: Microfluid. BioMEMS, Med. Microsystems X, 2012: p. 82510D. doi:10.1117/12.910269.

[114] H. Gunasingham, C. Tan, H. Ng, Pulsed amperometric detection of glucose usign enzyme electrode, J.Electroanal. Chem. 287 (1990) 349–362.

[115] R. Baronas, F. Ivanauskus, J. Kulys, Mathematical modeling of biosensors. An introduction for chemists and mathematicians, Springer Netherlands, 2010. doi:10.1007/b100321.

[116] L.D. Mell, J.T. Maloy, Model for the amperometric enzyme electrode obtained through digital simulation and applied to the immobilized glucose oxidase system, Anal. Chem. 47 (1975) 299–307. doi:10.1021/ac60352a006.

[117] L.D. Mell, J.T. Maloy, Amperometric response enhancement of the immobilized glucose oxidase enzyme electrode, Anal. Chem. 48 (1976) 1597–601. doi:10.1021/ac50005a045.

[118] L.D. Mell, J.T. Maloy, A model for the amperometric enzyme electrode obtained through digital simulation and applied to the immobilized glucose oxidase system, Anal. Chem. 47 (1975) 299–307. doi:10.1021/ac60352a006.

[119] A. Bergel, M. Comtat, Theoretical Evaluation of Transient Responses of an Amperometric Enzyme Electrode, Anal. Chem. 2909 (1984) 2904–2909.

[120] H. Durliat, M. Comtat, A. Baudras, Spectrophotometric and electrochemical determinations of L(+) lactate in blood by use of lactate dehydrogenase from yeast, Clin. Chem. 22 (1976) 1802–1805.

[121] S. Bacha, A. Bergel, M. Comtat, Modeling of amperometric biosensors by a finite-volume method, J. Electroanal. Chem. 359 (1993) 21–38. doi:10.1016/0022-0728(93)80398-2.

[122] S. Bacha, A. Bergel, M. Comtat, Transient response of multilayer electroenzymatic biosensors, Anal.Chem. 67 (1995) 1669–1678.

[123] T. Schulmeister, Mathematical treatment of concentration profiles and anodic current of amperometric enzyme electrodes with chemicallly-amplified response, Anal. Chim. Acta. 201 (1987) 305–310.

[124] F. Mizutani, T. Yamanaka, Y. Tanabe, K. Tsuda, An enzyme electrode for L-lactate with a chemically-amplified response, Anal. Chim. Acta. 177 (1985) 153–166. doi:10.1016/S0003-2670(00)82947-5.

[125] T. Schulmeister, Mathematical modelling of the dynamic behaviour of amperometric enzyme electrodes, Sel. Electrode Rev. 12 (1990) 203–260.

[126] W.J. Albery, A.R. Hillman, Transport and kinetics in modified electrodes, J. Electroanal. Chem. Interfacial Electrochem. 170 (1984) 27–49. doi:10.1016/0022-0728(84)80034-0.

[127] W.J. Albery, P.N. Bartlett, Amperometric enzyme electrodes: Part 1. Theory, J. Electrounal. Chem. 194 (1985) 211–222.

[128] W. Albery, John, P.N. Bartlett, D.H. Craston, Amperometric enzyme electrodes Part II. Conducting salts as electrode materials for the oxidation of glucose oxidase, J. Electroanal. Chem., 194. 194 (1985) 223–235.

[129] W.J. Albery, P.N. Bartlett, M. Bycroft, D.H. Craston, B.J. Driscoll, Amperometric enzyme electrodes. Part III. A conducting salt electrode for the oxidation of four different flavoenzymes, J. Electroanal. Chem. 218 (1987) 119–126. doi:10.1016/0022-0728(87)87010-9.

[130] W.J. Albery, P.N. Bartlett, A.E.G. Cass, K.W. Sim, Amperometric enzyme electrodes: Part IV. An enzyme electrode for ethanol, J Electroanal Chem. 218 (1987) 127–134. doi:10.1016/0022-0728(87)87011-0.

[131] P.N. Bartlett, K.F.E. Pratt, Modelling of processes in enzyme electrodes, Biosens. Bioelectron. 8 (1993) 451–462. doi:10.1016/0956-5663(93)80030-S.

[132] P.N. Bartlett, P. Tebbutt, R.G. Whitaker, Kinetic aspects of the use of modified electrodes and mediators in bioelectrochemistry, Prog. React. Kinet. 16 (1991) 55–156.

[133] W.J. Albery, P.N. Bartlett, B.J. Driscoll, R.B. Lennox, Amperometric enzyrne electrodes : Part 5. The homogeneous mediated mechanism, J. Electroanal. Chem., 323. 323 (1992) 77–102.

[134] R.S. Nicholson, I. Shain, Theory of Stationary Electrode Polarography: Single Scan and Cyclic Methods Applied to Reversible, Irreversible, and Kinetic Systems, Anal. Chem. 36 (1964) 706–723. doi:10.1021/ac60210a007.

[135] M. Rudolph, D.P. Reddy, S.W. Feldberg, A simulator for cyclic voltammetric responses, Anal. Chem. 66 (1994) 589A–600A.

[136] K. Yokoyama, Y. Kayanuma, Cyclic Voltammetric Simulation for Electrochemically Mediated Enzyme Reaction and Determination of Enzyme Kinetic Constants, Anal. Chem. 70 (1998) 3368–3376. doi:10.1021/ac9711807.

[137] K. Yokoyama, S. Koide, Y. Kayanuma, Cyclic voltammetric simulation of electrochemically mediated enzyme reaction and elucidation of biosensor behaviors., Anal. Bioanal. Chem. 372 (2002) 248–53. doi:10.1007/s00216-001-1203-9.

[138] M. Orlik, An improved algorithm for the numerical simulation of cyclic voltammetric curves affected by the ohmic potential drops and its application to the kinetics of bis(biphenyl)chromium(I) electroreduction, J. Electroanal. Chem. 575 (2005) 281–286. doi:10.1016/j.jelechem.2004.10.001.

[139] Z. Deng, X. Lin, Digital simulation of fast cyclic voltammogram by integration of the double

layer charging current, J. Electroanal. Chem. 464 (1999) 215–221.

[140] H. Cho, T. Kim, D. Yoon, A study on the computational simulation of cyclic voltammetry using semi-infinite diffusion model, J. Korean Electrochem. Soc. 14 (2011) 138–144.

[141] B.J. Adesokan, X. Quan, A. Evgrafov, M.P. Sørensen, A. Heiskanen, A. Boisen, Hydrodynamics studies of cyclic voltammetry for electrochemical micro biosensors, J. Phys. Conf. Ser. 574 (2015) 12008. doi:10.1088/1742-6596/574/1/012008.

[142] B.J. Adesokan, X. Quan, A. Evgrafov, A. Heiskanen, A. Boisen, M.P. Sørensen, Experimentation and numerical modeling of cyclic voltammetry for electrochemical micro-sized sensors under the influence of electrolyte flow, J. Electroanal. Chem. 763 (2016) 141–148. doi:10.1016/j.jelechem.2015.12.029.

[143] M.J. Bidwell, J.A. Alden, R.G. Compton, Hydrodynamic voltammetry with channel microband electrodes: The simulation of voltammetric waveshapes, J. Electroanal. Chem. 417 (1996) 119–128. doi:10.1016/S0022-0728(96)04739-0.

[144] C. Cannes, F. Kanoufi, A.J. Bard, Cyclic voltammetry and scanning electrochemical microscopy of ferrocenemethanol at monolayer and bilayer-modified gold electrodes, J. Electroanal. Chem. 547 (2003) 83–91. doi:10.1016/S0022-0728(03)00192-X.

[145] C. Cannes, F. Kanoufi, A.J. Bard, Cyclic voltammetric and scanning electrochemical microscopic study of menadione permeability through a self-assembled monolayer on a gold electrode, Langmuir. 18 (2002) 8134–8141. doi:10.1021/la0258906.

[146] J.F. Osma, M. Stoytcheva, eds., Biosensors: Recent advances and mathematical challenges, © OmniaScience (Omnia Publisher SL), 2014. doi:http://dx.doi.org/10.3926/oms.98.

[147] R.C. Cretu, D.M. Gligor, L. Muresan, I.C. Popescu, L.M. Muresan, Kinetic characterization of Prussian Blue-modified graphite electrodes for amperometric detection of hydrogen peroxide, J. Appl. Electrochem. 36 (2006) 1327–1332. doi:10.1007/s10800-006-9242-8.

[148] D.E. Ellis, M.A. Eckhoff, V.D. Neff, Electrochromism in the mixed-valence hexacyanides. 1. Voltammetric and spectral studies of the oxidation and reduction of thin films of Prussian blue, J. Phys. Chem. 85 (1981) 1225–1231. doi:10.1021/j150609a026.

[149] J.F. Keggin, F.D. Miles, Structures and Formulæ of the Prussian Blues and Related Compounds, Nature. 137 (1936) 577–578.

[150] F. Herren, A. Ludi, P. Fischer, W. Halg, Neutron Diffraction Study of Prussian Blue, Fe4[Fe(CN)6]3.xH2O. Location of Water Molecules and Long-Range Magnetic Order, Inorg. Chem. 19 (1980) 956–959. doi:10.1021/ic50206a032.

[151] A. Paolella, C. Faure, V. Timochevskii, S. Marras, G. Bertoni, G. Abdelbast, A. Vijh, M. Armand, K. Zaghib, A review on hexacyanoferrate-based materials for energy storage and smart windows: challenges and perspectives, J. Mater. Chem. A. (2017) 18919–18932. doi:10.1039/C7TA05121B.

[152] K. Itaya, N. Shoji, I. Uchida, Catalysis of the reduction of molecular oxygen to water at Prussian blue modified electrodes, J. Am. Chem. Soc. 106 (1984) 3423–3429. doi:10.1021/ja00324a007.

[153] K. Itaya, T. Ataka, S. Toshima, Spectroelectrochemistry and electrochemical preparation method of Prussian blue modified electrodes, J. Am. Chem. Soc. 104 (1982) 4767–4772. doi:10.1021/ja00382a006.

[154] K. Itaya, K. Shibayama, H. Akahoshi, S. Toshima, Prussian-blue-modified electrodes: An application for a stable electrochromic display device, J. Appl. Phys. 53 (1982) 804–805. doi:10.1063/1.329997.

[155] K. Itaya, H. Akahoshi, S. Toshima, Electrochemistry of Prussian Blue Modified Electrodes: An Electrochemical Preparation Method, J. Electrochem. Soc. 129 (1982) 1498–1500. doi:10.1149/1.2124191.

[156] A.A. Karyakin, E.E. Karyakina, L. Gorton, Prussian-Blue-based amperometric biosensors in flow-injection analysis, Talanta. 43 (1996) 1597–1606. doi:10.1016/0039-9140(96)01909-1.

[157] A.A. Karyakin, E.E. Karyakina, L. Gorton, On the mechanism of H2O2 reduction at Prussian Blue modified electrodes, Electrochem. Commun. 1 (1999) 78–82. doi:http://dx.doi.org/10.1016/S1388-2481(99)00010-7.

[158] A.A. Karyakin, Prussian blue and its analogues: Electrochemistry and analytical applications, Electroanalysis. 13 (2001) 813–819. doi:10.1002/1521-4109(200106)13:10<813::AID-ELAN813>3.0.CO;2-Z.

[159] F. Ricci, A. Amine, C.S. Tuta, A.A. Ciucu, F. Lucarelli, G. Palleschi, D. Moscone, Prussian Blue and enzyme bulk-modified screen-printed electrodes for hydrogen peroxide and glucose determination with improved storage and operational stability, Anal. Chim. Acta. 485 (2003) 111–120. doi:10.1016/S0003-2670(03)00403-3.

[160] A.N. Sekretaryova, M. Eriksson, A.P.F. Turner, Bioelectrocatalytic systems for health applications, Biotechnol. Adv. 34 (2016) 177–197. doi:10.1016/j.biotechadv.2015.12.005.

[161] P. Gros, A. Bergel, Improved model of a polypyrrole glucose oxidase modified electrode, J. Electroanal. Chem. 386 (1995) 65–73. doi:10.1016/0022-0728(94)03804-C.

[162] S.C. Barton, Chapter 8: Enzyme catalysis in biological fuel cells, in: W. Vielstich, H.A. Gasteiger, A. Lamm, H. Yokokawa (Eds.), Handb. Fuel Cells – Fundam. Technol. Appl., John Wiley & Sons, Ltd, 2010: pp. 1–19. http://www.wiley.com/WileyCDA/WileyTitle/productCd-0470723114.html.

[163] H.C. Chang, C.C. Wu, S.J. Ding, I.S. Lin, I.W. Sun, Measurement of diffusion and partition coefficients of ferrocyanide in protein-immobilized membranes, Anal. Chim. Acta. 532 (2005) 209–214. doi:10.1016/j.aca.2004.10.063.

[164] J. Kulys, R. Vidziunaite, Laccase based synergistic electrocatalytical system, Electroanalysis. 21

(2009) 2228–2233. doi:10.1002/elan.200904679.

[165] M. Mahosenaho, F. Caprio, L. Micheli, A.M. Sesay, G. Palleschi, V. Virtanen, A disposable biosensor for the determination of alpha-amylase in human saliva, Microchim. Acta. 170 (2010) 243–249. doi:10.1007/s00604-010-0360-y.

[166] D.A. Ellis, S.A. Mabury, J.W. Martin, D.C.G. Muir, Thermolysis of fluoropolymers as a potential source of halogenated organic acids in the environment., Nature. 412 (2001) 321–324. doi:10.1038/35085548.

[167] M. Feng, R. Qu, Z. Wei, L. Wang, P. Sun, Z. Wang, Characterization of the thermolysis products of Nafion membrane: A potential source of perfluorinated compounds in the environment, Sci. Rep. 5 (2015) 9859. doi:10.1038/srep09859.

[168] F. Ivanauskas, P. Katauskis, V. Laurinavičius, Mathematical modeling of biosensor action in the region between diffusion and kinetic modes, J. Math. Chem. 52 (2013) 689–702. doi:10.1007/s10910-013-0289-6.

[169] A. Ambrózy, L. Hlavatá, J. Labuda, Protective membranes at electrochemical biosensors, Acta Chim. Slovaca. 6 (2013) 35–41. doi:10.2478/acs-2013-0007.

[170] C. Heitner-Wirguin, Recent advances in perfluorinated membranes: structure, properties and applications, Recent Adv. Perfluorinated Membr. Struct. Prop. Appl. 120 (1996) 1–33.

[171] S. Banerjee, D.E. Curtin, Nafion® perfluorinated membranes in fuel cells, J. Fluor. Chem. 125 (2004) 1211–1216. doi:10.1016/j.jfluchem.2004.05.018.

[172] J. Lu, L.T. Drzal, R.M. Worden, I. Lee, Simple fabrication of a highly sensitive glucose biosensor using enzymes immobilized in exfoliated graphite nanoplatelets nafion membrane, Chem. Mater. 19 (2007) 6240–6246. doi:10.1021/cm702133u.

[173] Y. Lv, F. Wang, H. Zhu, X. Zou, C. Tao, J. Wang, Electrochemically reduced graphene oxide-nafion / Au nanoparticle modified electrode for hydrogen peroxide sensing, Nanomater. Nanotechnol. 6 (2016) 2–8. doi:10.5772/63519.

[174] A.A. Karyakin, E.A. Kotel'nikova, L. V. Lukachova, E.E. Karyakina, Optimal environment for glucose oxidase in perfluorosulfonated ionomer membranes: Improvement of first-generation biosensors, Anal. Chem. 74 (2002) 1597–1603. doi:10.1021/ac0155409.

[175] U. Latif, F.L. Dickert, R. Blach, H. Feucht, Biocompatible membranes and coatings for glucose sensor, J. Chem. Soc. Pakistan. 35 (2013) 17–22.

[176] J. Ramkumar, Nafion perfluorosulphonate membrane: Unique properties and various applications, in: Funct. Mater., Elsevier Inc., 2012: pp. 549–577. doi:10.1016/B978-0-12-385142-0.00013-1.

[177] W.Y. Hsu, T.D. Gierke, Ion transport and clustering in nafion perfluorinated membranes, J. Memb. Sci. 13 (1983) 307–326. doi:10.1016/S0376-7388(00)81563-X.

[178] A. Kusoglu, A.Z. Weber, New insights into perfluorinated sulfonic-acid ionomers, Chem. Rev. 117 (2017) 987–1104. doi:10.1021/acs.chemrev.6b00159.

[179] M.A. Modestino, A. Kusoglu, A. Hexemer, A.Z. Weber, R.A. Segalman, Controlling nafion structure and properties via wetting interactions, Macromolecules. 45 (2012) 4681–4688. doi:10.1021/ma300212f.

[180] P. Vanya, J. Sharman, J.A. Elliott, Mesoscale simulations of confined Nafion thin films, J. Chem. Phys. 147 (2017) 1–9. doi:10.1063/1.4996695.

[181] L. Chaabane, L. Dammak, D. Grande, C. Larchet, P. Huguet, S. V. Nikonenko, V. V. Nikonenko, Swelling and permeability of Nafion117 in water-methanol solutions: An experimental and modelling investigation, J. Memb. Sci. 377 (2011) 54–64. doi:10.1016/j.memsci.2011.03.037.

[182] J.A. Elliott, S. Hanna, A.M.S. Elliott, G.E. Cooley, The swelling behaviour of perfluorinated ionomer membranes in ethanol/water mixtures, Polymer (Guildf). 42 (2001) 2251–2253. doi:10.1016/S0032-3861(00)00538-3.

[183] Y. Freijanes, V.M. Barragán, S. Muñoz, Chronopotentiometric study of a Nafion membrane in presence of glucose, J. Memb. Sci. 510 (2016) 79–90. doi:10.1016/j.memsci.2016.02.054.

[184] A. Nováková, L. Schreiberová, I. Schreiber, Study of dynamics of glucose-glucose oxidase-ferricyanide reaction, Russ. J. Phys. Chem. A. 85 (2011) 2305–2309. doi:10.1134/S003602441113019X.

[185] G. Sin, K. V. Gernaey, Data handling and parameter estimation, in: Exp. Methods Wastewater Treat., 2016: pp. 201–234. doi:10.1017/CBO9781107415324.004.

[186] CAS © 2018 American Chemical Society, SciFinder ®, (n.d.). https://scifinder.cas.org/.

[187] Elsevier© RELX Intellectual Properties SA, Reaxys ®, (n.d.). https://new.reaxys.com/#/search/quick.

[188] A. Bolic, H. Larsson, S. Hugelier, A. Eliasson Lantz, U. Krühne, K. V. Gernaey, A flexible well-mixed milliliter-scale reactor with high oxygen transfer rate for microbial cultivations, Chem. Eng. J. 303 (2016) 655–666. doi:10.1016/j.cej.2016.05.117.

[189] N.K. Gill, M. Appleton, F. Baganz, G.J. Lye, Design and characterisation of a miniature stirred bioreactor system for parallel microbial fermentations, Biochem. Eng. J. 39 (2008) 164–176. doi:10.1016/j.bej.2007.09.001.

[190] H.L. Lee, P. Boccazzi, R.J. Ram, A.J. Sinskey, Microbioreactor arrays with integrated mixers and fluid injectors for high-throughput experimentation with pH and dissolved oxygen control, Lab Chip. 6 (2006) 1229–1235. doi:10.1039/B608014F.

[191] I. Grabowska, M. Sajnoga, M. Juchniewicz, M. Chudy, A. Dybko, Z. Brzozka, Microfluidic system with electrochemical and optical detection, Microelectron. Eng. 84 (2007) 1741–1743. doi:10.1016/j.mee.2007.01.248.

[192] F. Sassa, K. Morimoto, W. Satoh, H. Suzuki, Electrochemical techniques for microfluidic applications, Electrophoresis. 29 (2008) 1787–1800. doi:10.1002/elps.200700581.

[193] M. Van Leeuwen, Development of a bioreactor with integrated on-line sensing for batch and fed-batch cultivation on a 100 µL-scale, TU Delft, 2008.

[194] T. Van Daele, Model-based analysis as a tool for intensification of a biocatalytic process in a microreactor, Ghent University, 2017.

[195] P.R. Patnaik, Supervisory expert system-based intelligent optimization of a microbioreactor, Appl. Artif. Intell. 28 (2014) 91–110. doi:10.1080/08839514.2014.875678.

[196] I.P. Rosinha Grundtvig, A.E. Daugaard, J.M. Woodley, K. V. Gernaey, U. Krühne, Shape optimization as a tool to design biocatalytic microreactors, Chem. Eng. J. 322 (2017) 215–223. doi:10.1016/j.cej.2017.03.045.

[197] C. Hoffmann, I. Pereira Rosinha Grundtvig, J. Thrane, N. Garg, K. V. Gernaey, M. Pinelo, J.M. Woodley, U. Krühne, A.E. Daugaard, Experimental and computational evaluation of area selectively immobilized horseradish peroxidase in a microfluidic device, Chem. Eng. J. 332 (2018) 16–23. doi:10.1016/j.cej.2017.09.050.

[198] P. Bogaerts, A. Vande Wouwer, Software sensors for bioprocesses, ISA Trans. 42 (2003) 547–558. doi:10.1016/S0019-0578(07)60005-6.

[199] H. Sundström, S.O. Enfors, Software sensors for fermentation processes, Bioprocess Biosyst. Eng. 31 (2008) 145–152. doi:10.1007/s00449-007-0157-5.

[200] A. Chéruy, Software sensors in bioprocess engineering, J. Biotechnol. 52 (1997) 193–199. doi:10.1016/S0168-1656(96)01644-6.

[201] T. Patarinska, V. Trenev, S. Popova, Software sensors design for a class of aerobic fermentation processes, Int. J. 14 (2010) 99–118. http://www.clbme.bas.bg/bioautomation/2010/vol_14.2/files/14.2_02.pdf.

[202] H. Zhang, Software sensors and their applications in bioprocess, in: Stud. Comput. Intell., 2009: pp. 25–56. doi:10.1007/978-3-642-01888-6_2.

[203] T. Tajsoleiman, D. Semenova, A.C. Fernandes, J.K. Huusom, K. V. Gernaey, U. Krühne, An efficient experimental design strategy for modelling and characterization of processes, in: 27th Eur. Symp. Comput. Aided Process Eng., Elsevier Masson SAS, 2017: pp. 2827–2832. doi:10.1016/B978-0-444-63965-3.50473-6.

Appendix A: Model mechanism structure selection

Table S1 – Kinetic parameters for mechanism A

Mechanism A		
Kinetic Constant	Initial Value	Reference
k_1 $[\mathrm{M^{-1}s^{-1}}]$	13997	[64]
k_2 $[\mathrm{M^{-1}s^{-1}}]$	2.1×10^6	[64]
k_3 $[\mathrm{s^{-1}}]$	1152	[64]

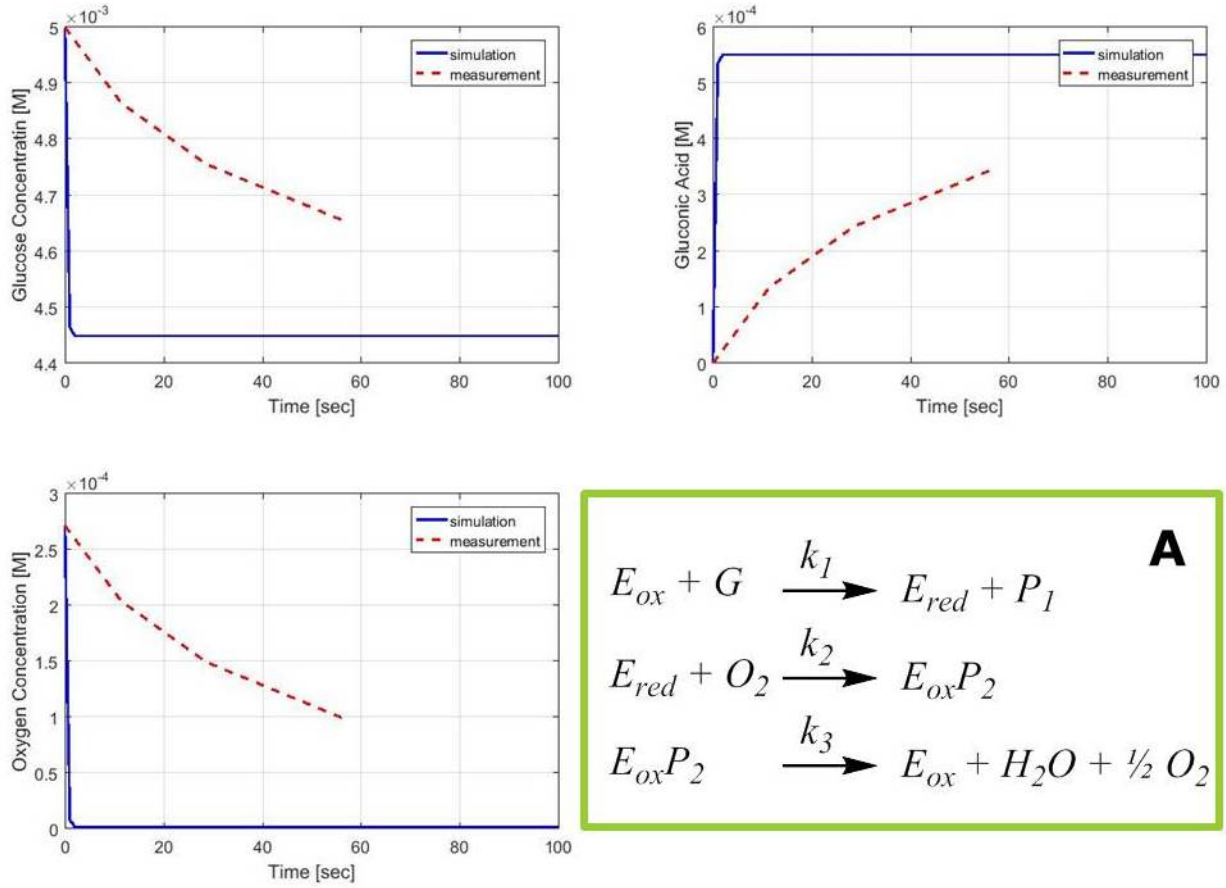

Figure S1 – *Mechanism A*. Comparison of the concentration profiles for glucose, gluconic acid and oxygen inside the microreactor: simulation results (*blue solid line*) vs. experimental data (*red dashed line*).

Table S2 – Kinetic parameters for mechanism B

Mechanism B		
Kinetic Constant	Initial Value	Optimized/Estimated Value
k_1 $[\mathrm{M^{-1}s^{-1}}]$	13997	1.2×10^{11}
k_2 $[\mathrm{M^{-1}s^{-1}}]$	2.1×10^{6}	6.65×10^{11}
k_3 $[\mathrm{s^{-1}}]$	1150	1.59×10^{5}
k_4 $[\mathrm{M^{-1}s^{-1}}]$	4.0×10^{8}	3.98×10^{8}

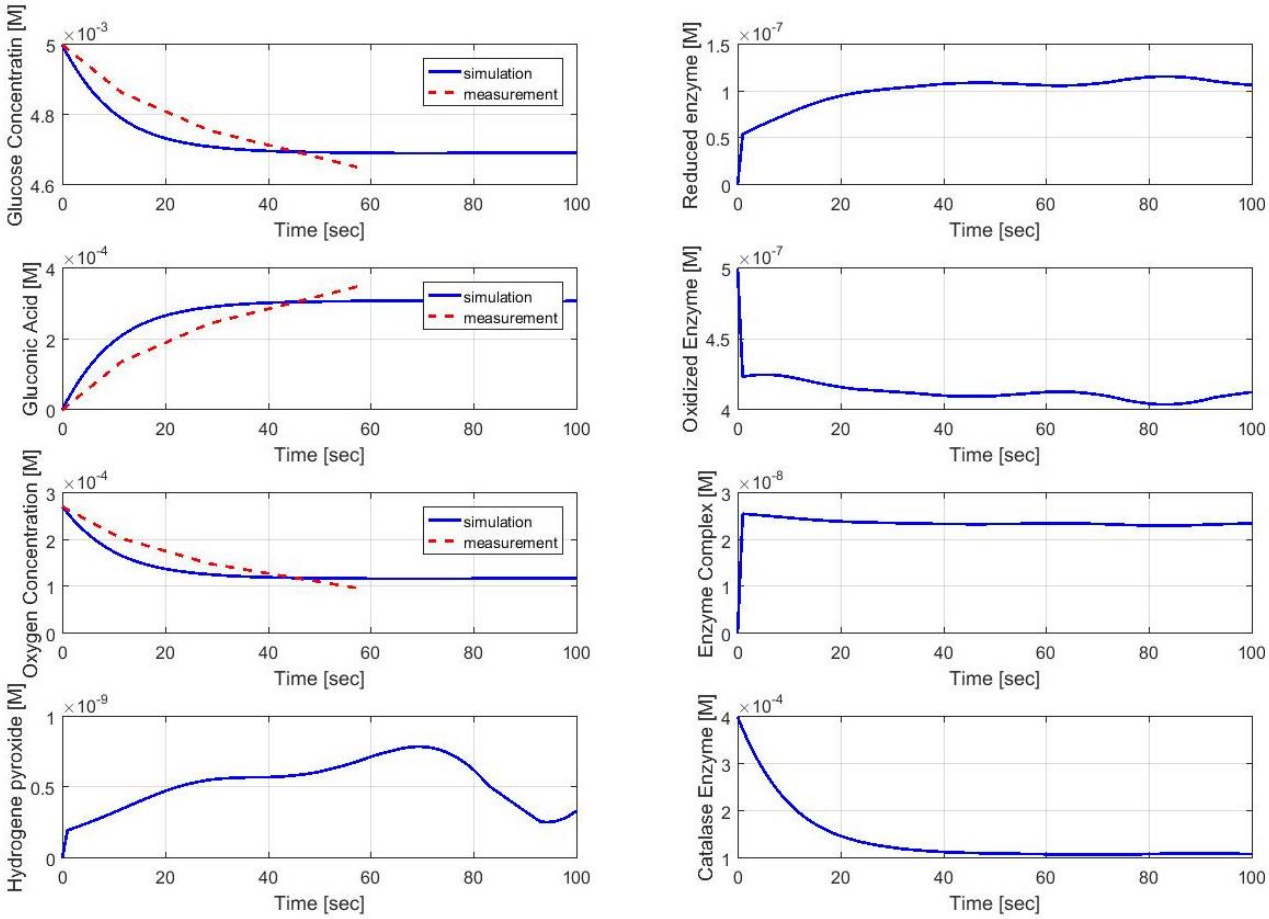

Figure S2 - *Mechanism B*. Comparison of the simulation results (*blue solid line*) and concentration profiles (no addition of extra catalase) inside the microreactor (*red dashed line*).

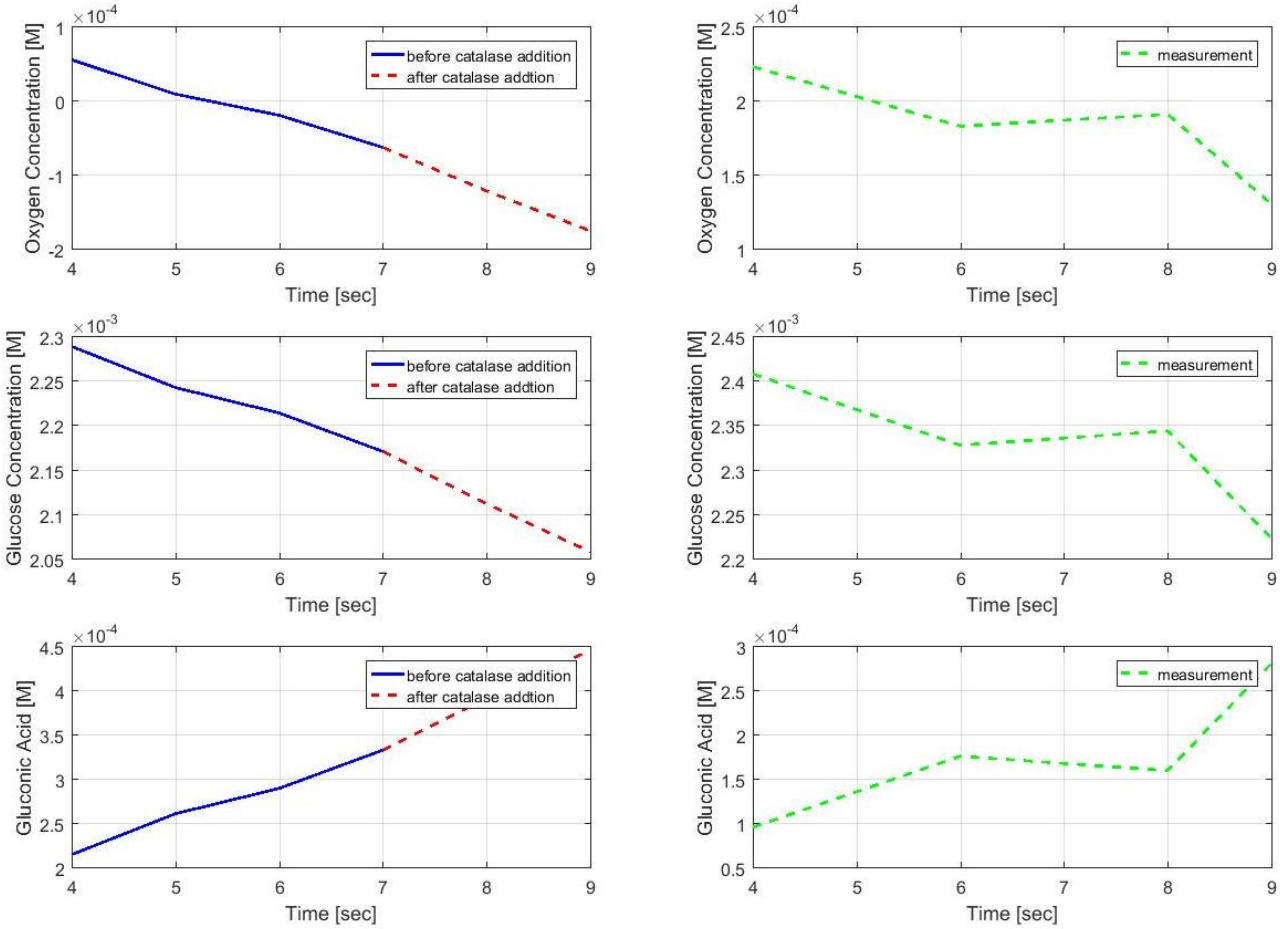

Figure S3 – *Mechanism B*. Comparison of the concentration profiles for glucose, gluconic acid and oxygen inside the microreactor before and after addition of catalase: simulation results *(blue solid line* – before catalase; *red dashed line* - after) *vs.* experimental data (*green dashed line*).

Table S3 – Kinetic parameters for mechanism C

Mechanism C	
Kinetic Constant	Optimized/Estimated Value
k_1 $[\mathrm{M^{-1}s^{-1}}]$	1.63×10^{11}
k_2 $[\mathrm{M^{-1}s^{-1}}]$	4.68×10^{11}
k_3 $[\mathrm{s^{-1}}]$	1.59×10^{5}
k_4 $[\mathrm{M^{-1}s^{-1}}]$	2.8×10^{8}

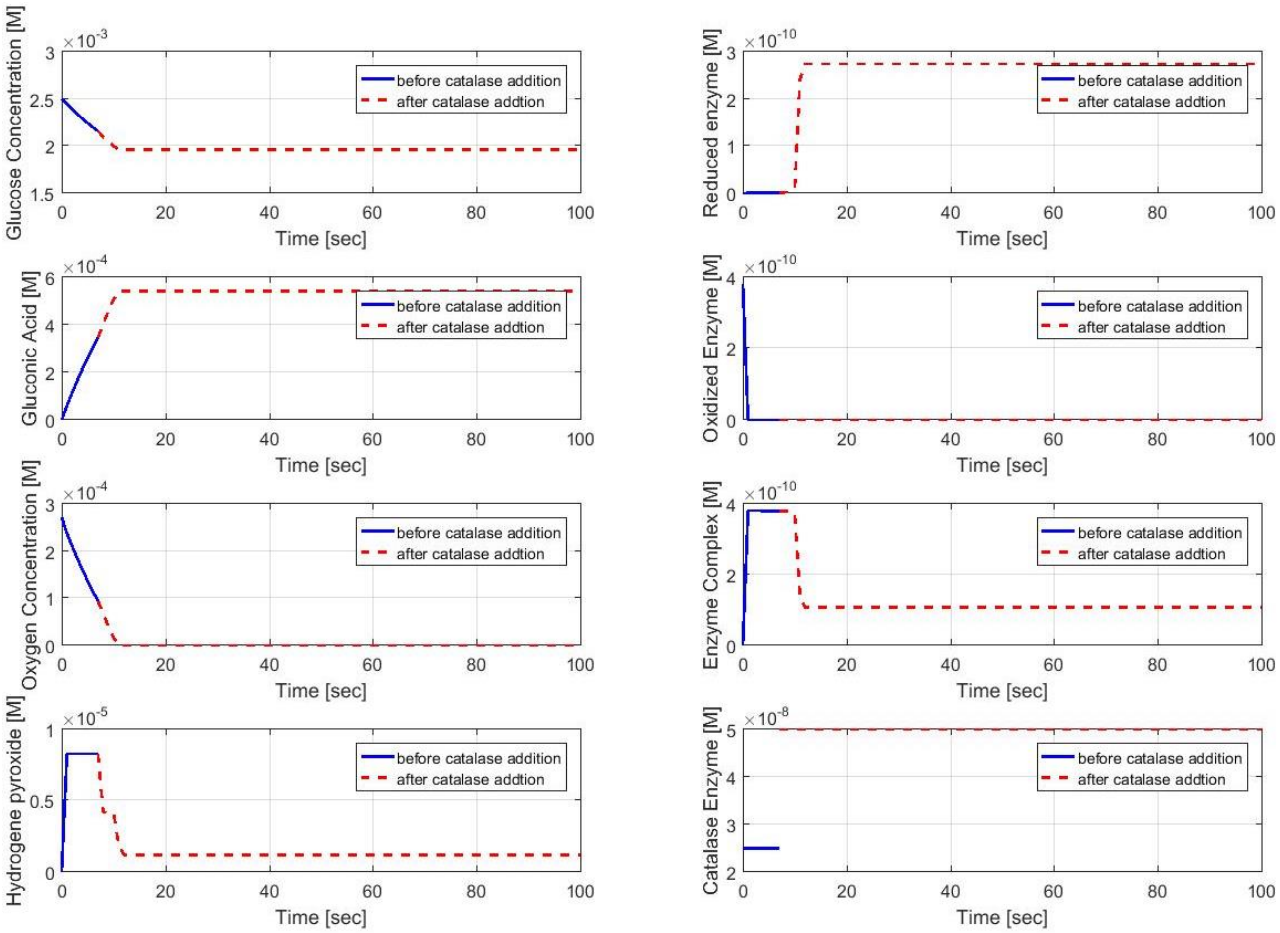

Figure S4 – *Mechanism C*. Comparison of the simulation results obtained for the concentration profiles inside the microreactor before (*blue solid line*) and after addition of catalase *(red dashed line*).

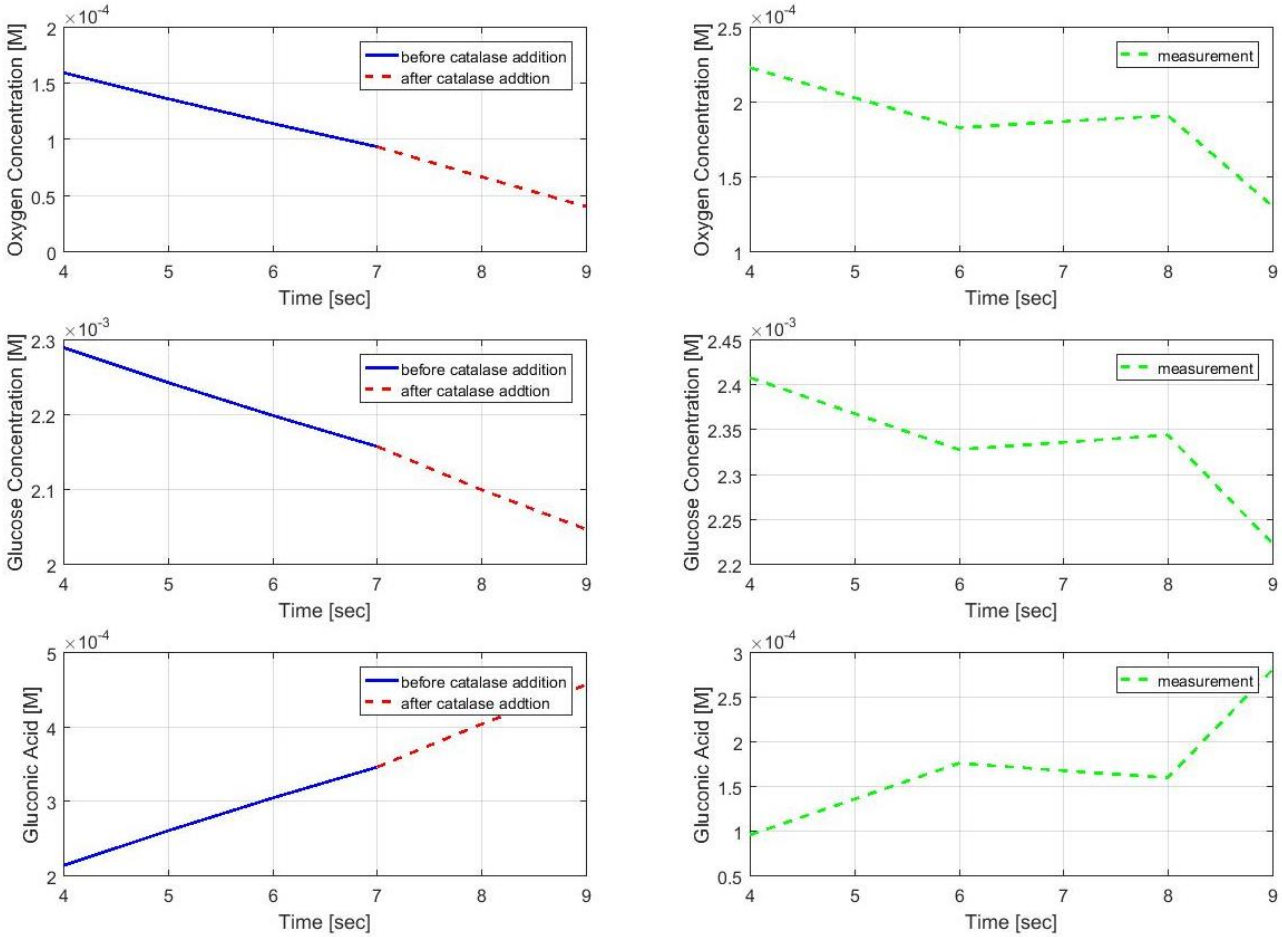

Figure S5 – *Mechanism C*. Comparison of the concentration profiles for glucose, gluconic acid and oxygen inside the microreactor before and after addition of catalase: simulation results *(blue solid line* – before catalase; *red dashed line* - after) *vs.* experimental data (*green dashed line*).

Table S4 – Kinetic parameters for mechanism D

Mechanism D	
Kinetic Constant	Optimized/Estimated Value
k_1 $[\mathrm{M^{-1}s^{-1}}]$	8.2×10^{-6}
k_2 $[\mathrm{M^{-1}s^{-1}}]$	7.0×10^{-4}

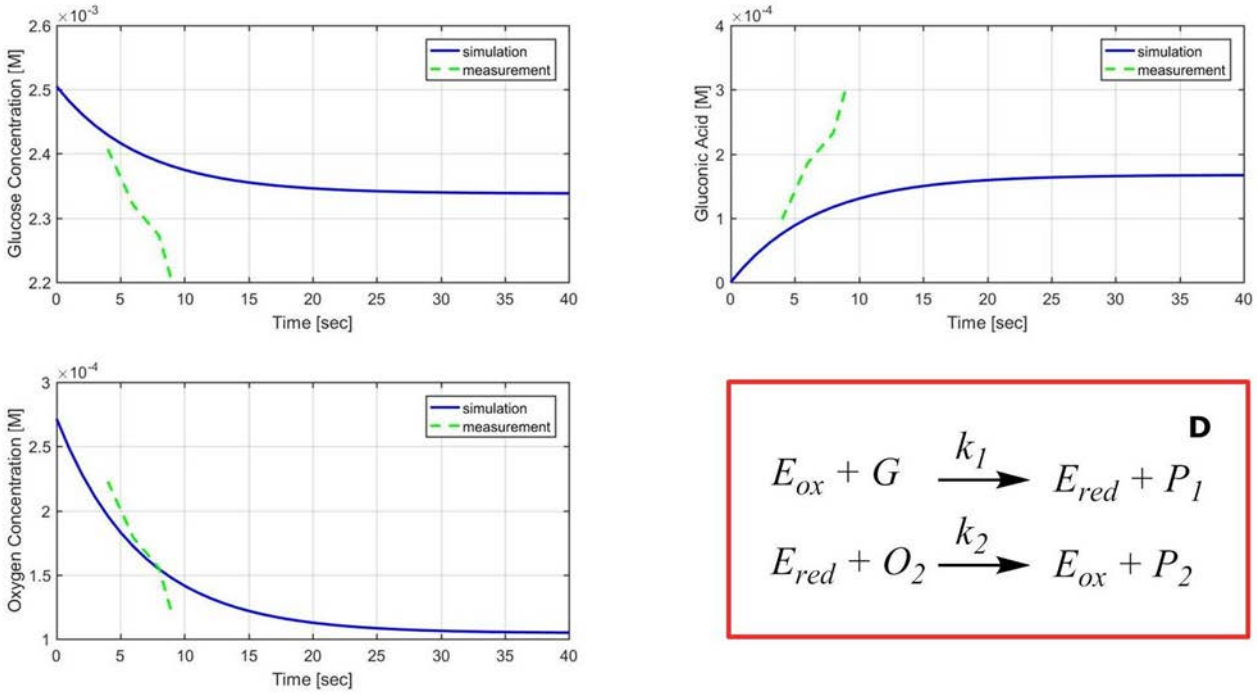

Figure S6 – *Mechanism D*. Comparison of concentration profiles for glucose, gluconic acid and oxygen inside the microreactor: simulation results (solid line) vs. experimental data (dashed line).

Table S5 – Kinetic parameters for mechanism E

Mechanism E		
Kinetic Constant	Optimized/Estimated Value	Comment
k_1 $[\mathrm{M^{-1}s^{-1}}]$	4.76×10^4	*before extra catalase*
k_2 $[\mathrm{M^{-1}s^{-1}}]$	4.87	
k_3 $[\mathrm{s^{-1}}]$	4.2×10^8	
k_1 $[\mathrm{M^{-1}s^{-1}}]$	5.63×10^4	*after extra catalase*
k_2 $[\mathrm{M^{-1}s^{-1}}]$	2.61	
k_3 $[\mathrm{s^{-1}}]$	6.93×10^8	

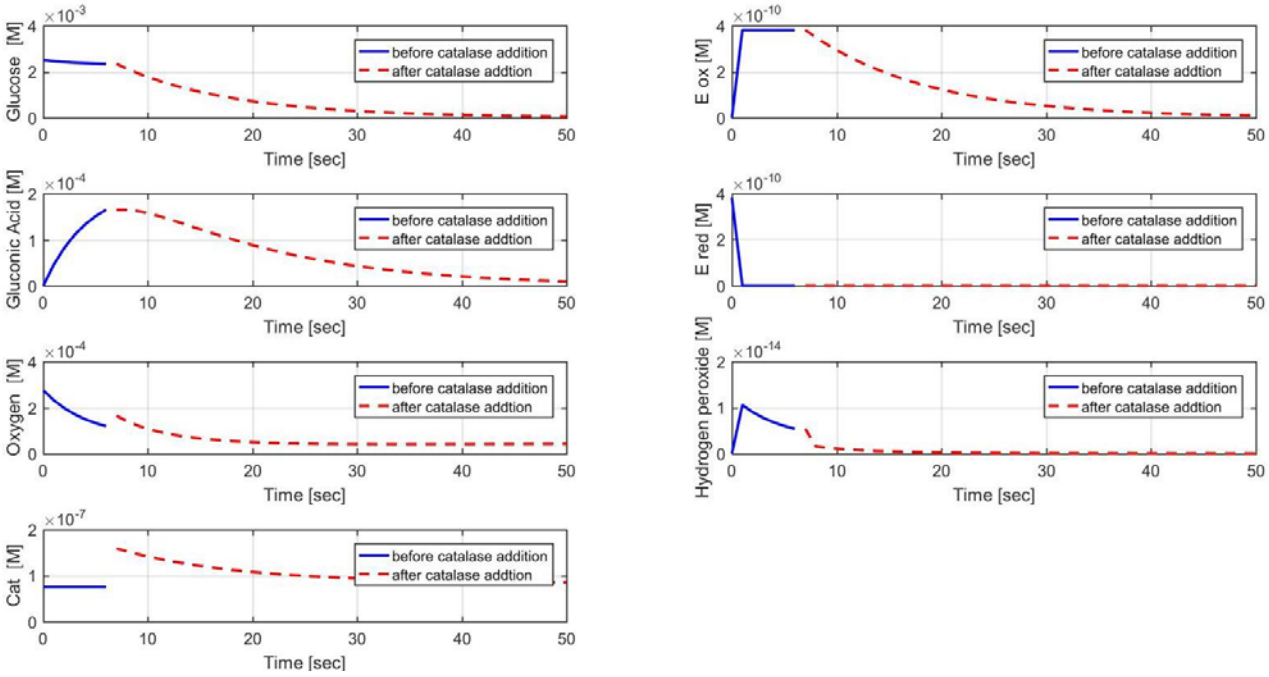

Figure S7 - *Mechanism E*. Comparison of the simulation results obtained for the concentration profiles inside the microreactor before (*blue solid line*) and after addition of catalase *(red dashed line*).

Appendix B: Enzyme activity measurement in mL- and µL- scale reactors

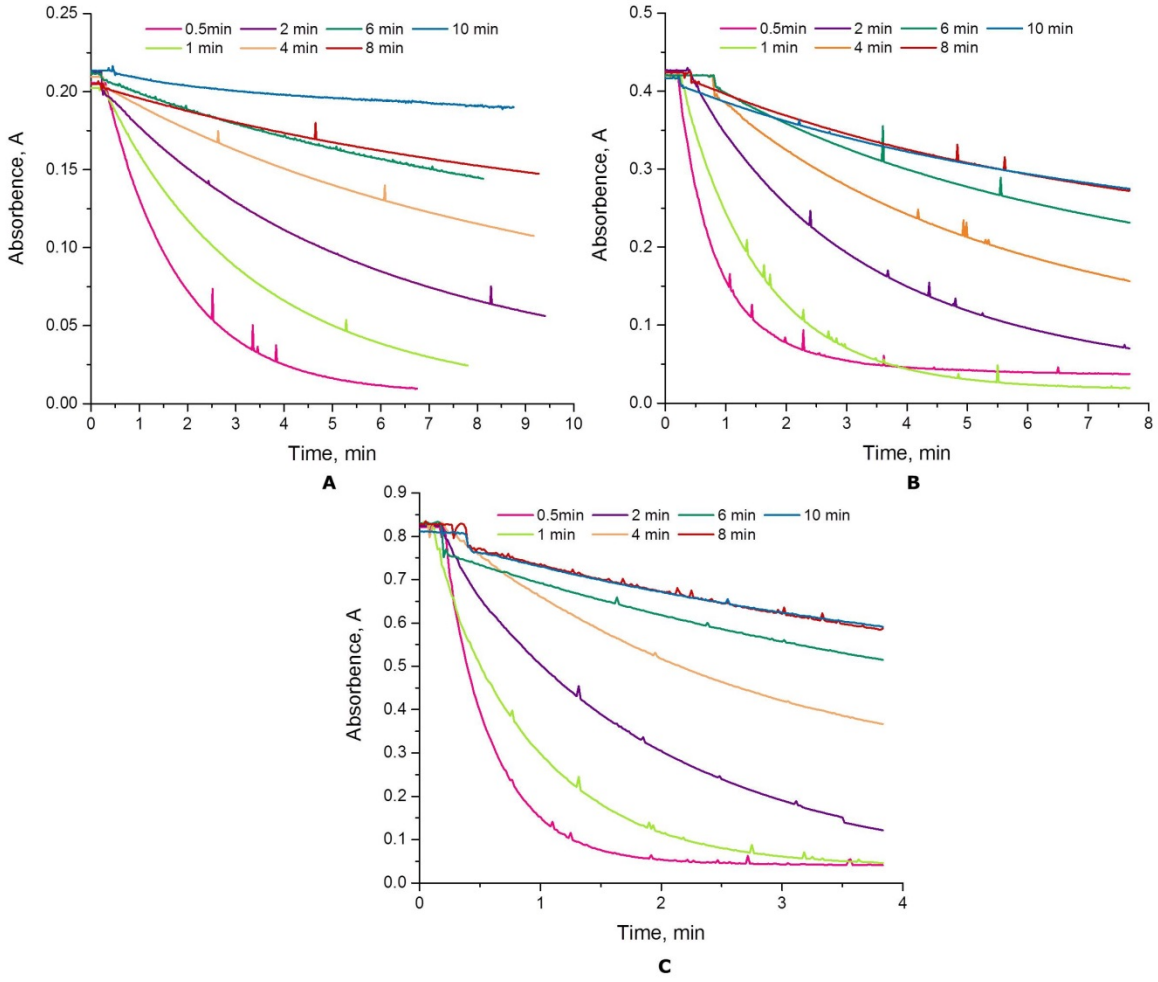

Figure S8 – The absorbance curves recorded in the presence of catalase for 5 mM (A), 10 mM (B) and 20 mM (C) of hydrogen peroxide.

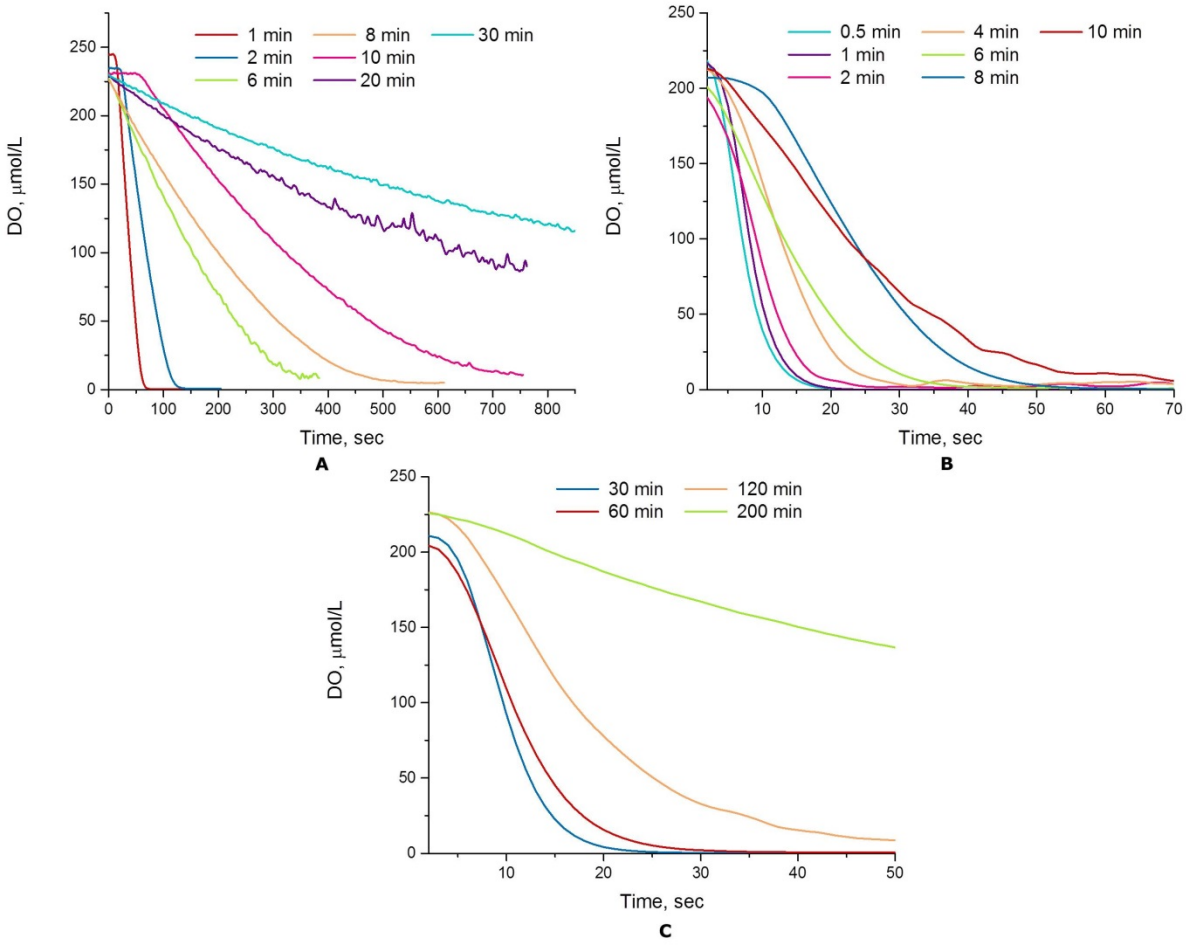

Figure S9 - Dynamic response of the oxygen consumption rates, expressed as the number of moles of oxygen dissolved in a stock glucose solution: 2.5 mM (A), 10 mM (B) and 100 mM (C) of glucose.

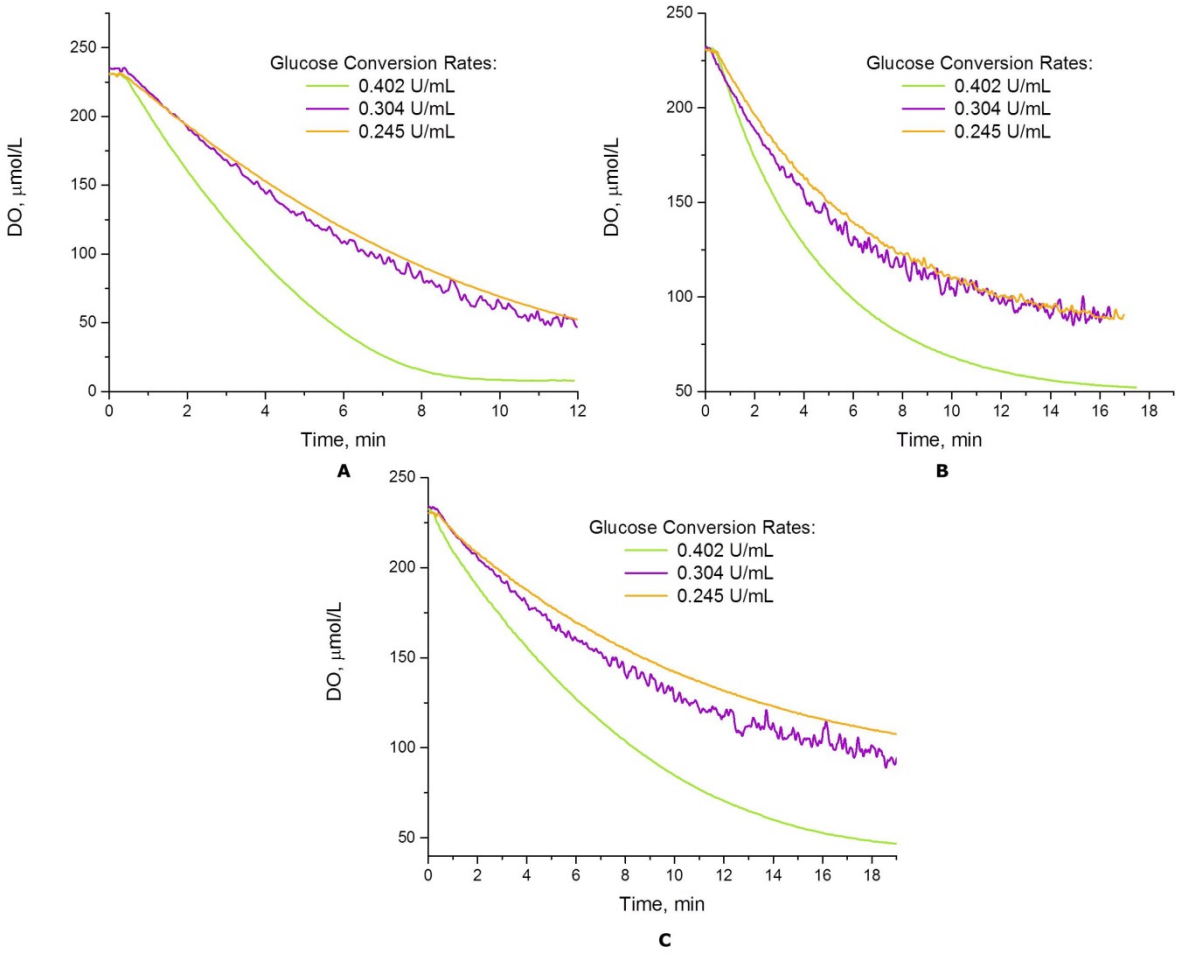

Figure S10- Dynamic response of the oxygen consumption rates, expressed as the number of moles of oxygen dissolved in the glucose/catalase solution. Experiments where the activity of catalase is equal to the activity of the glucose oxidase (A), 10 times higher than glucose oxidase (B) and 100 times higher than glucose oxidase (C), respectively, were compared for different glucose/glucose oxidase reaction velocities (0.402 U/mL, 0.304 U/mL and 0.245 U/mL).

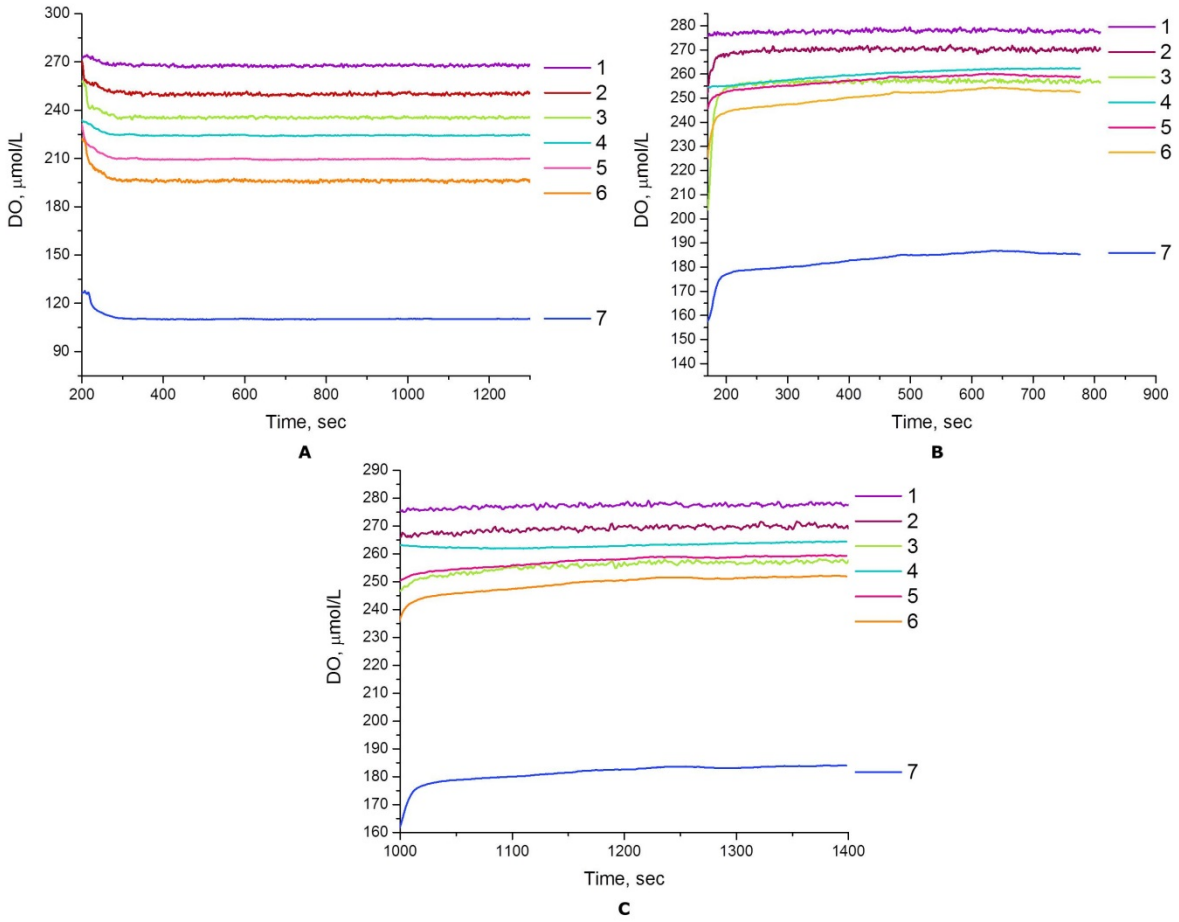

Figure S11 – The stable response of the oxygen consumption rates, expressed as the number of moles of dissolved oxygen measured by each sensor spot. The oxygen detection was studied for the catalase/glucose oxidase reaction in the presence of glucose (A). The addition of extra catalase (B) and hydrogen peroxide (C) solutions was performed inside the microchannel between sensor 3 and sensor 4. The numbers on the plots correspond to the sensor spot positions inside the microreactor shown in Figure 15.

Appendix C: Multi-analytical studies of biosensors

Table S6 – Results of the cyclic voltammetry studies obtained at different scan rates and number of scans (sc) for 2 and 4 layer glucose biosensors

Cyclic Voltammetry sensors were scanned from -0.5 to +0.5 V at different speeds											
sensor/parameter	E top, V	I top, µA	E bot, V	I bot, µA	Scan rate, v, mV	Δ E , V	Δ I, µA	Type	Itop/Ibot	time,sec	total time,min
S8, 1sc	-0.08	11.654	-0.11	-11.052		0.03	22.706		-1.055	202	
S8, 2sc	-0.08	16.405	-0.11	-12.596		0.03	29.001		-1.302	202	
S8, 3sc	-0.07	17.006	-0.11	-12.661	10	0.04	29.667		-1.343	202	16.83
S8, 4sc	-0.07	18.482	-0.1	-12.47		0.03	30.952		-1.482	202	
S8, 5sc	-0.07	18.956	-0.1	-12.978		0.03	31.934		-1.461	202	
S5, CV 1sc	-0.06	30.66	-0.11	-27.94		0.05	58.6		-1.097	102	
S5, CV 2sc	-0.06	35.97	-0.11	-30.32		0.05	66.29		-1.186	102	
S5, CV 3sc	-0.06	37.52	-0.12	-30.95	20	0.06	68.47		-1.212	102	8.5
S5, CV 4sc	-0.06	38.86	-0.12	-31.67		0.06	70.53		-1.227	102	
S5, CV 5sc	-0.06	38.38	-0.12	-31.61		0.06	69.99	2 layer senors	-1.214	102	
S6, CV 1sc	-0.04	61.48	-0.13	-52.86		0.09	114.34		-1.163	42	
S6, CV 2sc	-0.05	67.77	-0.14	-56.02		0.09	123.79		-1.210	42	
S6, CV 3sc	-0.04	69.95	-0.14	-56.87		0.1	126.82		-1.23	42	
S6, CV 4sc	-0.04	70.86	-0.14	-56.7		0.1	127.56		-1.25	42	
S6, CV 5sc	-0.04	70.58	-0.14	-56.97		0.1	127.55		-1.239	42	
S6, CV 6sc	-0.04	70.42	-0.14	-56.62		0.1	127.04		-1.244	42	
S6, CV 7sc	-0.04	69.69	-0.13	-55.8	50	0.09	125.49		-1.249	42	8.4
S6, CV 8sc	-0.04	69.17	-0.13	-55.9		0.09	125.07		-1.237	42	
S6, CV 9sc	-0.04	69.12	-0.13	-55.5		0.09	124.62		-1.245	42	
S6, CV 10sc	-0.04	68.18	-0.13	-55.94		0.09	124.12		-1.219	42	
S6, CV 11sc	-0.04	67.95	-0.13	-55.47		0.09	123.42		-1.225	42	
S6, CV 12sc	-0.04	68.03	-0.13	-55.14		0.09	123.17		-1.234	42	
S23, 1sc	-0.07	12.339	-0.1	-11.4		0.03	23.739		-1.082	202	
S23, 2sc	-0.06	14.67	-0.1	-12.493		0.04	27.163		-1.174	202	
S23, 3sc	-0.06	15.798	-0.1	-13.17	10	0.04	28.968		-1.200	202	16.83
S23, 4sc	-0.06	17.316	-0.1	-13.209		0.04	30.525		-1.311	202	
S23, 5sc	-0.06	17.83	-0.1	-13.333		0.04	31.163		-1.337	202	
S24, 1sc	-0.07	29.754	-0.12	-26.24		0.05	55.994		-1.134	102	
S24, 2sc	-0.07	34.283	-0.12	-30.164		0.05	64.447		-1.137	102	
S24, 3sc	-0.08	35.799	-0.12	-30.225	20	0.04	66.024		-1.184	102	8.5
S24, 4sc	-0.08	35.764	-0.12	-30.257		0.04	66.021		-1.182	102	
S24, 5sc	-0.07	36.233	-0.12	-30.583		0.05	66.816	4 layer sensors	-1.185	102	
S25, 1sc	-0.04	61.793	-0.13	-55.725		0.09	117.518		-1.109	42	
S25, 2sc	-0.05	67.257	-0.15	-63.36		0.1	130.617		-1.062	42	
S25, 3sc	-0.05	68.863	-0.15	-64.673	50	0.1	133.536		-1.065	42	3.5
S25, 4sc	-0.05	69.822	-0.15	-66.413		0.1	136.235		-1.051	42	
S25, 5sc	-0.05	70.663	-0.15	-65.714		0.1	136.377		-1.075	42	

Table S7 - Results of the cyclic voltammetry studies obtained in the presence of 0.01 M potassium ferricyanide at various scan rates for 2 and 4 layer glucose biosensors

ν, mV/sec	ν^½, V/sec	2 layer		4 layer	
		Ipa, A	Ipc, A	Ipa, A	Ipc, A
10	0.1	2.52E-05	-2.02E-05	1.34E-05	-9.93E-06
20	0.141421	4.74E-05	-3.58E-05	3.28E-05	-2.17E-05
50	0.223607	9.94E-05	-8.00E-05	7.70E-05	-5.45E-05
70	0.264575	1.29E-04	-1.06E-04	1.01E-04	-7.70E-05
100	0.316228	1.64E-04	-1.41E-04	1.31E-04	-1.09E-04

Table S8 - Results of the chronoamperometric and fiber-optic oxygen minisensor tandem studies of free enzyme (GOx) solution over the PB modified SPEs

Glucose Concentration*, mM	ItalSens PB – modified SPEs			
	Current at 180 sec, µA	DO at 180 sec, µmol/L	DO slope, µmol/L/sec	Enzyme Activity, U/µL
0.268	-0.293	154.67	-2.013	0.0122
0.357	-0.614	87.86	-3.155	0.0191
0.535	-0.972	22.678	-13.513	0.0819
0.775	-1.03	0	-6.48	0.039
0.994	-1.1	0	-19.54	0.118
1.226	-0.954	0	-30.13	0.183
1.463	-1	0	-42.87	0.260
2.0247	-1.45	0	-52.21	0.316
The glucose concentration values were confirmed via HPLC analysis				

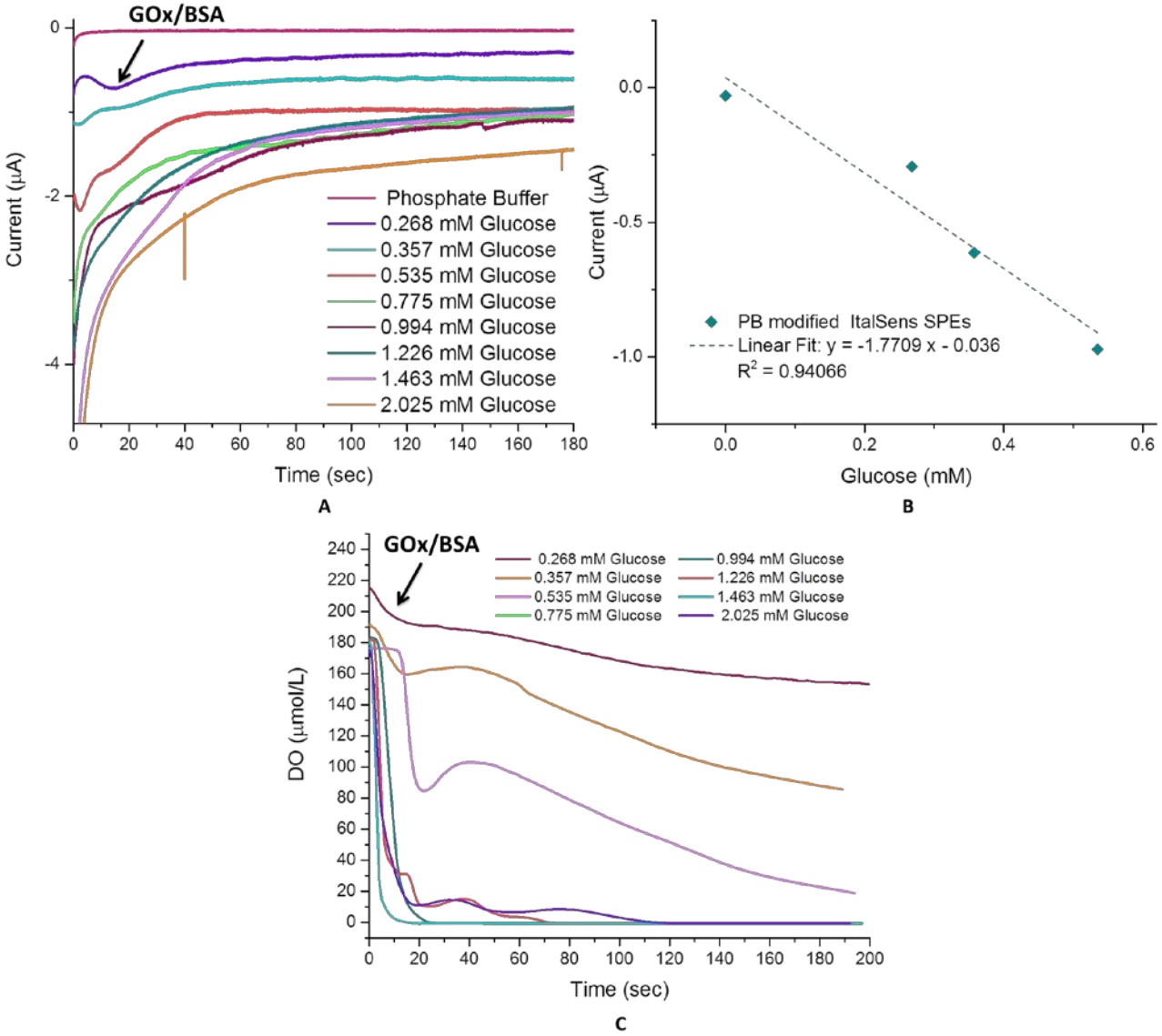

Figure S12 - The electrochemical response (A) and the oxygen consumption rates (C) measured for the glucose oxidation in the presence of a GOx/BSA mixture over PB modified SPEs (ItalSens). The calibration curve (B) was built for the linear electrochemical response of the PB modified SPEs towards glucose concentrations.

Table S9 - Results of the chronoamperometric and fiber-optic oxygen minisensor tandem studies of glucose biosensors in the presence of glucose.

GOx Stock	Stock B		Stock A	Stock B		Stock A	Stock B		Stock A	Stock B		Stock A
Glucose Concentration*, mM	2 layer current at 180 sec, µA	4 layer current at 180 sec, µA	4 layer current at 180 sec, µA	2 layer DO at 180 sec, µmol/L	4 layer DO at 180 sec, µmol/L	4 layer DO at 180 sec, µmol/L	2 layer DO slope, µmol/L/sec	4 layer DO slope, µmol/L/sec	4 layer DO slope, µmol/L/sec	2 layer Enzyme Activity, U/µL	4 layer Enzyme Activity, U/µL	4 layer, Enzyme Activity, U/µL
0	-0.334	-0.398	-0.29		-			-			-	
0.268	-0.327	-0.39	-0.300	228.33	199.12	167.31	0.316	0.987	0.314	0.0013	0.004	0.0013
0.357	-0.572	-0.473	-0.342	199.95	178.2	155.64	0.148	1.952	0.288	0.0006	0.0079	0.0012
0.535	-0.916	-0.655	-0.439	152.25	198.65	150.86	0.376	3.78	0.293	0.0015	0.0153	0.0012
0.775	-1.249	-0.908	-	127.54	58.47	-	0.236	10.65	-	0.001	0.043	-
0.994	-1.503	-1.152	-0.616	134.72	40.06	117.72	0.241	9.761	0.324	0.001	0.040	0.0014
1.226	-1.574	-1.313	-0.735	61.274	61.27	151.74	9.174	9.827	0.331	0.037	0.040	0.0014
1.463	-1.505	-1.437	-0.851	57.71	57.71	111.36	6.813	8.085	0.385	0.028	0.033	0.0016
2.0247	-	-1.394	-0.933	63.73	63.73	98.433	7.838	8.55	0.373	0.032	0.035	0.0015
The glucose concentration values were confirmed via HPLC analysis.												

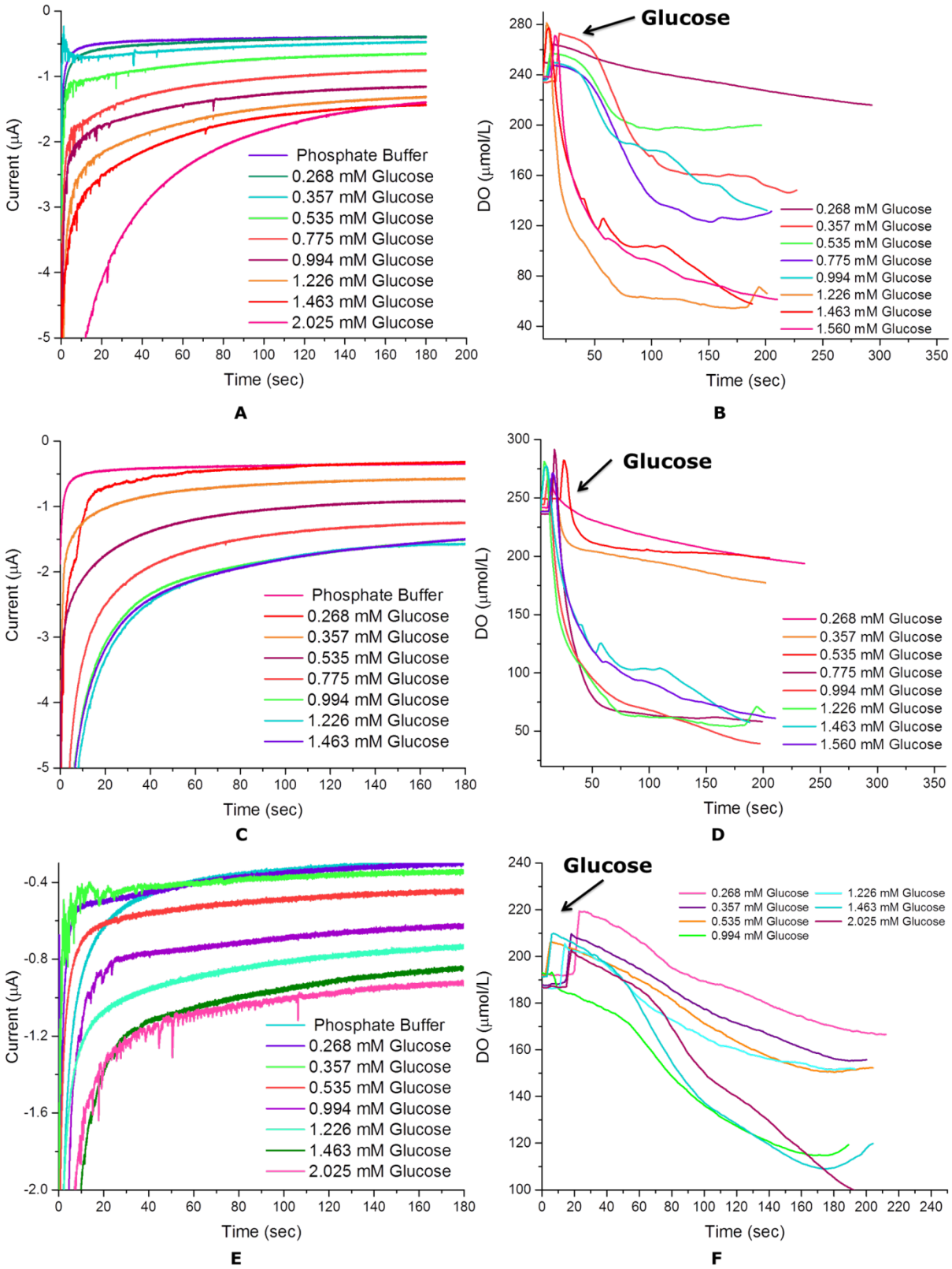

Figure S13 - The electrochemical response of the "two" layer GOx Stock B (A), "four" layer GOx Stock B (C) and "four" layer GOx Stock A (E) glucose biosensors in the presence of glucose. The oxygen consumption rates for "two" layer GOx Stock B (B), "four" layer GOx Stock B (D) and "four" layer GOx Stock A (F) glucose biosensors.

Table S10 - Results of the inductively coupled plasma mass spectrometry studies of glucose biosensors for Fe^{56} migration during cyclic voltammetry

sensor/parameter	time,sec	time point, sec	Fe56 in Kpi w/dilution factor, ppb	Scan Rate, mV/sec	Layers	Fe56 toal time point, ppb
S8, CV 1sc	202	202	267	10	2 layer	267
S8, CV 2sc	202	404	37.8			304.8
S8, CV 3sc	202	606	36			340.8
S8, CV 4sc	202	808	29.3			370.1
S8, CV 5sc	202	1010	66.4			436.5
S8, AM KPi	180	1190	69.6			506.1
S5, CV 1sc	102	102	59	20		59
S5, CV 2sc	102	204	61			120
S5, CV 3sc	102	306	43			163
S5, CV 4sc	102	408	60			223
S5, CV 5sc	102	510	50			273
S5, AM KPi	180	690	102			375
S6, CV 1sc	42	42	55	50		55
S6, CV 2sc	42	84	77			132
S6, CV 3sc	42	126	60			192
S6, CV 4sc	42	168	49			241
S6, CV 5sc	42	210	46			287
S6, CV 6sc	42	252	57			344
S6, CV 7sc	42	294	40			384
S6, CV 8sc	42	336	41			425
S6, CV 9sc	42	378	43			468
S6, CV 10sc	42	420	34			502
S6, CV 11sc	42	462	38			540
S6, CV 12sc	42	504	44			584
S6, AM Kpi	180	684	51			635
S23, CV 1sc	202	202	21.9	10	4 layer	21.9
S23, CV 2sc	202	404	23			44.9
S23, CV 3sc	202	606	36			80.9
S23, CV 4sc	202	808	37			117.9
S23, CV 5sc	202	1010	31.7			149.6
S23, AM KPi	180	1190	74.2			223.8
S24, CV 1sc	102	102	42	20		42
S24, CV 2sc	102	204	31.7			73.7
S24, CV 3sc	102	306	43			116.7
S24, CV 4sc	102	408	63.3			180
S24, CV 5sc	102	510	197.6			377.6
S24, AM KPi	180	690	93			470.6
S25, CV 1sc	42	42	24.7	50		24.7
S25, CV 2sc	42	84	20.7			45.4
S25, CV 3sc	42	126	172.2			217.6
S25, CV 4sc	42	168	224.9			442.5
S25, CV 5sc	42	210	382			824.5
S25, AM Kpi	180	390	47.3			871.8

Table S11 - Results of the inductively coupled plasma mass spectrometry studies of glucose biosensors for Fe^{56} migration during chronoamperometric studies

parameter/sensor	2 layer (10mV/sec)						2 layer (20mV/sec)					
Glucose (mM)	0	0.1	0.5	1	1.5	2	0	0.1	0.5	1	1.5	2
Current (μA)	-0.16	-0.241	-0.884	-1.75	-1.964	-2.114	-0.089	-0.136	-0.661	-1.556	-1.716	-1.832
Fe^{56} (ppb)	40.8	34.7	34.68	74.23	56.58	31.53	13.3	54.1	32.9	92.2	70.3	34.8
Total Fe^{56} (ppb)	272.52						297.6					

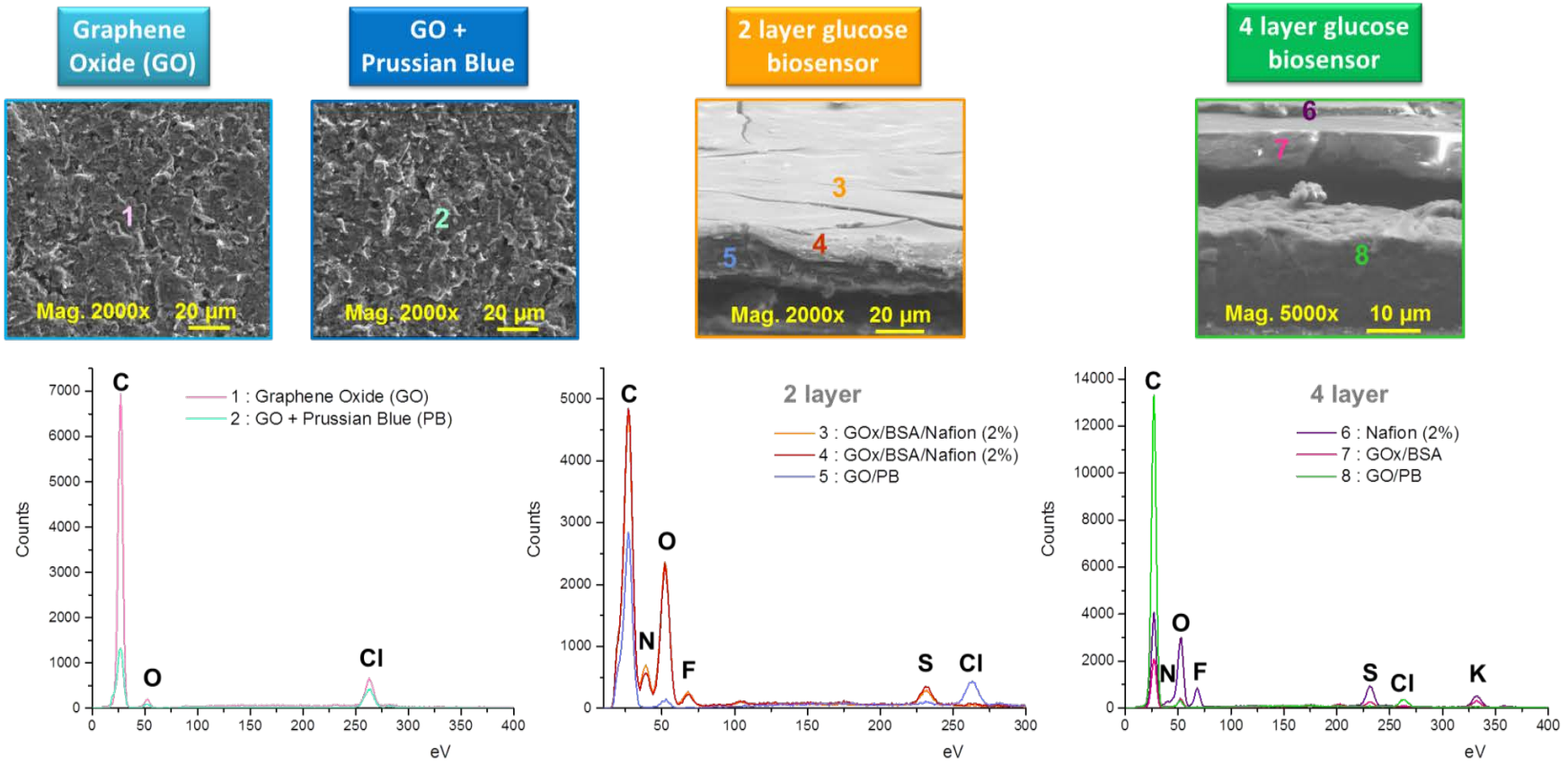

Figure S14 - SEM images and EDX spectra of graphene oxide (GO) film, GO film modified with Prussian Blue (PB), "two" and "four" layer glucose biosensors. The enlarged top views of GO film before (1) and after (2) modification with PB are shown. The layers for "two" and "four" layer glucose biosensors are shown in cross-section: (3),(4)-glucose oxidase (GOx)/bovine serum albumin (BSA)/Nafion (2%); (5), (8)-GO/PB; (6)-Nafion (2%) and (7)-GOx/BSA. The corresponding EDX spectra are presented below the SEM images.

Process and Systems Engineering Centre (PROSYS)
Department of Chemical and Biochemical Engineering
Technical University of Denmark
Søltofts Plads, Building 229
DK - 2800 Kgs. Lyngby
Denmark

Phone: +45 45 25 28 00
Web: www.kt.dtu.dk/forskning/prosys